Imperial College of Science, Technology and Medicine
Department of Physics

Selective Detection of Circularly Polarised Light using Chiral Organic Semiconductors

Matthew David Ward

Submitted in partial fulfilment of the requirements for the degree of
Doctor of Philosophy in Physics.
August 1, 2024

Abstract

Chiral organic semiconductors with sensitivity to circularly polarised light (CPL) handedness will enable miniaturised, low-cost, and wavelength-tuneable CPL photodetectors. These devices have the potential to revolutionise several technologies, including biosensing, quantum optics, and spintronics. In this thesis, chiral materials are applied to organic photodetector architectures to identify design rules that relate device architecture to conventional and CPL-selective figures of merit (FoM).

This thesis demonstrates the first published chiral fullerene phototransistor, reporting a photocurrent dissymmetry (g_{ph}) of $\leq 1.27 \pm 0.06$ for fullerenes with absorption dissymmetry factors (g_{abs}) of $\sim 10^{-3}$. This behaviour supports previous reports of g_{ph} enhancement relative to g_{abs} and is attributed to a CPL-selective shift of phototransistor threshold voltages.

This thesis also demonstrates a novel CPL-selective photodiode architecture using a blend of achiral poly(9,9-dioctylfluorene-alt-bithiophene) (F8T2) and chiral 1-aza[6]helicene (aza[6]H). Using this architecture, we show that conventional and CPL-selective photodetector FoM are antagonistic. We also show that CPL-selective FoM depend on the chiral donor layer and the achiral acceptor layer. Device optimisation yields photodiodes with the fastest response time reported to date ($t_{rise/fall} \approx 7\ \mu s$) with high CPL selectivity ($g_{ph} > 0.1$). We then model the behaviour of our F8T2:aza[6]H blends using transfer matrix optics (TMO). We find that TMO alone is insufficient to relate the device architecture to measured g_{ph}. We also explore the possibility of CPL-selective charge transport using time-of-flight mobility measurements. Hole transport is not observed to be CPL-selective and is highly dispersive, with a mobility of $\gtrsim 0.3\ cm^2V^{-1}s^{-1}$.

Finally, we develop two novel circularly polarised imaging systems, capable of spatially mapping circular dichroism in solid-state samples. The optimised system has a resolution of 100 μm and a sensitivity of 250 mdeg. This allows the processing of chiral samples to be observed *in situ* to accelerate processing optimisation.

Acknowledgements

I would like to express my gratitude to my supervisors, Prof. Alasdair Campbell J. Campbell, Prof. Jenny Nelson, and Prof. Matthew J. Fuchter for their outstanding supervision during the course of my PhD. I am especially grateful to Prof. Jenny Nelson for welcoming me into her group after the unfortunate passing of Prof. Alasdair Campbell J. Campbell towards the beginning of the second year of my PhD.

I also thank Dr. Jessica Wade for her constant guidance and support at every stage of the PhD, from experimental planning, interpretation of experimental results, and paper draft writing.

I thank Dr. Li Wan for his invaluable cleanroom and device fabrication training, without which none of the devices shown in this thesis would have been possible.

I thank Dr. Xingyuan Shi for his discussions on the subject of charge transport in organic semiconductors and for providing an electrical engineering perspective to high-speed measurements of photodetector bandwidth and time of flight mobility measurements.

I thank the academics of the EXSS department, the plastic electronics CDT and the staff of the EXSS group office.

I am also enormously grateful to my family and Brandon Guntoro. Without their constant emotional support, it is unlikely that I would have completed this PhD alongside the COVID-19 pandemic and the loss of my supervisor.

Declaration of Originality

Except where specific statement in each chapter is made to the work/data acquired and/or analysed by others, the work contained in this thesis is original and has not been submitted either wholly or in part to satisfy degree requirements at this or any other university.

Matthew David Ward
August 1, 2024

Copyright Statement

The copyright of this thesis rests with the author. Unless otherwise indicated, its contents are licensed under a Creative Commons Attribution-Non Commercial 4.0 International Licence (CC BY-NC). Under this licence, you may copy and redistribute the material in any medium or format. You may also create and distribute modified versions of the work. This is on the condition that: you credit the author and do not use it, or any derivative works, for a commercial purpose. When reusing or sharing this work, ensure you make the licence terms clear to others by naming the licence and linking to the licence text. Where a work has been adapted, you should indicate that the work has been changed and describe those changes. Please seek permission from the copyright holder for uses of this work that are not included in this licence or permitted under UK Copyright Law.

‘If we knew what it was we were doing, it would not be called research, would it?’

Albert Einstein

Contents

Abstract i

Acknowledgements iii

Declaration of Originality v

Copyright Statement vii

List of Figures xiii

List of Tables xxiv

Acronyms xxv

Chemical Names xxvii

1 Introduction 2

1.1 Context 2

1.2 Scope and Layout of Thesis 4

2 Background Theory 6

2.1 Introduction 6

2.2 Chiral Systems 6

2.3 Circularly Polarised Light and Circular Dichroism 7

2.4 The Molecular Origin of Circular Dichroism 18

2.4.1 Small Molecules 18

2.4.2 Larger Molecular Systems: Excitonically Coupled Chromophores 25

2.5 Chiral Organic Photodetector Devices 26

2.5.1 Organic Photoconductors 27

2.5.2 Organic Phototransistors 30

2.5.3 Organic Photodiodes 34

2.6 Photodetector Figures of Merit 36

2.6.1 Responsivity and External Quantum Efficiency 36

2.6.2 Dynamic Range 38

2.6.3 Response Speed 38

2.6.4 Dark Current and Dark Noise 41

2.6.5 Operational Lifetime 42

2.6.6 On-Off Ratio 43

2.6.7 Dissymmetry Factor of Photocurrent 43

2.7 Simulation of Absorption in CP-OPDs 44

2.7.1 Transfer Matrix Optics 44

2.7.2 Modifications for Optically Active Layers 50

2.8 Time of Flight Mobility 52

2.8.1 Principles of Operation 52

2.8.2 Spin-selective Excitation and Transport 56

3 Materials and Experimental Methods 58

3.1 Introduction 58

3.2 Materials 58

3.2.1 Bis[60]PCBM 58

3.2.2 F8T2 59

3.2.3 aza[6]H 59

3.2.4 PFO 60

3.2.5 PEDOT:PSS 60

3.2.6 Aluminium 60

3.3 Experimental Methods 60

3.3.1 Methods Used to Study Bis-PCBM Phototransistors 60

3.3.2 Methods Used to Study F8T2:aza[6]H Photodiodes 62

3.3.3 Methods Used in the Development of Circularly Polarised Imaging Systems 68

3.3.4 Methods Used in Device Modelling and Time of Flight Mobility Studies . 72

4 Bis-PCBM Phototransistor 74

4.1 Statement of Contribution 74

4.2 Motivation and Novelty 75

4.3 Introduction 75

4.4 Results and Discussion 78

4.5 Conclusion 91

5 F8T2:aza[6]H Photodiodes 92

5.1 Statement of Contribution 92

5.2 Motivation and Novelty 93

5.3 Introduction 94

5.4 Results and Discussion 95

5.5 Conclusion 105

5.6 Estimation of Experimental Uncertainties 106

6 Circularly Polarised Imaging System 107

6.1 Statement of Contribution 107

6.2 Motivation and Novelty 108

6.3 Introduction 109

6.4 Imaging system design 112

6.5 Results and Discussion 114

6.6 Conclusion 119

7 Device Modelling and Time of Flight Mobility 120

7.1 Statement of Contribution 120

7.2 Motivation and Novelty 120

7.3 Introduction 121

7.4 Results and Discussion 122

7.5 Conclusion 129

8 Conclusion **132**

8.1 Summary of PhD Work 132

8.2 Future Work 134

Bibliography **159**

A Reuse Permissions for Chapter 2 **160**

B Reuse Permission for Chapter 3 **161**

C Reuse Permission for Chapter 4 **164**

D Reuse Permission for Chapter 5 **166**

E Reuse Permission for Chapter 6 **168**

List of Figures

2.1 (a) A chiral molecule and it's non-superimposable mirror image, where the mirror plane has been drawn as a dotted line. (b) A non-exhaustive list of the categories of molecular chirality found in chemistry. The two principle forms discussed in this thesis are helical and inherent chirality. Adapted from [1] 8

2.2 (a,b) Elliptical, (c) linear and (d) circular polarisations (red) expressed as the sum of a linear sum of a linear polarisation confined to the x- (projection in orange) and y-plane (projection in blue). 10

2.3 Conventions for left- and right-handed circularly polarised light used in this work. Adapted from [2] (Public Domain) 11

2.4 A cross-sectional diagram of a Fresnel rhomb, indicating the phase change occurring at each internal reflection, the typical cutting angle for Quartz rhombs and the direction of the fast- and slow axis of this quarter waveplate. Adapted from [3] (Public Domain) 13

2.5 The electric field of elliptically polarised light (purple) expressed as the sum of a left- (red) and right-handed (blue) circularly polarised electric field. The ellipticity of the resultant electric field is shown here as θ. Adapted from [4] (Public Domain) 13

2.6 The precise (orange) and approximate (blue) equations for ellipticity expressed as a functions of ΔA. The percentage deviation (green) of the approximate expression from the precise expression becomes considerable ($> 1\%$) for $\Delta A > 0.213$. 16

2.7 Diagrams showing the direction of charge redistribution (black arrow) in achiral molecules (anthracene and coronene) and the two enantiomers of an achiral molecule (hexahelicene) during an electronic transition. The directions of the resulting electric and magnetic transition dipole moments are labelled $\boldsymbol{\mu}$ and $\mathbf{m}$, respectively. Note here that in the case of hexahelicene, we have simplified the directions of $\boldsymbol{\mu}$ and $\mathbf{m}$ to being either into or out of the plane for the straightforward explanation of the origin of circular dichroism in chiral organic molecules. In reality, these vectors will be misaligned for this transition by angle $\theta < 90^{\circ}$ (for the main band transition of hexahelicene, $\theta \approx 76^{\circ}$ [5]) which reduces the value of g according to Equation 2.35 24

2.8 (a) Splitting of excited state energy levels due to the interaction of two chirally arranged excitonically coupled chromophores. (b) Characteristic absorption and ellipticity spectra of excitonically coupled chromophores demonstrating Davydov splitting. (c) Model demonstrating the key parameters for the calculation of Davydov splitting: the electric transition dipole moment of each molecule ($\boldsymbol{\mu}_1$ and $\boldsymbol{\mu}_2$) and the displacement between the two dipole moments ($\mathbf{r}_{12}$). Reproduced from [6] with permission from the Royal Society of Chemistry. 25

2.9 The most common device architectures used for circularly polarised photodetectors. Plasmonic devices are not discussed in this work. Reproduced from [7] with permission from the Royal Society of Chemistry. 27

2.10 Step-by-step description of the photoconductive gain mechanism. (a) Electron and holes are excited by incident light. (b) Photogenerated electrons are rapidly extracted from the device at the positive terminal, whereas holes migrate with much slower velocity to the negative terminal. To maintain charge neutrality, electrons must be injected at the negative terminal as they are extracted from the positive terminal. This process repeats for many cycles (G_a) until electron-hole recombination occurs (c). Reproduced from [7] with permission from the Royal Society of Chemistry. 29

2.11 Organic transistor output characteristics (a), and transfer characteristics under the linear regime (b) and the saturated regime (c). Recreated from [8]. 33

2.12 Definitions of the rise and fall times (a), and bandwidth (b) of a photodetector. (a) Rise (fall) time is the time taken for the device photocurrent to increase (decrease) from 10% (90%) to 90% (10%) of its maximum photocurrent under square wave modulated illumination. (b) Bandwidth is the frequency of a sinusoid-modulated light source at which the photocurrent of the photodetector falls to -3 dB below the photocurrent measured at a modulation frequency of 0 Hz (i.e. continuous illumination). Reproduced from [7] with permission from the Royal Society of Chemistry. 39

2.13 The TMO model of a multilayer device on a transparent substrate. Here, j indicates the layer number (where m is the final layer in the multilayer stack), $E_j^{+/-}$ is the forward (+) and rearward (−) travelling optical electric field in layer j, n_j and k_j are the real and imaginary components of the complex refractive index of layer j and d_j is the thickness of layer j. T, T^*, T' correspond to the transmissivity at the substrate-multilayer interface, the air substrate interface, and the substrate-multilayer structure as a whole. R, R^*, R' corresponds to the reflectivity at the same interfaces. Recreated from [9]. 45

2.14 A simplified diagram of a typical ToF mobility measurement setup. Adapted from [10]. 53

2.15 Time of Flight (ToF) mobility measurement traces under the integration mode (a, b) and current mode (c, d) of measurement. ToF traces a) and c) are characteristic of low dispersion charge transport, indicating a low concentration of deep trap states and showing a clear transit time t_t. Traces b) and d) are characteristic of highly dispersive charge transport, where the arrival of carriers at the collecting electrode has been spread out by deep trap states. Adapted from [10]. 54

3.1 Molecular structures of the organic semiconductors used in this project. Due to the large number of Bis[60]PCBM enantiomers, the structures of these enantiomers are presented in Section 4. 59

3.2 Diagram of the experimental setup for CP photoFET measurements. As shown, the laser and polarising optics can be rotated out of position above the sample to allow the source, gate, and drain probes to be attached to each transistor with the aid of a camera. Once the source, drain, and gate electrodes have been connected, the laser and optics are rotated into position over the sample for measurements. Reproduced from [11] with permission from Wiley. 63

3.3 Experimental setup for the measurement of EQE, responsivity and spectral photocurrent dissymmetry. The device under test is illuminated with monochromatic light from a white light source that has passed through a scanning monochromator. Monochromatic light is chopped by an optical chopper and the chopped light is directed to a calibrated photodiode or the device under test. A linear polariser and Fresnel rhomb can be added in front of the beam to produce a circularly polarised beam. The photocurrent from the device under test and the calibrated photodiode are converted to voltages, which are measured via sensitive lock-in detection using a lock-in amplifier using the chopper controller signal as a reference frequency. Adapted from [7] 65

3.4 Experimental setup for measuring the linear dynamic range and current-voltage characteristics. Light from a high-power LED or laser is directed to a calibrated photodiode (for measuring light intensity) or the device under test. A linear polariser and quarter-wave plate may be added in the path of the light source for a circularly polarised beam. The intensity of the light source is controlled using a digital current source and the photocurrent of the calibrated photodiode and the device under test is measured using a source-measure unit. Adapted from [7] 66

3.5 Experimental setup for measuring the bandwidth, rise time and fall time. Light from a high-power LED or laser is split equally between a calibrated photodiode (for measurement of light intensity) and the device under test using a beamsplitter. A linear polariser and quarter-wave plate may be added in the path of the light source for a circularly polarised beam. For rise-time and fall-time measurements, a square-wave modulated light source should be used, and for bandwidth measurements, a frequency tuneable sinusoidally modulated light source should be used. The photocurrent of the device under test and the calibrated photodiode are converted to voltages using current preamplifiers and monitored using an oscilloscope. Reproduced with permission from [7] 67

4.1 The 13 pairs of bis[60]PCBM enantiomers, categorised into six bond types according to the positioning of the second adduct relative to 1,9 position of the first addend (A1): *cis*-2 (black), *cis*-3 (green), *e* (red), *trans*-2 (blue), *trans*-3 (orange) and *trans*-4 (purple) with dotted mirror planes depicted. For each isomer, R/S descriptors refer to addend stereochemistry and ^{f,s}C/^{f,s}A to the fullerene stereochemistry using the method defined by Diederich and Thilgen.[12] All isomer labels should be proceeded by "bis[60]PCBM", i.e., (S,S,^{f,s}C)13,14 becomes (S,S,^{f,s}C)13,14-bis[60]PCBM. The enantiomeric pairs contained within boxes represent those isolated in this study. 77

4.2 Experimental normalised CD spectra of one representative enantiomeric pair per substitution pattern in solution. Note that spectra here are expressed as molar extinction, $\Delta\varepsilon$, where the CD has been normalised for both the path length through the solution and the solution concentration. 80

4.3 a) Absorption dissymmetry factor g_{abs} of one enantiomer per pair of all the isolated bis[60]PCBM enantiomers. b) Six addition patterns on the cage (two types): non-inherently chiral with mirror symmetry (upper row) and inherently chiral with C2 symmetry (bottom row). c) Calculated CD spectra of the *e* isomer (*anti,S*)16,17 (left) and the *trans*-3 isomer (*S,S,* $^{f,s}C$)34,35 (right). The insets highlight the states with highest rotatory strength (state 25 and state 8) and the states with highest charge transfer character (state 43 and state 38). CT refers to the degree of charge transfer character, and e-h R indicates the root-mean-square distance of the electron–hole pair in Angstroms. The molecular pictures represent the distribution of the pair of "hole" (where the electron leaves upon excitation) and "electron" (where the excited electron goes to) for that excited state. On the bottom, electric and magnetic transition dipoles for the excited states 25 and 8 are displayed. 81

4.4 Device characteristics of bis[60]PCBM enantiomer pure photo-FETs. a,b) Variation of transfer curves of *e* isomer (anti,R)16,17-bis[60]PCBM (a) and *trans*-2 isomer (R,R, ^{f,s}A)49,59-bis[60]PCBM (b) upon exposure to left-handed and right-handed CPL with 95 and 0.34 $mW\ cm^{-2}$, respectively, compared to curves in the dark. $V_{DS} = 20\ V$. Dissymmetry factors for the photocurrent generation (g_{ph}) and its associated error are given by the green curve and shaded area, respectively. c) The light-intensity response of the *e* isomer (anti,R)16,17-bis[60]PCBM photoFET from 0.48 to 150 $mW\ cm^{-2}$ at different gate voltage from 0 to 100 V, $V_{DS} = 20\ V$. d) The device structure of photoFETs. e) Output characteristics of *e* isomer (anti,R)16,17-bis[60]PCBM photoFET at gate voltage between 0 and 100 V. f) Time-resolved L-CPL and R-CPL photoresponse was measured at 405 nm with an intensity of 92.3 $mW\ cm^{-2}$, a frequency of 0.05 Hz and $V_{DS} = V_{GS} = 40\ V$, showing a high stability and reversibility. 84

4.5 Intensity dependence (unpolarised light) of photoFET $I_{DS,ph}$ in the two device modes: photoconductive (a) and photovoltaic (b). Filled circles indicate experimental data and solid lines represent fits to Equation 4.1 (a) and Equation 4.2 (b). The black arrow indicates the direction of increasing V_{GS} from 44.94 V to 95.51 V. 86

4.6 Transfer curves of a racemic (anti,R/S)16,17-bis[60]PCBM photoFET in the absence of light and under L-CPL, R-CPL and unpolarised illumination at an intensity of 3.4 $mW\ cm^{-2}$. This device has been measured under each handedness of CPL twice in the following order: L-CPL #1, R-CPL #1, R-CPL #2 and L-CPL #2. g #1 and g #2 correspond to the photocurrent dissymmetry of racemic devices using the photocurrents of L-CPL #1 and R-CPL #1, and L-CPL #2 and R-CPL #2, respectively. 88

4.7 Saturation regime (black) $V_{DS} = 100\ V$ and linear regime (red) $V_{DS} = 20\ V$ transfer characteristics under dark conditions for the e isomer (anti,R)16,17-bis[60]PCBM photoFET device. 90

5.1 Absorption and g_{abs} spectra of F8T2 films and F8T2/C_{60} bilayers before (as cast) and after thermal annealing. As shown, the high g_{abs} chiral phase is only induced after thermal annealing and is not significantly reduced by adding a thermally evaporated C_{60} layer. Further spectroscopic and morphological characterisation of F8T2:aza[6]H blends has been carried out in our previous work and found to be consistent with this study.[13] 96

5.2 Influence of the blend donor layer thickness, t_D, on CP OPD performance while keeping the acceptor layer thickness at 30 nm. a) Molecular structures of F8T2 (top), [M]-aza[6]H and [P]-aza[6]H (middle), and the OPD architecture (bottom). b) Ellipticity of F8T2:[M]- (solid) and [P]-aza[6]H (dashed) blend layers. c) Unpolarised EQE and d) g_{ph} for F8T2:[M]-aza[6]H OPDs at 0 V bias. e) Current–voltage curves of F8T2:[M]-aza[6]H based OPDs under dark conditions (dashed) and unpolarised light (solid; with incident radiation 0.55 $mW\ cm^{-2}$, $\lambda_{ex} = 473\ nm$). f) g_{ph} of F8T2:[M]-aza[6]H (solid) and F8T2:[P]-aza[6]H (dashed) OPDs under reverse bias (0.21 $mW\ cm^{-2}$, $\lambda_{ex} = 473\ nm$). Shaded regions surrounding curves represent the estimated experimental uncertainty in the data. 98

5.3 g_{abs} as a function of F8T2:aza[6]H film thickness (with corrections for reflection), at wavelengths of (a) 482 nm, (b) 455 nm and (c) 510 nm. Distinct from our prior studies with F8T2:aza[6]helicene films, $|g_{abs}|$ increases with increasing film thickness, even after reflection losses are accounted for.[14, 15] We attribute this to the use of thinner films in this study ($t_A < 150$ nm) relative to our prior work, which results in coherent thin-film interference in our F8T2:aza[6]H, which is not accounted for in the reflection loss correction devised by Schulz *et al.* and implemented here.[14] 99

5.4 Influence of C_{60} acceptor layer thickness, t_A, on CP OPD performance with a fixed donor layer thickness of 77 nm. a) Unpolarised EQE and b) g_{ph} for F8T2:[M]- (solid) and [P]-aza[6]H (dashed) OPDs at zero bias. c) Current–voltage curves of F8T2:[M]-aza[6]H devices under dark conditions (dashed) and unpolarised light (solid; with incident radiation 0.57 $mW\ cm^{-2}$, $\lambda_{ex} = 473$ nm). d) g_{ph} of F8T2:[M]-aza[6]H (solid) and F8T2:[P]-aza[6]H (dashed) OPDs under reverse bias **(**0.22 $mW\ cm^{-2}$**,** $\lambda_{ex} = 473$ nm**).** Shaded regions surrounding curves represent the estimated experimental uncertainty in the data. 100

5.5 Device characteristics of optimised OPDs incorporating [M]-, [P]-, or [rac]-aza[6]H chiral additives. a) Reverse-biased unpolarised EQE and b) reverse biased g_{ph} for OPDs fine-tuned for operation in CD band **1** (solid, -1 V bias) or CD band **2** (dashed, -0.5 V bias). Note that the quarter-wave plate used in b) does not operate at a quarter-wave retardance below 400 nm (Grey). Unpolarised LDR of c) band **1**-oriented OPDs and d) band **2**-oriented OPDs, where dashed lines indicate the line of best fit. e) Non-CP switching response of band **1** (solid) and band **2** (dashed) OPDs under pulsing by a 2 kHz square-wave modulated laser. f) Frequency response of OPDs of band **1** (solid) and band **2** (dashed) OPDs, where the horizontal black line indicates the -3 dB point where the device bandwidth is determined. Incident radiation $\lambda_{ex} = 473$ nm for obtaining c) and d); and $\lambda_{ex} = 488$ nm used for e) and f). The shaded regions surrounding the curves represent the estimated experimental uncertainty in the data. 101

5.6 Proposed mechanism for the influence of a) t_D and b) t_A on CP OPD performance. For F8T2:[M]-aza[6]H devices, R-CPL is more strongly absorbed than L-CPL in the donor layer, therefore, the intensity of light that reaches the D–A interface is greater under L-CPL than under R-CPL, leading to an inversion of g_{ph} relative to g_{abs}. For thin t_A layers, the L-CPL transmitted through the achiral C_{60} layer is reflected off the back aluminium electrode, after which the handedness inverts (L-CPL becomes R-CPL, and vice versa). Following reflection, the CPL is of the appropriate handedness to be more preferentially absorbed by the chiral donor layer near the interface. 103

5.7 Absorption spectrum of a 50 nm C_{60} film. We attribute the lack of significant enhancement of $|g_{ph}|$ corresponding to the high energy band (**1**) to the greater absorbance at this wavelength relative to the absorbance at the wavelength of the longer wavelength band (**2**). 104

6.1 Schematics of the two- (a) and one-camera (b) circular dichroism imaging systems developed in this work alongside a photograph of the optimised system (c) with a black 3D printed enclosure to block stray light and enable system portability. . 112

6.2 A screenshot of the custom open source python graphical user interface used to control the one- and two-camera circular dichroism imagers. 113

6.3 Circular dichroism images of solid state F8BT:[P]-aza[6]H (a, b, c) and F8BT:[M]-aza[6]H (d, e, f) films at annealing temperatures of 50°C (a, d), 140°C (b, e), and 200°C (c, f) taken using the two camera circular dichroism imaging system at a wavelength of 470 nm. In each subfigure, "Left" and "Right" indicate the transmitted intensities of L-CPL and R-CPL (respectively), $\Delta A = A_L - A_R$ and "CD" is the measured ellipticity calculated using equation 2.7. The z-axis of "Left" and "Right" correspond to the intensity values of each camera pixel on a unitless linear intensity scale from 0-1. The z-axis of "ΔA" images are, like absorbance, unitless. The z-axis of "CD" images responds to the ellipticity of each pixel expressed in degrees. 115

6.4 Circular dichroism images of solid state F8BT:[P]-aza[6]H (a, b, c) and F8BT:[M]-aza[6]H (d, e, f) films at annealing temperatures of 50°C (a, d), 140°C (b, e), and 200°C (c, f) taken using the one camera circular dichroism imaging system at a wavelength of 470 nm. In each subfigure, "Left" and "Right" indicate the transmitted intensities of L-CPL and R-CPL (respectively), $\Delta A = A_L - A_R$ and "CD" is the measured ellipticity calculated using equation 2.7. The z-axis of "Left" and "Right" correspond to the intensity values of each camera pixel on a unitless linear intensity scale from 0-1. The z-axis of "ΔA" images are, like absorbance, unitless. The z-axis of "CD" images responds to the ellipticity of each pixel expressed in degrees. 116

6.5 Spatially averaged ellipticity of solid state F8BT:[M]-aza[6]H and F8BT:[P]-aza[6]H samples measured using the one camera system at a wavelength of 470 nm. 117

6.6 Spatially patterned solid state films of thermally annealed F8BT:[P]-aza[6]H with ring (a) and step (b) profiles (see Section 3.3.3). Images were captured using the 1-CCDI system under ambient conditions at a wavelength of 470 nm and using a conventional visible light camera (inset, scale in cm). Note that the circular pattern (a) is not noticeable when using the visible light camera, and as such, the intended patterning shape is indicated by a dotted line overlay. 118

6.7 A direct cross-comaprison between CD images of spatially patterned solid state F8BT:[P]-aza[6]H captured using Beamline 23 at the diamond light source (a) and the one camera CD imaging system (b). 118

7.1 Real (n, filled circles) and imaginary (k, crosses) components of the complex refractive indices of the device layers in a ITO/PEDOT:PSS/F8T2:[P]-aza[6]H/C_{60}/Al photodiode. 123

7.2 Transfer matrix optics model of an ITO/PEDOT:PSS/F8T2:[P]-aza[6]H/C_{60}/Al photodiode excited at a wavelength of 470 nm. Here a C_{60} thickness of 30 nm and F8T2:[P]-aza[6]H thicknesses of 77 nm (a) and 140 nm (b) are studied. $|E|^2$ is the intensity of the optical electric field, Q is the time-averaged absorption of optical power, and g_Q indicates the difference in time-averaged absorption of optical power under L- and R-CPL normalised by their average (i.e. $g_Q = 2(Q_L - Q_R)/(Q_L + Q_R)$). 125

7.3 Transfer matrix optics model of an ITO/PEDOT:PSS/F8T2:[P]-aza[6]H/C_{60}/Al photodiode excited at a wavelength of 510 nm. Here a F8T2:[P]-aza[6]H thickness of 77 nm and a C_{60} acceptor layer thickness of 10 nm and (a) and 40 nm (b) are studied. $|E|^2$ is the intensity of the optical electric field, Q is the time-averaged absorption of optical power, and g_Q indicates the difference in time-averaged absorption of optical power under L- and R-CPL normalised by their average (i.e. $g_Q = 2(Q_L - Q_R)/(Q_L + Q_R)$) 127

7.4 Time of flight mobility current transient for a glassy phase PFO sample with a thickness of 1.8 μm at a bias of 10 V. 128

7.5 Time of flight mobility transients of 2.131 ± 0.045 μm thick samples of F8T2:[M]-aza[6]H measured using unpolarised (a) and circularly polarised (b) excitation at 470 nm under 5 and 10V biases 130

List of Tables

2.1 Amplitude and phase conditions for the three common polarisations of light. . . 9

2.2 Summary of the key figures of merit for all CP selective photodetectors published to date. The measurement conditions for these figures correspond to the same conditions which yield the greatest photocurrent dissymmetry, not simply the optimum reported value in each case. Missing figures of merit are marked by grey cells and figures of merit which do not apply to the device architecture reported are marked with an "x". Where figures of merit have not been reported, they have been extracted from graphical data using data extraction software where possible. *These values have been incorrectly reported in their original articles and have been corrected here. Reproduced from [7] with permission from the Royal Society of Chemistry. 37

3.1 List of parts used to assemble the two- and one-camera CD imaging systems. Prices are accurate at the time of writing, September 2022. 71

6.1 Comparison of previously published CD-imaging systems. 110

Acronyms

CD Circular Dichroism.

CISS Chirality Induced Spin Selectivity.

CPL Circularly Polarised Light.

CW Continuous Wave.

EQE External Quantum Efficiency.

HOMO Highest Occupied Molecular Orbital.

L-CPL Left-handed Circularly Polarised Light.

LDR Linear Dynamic Range.

LUMO Lowest Unoccupied Molecular Orbital.

MMSE Mueller Matrix Spectroscopic Ellipsometry.

NEP Noise Equivalent Power.

OEF Optical Electric Field.

OPC Organic Photoconductor.

OPD Organic Photodiode.

OPT Organic Phototransistor.

OPV Organic Photovoltaic.

OSC Organic Semiconductor.

PEM Photoelastic Modulator.

QWP Quarter-Wave Plate.

R-CPL Right-handed Circularly Polarised Light.

TMO Transfer Matrix Optics.

ToF Time of Flight.

Chemical Names

aza[6]H 1-aza[6]helicene.

bis[60]PCBM Dimethyl 4,4'-[61,62-diphenly,3'H,3"H-dicyclopropa(C_{60}—I_h)[5,6]fulleren-1,9:X,Y-diyl]dibutanoate.

F8T2 Poly(9,9-dioctylfluorene-alt-bithiophene).

PEDOT:PSS Poly(3,4-ethylenedioxythiophene):poly(styrenesulfonate).

PFO Poly(9,9-di-n-octylfluorenyl-2,7-diyl).

Chapter 1

Introduction

1.1 Context

Organic Photovoltaic (OPV)[1] devices have made significant strides in recent decades. Beginning from single layer devices with examples as early as 1973 demonstrating power conversion efficiencies below 10^{-4}% [16, 17], performance has grown rapidly through the development of the bilayer heterojunction architecture (0.04% [18]), the bulk heterojunction (2.9% [19]) and, more recently, ternary systems with efficiencies exceeding 19% [20]. With power conversion efficiencies approaching that of commercially available monocrystalline n-Si heterojunction cells ($\sim$ 20% [21]), there is a strong argument that the application of OPVs to commercial energy generation has reached maturity, with a number of pilot projects already complete and generating solar energy[22].

In light of the maturation of organic solar cells, increased attention has been paid to the advancement of other organic semiconductor architectures that leverage photovoltaic and photoconductive behaviour. This includes Organic Photoconductor (OPC), Organic Phototransistor (OPT) and Organic Photodiode (OPD) architectures in their use as photodetectors. Unlike organic solar cells, many figures of merit of these devices already meet or exceed those of their

[1] Acronyms for commonly used terms and abbreviations for chemical names are provided in the sections **Acronyms** and **Chemical Names**, respectively.

commercial inorganic counterparts, such as their high (> 100%) External Quantum Efficiency (EQE) due to gain mechanisms absent in organic solar cells (see Section 2.5.1)[23] and their sensitivity to low light levels due to low dark noise (i.e. Detectivity, see Section 2.6.4)[24]. While there is active research in the further improvement of the figures of merit of organic photodetectors, there is also interest in exploiting novel properties of organic photodetectors that are absent in their inorganic counterparts, such as flexibility, tuneability, and wavelength selectivity (e.g. for colour imaging applications). [24, 25, 26, 27] In this thesis we turn our attention to the possibility of using chiral organic semiconductors to achieve selectivity in the detection of circularly polarised light.

Most inorganic and organic photodetectors are not selective in their response to polarised light, such as circularly polarised light. This poses a challenge for applications that require the selective detection of circularly polarised light and makes the miniaturisation of these technologies impractical. Applications include encrypted light-based communications,[28, 29] polariser- and retarder-free Stokes imaging without the need of complex metasurfaces,[30] multichannel data processing,[31] determination of the absolute configuration of chiral molecules,[32] polarisation-enhanced environmental monitoring through next-generation machine vision [33, 34, 35] and detection of chiral biomarkers in medical imaging [36].

Achieving a selective photoresponse to circularly polarised light using commercial photodetectors requires the use of filters which have a number of disadvantages. For example, the need for several optical components reduces the compactness of the system and increases the cost of mass manufacturing, since each optical element requires additional manufacturing steps. Further, birefringent circular polarisation filters operate effectively at single wavelengths, requiring many costly filters to cover a wide wavelength range. While passive broadband filters exist, their ability to selectively filter circularly polarised light is either imperfect (i.e. Using achromatic quarter-wave plates), costly (using superachromatic quarter-wave plates), or bulky (using a fresnel rhomb). Active filters, such as commercial photoelastic modulators (PEMs), enable rapid switching between the transmission of Left-handed Circularly Polarised Light (L-CPL) and Right-handed Circularly Polarised Light (R-CPL) over a broad wavelength range, however, these systems are large, making them unsuitable for portable applications, and are

often prohibitively expensive (>£10,000).

The objective of this project is to develop novel organic photodetectors with intrinsic selectivity for circularly polarised light, without the need for additional optics. This can be achieved by using chiral organic semiconductor molecules as the photoactive layer in these devices.

Chiral organic molecules demonstrate Circular Dichroism (CD), that is, one enantiomer of a chiral molecule selectively absorbs L-CPL and the other enantiomer selectively absorbs R-CPL.[37] As a result, by incorporating one enantiomer of a chiral organic semiconductor into the active layer of an organic photodetector device, the absorption of light and the resulting photoresponse of the device can become selective to the handedness of circularly polarised light used to illuminate it. This has the potential to drastically reduce the complexity and cost of the selective detection of circularly polarised light and the technology that makes use of selective CPL detection, corresponding to a reduction in the cost and size of systems that make use of circularly polarised light.

The key challenge to the development of photodetectors is the simultaneous optimisation of conventional device figures of merit, such as EQE, and degree of selectivity of the devices photoresponse to the detection of circularly polarised light. This is a result of the fact that device properties such as layer morphology, layer thickness, and processing conditions that optimise conventional device figures of merit may reduce the selectivity of the device's photoresponse to circularly polarised light and *vice versa*. Details of the balanced optimisation of the CP selectivity and conventional device figures of merit will be discussed throughout this thesis.

1.2 Scope and Layout of Thesis

This thesis presents the work performed since 2018 following the optimisation of several chiral blend systems (chiral small molecule additive / achiral polymer blend) by Wade, Wan *et al.*[15, 38] The thesis is arranged as follows:

Chapter 2 provides the background necessary to understand chiral molecular systems and the

fundamental origins of their selective interaction with CPL. This chapter will also introduce the three main organic photodetector architectures (photodiodes, phototransistors and photoconductors), discuss the figures of merit necessary to quantify the performance of photodetectors (both general and those specific to CPL detection), and provide a summary of the figures of merit of published devices that demonstrate CPL selectivity. Finally, this chapter also discusses both Transfer Matrix Optics (TMO) and Time of Flight (ToF) theory, for modelling light absorption and charge transport, respectively, in the materials under study.

Chapter 3 details the materials used in this work and both the experimental protocols and the equipment developed for the fabrication and testing of photodetectors sensitive to CPL.

Chapter 4 presents the first published work of this thesis based on the incorporation of single enantiomers of the chiral acceptor bis[60]PCBM into a chiral organic phototransistor architecture sensitive to CPL.

Chapter 5 presents the second published work of this thesis based on the use of a chiral blend system of F8T2 and aza[6]H previously developed by Wade, Wan *et al.* as the donor layer and achiral C60 as the acceptor layer in a planar heterojunction organic photodiode. This study explores the structure function relationship of photodiodes making use of chiral donors and achiral acceptors and proposes a heuristic model of device behaviour.

Chapter 6 describes the development of a novel imaging system that can measure the spatial uniformity of the circular dichroism in chiral solid-state samples *in-situ* during the solution processing of these samples. This device is intended to accelerate the rate at which the post-processing of chiral samples is optimised.

Chapter 7 builds upon the work of Chapter 5 by developing a Transfer Matrix Optics model of the photodiode architecture to understand the structure-function relationship of this device at a fundamental level.

Chapter 8 summarises the main findings of this work, discusses any unanswered questions, and future studies which could be carried out to resolve these unanswered questions.

Chapter 2

Background Theory[1]

2.1 Introduction

In this section, we will introduce the basic concepts necessary to understand the properties of chiral materials and their interaction with circularly polarised light. We will then discuss the fundamentals of organic photodetector devices, outline the figures of merit that quantify their performance, and describe how the incorporation of chiral systems in these devices can be used to selectively detect circularly polarised light. This section also presents existing examples of organic photodetectors in the literature and cross-compares their figures of merit to suggest an optimal design strategy for highly selective circularly polarised photodetectors. Finally, this section will review the theory of Transfer Matrix Optics (TMO) and Time of Flight (ToF) mobility to enable the modelling of optical absorption and charge transport within photodetector devices.

2.2 Chiral Systems

A chiral object is one that cannot be superimposed on its own mirror image (Figure 2.1). This is due to the lack of a mirror plane, centre of inversion or a rotation-reflection axis. On the

[1]Reuse permissions for this chapter have been included in the appendices.

other hand, objects that can be superimposed on their mirror images are said to be achiral.[37] Chirality can arise in molecular structures and can be categorised into several groups (Figure 2.1). The two principal forms discussed in this thesis are helical chirality and inherent. Inherent chirality is defined as *"arising from the introduction of a curvature in an ideal planar structure that is devoid of perpendicular symmetry planes in its bidimensional representation"* [39]. In summary, this refers to a molecular structure whose structure is achiral when represented in two dimensions but demonstrates chirality when accounting for its curvature into the third dimension. This form of chirality can occur in molecules such as calixarenes[40] and chiral fullerenes[11], with the latter being studied in this work. Helical chirality refers to chirality arising from the arrangement of atoms in a molecule along a screw rotation.[41] The textbook examples of helical chirality are the helicenes (Helical example, Figure 2.1), consisting of benzene rings joined together in a circular pattern to form a left- or right-handed helix. In prior studies by the Campbell and Fuchter groups [38, 42, 13, 43, 44, 45, 46] and in this work [47], we study a 6 ring member of the helicene family: 1-aza[6]helicene (aza[6]H hereafter).

A unique property of chiral molecules is their selective absorption and emission of circularly polarised light.

2.3 Circularly Polarised Light and Circular Dichroism

As is commonly known, most unfiltered light sources are unpolarised,[2] that is, the direction of the electric field vector of light emitted by the source is random as a function of time and distance from the emitter.[48] Polarised light, on the other hand, may be considered as a superposition of two orthogonal linear polarisations of light aligned in the x and y planes, where the electric field is propagating in the z direction, the magnitudes of the components of the x and y planes are A_x and A_y, respectively, and the phase difference between the components of the x and y planes is ϕ (Figure 2.2).[48] For polarised light, the most general state of polarisation is elliptical, where the electric field vector rotates clockwise or anticlockwise in an ellipse as it

[2] As discussed by Hecht, more appropriate terms are *natural light* or *randomly polarised light*, but we will use *unpolarised light* throughout as this is more commonly used in the field.[48]

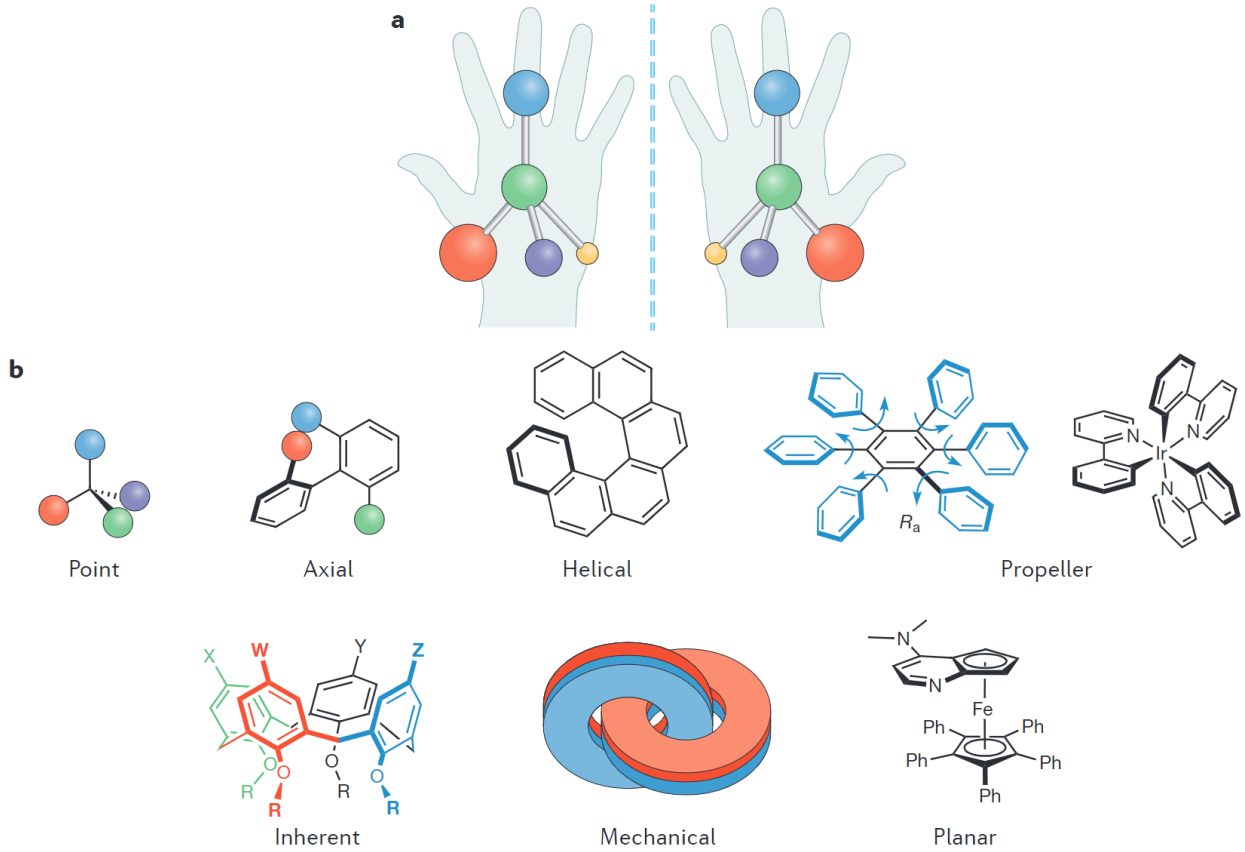


Figure 2.1: (a) A chiral molecule and it's non-superimposable mirror image, where the mirror plane has been drawn as a dotted line. (b) A non-exhaustive list of the categories of molecular chirality found in chemistry. The two principle forms discussed in this thesis are helical and inherent chirality. Adapted from [1]

Table 2.1: Amplitude and phase conditions for the three common polarisations of light.

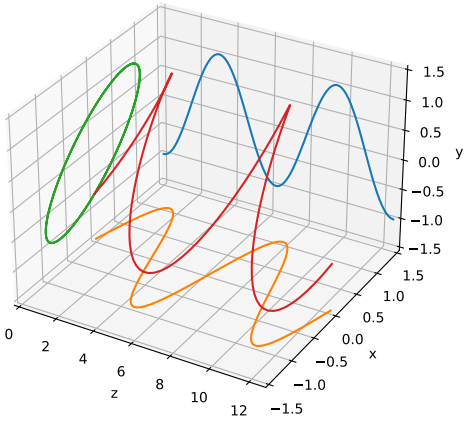
Polarisation	**Amplitude**	**Phase**
Elliptical	$A_x = A_y$	$\phi \neq n\pi/2,\ n \in \mathbb{Z}$
	$A_x \neq A_y$	$\phi \neq m\pi,\ m \in \mathbb{Z}$
Linear	$A_x = A_y$	$\phi = n\pi/2$, even values of n
	$A_x \neq A_y$	$\phi = m\pi, m \in \mathbb{Z}$
Circular	$A_x = A_y$	$\phi = n\pi/2$, odd values of n

propagates through space (Figures 2.2a and 2.2b).[48] When $A_x = A_y$, elliptical polarisation arises when $\phi \neq n\pi/2$, where $n \in \mathbb{Z}$ (Figure 2.2a). When $A_x = A_y$ *and* $\phi = n\pi/2$, there are two special cases. For even values of n, there is a half-wavelength phase lead/delay and the electric field is linearly polarised, which means that the electric field is confined to one plane as it propagates in the z direction (Figure 2.2c). When n is odd, there is a quarter-wavelength phase lead/delay and the electric field is circularly polarised, meaning that the electric field traces a circle in a clockwise or anticlockwise direction as it propagates in the z direction (Figure 2.2d).[48] For the case where $A_x \neq A_y$, linearly polarised light is generated for $\phi = m\pi$, where $m \in \mathbb{Z}$, and all other values of ϕ produce elliptically polarised light.[48]

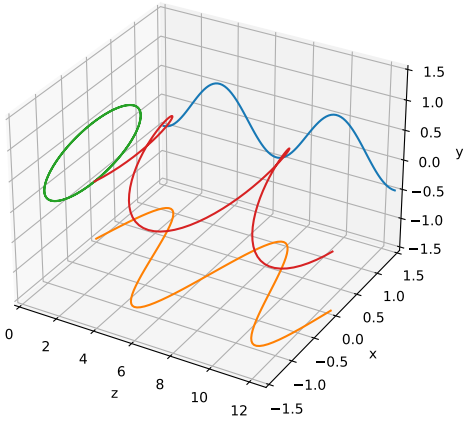
Circular and elliptical polarisations of light may be described as left-handed (L-) or right-handed (R-) depending on whether the electric field vector rotates clockwise or anticlockwise as it propagates in the z direction.[48] There are two conflicting definitions for labelling left- and right-handed polarisations, both of which are in active use.[3][49, 50, 51, 52] In this thesis, we use the definitions shown in Figure 2.3, as this matches the same definition of circularly polarised light used by the commercial CD spectrometer used in this work.[53] This spectrometer is used as a benchmark to ensure consistency between characterisation techniques.

As shown in Figure 2.3, circularly polarised light is generated using a Linear Polariser (LP) and a Quarter Waveplate (QWP). The role of the LP is to linearly polarise light from an unpolarised light source. The linear polariser is aligned at a 45°angle to the coordinate system, such that $A_x = A_y$ and $\phi = 0$ (Figure 2.2c). To convert linearly polarised light to circularly polarised light, the required quarter-wavelength phase lead/delay is introduced using a birefringent or fresnel rhomb quarter-waveplate. In the case of a birefringent quarter waveplate, the waveplate

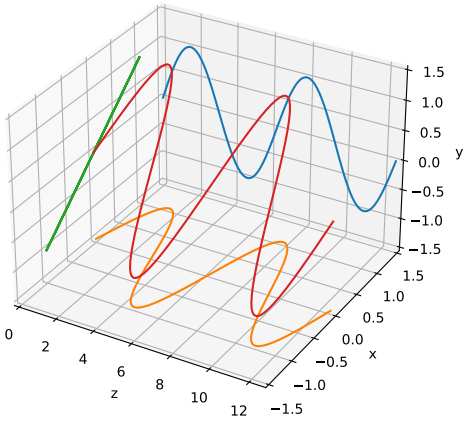
[3]Determining which of these definitions is "correct" is left as an exercise for the reader.



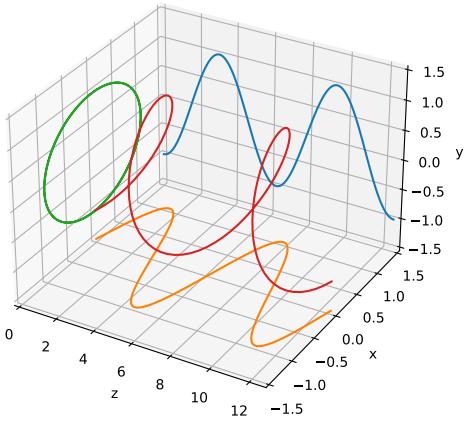
(a) Elliptical polarisation: Amplitude match and phase mismatch



(b) Elliptical polarisation: Magnitude mismatch and phase match



(c) Linear polarisation



(d) Circular polarisation

Figure 2.2: (a,b) Elliptical, (c) linear and (d) circular polarisations (red) expressed as the sum of a linear sum of a linear polarisation confined to the x- (projection in orange) and y-plane (projection in blue).

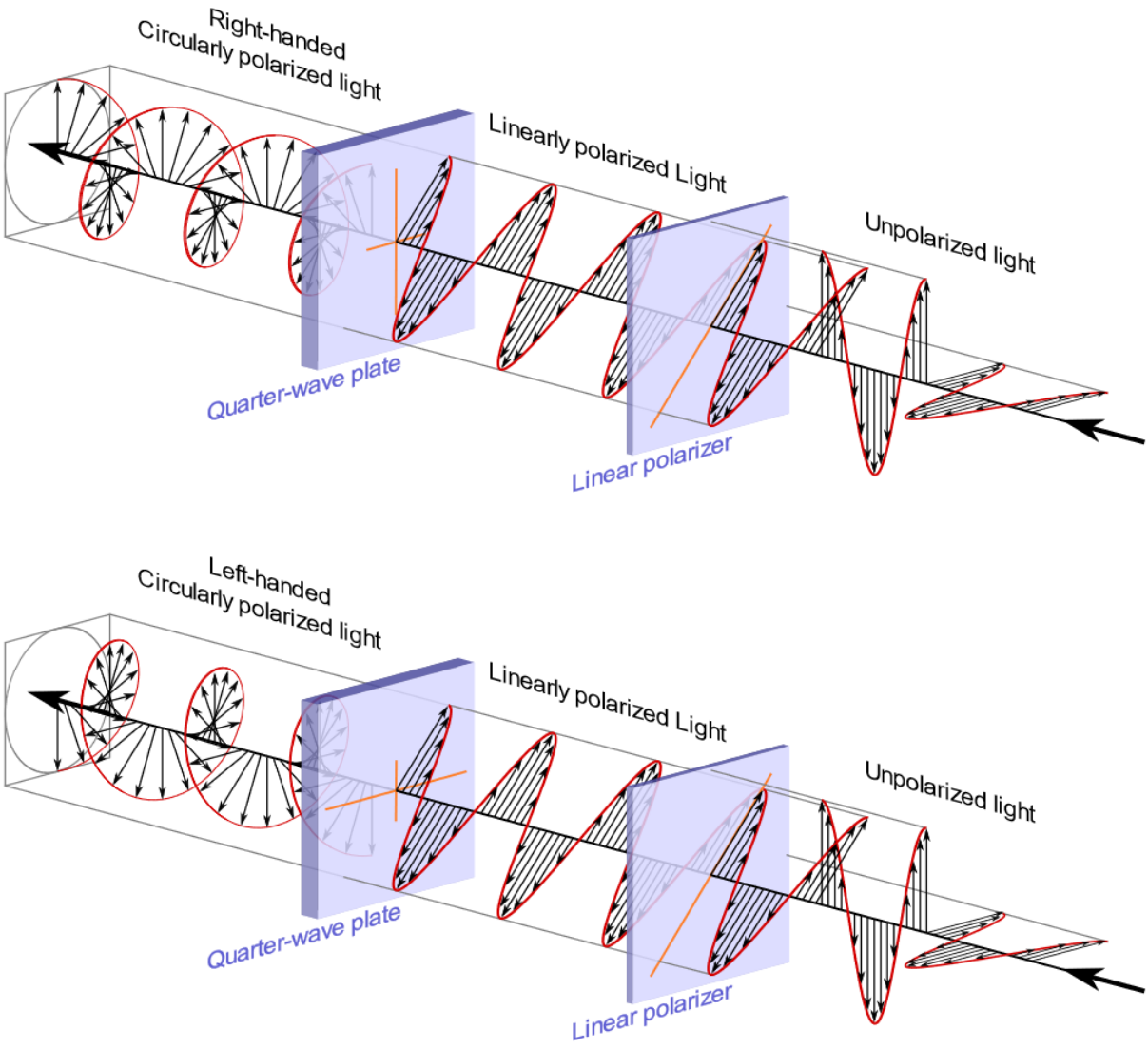


Figure 2.3: Conventions for left- and right-handed circularly polarised light used in this work. Adapted from [2] (Public Domain)

has two orthogonal axes - the fast and slow axes - which have different refractive indices (n_f and n_s, respectively). When the vertical and horizontal components of circularly polarised light are aligned along the fast and slow axes of a birefringent plate, the phase difference between these two components increases proportionally with the transmission distance through the plate, d:

$$\phi = \frac{2\pi}{\lambda} d\,(n_s - n_f) \tag{2.1}$$

In the case of a birefringent quarter waveplate, d is finely tuned such that the decrease in phase difference between the vertical and horizontal components is a quarter wavelength, converting linearly polarised light to circularly polarised light. [48] Due to the wavelength dependence of Equation 2.1, birefringent waveplates typically operate at single wavelengths (excluding more complex achromatic and superachromatic QWPs where many birefringent plates are used). [48, 54] For fresnel rhomb quarter waveplates, the quarter wavelength phase delay is a result of the phase change caused by the total internal reflection of light. For a quartz rhomb cut at a 54.6° angle (Figure 2.4), each total internal reflection of light yields an eighth wavelength delay. For normally incident linearly polarised light at a 45° angle to the fast-axis of the fresnel rhomb two such internal reflections occur, resulting in an overall phase delay of a quarter wavelength between the vertical and horizontal electric field components, yielding circularly polarised light.[48] Since the fresnel rhomb relies upon total internal reflection, rather than wavelength-dependent birefringence, to achieve a quarter wave phase delay, the fresnel rhomb is approximately achromatic over the visible wavelength range (i.e. where quartz is transparent).[48]

As shown in Figure 2.5, elliptically polarised light can also be expressed as a linear sum of L- and R-CPL. The angle formed between the vertex and the covertex of the ellipse traced by the electric field vector is referred to as the ellipticity of polarisation, $-45° \leq \theta \leq 45°$. An ellipticity of $-45°$ indicates a pure L-CPL polarisation, a value of 45° indicates a pure R-CPL polarisation, and a value of 0° indicates that the L- and R-CPL components are equal, resulting in linearly polarised light. All other angles in the specified range represent elliptically polarised light.[55]

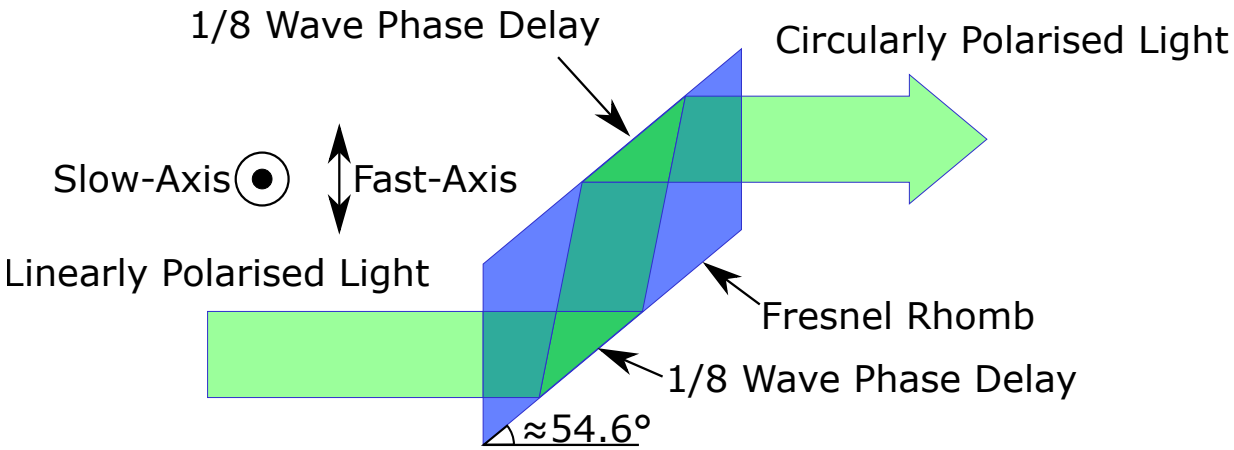


Figure 2.4: A cross-sectional diagram of a Fresnel rhomb, indicating the phase change occurring at each internal reflection, the typical cutting angle for Quartz rhombs and the direction of the fast- and slow axis of this quarter waveplate. Adapted from [3] (Public Domain)

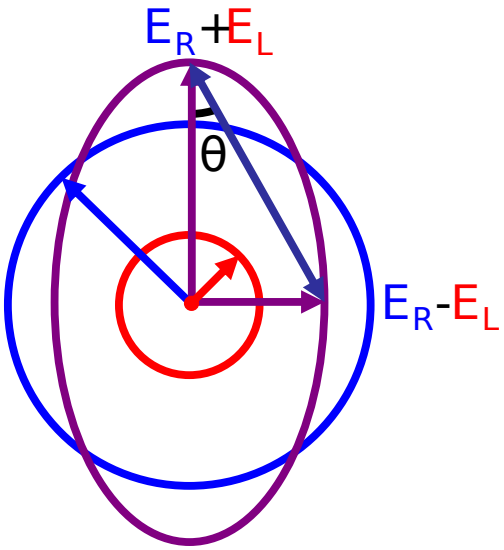


Figure 2.5: The electric field of elliptically polarised light (purple) expressed as the sum of a left- (red) and right-handed (blue) circularly polarised electric field. The ellipticity of the resultant electric field is shown here as θ. Adapted from [4] (Public Domain)

Chiral molecules selectively absorb circularly polarised light depending on the enantiomer of the molecule under illumination; one enantiomer will have an absorption coefficient higher for L-CPL than that of R-CPL, and the mirror image of this enantiomer will have a greater absorption coefficient for R-CPL than that of L-CPL. This property is referred to as Circular Dichroism (CD), which can be quantified in terms of degrees of ellipticity, θ. [56, 55] When used as a measure of circular dichroism, θ represents the ellipticity of the polarisation after a linearly polarised light source (consisting of L- and R-CPL of equal magnitude, with an initial ellipticity of 0°) has passed through a sample under test. If the material does not have selectivity for L-CPL or R-CPL at the wavelength of excitation, the ellipticity of polarisation for light transmitted through the sample remains 0° as the magnitudes of L-CPL or R-CPL after transmission, while possibly reduced, remain equal in magnitude to each other. For materials with circular dichroism, the ellipticity of polarised light will be non-zero as one handedness of CPL will be more strongly absorbed after transmission through the sample under test, leading to a mismatch in the magnitude of R-CPL relative to L-CPL.[56, 55] The ellipticity of polarisation after transmission through a sample is expressed as:

$$\tan\theta = \frac{E_R - E_L}{E_R + E_L} \tag{2.2}$$

where E_L and E_R are the magnitudes of the left- and right-handed electric field components of the elliptical polarisation transmitted through the sample under test.[56, 55] Given that the intensity of light is proportional to the square of electric field magnitude, this may be expressed as

$$\tan\theta = \frac{I_R^{1/2} - I_L^{1/2}}{I_R^{1/2} + I_L^{1/2}} \tag{2.3}$$

For a sample illuminated by linearly polarised or unpolarised light, the incident intensity of left- and right-handed circularly polarised light are equal (I_0). For an optically thick absorbing sample (that is, a sample without optical interference effects), the intensity of left- or right-handed circularly polarised light transmitted through the sample is given by

$$I = I_0 e^{-A\ln(10)} \tag{2.4}$$

where A is the absorbance of the sample. Applying this result to equation 2.3 we find:

$$\begin{aligned}
\tan\theta &= \frac{I_R^{1/2} - I_L^{1/2}}{I_R^{1/2} + I_L^{1/2}} \\
&= \frac{I_0 e^{-A_R \frac{\ln(10)}{2}} - I_0 e^{-A_L \frac{\ln(10)}{2}}}{I_0 e^{-A_R \frac{\ln(10)}{2}} + I_0 e^{-A_L \frac{\ln(10)}{2}}} \\
&= \frac{e^{-A_R \frac{\ln(10)}{2}} - e^{-A_L \frac{\ln(10)}{2}}}{e^{-A_R \frac{\ln(10)}{2}} + e^{-A_L \frac{\ln(10)}{2}}} \\
&= \frac{e^{(A_L - A_R)\frac{\ln(10)}{2}} - 1}{e^{(A_L - A_R)\frac{\ln(10)}{2}} + 1} \\
&= \frac{e^{\Delta A \frac{\ln(10)}{2}} - 1}{e^{\Delta A \frac{\ln(10)}{2}} + 1} \\
&= \tanh\left(\Delta A \frac{\ln(10)}{4}\right)
\end{aligned} \tag{2.5}$$

where A_L and A_R are the absorbances of the sample under illumination by left- and right-handed circularly polarised light, ΔA is the difference between A_L and A_R (that is, $\Delta A = A_L - A_R$), and we have used the fact that the incident intensities of L-CPL and R-CPL are equal (that is, $I_L = I_R = I_0$). This yields the following expression for θ in units of radians:

$$\theta = \tan^{-1}\left[\tanh\left(\Delta A \frac{\ln(10)}{4}\right)\right] \text{ rad.} \tag{2.6}$$

or, more commonly, in units of degrees (°) or millidegrees (mdeg):

$$\theta = \tan^{-1}\left[\tanh\left(\Delta A \frac{\ln(10)}{4}\right)\right]\left[\frac{180}{\pi}\right]^{\circ}. \tag{2.7}$$

For small values of ΔA, this simplifies to:

$$\theta \approx \Delta A \frac{\ln(10)}{4}\frac{180}{\pi}^{\circ} = 32.982\ \Delta A^{\circ}. \tag{2.8}$$

Figure 2.6 shows the agreement between the precise and approximate equations for ellipticity as a function of ΔA. As shown, the percentage deviation between the two equations remains less than 1% for $\Delta A < 0.213$, but this deviation increases significantly above this value.

As the absorbance of light in a sample under test is proportional to the path length of light

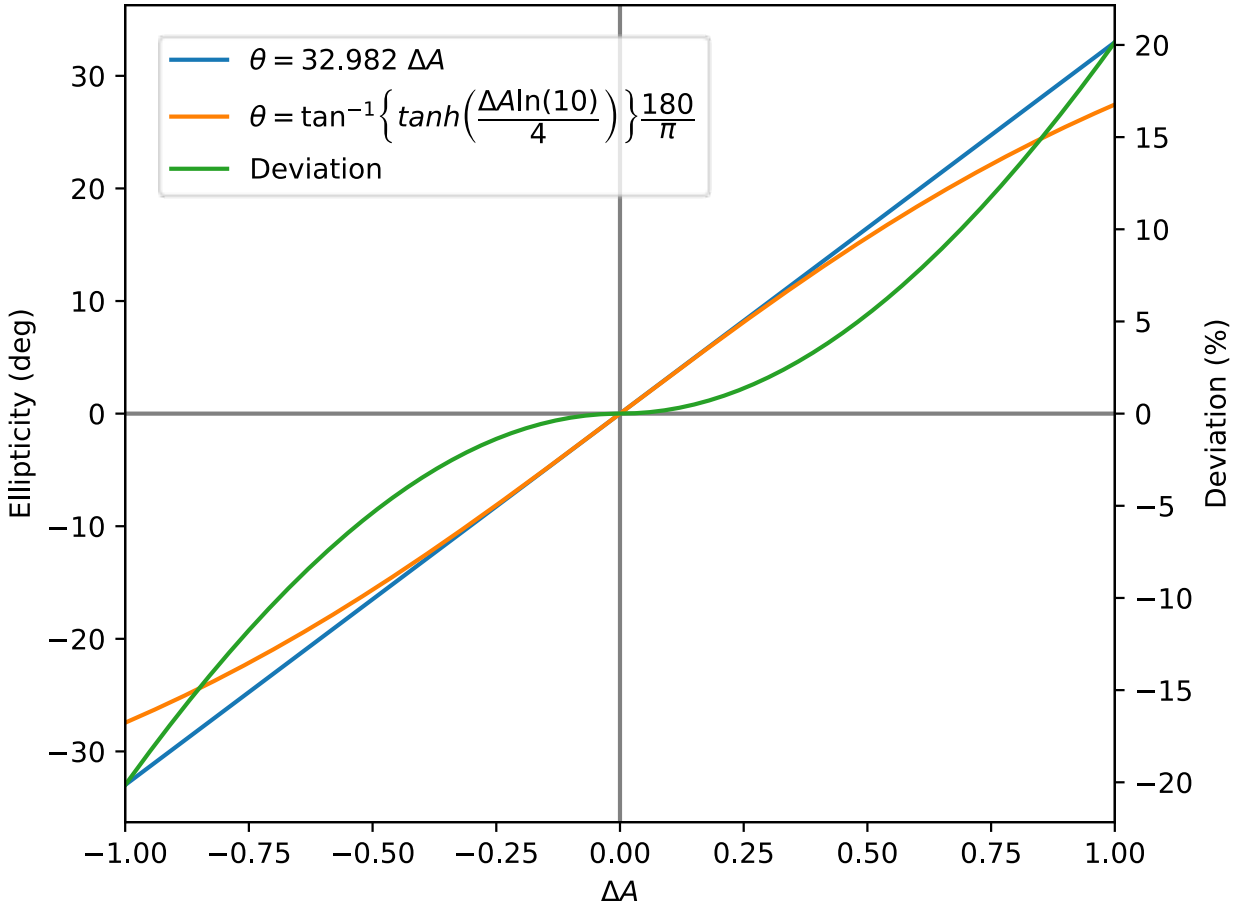


Figure 2.6: The precise (orange) and approximate (blue) equations for ellipticity expressed as a functions of ΔA. The percentage deviation (green) of the approximate expression from the precise expression becomes considerable ($> 1\%$) for $\Delta A > 0.213$.

through the sample (and concentration for solutions), θ is an extensive material property (dependent on the amount of material under study) rather than an intensive one (independent of the amount of material under study). To enable meaningful cross-comparison between different samples under test, the dissymmetry factor of absorption, g_{abs} is defined:[57]

$$g_{abs} = \frac{A_L - A_R}{\frac{1}{2}(A_L + A_R)} \tag{2.9}$$

For solutions, absorbance is given by the Beer-Lambert law:

$$A = \epsilon c l \tag{2.10}$$

where ϵ is the molar extinction coefficient of the solution, c is the solution concentration and l is the path length of light through the solution. Applying this to equation 2.9 yields:

$$\begin{aligned} g_{abs} &= \frac{A_L - A_R}{\frac{1}{2}(A_L + A_R)} \\ &= \frac{\epsilon_L c l - \epsilon_R c l}{\frac{1}{2}(\epsilon_L c l + \epsilon_R c l)} \\ &= \frac{\epsilon_L - \epsilon_R}{\frac{1}{2}(\epsilon_L + \epsilon_R)}. \end{aligned} \tag{2.11}$$

where ϵ_L and ϵ_R are the molar extinction coefficients under L-CPL and R-CPL, respectively. Similarly for a bulk solid with spatially uniform optical properties, the absorbance is given by

$$A = \alpha l \tag{2.12}$$

where α is the absorption coefficient of the bulk solid under test. Similarly, applying this to equation 2.9 gives the following:

$$\begin{aligned} g_{abs} &= \frac{A_L - A_R}{\frac{1}{2}(A_L + A_R)} \\ &= \frac{\alpha_L l - \alpha_R l}{\frac{1}{2}(\alpha_L l + \alpha_R l)} \\ &= \frac{\alpha_L - \alpha_R}{\frac{1}{2}(\alpha_L + \alpha_R)}. \end{aligned} \tag{2.13}$$

where α_L and α_R are the absorption coefficients under L-CPL and R-CPL, respectively. Note that in both equations 2.11 and 2.13, g_{abs} for materials with spatially uniform optical properties depends only on intensive material properties ($\epsilon_{L,R}$ and $\alpha_{L,R}$, respectively) and is thus an intensive property itself for materials with spatially uniform optical properties. As a result, g_{abs} enables a meaningful cross-comparison of the circular dichroism between distinct materials under test.

2.4 The Molecular Origin of Circular Dichroism

2.4.1 Small Molecules

The origin of Circular Dichroism in small OSC molecules can be derived from first principles; however, a qualitative understanding (through not strictly precise from a quantum-mechanical perspective) of how a chiral molecular structure can lead to circular dichroism can be more practically useful. We will first derive the Rosenfeld equation, which governs the magnitude of circular dichroism in small molecules, before moving on to discuss a more intuitive pictorial interpretation of this equation.

Quantitative Approach

The classical energy for the interaction between light and a molecule is given by:

$$H^{int} = -\boldsymbol{\mu} \cdot \mathbf{E} - \mathbf{m} \cdot \mathbf{B} \ (+ \ Higher \ order \ multipole \ terms) \tag{2.14}$$

where $\mathbf{E}$ and $\mathbf{B}$ are the electric and magnetic components of the incident light and $\boldsymbol{\mu}$ and $\mathbf{m}$ are the electric and magnetic dipole moments of the molecule, defined as:

$$\boldsymbol{\mu} = e \sum_j \mathbf{r_j} \tag{2.15}$$

and

$$\mathbf{m} = \frac{e}{2m_e} \sum_j [\mathbf{r_j} \times \mathbf{p_j}] \tag{2.16}$$

where $\mathbf{r_j}$ and $\mathbf{p_j}$ are the position and momentum vectors of the jth electron of the molecule, respectively, and all other symbols have their usual meanings.[58] Since molecular transitions are quantised, we need to convert the interaction energy (the classical interpretation) into an interaction Hamiltonian (the quantum mechanical interpretation):

$$\tilde{H}^{int} = -\tilde{\boldsymbol{\mu}} \cdot \mathbf{E} - \tilde{\mathbf{m}} \cdot \mathbf{B} \tag{2.17}$$

where $\boldsymbol{\mu}$ and $\mathbf{m}$ have become quantum operators.[58] Now that the interaction Hamiltonian has been formed, we can calculate the probability of a transition in the molecule per unit time (i.e. a transition rate) from an initial state (i) to a final state (f) using Fermi's golden rule:

$$\begin{aligned} P(|i\rangle \to |f\rangle) &= k' \left| \langle f| \tilde{H}^{int} |i\rangle \right|^2 \\ &= k' \langle f| \tilde{H}^{int} |i\rangle^* \langle f| \tilde{H}^{int} |i\rangle \\ &= k' \langle i| \tilde{H}^{int} |f\rangle \langle f| \tilde{H}^{int} |i\rangle . \end{aligned} \tag{2.18}$$

Here, for simplicity, k' contains the physical constants of Fermi's golden rule and the density of states at the energy of the final state, $\rho(E_f)$.[58, 59, 60] Substituting in the interaction the Hamiltonian yields the following.

$$\begin{aligned} P(|i\rangle \to |f\rangle) = k \Big\{ &\langle i| \tilde{\boldsymbol{\mu}} |f\rangle \cdot \hat{\mathbf{e}}^* + \langle i| \tilde{\mathbf{m}} |f\rangle \cdot \hat{\mathbf{b}}^* \Big\} \\ &\Big\{ \langle f| \tilde{\boldsymbol{\mu}} |i\rangle \cdot \hat{\mathbf{e}} + \langle f| \tilde{\mathbf{m}} |i\rangle \cdot \hat{\mathbf{b}} \Big\} \end{aligned} \tag{2.19}$$

where $\hat{\mathbf{b}}$ and $\hat{\mathbf{e}}$ are the unit vectors in the directions of B and E respectively. Note that k now contains $|\mathbf{E}|$ and $|\mathbf{B}|$.[58] Expanding and simplifying:

$$\begin{aligned} P(|i\rangle \to |f\rangle) = k \Big\{ &\boldsymbol{\mu}^{fi} \cdot \hat{\mathbf{e}}^* \boldsymbol{\mu}^{if} \cdot \hat{\mathbf{e}} + \mathbf{m}^{fi} \cdot \hat{\mathbf{b}}^* \mathbf{m}^{if} \cdot \hat{\mathbf{b}} \Big\}_I \\ &+ k \Big\{ \boldsymbol{\mu}^{fi} \cdot \hat{\mathbf{e}}^* \mathbf{m}^{if} \cdot \hat{\mathbf{b}} + \boldsymbol{\mu}^{if} \cdot \hat{\mathbf{e}} \mathbf{m}^{fi} \cdot \hat{\mathbf{b}}^* \Big\}_{II} \end{aligned} \tag{2.20}$$

where

$$\begin{aligned}
\boldsymbol{\mu}^{if} &= \langle f|\,\tilde{\boldsymbol{\mu}}\,|i\rangle\,, \\
\boldsymbol{\mu}^{fi} &= \langle i|\,\tilde{\boldsymbol{\mu}}\,|f\rangle\,, \\
\mathbf{m}^{if} &= \langle f|\,\tilde{\boldsymbol{\mu}}\,|i\rangle\,, \\
\mathbf{m}^{fi} &= \langle i|\,\tilde{\boldsymbol{\mu}}\,|f\rangle\,.
\end{aligned} \tag{2.21}$$

To solve equation 2.20, we require expressions for $\hat{\mathbf{e}}$ and $\hat{\mathbf{b}}$. For circularly polarised light, the polarisation vectors are defined as:

$$\hat{\mathbf{e}}_l = \frac{1}{\sqrt{2}}(0, 1, -i) \tag{2.22}$$

$$\hat{\mathbf{e}}_r = \frac{1}{\sqrt{2}}(0, 1, i) = \hat{\mathbf{e}}_l^* \tag{2.23}$$

We can also deduce the form of $\hat{\mathbf{b}}$ using the fact that this vector is perpendicular to $\hat{\mathbf{e}}$ and the wavevector unit vector ($\hat{\mathbf{k}}$) which defines the direction of propagation, that is,

$$\hat{\mathbf{b}} = \hat{\mathbf{k}} \times \hat{\mathbf{e}} \tag{2.24}$$

thus,

$$\begin{aligned}
\hat{\mathbf{b}}_l &= \frac{1}{\sqrt{2}}(1, 0, 0) \times (0, 1, -i) \\
&= \frac{1}{\sqrt{2}}(0, i, 1) = \hat{\mathbf{b}}_r^*
\end{aligned} \tag{2.25}$$

respectively, for an EM wave travelling in the x direction.[58] Returning to Fermi's golden rule, we note that in the absence of an external magnetic field, $|i\rangle$ and $|f\rangle$ can be chosen to be real wavefunctions, thus, $\boldsymbol{\mu}^{if} = \boldsymbol{\mu}^{fi}$ and $\mathbf{m}^{fi} = -\mathbf{m}^{if}$ since $\tilde{\mathbf{m}}$ is imaginary.[58] Using the above

results, we solve for the probability of left- and right-handed transitions:

$$\begin{aligned} A_l =& P(|i\rangle \rightarrow |f\rangle)_l \\ =& k\left\{\boldsymbol{\mu}^{fi}\cdot\hat{\mathbf{e}}_l^*\boldsymbol{\mu}^{if}\cdot\hat{\mathbf{e}}_l + \mathbf{m}^{fi}\cdot\hat{\mathbf{b}}_l^*\mathbf{m}^{if}\cdot\hat{\mathbf{b}}_l\right\}_I \\ &+k\left\{\boldsymbol{\mu}^{fi}\cdot\hat{\mathbf{e}}_l^*\mathbf{m}^{if}\cdot\hat{\mathbf{b}}_l + \boldsymbol{\mu}^{if}\cdot\hat{\mathbf{e}}_l\mathbf{m}^{fi}\cdot\hat{\mathbf{b}}_l^*\right\}_{II} \end{aligned} \tag{2.26}$$

$$\begin{aligned} A_r =& P(|i\rangle \rightarrow |f\rangle)_r \\ =& k\left\{\boldsymbol{\mu}^{fi}\cdot\hat{\mathbf{e}}_l\boldsymbol{\mu}^{if}\cdot\hat{\mathbf{e}}_l^* + \mathbf{m}^{fi}\cdot\hat{\mathbf{b}}_l\mathbf{m}^{if}\cdot\hat{\mathbf{b}}_l^*\right\}_I \\ &+k\left\{\boldsymbol{\mu}^{fi}\cdot\hat{\mathbf{e}}_l\mathbf{m}^{if}\cdot\hat{\mathbf{b}}_l^* + \boldsymbol{\mu}^{if}\cdot\hat{\mathbf{e}}_l^*\mathbf{m}^{fi}\cdot\hat{\mathbf{b}}_l\right\}_{II} \end{aligned} \tag{2.27}$$

We can now calculate the circular dichroism of the molecule under illumination using the following definition:

$$CD = A_l - A_r \tag{2.28}$$

thus,

$$\begin{aligned} CD = k\Big\{&\left(\boldsymbol{\mu}^{fi}\cdot\hat{\mathbf{e}}_l^*\boldsymbol{\mu}^{if}\cdot\hat{\mathbf{e}}_l + \mathbf{m}^{fi}\cdot\hat{\mathbf{b}}_l^*\mathbf{m}^{if}\cdot\hat{\mathbf{b}}_l\right) \\ &-\left(\boldsymbol{\mu}^{fi}\cdot\hat{\mathbf{e}}_l\boldsymbol{\mu}^{if}\cdot\hat{\mathbf{e}}_l^* + \mathbf{m}^{fi}\cdot\hat{\mathbf{b}}_l\mathbf{m}^{if}\cdot\hat{\mathbf{b}}_l^*\right)\Big\}_I \\ &+k\Big\{\left(\boldsymbol{\mu}^{fi}\cdot\hat{\mathbf{e}}_l^*\mathbf{m}^{if}\cdot\hat{\mathbf{b}}_l + \boldsymbol{\mu}^{if}\cdot\hat{\mathbf{e}}_l\mathbf{m}^{fi}\cdot\hat{\mathbf{b}}_l^*\right) \\ &-\left(\boldsymbol{\mu}^{fi}\cdot\hat{\mathbf{e}}_l\mathbf{m}^{if}\cdot\hat{\mathbf{b}}_l^* + \boldsymbol{\mu}^{if}\cdot\hat{\mathbf{e}}_l^*\mathbf{m}^{fi}\cdot\hat{\mathbf{b}}_l\right)\Big\}_{II} \end{aligned} \tag{2.29}$$

As our wavefunctions are real, $\boldsymbol{\mu}^{fi}\cdot\hat{\mathbf{e}}_l^*\boldsymbol{\mu}^{if}\cdot\hat{\mathbf{e}}_l = \boldsymbol{\mu}^{fi}\cdot\hat{\mathbf{e}}_l\boldsymbol{\mu}^{if}\cdot\hat{\mathbf{e}}_l^*$ and the equivalent magnetic terms in bracket I are also equal.[58] This means that the term I cancels out:

$$\begin{aligned} CD = k&\left(\boldsymbol{\mu}^{fi}\cdot\hat{\mathbf{e}}_l^*\mathbf{m}^{if}\cdot\hat{\mathbf{b}}_l + \boldsymbol{\mu}^{if}\cdot\hat{\mathbf{e}}_l\mathbf{m}^{fi}\cdot\hat{\mathbf{b}}_l^*\right) \\ &-\left(\boldsymbol{\mu}^{fi}\cdot\hat{\mathbf{e}}_l\mathbf{m}^{if}\cdot\hat{\mathbf{b}}_l^* + \boldsymbol{\mu}^{if}\cdot\hat{\mathbf{e}}_l^*\mathbf{m}^{fi}\cdot\hat{\mathbf{b}}_l\right) \end{aligned} \tag{2.30}$$

Using $\boldsymbol{\mu}^{fi} = \boldsymbol{\mu}^{if}$ and $\mathbf{m}^{fi} = -\mathbf{m}^{if}$, we can simplify further to:

$$\begin{aligned} CD &= k\left(\boldsymbol{\mu}^{fi}\cdot\hat{\mathbf{e}}_l^*\mathbf{m}^{if}\cdot\hat{\mathbf{b}}_l - \boldsymbol{\mu}^{fi}\cdot\hat{\mathbf{e}}_l\mathbf{m}^{if}\cdot\hat{\mathbf{b}}_l^*\right) \\ &\quad -\left(\boldsymbol{\mu}^{fi}\cdot\hat{\mathbf{e}}_l\mathbf{m}^{if}\cdot\hat{\mathbf{b}}_l^* - \boldsymbol{\mu}^{fi}\cdot\hat{\mathbf{e}}_l^*\mathbf{m}^{if}\cdot\hat{\mathbf{b}}_l\right) \\ &= 2k\left(\boldsymbol{\mu}^{fi}\cdot\hat{\mathbf{e}}_l^*\mathbf{m}^{if}\cdot\hat{\mathbf{b}}_l - \boldsymbol{\mu}^{fi}\cdot\hat{\mathbf{e}}_l\mathbf{m}^{if}\cdot\hat{\mathbf{b}}_l^*\right) \end{aligned} \tag{2.31}$$

Finally, we solve the dot products using the equations 2.22, 2.23, and 2.25:

$$\begin{aligned} CD &= 2ik\left(\mu_Y^{fi}m_Y^{if} + \mu_Z^{fi}m_Z^{if}\right) \\ &= 2k\Im\left(\mu_Y^{fi}m_Y^{if} + \mu_Z^{fi}m_Z^{if}\right) \end{aligned} \tag{2.32}$$

This solution assumes a fixed orientation of the molecule relative to the incident light, such as in the case of oriented films of chiral molecules.[61] For randomly oriented molecules, such as those in solution or isotropic disordered thin films of molecules,[58] a rotational average of the solution is taken, which yields the result:

$$CD = \frac{4}{3}k\Im\left(\boldsymbol{\mu}^{fi}\cdot\mathbf{m}^{if}\right) \tag{2.33}$$

which, neglecting constants, gives us the Rosenfeld equation for rotatory strength:

$$\begin{aligned} R &= \Im\left(\boldsymbol{\mu}\cdot\mathbf{m}\right) \\ &= \Im\left(|\boldsymbol{\mu}||\mathbf{m}|\cos\theta\right) \end{aligned} \tag{2.34}$$

where θ is the relative angle between $\boldsymbol{\mu}$ and $\mathbf{m}$.[58]. Rotatory strength is proportional to the integral of the CD band in a CD spectrum and is related to the dissymmetry factor of absorption via:

$$g = \frac{4R}{D} = \frac{4\Im\left(|\boldsymbol{\mu}||\mathbf{m}|\cos\theta\right)}{|\boldsymbol{\mu}|^2 + |\mathbf{m}|^2} \tag{2.35}$$

where $D = |\boldsymbol{\mu}|^2 + |\mathbf{m}|^2$ is the dipole strength of the transition.[57, 56]

For small molecular systems, it is often the case that $|\boldsymbol{\mu}| >> |\mathbf{m}|$, leading to the frequent

simplification:

$$g \approx 4\frac{|\mathbf{m}|}{|\boldsymbol{\mu}|}\cos\theta \tag{2.36}$$

A consequence of equation 2.36 for small molecules is that the magnitude of g_{abs} is limited by the small values of $\mathbf{m}$ relative to $\boldsymbol{\mu}$. This leads to an apparent g_{abs} ceiling of $< 10^{-2}$ for small molecules. [6]

Qualitative Approach

The derivation of the Rosenfeld equation above, while rigorous, does not provide much physical insight into which molecules demonstrate CD, which do not, and why CD could be large or small in a given molecule. For this, a qualitative approach is needed to interpret Equation 2.34.

The electronic transition dipole moment, $\boldsymbol{\mu}$ may be considered as the net linear displacement of charge in a molecule after an electronic transition.[62] Similarly, the magnetic transition dipole moment, $\mathbf{m}$, may be considered as the net circulation of charge during an electronic transition.[62] In order for a transition to demonstrate CD (i.e. for the Rosenfeld equation to be non-zero), the redistribution of charge during an electronic transition must be helical, consisting of both linear displacement ($\boldsymbol{\mu} \neq 0$) and circulation of charge ($\mathbf{m} \neq 0$). In an achiral (i.e. non-chiral) molecule, the redistribution of charge in an electronic transition is always planar, that is, there is only a linear displacement of charge in a transition ($\boldsymbol{\mu} \neq 0$, $\mathbf{m} = 0$) as demonstrated in the case of anthracene or there is only circulation of charge ($\mathbf{m} \neq 0$, $\boldsymbol{\mu} = 0$) as shown for coronene (Figure 2.7).[62] As a result, $R = 0$ for achiral molecules and they do not demonstrate CD.

Now consider the enantiomers of the chiral small molecule hexahelicene (Figure 2.7). In the electronic transition shown, the charge is displaced from the lowest benzene ring in the structure to the highest. In doing so, we observe not only a circulation of charge around the helix ($\mathbf{m} \neq 0$), but also a linear displacement along the axis of the helix ($\boldsymbol{\mu} \neq 0$), satisfying the conditions for circular dichroism ($\boldsymbol{\mu} \cdot \mathbf{m} \neq 0$).[62] The sign of CD is determined by the enantiomer of the helicene. For one enantiomer of helicene, $\boldsymbol{\mu}$ and $\mathbf{m}$ are coaligned, corresponding to positive

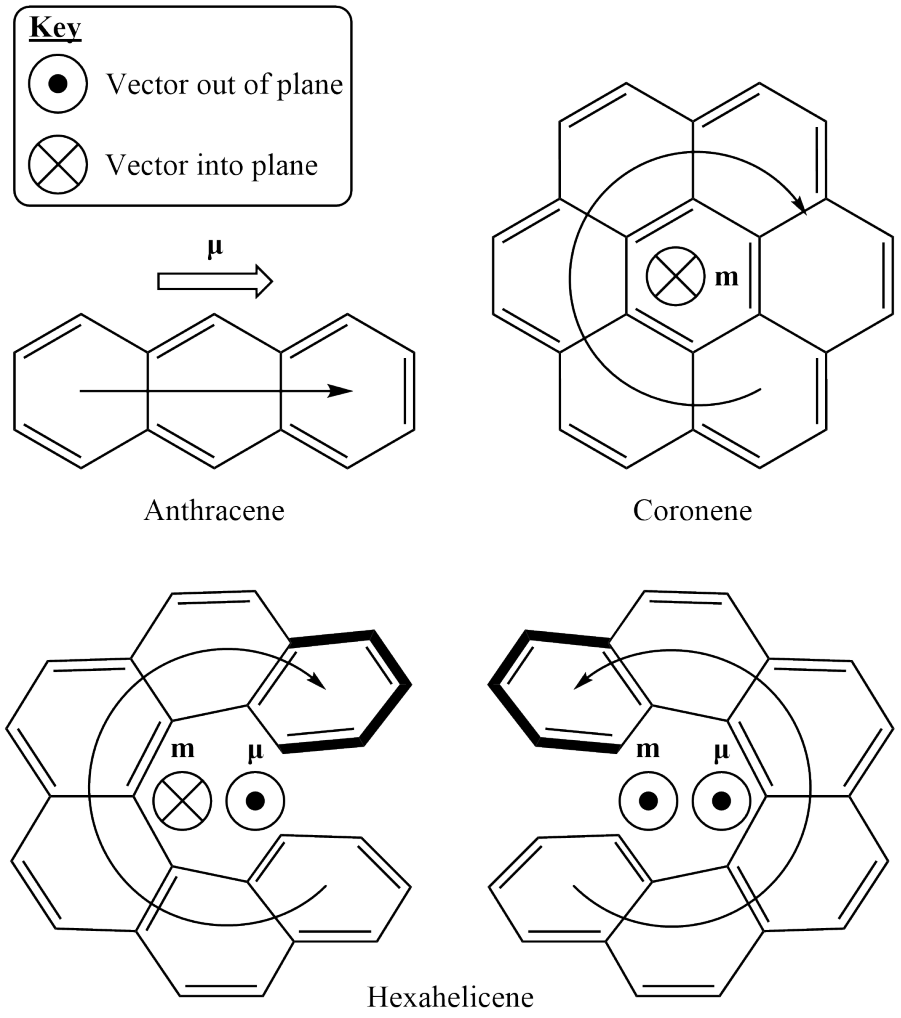


Figure 2.7: Diagrams showing the direction of charge redistribution (black arrow) in achiral molecules (anthracene and coronene) and the two enantiomers of an achiral molecule (hexahelicene) during an electronic transition. The directions of the resulting electric and magnetic transition dipole moments are labelled $\boldsymbol{\mu}$ and $\mathbf{m}$, respectively. Note here that in the case of hexahelicene, we have simplified the directions of $\boldsymbol{\mu}$ and $\mathbf{m}$ to being either into or out of the plane for the straightforward explanation of the origin of circular dichroism in chiral organic molecules. In reality, these vectors will be misaligned for this transition by angle $\theta < 90°$ (for the main band transition of hexahelicene, $\theta \approx 76°$ [5]) which reduces the value of g according to Equation 2.35

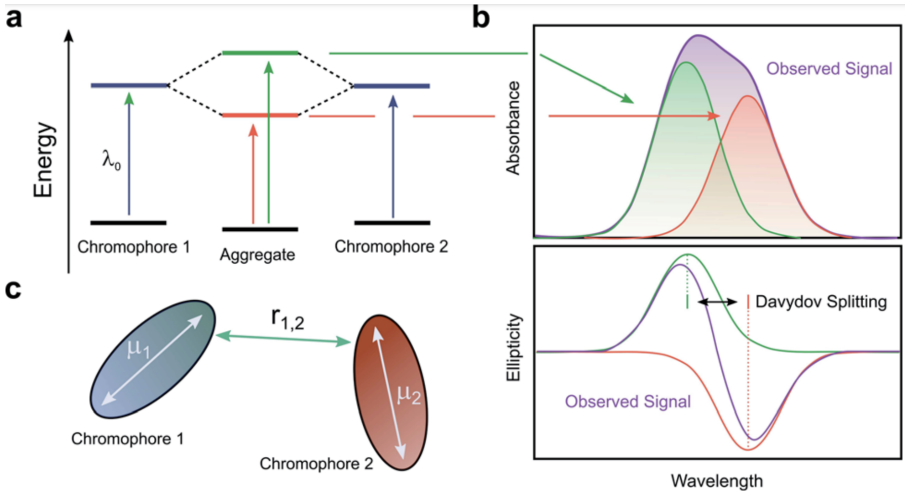


Figure 2.8: (a) Splitting of excited state energy levels due to the interaction of two chirally arranged excitonically coupled chromophores. (b) Characteristic absorption and ellipticity spectra of excitonically coupled chromophores demonstrating Davydov splitting. (c) Model demonstrating the key parameters for the calculation of Davydov splitting: the electric transition dipole moment of each molecule ($\boldsymbol{\mu}_1$ and $\boldsymbol{\mu}_2$) and the displacement between the two dipole moments ($\mathbf{r}_{12}$). Reproduced from [6] with permission from the Royal Society of Chemistry.

CD ($\boldsymbol{\mu} \cdot \mathbf{m} > 0$) For the opposite handedness of helicene, $\boldsymbol{\mu}$ and $\mathbf{m}$ are anti-aligned and the observed CD is negative ($\boldsymbol{\mu} \cdot \mathbf{m} < 0$).[62] These observations are not unique; transitions in all chiral molecules are helical and therefore exhibit CD, with mirror enantiomers demonstrating equal magnitude CD spectra with opposite signs. [62]

2.4.2 Larger Molecular Systems: Excitonically Coupled Chromophores

The discussion above for small molecules refers to chiral chromophores in isolation without interaction between neighbouring chromophores. More realistically, in a larger molecule containing many chromophores or in a solid-state configuration where chromophores of adjacent molecules may pack closely together, chromophores with the same or similar excitation wavelengths may couple to each other. [63, 6, 64]

For coupling between two equivalent chromophores which are chirally arranged relative to each other (e.g. by a chiral spacer group), the two otherwise degenerate excited states of the chromophores are split by the Davydov energy, $2V_{12}$ (Figure 2.8a) which may be approximated

using a Coulomb dipole-dipole interaction:

$$V_{12} = \frac{\mu_1 \mu_2}{r_{12}^3} \left[\mathbf{e}_1 \cdot \mathbf{e}_2 - 3 \left(\mathbf{e}_1 \cdot \mathbf{e}_{12} \right) \left(\mathbf{e}_2 \cdot \mathbf{e}_{21} \right) \right] \tag{2.37}$$

where μ_1 and μ_2 are the intensities of the electric transition dipoles, r_{12} is the distance between the two dipoles and $\mathbf{e}_i$ are the unit vectors corresponding to the directions of the electric transition dipole moments ($\mathbf{e}_1$ and $\mathbf{e}_2$) and the displacement between the dipole moments ($\mathbf{e}_{12}$). [63, 64] Transitions from the ground state to the two split energy levels appear as a characteristic bisignate couplet in the CD spectrum (Figure 2.8b, referred to as the "Cotton effect") of the system under study.[63, 6, 64] The rotational strengths of these transitions are equal and opposite, with a magnitude given by:[63, 6, 64]

$$R_{1,2} \propto \mathbf{r}_{12} \cdot \boldsymbol{\mu}_1 \times \boldsymbol{\mu}_2 \tag{2.38}$$

As discussed in section 2.4.1, the limiting factor in the size of g_{abs} for an isolated chromophore in a small molecule is most often the magnitude of the magnetic dipole moment $\mathbf{m}$. Equation 2.38 indicates that for larger systems containing excitonically coupled chromophores, the rotational strength (and therefore g_{abs}) is no longer limited by the magnetic dipole moment[4] and is instead governed by the magnitude of $\boldsymbol{\mu}_1$ and $\boldsymbol{\mu}_2$ (which are significantly larger than the magnitude of $\mathbf{m}$), the relative orientation of $\boldsymbol{\mu}_1$ and $\boldsymbol{\mu}_2$ (being maximised when the two are perpendicular) and the displacement between them ($\mathbf{r}_{12}$, Figure 2.8c). In this way, the value of g_{abs} of excitonically coupled systems can be significantly higher than that of small molecules, reaching as high as $\sim 0.1 - 1$ in some cases. [14, 15]

2.5 Chiral Organic Photodetector Devices

The architectures of the four most common organic photodetector devices are shown in Figure 2.9. In this section, we will discuss the operating principles of these devices and show how

[4] In fact, the transitions on the individual chromophores needn't have magnetic transition dipole moments at all.

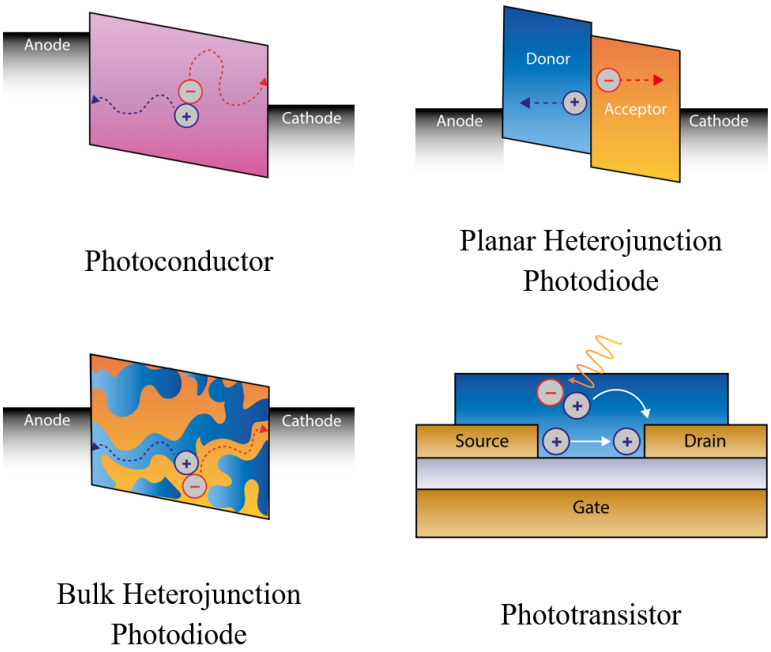


Figure 2.9: The most common device architectures used for circularly polarised photodetectors. Plasmonic devices are not discussed in this work. Reproduced from [7] with permission from the Royal Society of Chemistry.

different classes of chiral materials may be suited to each architecture.

2.5.1 Organic Photoconductors

An Organic Photoconductor (OPC) is a photodetector architecture consisting of two electrodes separated by a semiconductor layer. For an OSC active layer, the concentration of carriers in this layer is exceedingly small, so that, even under an applied electric field, no appreciable current flows between the electrodes, and the device is effectively an insulator.

Under excitation by photons with an energy greater than the optical bandgap of the active layer, excitons are created in the active layer, which can dissociate into electron and hole polarons. Under the influence of an applied bias between the electrodes, photogenerated electron and hole polarons are extracted at the positive and negative electrodes, respectively. In this case, the extracted photocurrent under illumination is given by:

$$I_{ph} = \left(q\eta\frac{P_{opt}}{h\nu}\right)\left(\frac{\mu\tau_{Rec}V}{L^2}\right) = I_p G_a \tag{2.39}$$

where q is the electron charge, η is the photocurrent external quantum efficiency, P_{opt} is the incident optical power, $h\nu$ is the incident photon energy, μ is the majority carrier mobility, τ_{Rec} is the electron–hole recombination time, V is the applied voltage between the electrodes, and L is the photoconductor electrode spacing.[65, 66] To gain a more intuitive understanding of device behaviour, this equation can be divided into two parts: I_p is the primary photocurrent (i.e., I_{ph} in the absence of gain mechanisms):

$$I_p = q\eta\frac{P_{opt}}{h\nu} \tag{2.40}$$

and G_a is the device gain, given by:

$$G_a = \frac{\mu\tau_{Rec}V}{L^2} = \frac{\tau_{Rec}}{\tau_{Trans}} \tag{2.41}$$

where τ_{Trans} is the average time taken for charges to transit from one electrode to the other:[65, 66]

$$\tau_{Trans} = \frac{L^2}{\mu V}. \tag{2.42}$$

The gain mechanism for photoconductors is detailed in Figure 2.10 for an n-type semiconductor.[5] When electron and hole polarons are generated by dissociating an optically excited exciton (Figure 2.10a), the electron and hole polarons begin to migrate toward the cathode and anode, respectively, under the action of an external bias (Figure 2.10b). Due to the higher electron mobility relative to the hole mobility for the n-type semiconductor, electrons are extracted more rapidly from the device than the holes.[65, 66] If an electron is extracted from the device prior to recombination (i.e. $\tau_{Rec} > \tau_{Trans}$), an electron must be simultaneously injected at the anode to maintain the charge neutrality of the device.[65, 66] This process of repeated electron extraction and charge neutrality – maintaining electron injection repeats until recombination of electron and hole polarons occurs (Figure 2.10c).[65, 66]

The gain of the photodetector is determined by the number of times a single photogenerated electron polaron is extracted at the cathode (and thus reinjected at the anode). As shown in

[5]Note that the mechanism for p-type semiconductors is identical aside from the fact that, in this case, hole polarons are the rapidly extracted and re-injected carriers and electron polarons are the slow moving carriers.

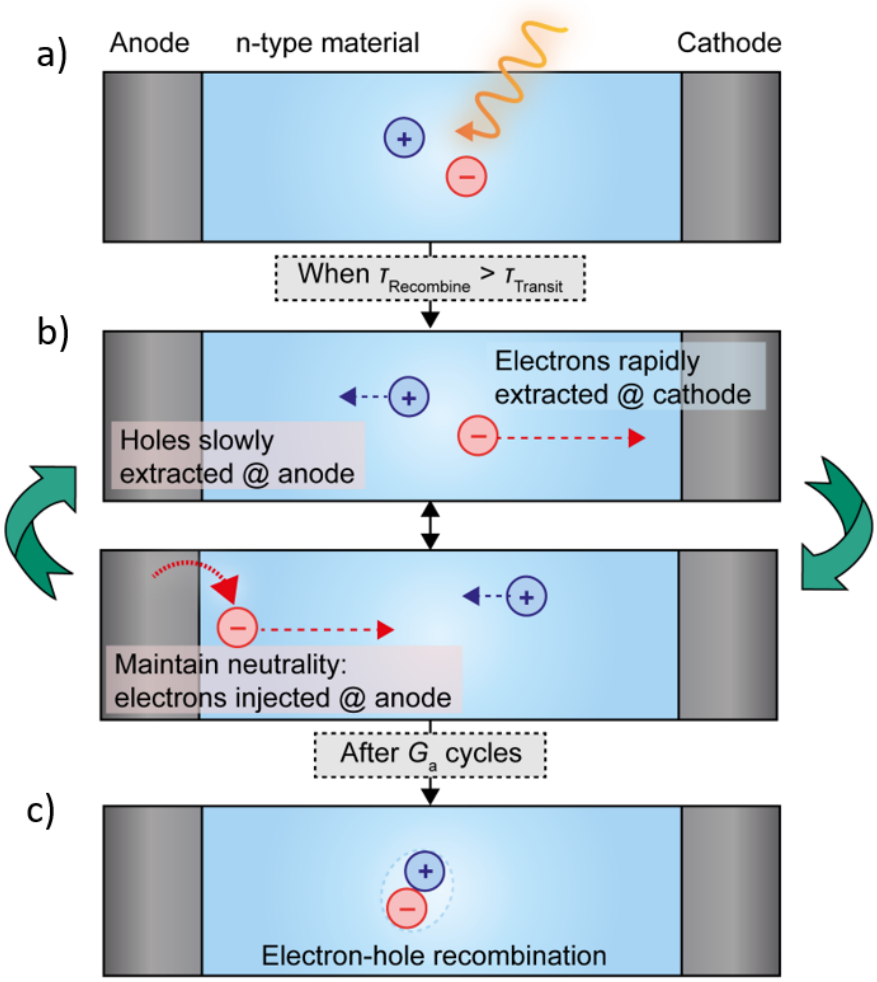


Figure 2.10: Step-by-step description of the photoconductive gain mechanism. (a) Electron and holes are excited by incident light. (b) Photogenerated electrons are rapidly extracted from the device at the positive terminal, whereas holes migrate with much slower velocity to the negative terminal. To maintain charge neutrality, electrons must be injected at the negative terminal as they are extracted from the positive terminal. This process repeats for many cycles (G_a) until electron-hole recombination occurs (c). Reproduced from [7] with permission from the Royal Society of Chemistry.

Equation 2.41, this is determined by the ratio between the charge transit time of the electron between the cathode and anode (τ_{Trans}) and the average time taken for the photogenerated electron to recombine with a hole (τ_{Rec}). This gain enables the ratio between the number of extracted charges and the number of incident photons on the OPC (i.e., the External Quantum Efficiency (EQE)) to exceed 100%.[65, 66]

Perovskites are particularly well suited to the photoconductor geometry due to their large effective carrier mobilities ($0.1 - 10\ cm^2\ V^{-1}\ s^{-1}$) and long carrier lifetimes ($10^{-6}\ s$), which allows significant G_a.[67, 68, 69, 70] Carriers with long τ_{Rec} persist once the light is switched off, which means that these devices can be slow to respond and have low bandwidths. Chiral perovskite photoconductors generally suffer from poor CP selectivity in absorption (g_{abs}) due to weak intrinsic chiroptical activity; however, several recent examples have demonstrated that reducing the dimensionality of the perovskite structure (from quasi-2D to 2D or from 2D to 1D) can enhance g_{abs} by introducing greater asymmetry and helicity into the crystal structure of the perovskite.[71, 72, 73]

2.5.2 Organic Phototransistors

An Organic Phototransistor (OPT) is a photodetector architecture that shares a design similar to the OPC, with two electrodes, known as the source and drain, in contact with a semiconductor layer. However, the OPT has a third electrode referred to as the gate electrode which is insulated from the semiconductor by a dielectric layer.[8] The source electrode is defined as the ground of the system (0 V), acting as an (effectively) unlimited supply of electrons and holes for the system.[8] The drain electrode is positively or negatively biased relative to the source electrode to apply an external electric field to the semiconductor.[8] The gate electrode acts to modulate the concentration of carriers in the phototransistor at the semiconductor-dielectric interface.[8]

As with the photoconductor, if a bias is applied to the drain electrode in the absence of a gate bias and under dark conditions, no appreciable current will flow through the device due to the

absence of significant charge carrier density in the OSC layer.[8] For an n-type semiconductor,[6] if a positive voltage bias is applied to the gate electrode, electrons are injected at the source electrode and begin to accumulate at the interface between the dielectric and semiconductor.[8] The initially injected charges fill trap states at this interface and cannot contribute to significant current flow between the source and drain electrodes.[8] At a critical gate voltage, referred to as the threshold voltage, V_{th}, the majority of the trap states at the dielectric-semiconductor interface have been filled and charges injected as the gate bias is further increased are mobile.[8] In the absence of a drain bias, the density (per unit area) of mobile charges accumulated at the dielectric-semiconductor interface, Q, is given by

$$Q = C(V_g - V_{th}) \tag{2.43}$$

where C is the capacitance of the dielectric layer and V_g is the applied gate voltage.[8] If a gate bias is applied, the voltage within the transistor channel varies linearly from zero at the source ($V(x = 0) = 0V$) electrode to V_d at the drain electrode.[8] The concentration of accumulated charges at the interface is then given by:[8]

$$Q(x) = C(V_g - V_{th} - V(x)) \tag{2.44}$$

If $V_g - V_{th} >> V_d$, there is a non-zero concentration of mobile charges along the entire length of the transistor channel and the transistor is ohmic, and the transistor is said to operate in the linear regime.[8] When $V_g - V_{th} = V_d$, the concentration of mobile carriers is zero at the drain electrode.[8] The point where $Q = 0$ is referred to as the pinch-off point and moves towards the source electrode as the drain voltage is further increased.[8] Current continues to flow in the device, as charges are drawn across the depletion region by the potential difference between the source electrode and pinch-off point, which is $V_g - V_{th}$.[8] As this potential difference is independent of V_d, further increases of drain voltage does not significantly increase drain current and the transistor is said to be operating in the saturation regime.[8]

[6]The operating principles for a p-type phototransistor are identical, aside from the fact that "hole polarons" replace "electron polarons" and the signs of the biases applied to the drain and gate electrodes are reversed in the description to follow.

Under the gradual channel approximation (i.e., the gate field is significantly larger than the source-gate field), the absolute drain current is given by ohms law:

$$I_d = WQ\mu F \tag{2.45}$$

where W is the width of the transistor channel, μ is the mobility of charge carriers, and $F = dV/dx$ is the electric field in the channel.[8] Combining this with equation 2.44, we find:

$$I_d\ dx = WC(V_g - V_{th} - V(x))\mu\ dV \tag{2.46}$$

which may be integrated to yield:[8]

$$I_d \int_0^L dx = WC\mu \int_0^{V_d} (V_g - V_{th} - V(x))\, dV \tag{2.47}$$

$$I_d = \frac{W}{L}\mu C \left[(V_g - V_{th})V_d - \frac{V_d^2(x)}{2}\right]. \tag{2.48}$$

Under the linear regime condition ($V_d << V_g - V_{th}$) the term in V_d^2 may be safely neglected:[8]

$$I_d = \frac{W}{L}\mu_{lin} C(V_g - V_{th})V_d. \tag{2.49}$$

Under saturated conditions, V_d is replaced by the potential difference between the source electrode and pinch-off point:[8]

$$I_d = \frac{W}{2L}\mu_{sat} C(V_g - V_{th})^2. \tag{2.50}$$

The behaviour of a transistor under varying drain voltage (output characteristics) and varying gate biases (transfer characteristics) are provided in Figure 2.11.[8]

The above equations describe transistor behaviour under dark conditions. When a p-type device is exposed to photons with an energy greater than the optical bandgap of the semiconductor, electron and hole polarons are generated through the dissociation of photogenerated excitons. The hole polarons flow to the drain electrode and the electron polarons flow to the source electrode. If the gate voltage of the phototransistor is below the threshold voltage ($V_g < V_{th}$),

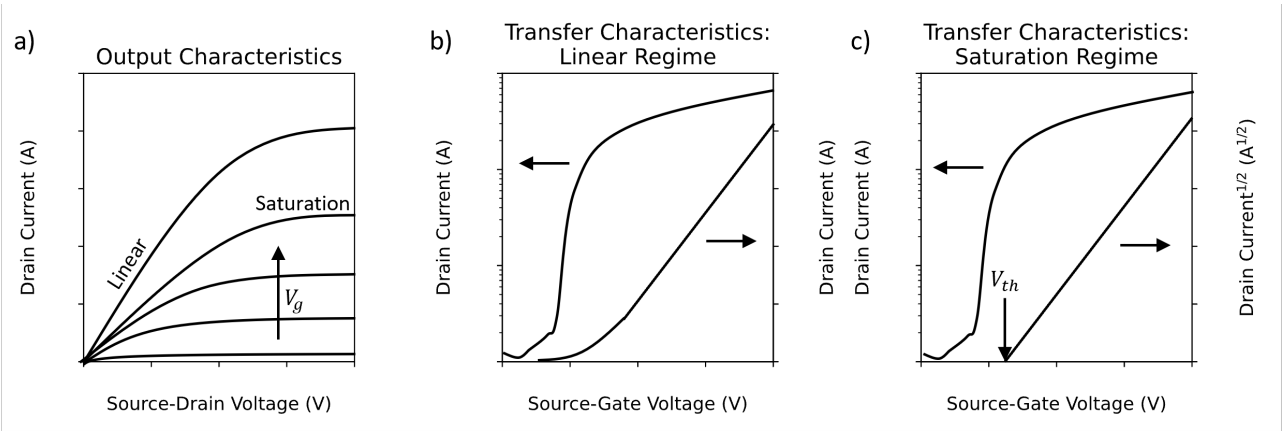


Figure 2.11: Organic transistor output characteristics (a), and transfer characteristics under the linear regime (b) and the saturated regime (c). Recreated from [8].

the phototransistor is said to operate in photoconductive mode and demonstrates an identical photoresponse as an OPC, with a photocurrent given by Equation 2.39.[65, 66] For the case where the gate voltage is above the threshold voltage ($V_g > V_{th}$), the phototransistor operates in photovoltaic mode.[65, 66] In photovoltaic mode, photogenerated holes are extracted at the drain electrode whereas photogenerated electrons accumulate at the source electrode.[65, 66] Electrons which accumulate at the source electrode serve to lower the barrier to hole injection at this electrode, further increasing the measured photocurrent by causing a reduction in the threshold voltage (ΔV_{th}).[65, 66] Under this photovoltaic regime, the photocurrent generated by the phototransistor is given by:

$$I_{ph} = g_m \Delta V_{th} = \frac{AkT}{q} \ln\left(1 + \frac{\eta q \lambda P_{opt}}{I_{pd} hc}\right) \tag{2.51}$$

where g_m is the transconductance, A is a proportionality constant, kT/q is the thermal voltage, η is the photogeneration quantum efficiency, hc/λ is the photon energy and I_{pd} is the dark current for *minority* carriers (electron polarons in the case of a p-type semiconductor).[65, 66]

Both chiral small molecules (e.g. helicenes and chiral fullerenes) and chiral polymeric systems (polyfluorene-based (co)polymers) have been evaluated in selective CP phototransistors, achieving very high photocurrent dissymmetry factors ($g_{ph} \sim 1$). [45, 74, 11] For our own studies of phototransistors based on chiral fullerene bis-PCBM (Chapter 4), we attribute the large photocurrent dissymmetry of chiral phototransistors to the greater shift of the threshold voltage

under the preferentially absorbed handedness of CPL.[11] This creates a condition close to the threshold voltage of the transistor where the transistor is in the 'on' state for the preferentially absorbed handedness of CPL and in the 'off' state for the opposite handedness, leading to a large g_{ph} value of 1.3, despite a low g_{abs} of 6.3×10^{-4}.[11]

Although phototransistors can demonstrate enhanced CP selectivity, the nonlinear optical response and restricted photoactive area can add additional complexity to evaluating their potential benefits. The development of high-mobility long recombination lifetime chiral OSCs should greatly improve CP phototransistor performance.

2.5.3 Organic Photodiodes

A heterojunction photodiode is perhaps the most familiar organic photodetector. The two most common architectures for a photodiode are shown in Figure 2.9. As shown, the active layer of the photodiode consists of an electron donor and an electron acceptor layer (referred to as a donor and acceptor layer, respectively, hereafter).[8, 24] Of the two layers in the device, the donor layer is the OSC with the shallower Highest Occupied Molecular Orbital (HOMO) and Lowest Unoccupied Molecular Orbital (LUMO) levels and the acceptor layer is the OSC with the deeper Highest Occupied Molecular Orbital (HOMO) and Lowest Unoccupied Molecular Orbital (LUMO) levels.[8, 24]

When a photon with energy greater than the bandgap of the donor (acceptor) is incident on this layer, an exciton can be generated. This neutral exciton may move under diffusion to the interface between the donor and acceptor.[8, 24] The average distance an exciton can diffuse from the point of photoexcitation before recombination is referred to as the exciton diffusion length, which is typically 1-10 nm in OSCs. [75] This limits the thickness of the donor and acceptor layers in a bilayer photodiode architecture (Figure 2.9).[8, 24] This exciton diffusion limited thickness may be overcome, in part, by using a bulk heterojunction architecture (Figure 2.9) where the donor and acceptor layer are intermixed. In this way, through careful engineering of the phase separation between the donor and acceptor layers, the active layer of the device

may be thicker, while retaining a high probability that excitons are photogenerated in less than a diffusion length from the donor-acceptor interface.[8, 24]

For a given photodiode architecture, the donor and acceptor layers are selected so that the energy difference between the HOMO and LUMO levels of the donor and acceptor is sufficiently large to overcome the exciton binding energy.[8, 24] This binding energy represents the coulombic attraction between the electron and hole polarons and must be overcome to dissociate the exciton into its constituent polarons.[8, 24] Once separated, the electron and hole polarons are extracted at the anode and cathode, respectively, and measured as the device photocurrent.

Anode and cathode materials are selected to optimise the workfunction matching between the HOMO of the acceptor and the LUMO of the donor, which maximises the built-in potential of the device.[8, 24] The difference in work-functions of the anode and cathode establishes a built-in voltage in the device.[8, 24] Unlike the phototransistor or photoconductor, which conventionally use electrodes made from the same conductor, this built-in voltage enables photocurrent extraction from the photodiode in the absence of an external voltage bias (i.e. under short-circuit conditions), enabling low noise, low dark current detection.[8, 24] An additional external bias may be applied to these devices, increasing the internal electric field.[8, 24] This larger field increases the rate of charge extraction (enhancing the device response speed) and also increases the responsivity of the detector.[8, 24] Unlike the phototransistor and photoconductor architectures, however, photodiodes do not typically demonstrate gain mechanisms (excluding less common processes such as interfacial trap-controlled charge injection[76]), limiting their EQE to $\leq 100\%$.[8, 24]

In 2019 Kim *et al.* demonstrated heterojunction CP OPDs with $g_{ph} \sim 0.1$ by blending achiral polymer, P3CT, with a chiral small molecule additive, 1,1'-binaphthyl.[77] Appropriate thin-film processing caused the chiral small molecule to phase separate from the blend, and chirality transfer from the chiral additive to the polymer–molecule hetero-aggregates gave rise to strong CP absorption: a self-organised, circularly selective heterojunction. We have recently shown that highly selective photodiodes with $g_{ph} \sim 0.9$ can be realised in a simple, bilayer architecture (Chapter 5). In these devices, selectivity to CP light occurs within the achiral polyfluorene-

based (co-)polymer (F8T2): chiral small molecule (1-aza[6]helicene) additive donor layer, and exciton dissociation occurs at the donor-acceptor (C60) interface. Although chiral nonfullerene acceptors (NFAs) are yet to be realised, NFA-based photodiodes hold immense promise for next-generation devices, as they can harness longer wavelength radiation and have surprisingly long exciton diffusion lengths.[78, 79]

2.6 Photodetector Figures of Merit

To quantitatively assess the performance of different circularly polarised photodetectors, we must first introduce their figures of merit. In this section, we will first introduce those figures of merit that apply to photodetectors that are insensitive to polarisation before discussing those figures specific to circularly polarised light detection. A summary of the figures of merit of circularly polarised photodetectors reported in the literature is provided in Table 2.2.

2.6.1 Responsivity and External Quantum Efficiency

Responsivity (R) is the ratio of the photocurrent (I_{ph}) produced by a photodetector and the optical power incident on it (P_{opt}) at a given wavelength:[66, 24]

$$R = \frac{I_{ph}}{P_{opt}} \tag{2.52}$$

External quantum efficiency (EQE) is a closely related quantity and describes the ratio of the number of charges extracted to the number of incident photons at a particular wavelength and voltage bias:

$$EQE = \left[\frac{I_{ph}}{e}\right]\left[\frac{P_{opt}}{E_{phot}}\right]^{-1} = \left[\frac{I_{ph}}{P_{opt}}\right]\left[\frac{E_{phot}}{e}\right] = R\frac{hc}{e\lambda} \tag{2.53}$$

where $E_{phot} = hc/\lambda$ is the energy of the incident photons, e is the elementary charge, h is Planck's constant, c is the speed of light and λ is the wavelength of the incident light.[66, 24]

Although the OPT and OPC gain mechanisms can result in EQEs greater than 100%, the EQE

Device	Category	Ref	$\lvert g_{abs}\rvert$	$\lvert g_{ph}\rvert$	LDR (dB)	EQE (%)	R (A/W)	B (Hz)	I_{dark} (A)	J_{dark} (A/cm2)	$D*$ (Jones)	t_r, t_f (ms)	On/ Off	λ_{max} (nm)
Phototransistors	Organic small molecule	[45]		1.8					10^{-10}			2.6, 6.2	10^3	365
		[80]	1.7×10^{-3}	1.0×10^{-2}		8.9×10^1	4.5×10^{-1}		10^{-8}		2.1×10^{10}			730
		[80]	7.5×10^{-3}	5.7×10^{-2}					10^{-8}					635
		[11]	6.3×10^{-4}	1.3					10^{-11}			<43, <43	10^3	405
		[11]	1.8×10^{-3}	2.6×10^{-1}					10^{-9}				10^3	405
	Organic small molecule nanowires	[81]	1.3×10^{-3}	4.5×10^{-1}		2.3×10^4	8.5×10^1		10^{-12}				10^4	460
	Organic small molecule single crystal	[82]		1.3×10^{-1}		3.0×10^5	1.2×10^3		10^{-8}		2.9×10^{13}	<50, <50	$10^7 >$	495
	0D organic-inorganic hybrid materials	[83]	5.2×10^{-2}	2.1×10^{-1}		1.4×10^5	4.5×10^2							405
	Organic polymer	[74]		1.9		1.3×10^{-3}	4.6×10^{-6}		10^{-9}		1.5×10^7		10^3	450
	Chiral cellulose nanocrystal films	[84]											10^7	405
Photodiode	Organic polymer – small molecule blend	[47]	3.0×10^{-2}	4.1×10^{-1}	80	8.4	3.5×10^{-2}	5.6×10^4	10^{-11}	10^{-10}		7×10^{-3}, 7×10^{-3}	x	510
		[47]	2.0×10^{-1}	1.2×10^{-1}	80	5.2	1.9×10^{-2}	5.6×10^4	10^{-11}	10^{-10}		7×10^{-3}, 7×10^{-3}	x	455
		[77]		1.0×10^{-1}		1.8×10^{-1}	5.4×10^{-4}					N/A, $> 25 \times 10^4$	x	375
	Organic polymer	[85]	5.6×10^{-2}	1.7×10^{-2}									x	543
	Organic small molecule	[86]	1.0×10^{-1}	9.0×10^{-2}	36	4.7×10^1	2.1×10^{-1}						x	543
	Organic polymer nanowires	[87]	2.0×10^{-3}	9.4×10^{-2}		2.6×10^1	1.1×10^{-1}				1.2×10^{11}		x	532
	1D perovskite	[72]	4.0×10^{-2}	1.8		8.8×10^1	2.8×10^{-1}		10^{-7}	10^{-6}			x	395
	2D perovskites	[88]	3.8×10^{-5}	1.0×10^{-1}									x	486
	Quasi-2D perovskite	[89]		6.9×10^{-1}		4.4×10^{-2}	1.9×10^{-4}				1.7×10^{11}	2.0, 2.4	x	520
Photoconductor	1D perovskite	[68]		9.7×10^{-2}	35	3.9×10^1	1.2×10^{-1}	1.5×10^2	10^{-12}		7.1×10^{11}		x	395
	2D perovskites	[90]		3.0×10^{-1}		1.1×10^2	4.4×10^{-1}	1.1×10^1	10^{-13}		2.2×10^{11}	100, 100	x	518
		[91]		2.0×10^{-1}		1.4×10^2	6.0×10^{-1}	2.3	10^{-14}		3.1×10^{11}	22, 34	x	520
		[69]	1.3×10^{-3}	3.0×10^{-1}	12	5.2×10^{-3}	2.2×10^{-5}		10^{-11}		1.2×10^7	580, 960	x	520
	Quasi-2D perovskite	[70]	5.6×10^{-4}	2.0×10^{-1}	42*	9.5	4.1×10^{-2}	1.5×10^2	10^{-12}		8.7×10^9	3.5, 4.9	x	532
	2D-perovskite nanowires	[92]		1.5×10^{-1}	77*	1.2×10^4	4.7×10^1	1.5×10^3			9.7×10^{12}	0.27, 0.26	x	505
	Quasi-2D perovskite	[73]	5.0×10^{-3}	1.5×10^{-1}		4.8×10^3	1.6×10^1		10^{-10}				x	405
Plsmc.	Silver antennae	[93]		1.1	24	1.9×10^{-1}	2.1×10^{-3}						x	1340
	Graphene/gold antennae	[94]	8.0×10^{-2}	1.5		8.7×10^{-6}							x	4250
	Gold antennae	[95]	1.2	1.2		2.1	2.6×10^{-2}						x	1560
Filter	Cholesteric liquid crystal films	[96]		1.9					10^{-7}			260, 310	10^4	830
	Carbon dot nanomaterials	[97]											x	450

Table 2.2: Summary of the key figures of merit for all CP selective photodetectors published to date. The measurement conditions for these figures correspond to the same conditions which yield the greatest photocurrent dissymmetry, not simply the optimum reported value in each case. Missing figures of merit are marked by grey cells and figures of merit which do not apply to the device architecture reported are marked with an "x". Where figures of merit have not been reported, they have been extracted from graphical data using data extraction software where possible. *These values have been incorrectly reported in their original articles and have been corrected here. Reproduced from [7] with permission from the Royal Society of Chemistry.

of the photodiodes is limited to 100%. Remarkably, the responsivities of 2D chiral perovskite nanowire photodetectors ($R = 47\ AW^{-1}$ at 505 nm) already exceed the responsivities of silicon-based devices ($R = 0.6\ AW^{-1}$ at 930 nm). [92, 98]

2.6.2 Dynamic Range

Dynamic range represents the range of light intensities over which a given photodetectors photocurrent will change with the changing light intensity incident on it. A more restrictive definition is Linear Dynamic Range (LDR), which represents the range of light intensities over which the photoresponse of a photoconductor increases *linearly* with incident light intensity. This is defined as:[24]

$$LDR = 20 \log_{10} \left(\frac{I_{max}}{I_{min}} \right) \tag{2.54}$$

where I_{max} and I_{min} are the maximum and minimum photocurrent values where the photocurrent increases linearly with the intensity of incident light, respectively.[24]

Although an important figure of merit for OPDs, LDR is rarely reported in the literature on CP OPDs (see Table 2.2). Large LDR can be achieved by suppressing noise current (reducing I_{min}) and is desirable for machine vision applications where images may contain both intense bright spots and low-light regions that must be accurately measured. Our achiral polyfluorene-based (co-)polymer: chiral small molecule (1-aza[6]helicene) photodiodes achieve an LDR of $\sim$ 80 decibels, which is considerably higher than that of InGaAs ($\sim$ 66 dB) and rivals both silicon (120 dB) and nonchiral OPDs ($\sim$ 100 dB).[47, 99]

2.6.3 Response Speed

The response speed of a photodetector quantifies the speed with which a photodetector can respond to a change in light intensity. This sets limits on the applications of photodetectors of a given speed. The response speed is quantified by the rise and fall times (t_{rise} and t_{fall}, respectively, Figure 2.12a) or the bandwidth (B, Figure 2.12b). t_{rise} represents the time taken

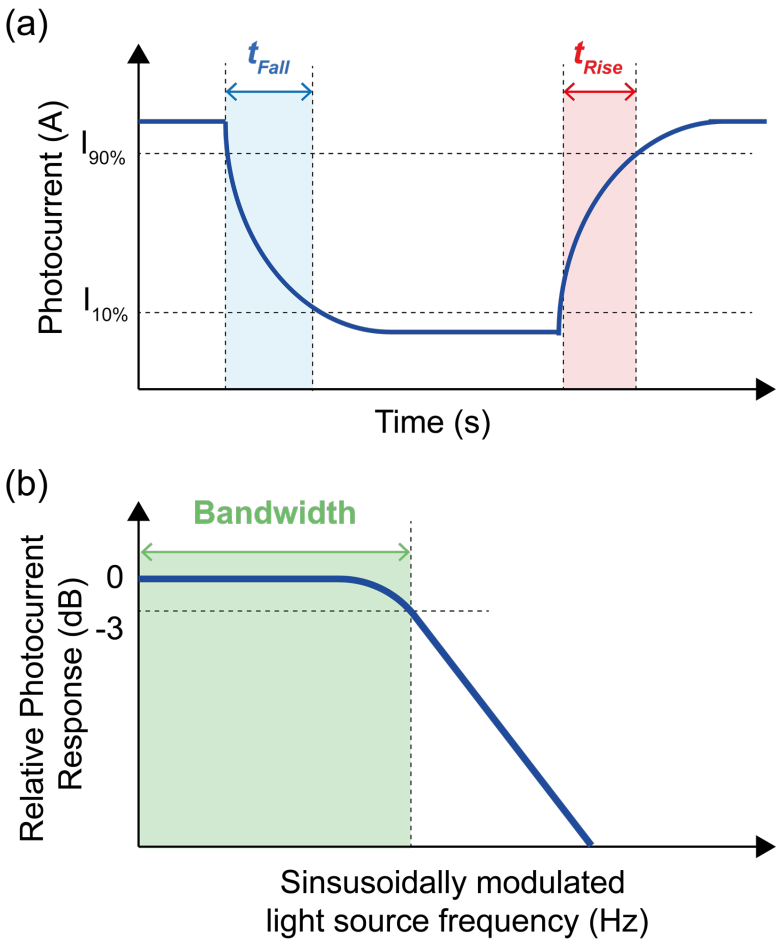


Figure 2.12: Definitions of the rise and fall times (a), and bandwidth (b) of a photodetector. (a) Rise (fall) time is the time taken for the device photocurrent to increase (decrease) from 10% (90%) to 90% (10%) of its maximum photocurrent under square wave modulated illumination. (b) Bandwidth is the frequency of a sinusoid-modulated light source at which the photocurrent of the photodetector falls to -3 dB below the photocurrent measured at a modulation frequency of 0 Hz (i.e. continuous illumination). Reproduced from [7] with permission from the Royal Society of Chemistry.

for the photocurrent of a photodiode to rise from 10% to 90% of its maximum value when exposed to a square-wave modulated light source. Similarly, t_{fall} represents the time it takes for the photocurrent of a photodiode to fall from 90% to 10% of its maximum value when exposed to a square-wave modulated light source.

The bandwidth (also known as the "3 dB frequency") of a photodetector is the frequency at which the photoresponse of the photodetector exposed to a light source with sinusoidally varying intensity falls to 3 dB below the photoresponse of the photodetector under Continuous Wave (CW) illumination. In other words, the bandwidth of a detector is the frequency at which the following condition is satisfied:

$$20\ \log_{10}\left(\frac{A_{CW}}{A_{sin}(f=B)}\right) = -3\ \text{dB} \tag{2.55}$$

where A_{CW} is the photoresponse of the photodetector under CW illumination $A_{sin}(f)$ is the frequency-dependent amplitude of the photoresponse of the photodiode under exposure to a light source with sinusoidally varying intensity with a modulation frequency of f.

To date, the fastest organic CP selective photodetectors are our own photodiodes based on chiral small molecule (1-aza[6]helicene) – achiral polymer (F8T2) blends, with a bandwidth of 56 kHz.[47] While suitable for imaging applications, which require frame rates of approximately 100 Hz, this bandwidth falls short of the bandwidth of InGaAs detectors used in fibre optic communications, with bandwidths in the 10 GHz range and rise times on the order of picoseconds.[24, 100] The low trap density and high charge carrier mobility of hybrid perovskite materials afford them both high LDR and ultra-fast response times. Recently, response times of < 10 ns have been reported in non-chiral perovskite/organic bulk heterojunction photodetectors based on MAPbI3 and F8IC.[101] The fast response time is attributed to (i) the high hole mobility of MAPbI3, (ii) the high electron mobility of F8IC and (iii) the suppression of RC delay times due to the reduced active area of these devices (and therefore reduced device capacitance, C). The use of chiral active layers with high charge carrier mobilities and devices with small active areas should be further explored to increase the speed of CP selective detectors to be compatible with communication applications.

2.6.4 Dark Current and Dark Noise

The dark current represents the current flow through a photodetector under dark conditions for a given device bias. The dark current may be measured under dark conditions and subtracted from the current measured from the device under exposure to a light source to determine the photocurrent of the photodetector.

Dark noise, however, represents the random fluctuations in the dark noise that cannot be eliminated from either the dark current or photocurrent by simple subtraction. Dark noise places a fundamental limit on the smallest measurable signal by a given photodetector, as any optical signal smaller than the amplitude of the dark noise of the photodetector will be effectively masked by the dark noise. Measurement of signals with a smaller amplitude of the dark noise of a detector requires advanced detection techniques such as lock-in amplification.

Dark noise is typically expressed as follows:

$$\begin{aligned} i_{noise} &= \sqrt{i_{shot}^2 + i_{thermal}^2 + i_{1/f}^2 + i_{g-r}^2} \\ &= \sqrt{2ei_dB + \frac{4kTB}{R_{sh}} + i(f,B)_{\frac{1}{f}}^2 + i(f,B)_{g-r}^2} \end{aligned} \tag{2.56}$$

where i_{shot} is the shot noise, corresponding to the quantised extraction of electrons in a photodetector; $i_{thermal}$ is the thermal noise due to the distributed thermal energy of the carriers in the photodetector; $i_{1/f}$ is the "1/f" noise, whose magnitude is inversely proportional to frequency; and i_{g-r}^2 is the geminate recombination, corresponding to the recombination of geminate electron-hole polaron pairs.[24, 102] Although the shot and thermal noise are frequency independent quantities whose magnitude can be predicted analytically from the dark current, i_d, electrical bandwidth, B, temperature, T and shunt resistance R_{sh} of the device. $1/f$ and geminate-recombination noise are more complex frequency-dependent noise sources that are not trivial to predict.

Two quantities closely related to the noise current are the Noise Equivalent Power (NEP) and

the specific detectivity (D^*) of a photodetector. The noise equivalent power is represents the minimum light intensity which can be detected above the noise current of the photodetector and is given by:[24]

$$\text{NEP} = \frac{I_{noise}}{R\sqrt{B}} \tag{2.57}$$

The noise equivalent power is dependent on the active area of the photodetector. To enable a meaningful comparison between devices of differing active areas, the specific detectivity of a photodetector is defined as the inverse of the NEP normalised for the active area of the device:[24]

$$D^* = \frac{\sqrt{A}}{\text{NEP}} \tag{2.58}$$

By normalising NEP for the area of the device, devices with different active areas can be compared. By inverting the normalised NEP, a highly sensitive photodetector (i.e. one which can detect low light intensities) has a high specific detectivity, and a poor sensitivity photodetector has a low detectivity, making for a more intuitive measure of detector sensitivity.

The highest detectivity for a CP selective photodetector was reported as 2.9×10^{13} Jones for a phototransistor based on an organic small molecule single crystal, relative to a value of 2.3×10^{11} Jones for a typical Si photodiode. [82, 103]

2.6.5 Operational Lifetime

The operational lifetime of a photodetector is the time for which the photodetector responsively remains approximately constant under fixed bias and illumination conditions. For CP selective photodetectors, this must also include the stability of the dissymmetry of the photocurrent over time.

After fabrication, most photodetectors initially undergo a rapid degradation of device responsivity, referred to as "burn-in", followed by a slower and more stable decay period (post-burn-in), which must be taken into account in the measurement of operational lifetime. [104, 105] This is particularly common in perovskite devices.[105] Post–burn–in degradation is the more meaningful measure of device lifetime, as this is more representative of long-term device performance.

To the best knowledge of the authors, only one report on the operational lifetime of a CP selective photodetector has been published. This device was a quasi-2D perovskite photoconductor with a reported operational lifetime of one month. [73]

2.6.6 On-Off Ratio

The on-off ratio ($R_{on/off}$) is a figure of merit, which is used almost exclusively with respect to transistors and phototransistors, and refers to the ratio between the drain current in the on- and off-state, specifically:

$$R_{on/off} = \frac{I_d(V_g = V_d = V)}{I_d(V_g = 0,\ V_d = V)} \tag{2.59}$$

A high $R_{on/off}$ is favourable, as this indicates that a low driving voltage is needed to achieve a good signal-to-noise ratio. [8] The need for a lower driving voltage also reduces the power consumption of circuits that use the transistor or phototransistor under test, which is essential for low-power applications such as IoT devices.

To date, the highest recorded on–off ratio for a CP selective phototransistor is over 10^7, exceeding the on–off ratios of some inorganic phototransistors. [82, 106]

2.6.7 Dissymmetry Factor of Photocurrent

The dissymmetry factor of the photocurrent, g_{ph}, is a figure of merit that is used exclusively with respect to photodetectors with a selective photoresponse to circularly polarised light. g_{ph} is one means of quantifying the degree to which a photodetector is selective in its response to circularly polarised light and is defined analogously to g_{abs}:

$$g_{ph} = \frac{I_L - I_R}{\frac{1}{2}(I_L + I_R)} \tag{2.60}$$

where I_L and I_R are the device photocurrents under L- and R-CPL respectively. g_{ph} is effectively the difference in photocurrent under L- and R-CPL normalised by the average of these two quantities. This allows devices with different responsivities and operating wavelengths to be

meaningfully compared. As with g_{abs}, g_{ph} provides a finite scale for device comparison, with a value of +2 indicating an exclusive photoresponse to L-CPL and a value of -2 indicating an exclusive photoresponse to R-CPL

2.7 Simulation of Absorption in CP-OPDs

In this section, we introduce Transfer Matrix Optics (TMO) as a means to calculate the Optical Electric Field (OEF) and time averaged power absorption as a function of position in an OPD. We will then demonstrate how straightforward modifications to this technique may be made to account for the circular dichroism and circular birefringence of the device active layer under L-CPL and R-CPL illumination.

2.7.1 Transfer Matrix Optics

The modelling of the OEF in a multilayer device is a complex problem, requiring a number of optical effects to be taken into account such as reflection and transmission at the interface between two layers, absorption and change in phase of the OEF during the propagation through a given layer, and the superposition of forward and backward (i.e., Reflected) light within each layer. All of these effects can be modelled using TMO.[107, 9]

In TMO, a device such as an OPD is modelled as a multilayer structure between two semi-infinite layers (Figure 2.13): the substrate on which light is incident ($j = 0$) and the layer of air on the opposing of the device multilayer ($j = m + 1$).[9] The multilayer consists of individual layers ($j = 1,\ 2,\ 3, \ldots, m$), with thicknesses, d_j, and complex indices of refraction $\bar{n}_j = n_j + ik_j$.[9, 107] In brief, n_j influences the rate of phase change of the OEF within a given layer, and is defined by the familiar expression:

$$n_j = \frac{c}{v_j} \tag{2.61}$$

where v_j is the speed of light within layer j. k_j, on the other hand, describes the absorption of

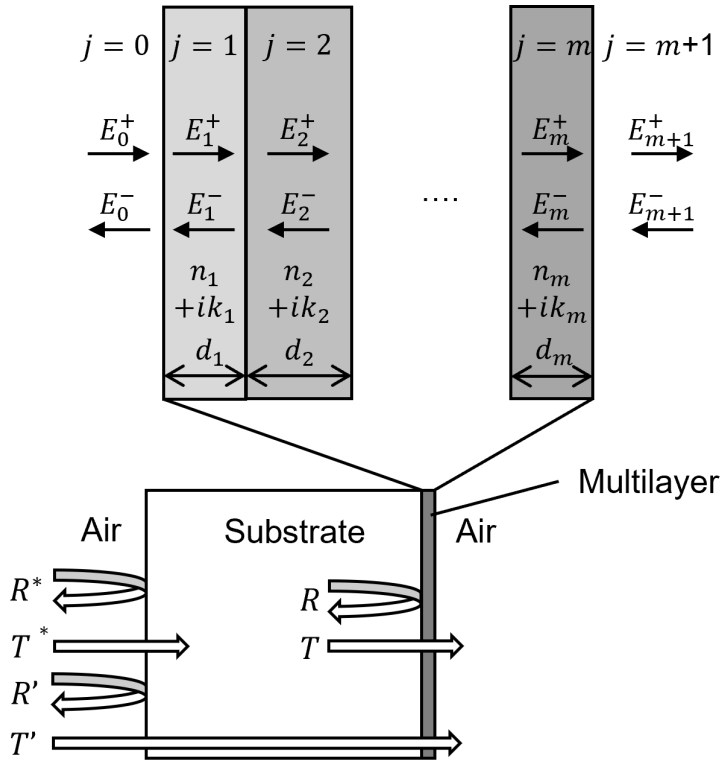


Figure 2.13: The TMO model of a multilayer device on a transparent substrate. Here, j indicates the layer number (where m is the final layer in the multilayer stack), $E_j^{+/-}$ is the forward (+) and rearward (−) travelling optical electric field in layer j, n_j and k_j are the real and imaginary components of the complex refractive index of layer j and d_j is the thickness of layer j. T, T^*, T' correspond to the transmissivity at the substrate-multilayer interface, the air substrate interface, and the substrate-multilayer structure as a whole. R, R^*, R' corresponds to the reflectivity at the same interfaces. Recreated from [9].

light within each layer, related to the absorption coefficient by the expression:

$$\alpha_j = \frac{4\pi k_j}{\lambda} \tag{2.62}$$

At the interface between two adjacent layers j and k, the OEF is described by:

$$\begin{bmatrix} \bar{E}_j^+ \\ \bar{E}_j^- \end{bmatrix} = I_{jk} \begin{bmatrix} \bar{E}_k^+ \\ \bar{E}_k^- \end{bmatrix} = \begin{bmatrix} \frac{1}{t_{jk}} & \frac{r_{jk}}{t_{jk}} \\ \frac{r_{jk}}{t_{jk}} & \frac{1}{t_{jk}} \end{bmatrix} \begin{bmatrix} \bar{E}_k^+ \\ \bar{E}_k^- \end{bmatrix} \tag{2.63}$$

where $\bar{E}_j^{\pm}$ and $\bar{E}_k^{\pm}$ are the components of the OEF travelling in the forward (+) and rearward (−) directions in layers j and k, respectively, I_{jk} is the interface matrix between layers j and k and the variables r_{jk} and t_{jk} are the Fresnel complex reflection and transmission coefficients, given by:[9]

$$r_{jk} = \frac{\bar{n}_j - \bar{n}_k}{\bar{n}_j + \bar{n}_k} \tag{2.64}$$

and

$$t_{jk} = \frac{2\bar{n}_j}{\bar{n}_j + \bar{n}_k} \tag{2.65}$$

In short, I_{jk} accounts for all reflection and transmission effects at the interface between two device layers with differing $\bar{n}_j$.[9, 107] The propagation through layer j results in an accompanying absorption and phase change of the OEF. This is described by the layer matrix:[9, 107]

$$L_j = \begin{bmatrix} e^{-i\xi_j d_j} & 0 \\ 0 & e^{i\xi_j d_j} \end{bmatrix} \tag{2.66}$$

where ξ_j is defined as

$$\xi_j = \left(\frac{2\pi}{\lambda}\right) \bar{n}_j \tag{2.67}$$

To account for reflection effects due to the presence of the device substrate and transmission through the device back-contact, the relationship between the OEF in layers $j = 0$ and $j = m+1$

must be related. This is accomplished using the transfer matrix, S:[9]

$$\begin{bmatrix} \bar{E}_0^+ \\ \bar{E}_0^- \end{bmatrix} = S \begin{bmatrix} \bar{E}_{m+1}^+ \\ \bar{E}_{m+1}^- \end{bmatrix} = S \begin{bmatrix} \bar{E}_{m+1}^+ \\ 0 \end{bmatrix} = \begin{bmatrix} S_{11} & S_{12} \\ S_{21} & S_{22} \end{bmatrix} \begin{bmatrix} \bar{E}_{m+1}^+ \\ 0 \end{bmatrix} = \begin{bmatrix} S_{11}\bar{E}_{m+1}^+ \\ S_{21}\bar{E}_{m+1}^+ \end{bmatrix} \tag{2.68}$$

where

$$S = \left(\prod_{n=1}^{m} I_{(n-1)n} L_n \right) \cdot I_{m(m+1)} \tag{2.69}$$

Note that since the device is illuminated from the substrate side ($j = 0$) and layer $j = m+1$ is semi-infinite, there is no backward travelling (i.e. reflected) wave from the layer $j = m+1$, thus, $\bar{E}_{m+1}^- = 0$.[9] By inspection, it is clear that S simply corresponds to the sequential application of the interface and layer matrices for every interface and layer between the $j = 0$ and $j = m+1$ to account for all optical effects within these layers. This relation can be used to determine the Fresnel transmission and reflection coefficients of the multilayer stack as a whole:[9, 107]

$$r = \frac{\bar{E}_0^-}{\bar{E}_0^+} = \frac{S_{21}}{S_{11}} \tag{2.70}$$

$$t = \frac{\bar{E}_{m+1}^+}{\bar{E}_0^+} = S_{11}^{-1} \tag{2.71}$$

This may in turn be used to determine the absorption efficiency of the multilayer stack

$$\eta_A = 1 - T - R \tag{2.72}$$

where T and R are the transmissivity and reflectivity of the multi-layer stack, which are related to the Fresnel coefficients by:[9]

$$T = |t|^2 \frac{\bar{n}_{m+1}}{\bar{n}_0} \tag{2.73}$$

$$R = |r|^2 \tag{2.74}$$

Up to this point, a number of optical effects due to the substrate have been neglected (note that $\bar{E}_0^+$ is the OEF incident on the substrate-multilayer interface and not the air-substrate interface). This can be accounted for by correcting T and R for the reflections at the air-

substrate and substrate-multilayer interface:[9]

$$R' = \frac{R^* + R - 2R^*R}{1 - R^*R} \tag{2.75}$$

$$T' = \frac{T^*T}{1 - R^*R} \tag{2.76}$$

where

$$R^* = \left|\frac{1 - \bar{n}_0}{1 + \bar{n}_0}\right|^2 \tag{2.77}$$

$$T^* = n_0 \left|\frac{2}{1 + \bar{n}_0}\right| \tag{2.78}$$

The true absorption efficiency is thus given by

$$\eta_A = 1 - T' - R' \tag{2.79}$$

To determine the electric field in layer j, we need to account for all optical effects acting on the forward and rearward travelling OEFs from layers $k < j$ and $k > j$ respectively.[9] To achieve this, the transfer matrix can be split into three components:[9, 107]

$$S = S_j^- L_j S_j^+ \tag{2.80}$$

where

$$S_j^- = \left(\prod_{n=1}^{j-1} I_{(n-1)n} L_n\right) \cdot I_{(j-1)j} \tag{2.81}$$

and

$$S_j^+ = \left(\prod_{n=j+1}^{m} I_{(n-1)n} L_n\right) \cdot I_{m(m+1)} \tag{2.82}$$

By inspection, it is clear that S_j^- and S_j^+ represents all interface and propagation effects in the layers to the left and right of layer j, respectively. Using these matrices, the overall OEF in layer j can be determined by calculating the forward and rearward travelling electric field in layer j at the left interface. This is achieved by relating the electric field in layer j to layers 0

and $m+1$ via:[9]

$$\begin{bmatrix} \bar{E}_0^+ \\ \bar{E}_0^- \end{bmatrix} = S_j^- \begin{bmatrix} \bar{E}_j^+ \\ \bar{E}_j^- \end{bmatrix} = \begin{bmatrix} S_{j11}^- & S_{j12}^- \\ S_{j21}^- & S_{j22}^- \end{bmatrix} \begin{bmatrix} \bar{E}_j^+ \\ \bar{E}_j^- \end{bmatrix} = \begin{bmatrix} S_{j11}^- \bar{E}_j^+ + S_{j12}^- \bar{E}_j^- \\ S_{j21}^- \bar{E}_j^+ + S_{j22}^- \bar{E}_j^- \end{bmatrix} \tag{2.83}$$

$$\begin{bmatrix} \bar{E}_j^+ \\ \bar{E}_j^- \end{bmatrix} = L_j S_j^- \begin{bmatrix} \bar{E}_{m+1}^+ \\ \bar{E}_{m+1}^- \end{bmatrix} = \begin{bmatrix} e^{-i\xi_j d_j} & 0 \\ 0 & e^{i\xi_j d_j} \end{bmatrix} \begin{bmatrix} S_{j11}^+ & S_{j12}^+ \\ S_{j21}^+ & S_{j22}^+ \end{bmatrix} \begin{bmatrix} \bar{E}_{m+1}^+ \\ 0 \end{bmatrix} = \begin{bmatrix} e^{-i\xi_j d_j} & S_{j11}^+ \bar{E}_{m+1}^+ \\ e^{i\xi_j d_j} & S_{j21}^+ \bar{E}_{m+1}^+ \end{bmatrix} \tag{2.84}$$

This allows the normalised forward (t^+) and backward (t^-) travelling electric field to be calculated in layer j, normalised by the incident intensity at $j = 0$:[9]

$$\bar{E}_j^+ = e^{-i\xi_j d_j} S_{j11}^+ \bar{E}_{m+1}^+ \tag{2.85}$$

$$\bar{E}_j^- = e^{i\xi_j d_j} S_{j21}^+ \bar{E}_{m+1}^+ \tag{2.86}$$

$$\bar{E}_0^+ = S_{j11}^- \bar{E}_j^+ + S_{j12}^- \bar{E}_j^- = S_{j11}^- \left[e^{-i\xi_j d_j} S_{j11}^+ \bar{E}_{m+1}^+ \right] + S_{j12}^- \left[e^{i\xi_j d_j} S_{j21}^+ \bar{E}_{m+1}^+ \right] \tag{2.87}$$

Thus:[9]

$$t^+ = \frac{\bar{E}_j^+}{\bar{E}_0^+} \tag{2.88}$$

$$= \frac{e^{-i\xi_j d_j} S_{j11}^+ \bar{E}_{m+1}^+}{S_{j11}^- \left[e^{-i\xi_j d_j} S_{j11}^+ \bar{E}_{m+1}^+ \right] + S_{j12}^- \left[e^{i\xi_j d_j} S_{j21}^+ \bar{E}_{m+1}^+ \right]} \tag{2.89}$$

$$= \frac{\frac{1}{S_{j11}^-}}{1 + \frac{S_{j12}^- S_{j21}^+}{S_{j11}^- S_{j11}^+} e^{i2\xi_j d_j}} \tag{2.90}$$

$$t^- = \frac{\bar{E}_j^-}{\bar{E}_0^+} \tag{2.91}$$

$$= \frac{e^{i\xi_j d_j} S_{j21}^+ \bar{E}_{m+1}^+}{S_{j11}^- \left[e^{-i\xi_j d_j} S_{j11}^+ \bar{E}_{m+1}^+\right] + S_{j12}^- \left[e^{i\xi_j d_j} S_{j21}^+ \bar{E}_{m+1}^+\right]} \tag{2.92}$$

$$= \frac{\frac{1}{S_{j11}^-}}{1 + \frac{S_{j12}^- S_{j21}^+}{S_{j11}^- S_{j11}^+} e^{i2\xi_j d_j}} \frac{S_{j21}^+}{S_{j11}^+} e^{i2\xi_j d_j} \tag{2.93}$$

$$= t^+ \frac{S_{j21}^+}{S_{j11}^+} e^{i2\xi_j d_j} \tag{2.94}$$

The total electric field in layer as a function of position in layer j is thus given by the sum of the forward and rearward travelling waves:[9]

$$\bar{E}_j(x) = \bar{E}_j^+(x) + \bar{E}_j^-(x) = \left(t^+ e^{i\xi_j x} + t^- e^{-i\xi_j x}\right) \bar{E}_0^+ \tag{2.95}$$

This can, in turn, be expressed as a time-averaged absorbed power as a function of position:[9]

$$Q_j(x) = \frac{4\pi c \varepsilon_0 k_j n_j}{2\lambda} \left|\bar{E}_j(x)\right|^2 \tag{2.96}$$

2.7.2 Modifications for Optically Active Layers

Whilst the above TMO model incorporates many of the optical effects present in multilayer devices, it fails to account for optical activity in any of the device layers when illuminated with CPL. To do so requires three possible effects to be taken into consideration: the change in handedness of CPL on reflection at normal incidence to an interface, the circular dichroism of the optically active layer, and the circular birefringence (if any) of the optically active layer.

To address the first of these points, we first assume that under CP illumination, reflection at any interface leads to a change in handedness of CPL (i.e. L-CPL becomes R-CPL and vice versa). This leads logically to the conclusion that all forward-travelling CP OEFs share the same handedness as the incident light and that rearward (i.e. reflected light) travelling optical fields are of the opposite handedness to the incident CPL.

For the standard TMO model discussed previously, it is assumed that for each layer, the complex

refractive index for the forward and backward travelling waves is the same. To account for circular dichroism and circular birefringence in an optically active layer, we require a different complex refractive index for forward (+) and backward (−) travelling waves for this layer - one corresponding to L-CPL and the other corresponding to R-CPL, that is

$$\bar{n}_j^+ = n_j^+ + ik_j^+ \tag{2.97}$$

$$\bar{n}_j^- = n_j^- + ik_j^- \tag{2.98}$$

where $n_j^+ \neq n_j^-$ to account for circular birefringence, and $k_j^+ \neq k_j^-$ to account for circular dichroism. It is important to note here that $\bar{n}_j^+$ and $\bar{n}_j^-$ correspond to the refractive index of the optically active medium for the incident and reflected handedness, respectively. As a result, $\bar{n}_j^+$ and $\bar{n}_j^-$ must be changed according to the incident handedness of CPL.

It is straightforward to relate the extinction coefficient for L-CPL (k_L) and R-CPL (k_R) to the g_{abs} value of the optically active layer:

$$g_{abs} = 2\frac{A_L - A_R}{A_L + A_R} = 2\frac{\alpha_L - \alpha_R}{\alpha_L + \alpha_R} \tag{2.99}$$

where α_L and α_R are the absorption coefficients of L-CPL and R-CPL respectively. In turn, α is related to k via:

$$\alpha = \frac{4\pi k}{\lambda} \tag{2.100}$$

thus:

$$g_{abs} = 2\frac{k_L - k_R}{k_L + k_R} = 2\frac{1 - \frac{k_R}{k_L}}{1 + \frac{k_R}{k_L}} \tag{2.101}$$

By defining the average (i.e. unpolarised) extinction coefficient:

$$k = \frac{k_L + k_R}{2} \tag{2.102}$$

an expression for k_L may be derived:

$$\frac{k_R}{k_L} = \frac{2k}{k_L} - 1 \tag{2.103}$$

$$g_{abs} = 2\left[\frac{k_L}{k} - 1\right] \Rightarrow k_L = k\left[\frac{g_{abs}}{2} + 1\right] \tag{2.104}$$

Similarly, for k_R

$$k_R = k\left[1 - \frac{g_{abs}}{2}\right] \tag{2.105}$$

Aside from these influences, all other aspects of the TMO model are unchanged.

The modifications required to account for reflection and circular dichroism were first outlined by Gilot *et al.*, however, we make an important distinction with the CP TMO method employed in our case.[85] In the CP TMO model developed by Gilot *et al.* the Poynting vectors of incoming and outgoing (i.e., reflected) CPL are calculated separately. The ingoing and outgoing Poynting vectors are then summed to determine the total time averaged power absorbed under L-CPL and R-CPL in the regions of interest, specifically, in the chiral PFDTBT within one exciton diffusion length of the PFDTBT/C60 and PFDTBT/PEDOT:PSS interfaces, and in the entirety of the C60 layer. The difference in total power absorption in these regions is then used as an estimate for g_{ph}. In our case, however, we build on the work of Gilot *et al.* by taking a finer grained modelling approach and consider the power absorption as a function of depth in the device to later model the device EQE spectra for L-CPL and R-CPL under various biasing conditions.

2.8 Time of Flight Mobility

In this section, we will discuss the theory of Time of Flight (ToF) mobility measurements as a means to measure charge transport in OSCs. We will also discuss the application of this technique to chiral OSC materials and the possibility of spin-selective excitation and transport in chiral OSCs.

2.8.1 Principles of Operation

A simplified diagram of a typical experimental setup used for ToF measurements is shown in Figure 2.14.[10] As shown, the device under test is a layer of a solid-state OSC of thickness d,

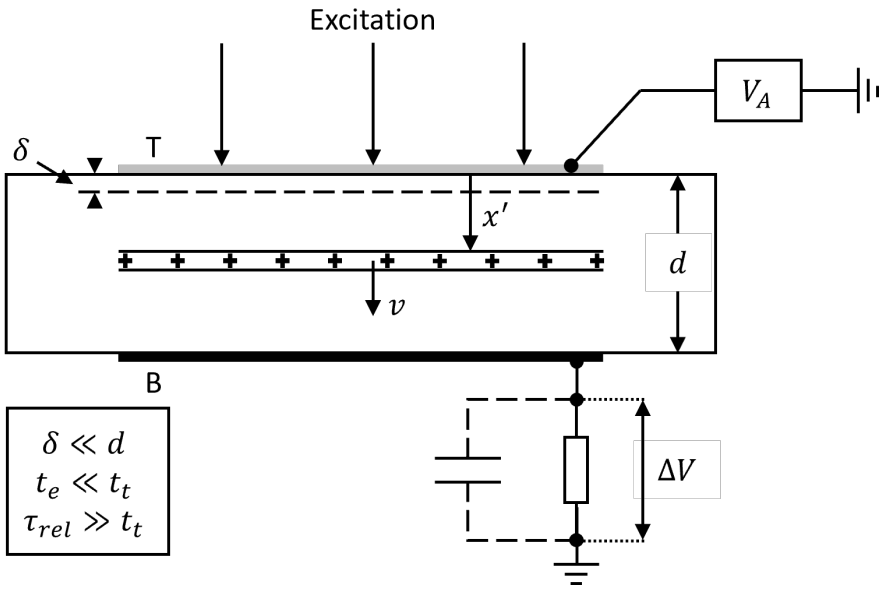


Figure 2.14: A simplified diagram of a typical ToF mobility measurement setup. Adapted from [10].

in contact with a metallic top electrode (T) and a metallic bottom electrode (B) and exposed to a pulsed light source.[10] T must be at least partially transparent to the intended excitation wavelength to allow the pulsed light source to photoexcite excitons in the OSC layer under test and is held at bias V_A.[10] T and B must be blocking contacts to ensure that, in the idealised case, the only free carriers present in the OSC layer are due to optical excitation and that applying a bias to T does not result in charge injection.[10] B is connected to ground through a resistor R.[10] The value of R must be small relative to the resistance of the ToF device under test. This is to ensure that the majority of the voltage applied to T is dropped across the ToF device, rather than the sensing resistor, R, which allows the electric field within the OSC layer as to be closely approximated as $F = V_A/d$.[10]

To initiate a ToF mobility measurement, the T side of the device is exposed to a laser pulse with a photon energy greater than the OSC bandgap. The thickness of the OSC layer must be large compared to the absorption depth, δ, of the OSC at the chosen excitation wavelength (i.e., $\delta << d$) and the duration of the pulse of the excitation light source, t_e should be considerably shorter than the transit time t_t of carriers across the OSC layer (i.e., $t_e << t_t$).[10] If these conditions are satisfied, the incident light pulse photoexcites a thin sheet of excitons (with thickness $\sim \delta$) in the OSC layer at the interface with T.

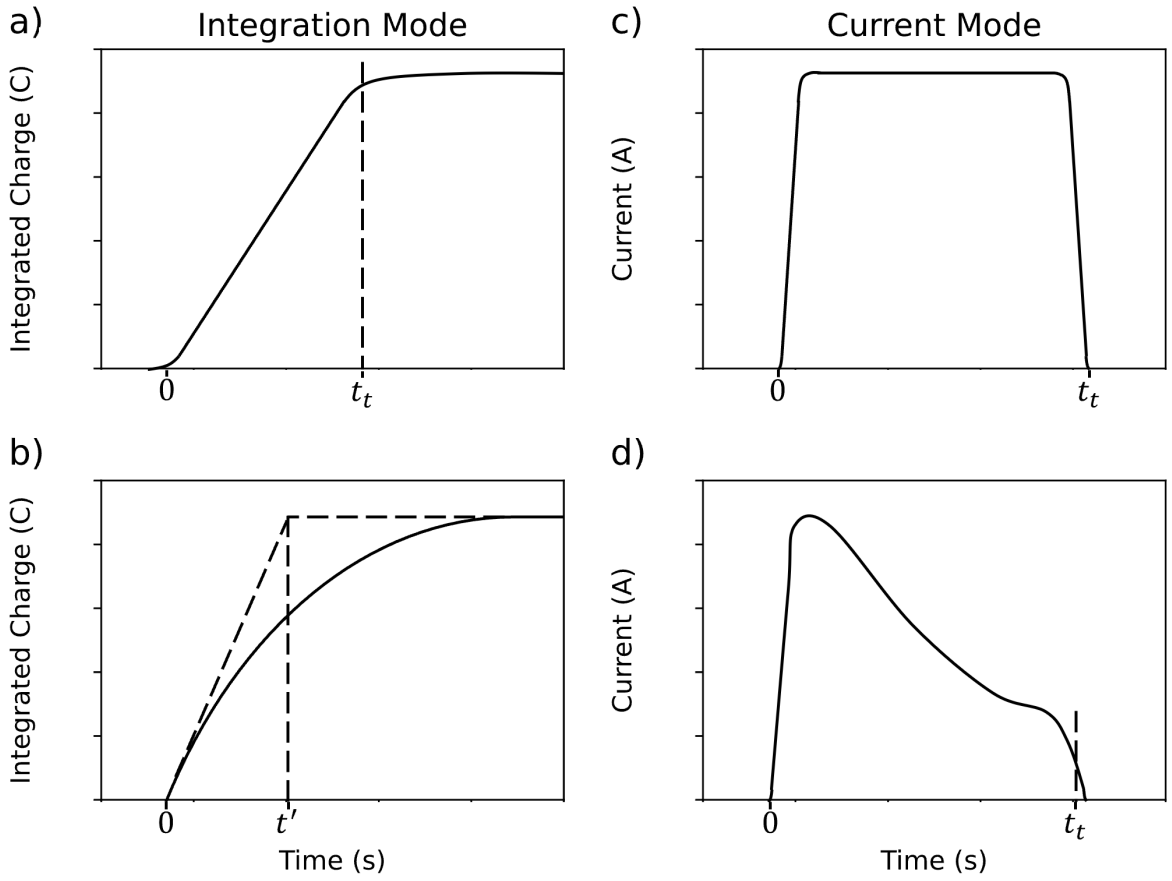


Figure 2.15: Time of Flight (ToF) mobility measurement traces under the integration mode (a, b) and current mode (c, d) of measurement. ToF traces a) and c) are characteristic of low dispersion charge transport, indicating a low concentration of deep trap states and showing a clear transit time t_t. Traces b) and d) are characteristic of highly dispersive charge transport, where the arrival of carriers at the collecting electrode has been spread out by deep trap states. Adapted from [10].

Under the action of the external bias, excitons generated by the pulsed light source may be separated into their constituent electron and hole polarons. For the measurement of hole mobility,[7] V_A is positive. This causes a drift current of a thin sheet of hole polarons from the T-OSC interface to to the B-OSC interface.[10] The drift current caused by the generation and transit of holes through a given OSC and their subsequent extraction via B is monitored using the voltage drop over R using an oscilloscope.[10] This may be measured using the total integrated charge collected from B as a function of time (referred to as "integration mode" hereafter, Figure 2.15a,b) or the current flow through the ToF device as a function of time (referred to as "current mode" hereafter, Figure 2.15c,d).[10]

[7]The procedure for electron mobility measurements are identical, aside from the use of a negative V_A.

The shape of the charge extraction current profile is governed by the degree to which the thin sheet of holes disperse during their transit across the OSC layer.[10] This is largely the result of non-uniform hopping of charges through the OSC layer due to the presence of trap states within this layer.[10] In the ideal case where charges do not disperse significantly during their transit through the OSC layer, the ideal ToF curve is produced (Figure a,c). In current mode, this consists of a sharp increase in current caused by the sudden photogeneration of excitons, followed by a constant current period corresponding to the transit of charges across the device, and finally the "knee point" and decline of the ToF current, indicating the arrival and extraction of the photogenerated holes at the non-transparent electrode.[10] In this non-dispersive case, the initial sharp rise of the ToF current may be taken as $t = 0$, i.e. the time at which photogenerated holes begin their transit towards the non-transparent electrode.[10] The knee point is t_t and represents the time taken for charges to transit the thickness of the OSC layer (d) and can be used to determine the drift velocity of carriers, $v = d/t_t$. Using known values of d and t_t, the familiar expression may be used to determine the drift mobility of carriers:[10]

$$\mu = \frac{v}{F} = \frac{d}{t_t} \Big/ \frac{V_A}{d} = \frac{d^2}{t_t V_A} \tag{2.106}$$

For the alternative case of highly dispersive transport, the initially thin layer of holes disperses during transit through the OSC layer due to a greater concentration of deep trap states.[10] As a result, the time at which the charge packet arrives at the opposing electrode is ill-defined, caused by the knee point visible in current mode operation to become spread out (Figure 2.15d).[10] In extreme cases, the knee point and hence t_t is not visible at all from current mode measurements due to large dispersion of carriers. In this case, it can be more appropriate to use integration mode and define the transit time as the time taken for a fraction (e.g. 50%) of the total photoexcited charge to be extracted from the device as this (unlike a broad, poorly defined knee point) is straightforward to define mathematically in the charge extraction curve. [108, 109]

2.8.2 Spin-selective Excitation and Transport

There has been considerable recent interest in spin-selective excitation and spin-selective charge transport, particularly for the Chirality Induced Spin Selectivity (CISS) effect, where chiral organic materials have been shown to demonstrate room temperature spin filtering at room temperature, with the filtered spin determined by the enanatiomer of the chiral molecule used.[110, 111] In Section 2.6, a number of perovskite CP-selective photodetector examples discuss spin-selective behaviour as a means to explain significantly larger g_{ph} values relative to the g_{abs} of the chiral perovskites used in their architecture. This spin enhancement is divided into two parts: direct optical excitation of spin-polarised electrons with circularly polarised light [112] and spin-selective charge transport [113]. The direct excitation of spin-polarised carriers is believed to be a result of the strong spin-orbit coupling present due to the strong atomic spin-orbit coupling of lead and iodine in the perovskite structure.[112] Spin-selective transport is attributed to a reduced effective mass of spin-polarised carriers. [113]

In organic molecules, spin-selective excitation corresponds to the direct optical excitation of the triplet state from the ground state - a conventionally forbidden transition. Although selective *electrical excitation*, transport, and filtration of spin-polarised carriers have been demonstrated in organic molecules,[114] Szumska *et al.* demonstrate that *optical excitation* of triplet states requires large spin-orbit coupling of heavy atoms in the OSC [115]. For the materials investigated in this thesis, heavy atoms have been absent in the selected semiconductors and thus the spin-selective optical excitation of triplets is unlikely to be a factor in the CP selectivity of the device response.

Spin-orbit coupling has been observed to be enhanced in *curved* organic materials (including OSCs) where heavy metal atoms are absent, such as fullerenes,[116, 117], curved graphene,[117] nanotubes,[117, 118] and nanotube caps.[117] This enhanced spin-orbit coupling arises from the symmetry-breaking caused by the curvature of these molecular structures.[118] However, to the best knowledge of the author, there are no experimental observations of the direct optical excitation of triplet states in these materials. For this reason, spin-selective optical excitation of triplets arising from the curvature of materials studied in this thesis have also been neglected

in this work.

Chapter 3

Materials and Experimental Methods[1]

3.1 Introduction

Photodetectors sensitive to circularly polarised light are comparatively novel relative to other well-established organic semiconductor devices such as OLEDs and OPVs. As such, standard characterisation procedures for CP-OPDs are not widespread. In this section, we present the standardised measurement protocols used in this project, drawn from existing examples in the literature and those developed during the course of this project.

3.2 Materials

The molecular structures of the organic semiconductors used in this PhD are shown in Figure 3.1.

3.2.1 Bis[60]PCBM

Dimethyl 4,4'-[61,62-diphenly,3'H,3"H-dicyclopropa(C_{60}—I_h)[5,6]fulleren-1,9:X,Y-diyl]dibutanoate, referred to as Bis[60]PCBM hereafter. This material was provided by the Dennis group (Queen

[1]Reuse permissions for this chapter have been included in the appendices.

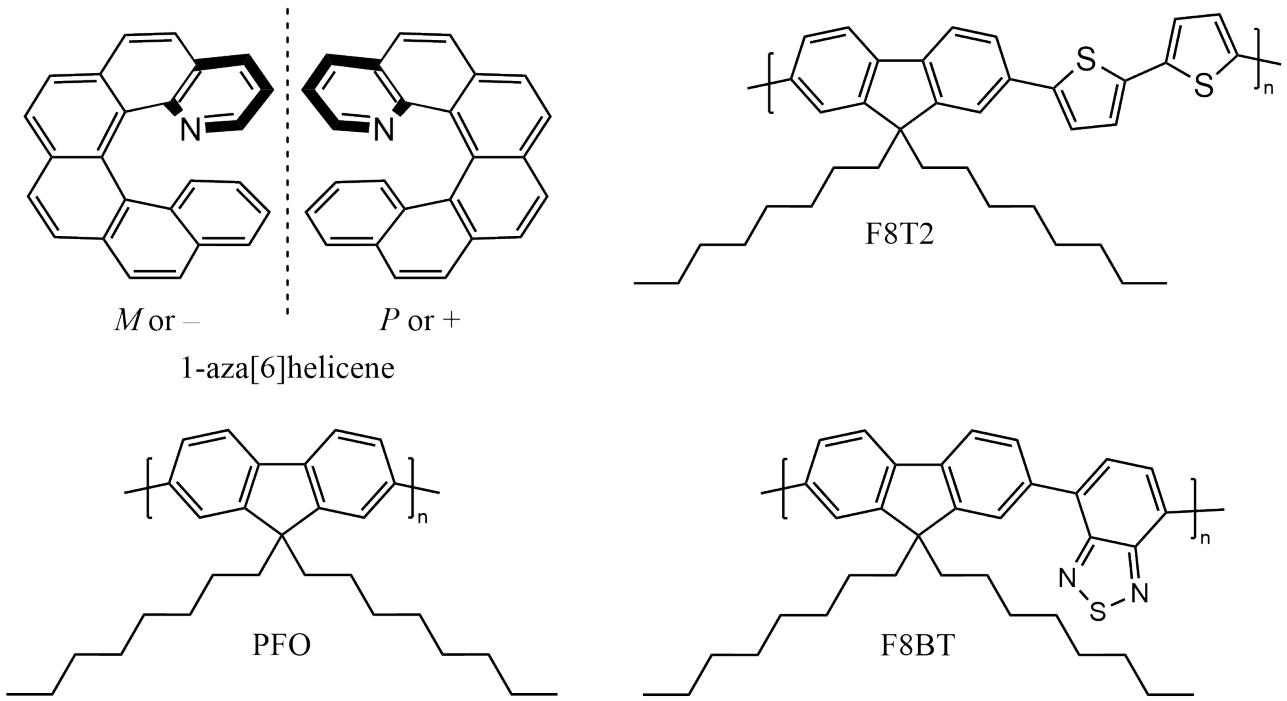


Figure 3.1: Molecular structures of the organic semiconductors used in this project. Due to the large number of Bis[60]PCBM enantiomers, the structures of these enantiomers are presented in Section 4.

Mary University of London) and was separated into its constituent enantiomers and purified ($> 99\%$) by Wenda Shi.

3.2.2 F8T2

Poly(9,9-dioctylfluorene-*alt*-bithiophene), referred to as F8T2 hereafter. This material was provided by Solaris Chem Inc. with $M_w = 27$ kDa and a purity of $> 99\%$.

3.2.3 aza[6]H

1-aza[6]helicene, referred to as aza[6]H hereafter. Both $[M]$- and $[P]$-aza[6]H enantiomers and racemic aza[6]H were provided by the Fuchter group at a purity of $> 95\%$.

3.2.4 PFO

Poly(9,9-di-n-octylfluorenyl-2,7-diyl), referred to as PFO hereafter. This material was provided by Cambridge Display Ltd with M_w = 484.2 kDa and M_n = 182.4 kDa. The manufacturer conducted extensive post-synthesis purification of this material to remove ionic impurities and catalyst residues; however, the final purity is not known.

3.2.5 PEDOT:PSS

Poly(3,4-ethylenedioxythiophene):poly(styrenesulfonate), referred to as PEDOT:PSS hereafter. This material was provided by the Heraeus Group. Clevios™ P VP AI 4083, work function ∼5.2 eV.

3.2.6 Aluminium

Aluminium pellets (Al, 99.99% purity) for thermal evaporation were purchased from Kurt J. Lesker Company®.

3.3 Experimental Methods

3.3.1 Methods Used to Study Bis-PCBM Phototransistors

CD and UV-Vis

The CD spectra of each enantiomer were recorded in toluene approximately 0.2 mg/ml on a JASCO J-810 CD spectrophotometer at room temperature. The selected scanning range was 360 to 700 nm with a 200 nm/min rate, a bandwidth of 1 nm and three-fold accumulation. Thin-film CD spectra were acquired using a Chirascan from Applied Photophysics. UV-vis measurements were performed using an Agilent Cary 5000 UV-Vis spectrophotometer.

Microscopy

Topographic atomic force micrographs were acquired using a Park NX10 in non-contact mode on both Si/SiO2 (OFET) and quartz substrates. The scanning speed was 1 Hz and the image size was 512 px × 512 px. Cross-polarised microscope images were acquired using a Zeiss microscope and a digital camera at 10× optical magnification.

Calculations

All DFT calculations were performed using Gaussian '16.[119] Under the assumption that alkyl chains have a negligible impact on the chiroptical properties of the entire molecule, the addends of all structures were first 'trimmed' to leave a methyl group. The phenyl group was preserved. The geometries were relaxed, including an IFPCM solvent model for toluene using B3LYP/6-31G(d) method. TD-DFT calculations (50 excited states with singlet symmetry) were then performed at the same level of theory. The simulated CD spectra were compared with the experimental ones by means of the software SpecDis. Half-height peak-widths of the gaussian distributions were chosen by the software in order to best match the experimental and simulated spectra. An appropriate broadening factor σ for Gaussian curves and appropriate shift was chosen by a similarity algorithm to maximise agreement between the calculated and experimental spectra. TD-DFT results were further analysed by TheoDORE software using the Natural Transition Orbitals formalism.[120, 121, 122]

Substrate Cleaning and Treatment

Prepatterned transistor wafer substrates (provided by Fraunhofer IPMS) with 30 nm thick gold electrodes and a 230 nm thick SiO_2 dielectric layer were used to prepare chiral fullerene phototransistors with channel lengths of 2.5 to 20 μm and widths of 2 mm. To remove the photoresist coating from the substrates and clean the underlying surface, the substrate is cleaned by ultrasonication, first in acetone (15 min) followed by isopropyl alcohol (15 min) and finally in a 2% concentration solution of Hellmanex III (15 min). The substrates were then subjected

to 3 min of UV-Ozone treatment at a power of 80 W using an Emitech K1050X plasma asher.

Solution Processing and Spin-Coating

The substrates were modified with HMDS by dynamic spin coating (500 rpm × 5s, 4000 rpm × 55 s) and thermally annealed at 120°C for 5 min. Bis[60]PCBM enantiomers were dissolved at 15 mg/ml in chlorobenzene and spin-coated (500 rpm × 60 s, 3000 rpm × 40 s) on transistor substrates, followed by annealing at 120°C for 1 hour and then annealing at 90°C under nitrogen for 3 hours.

Output and Transfer Characteristics

The output and transfer characteristics were measured under nitrogen using an Agilent B2900A series source/measure unit (SMU). The sensitivity of the phototransistors to unpolarised and CP light was determined using a 405 nm 50 mW diode laser (T220AX1670GD-P405150, Anford), which was polarised using a wire grid linear polariser (WP25M-VIS, Thorlabs) and a 405 nm quarter-wave plate (WPMQ05M-405, Thorlabs). For continuous illumination, the intensity of this light source was controlled by varying the current supplied by a Keithley 2400 Series SMU and for temporal measurements, the laser was pulsed with an Agilent 33210A Function/Arbitrary Waveform Generator. The intensity of the light source measured using a laser power meter (LaserCheck, Coherent) at the position of the phototransistor under test. A schematic of the equipment used for these measurements is shown in Figure 3.2.

3.3.2 Methods Used to Study F8T2:aza[6]H Photodiodes

Substrate Cleaning and Treatment

Pre-patterned 12.0 × 12.0 mm substrates with 145 ± 10 nm ITO on Eagle XG glass (Thin Film Devices, Inc.) were used to prepare CP OPDs with active areas of 1.5 × 3.0 mm^2. The substrates were cleaned by ultrasonication, first in acetone (15 min) followed by isopropyl

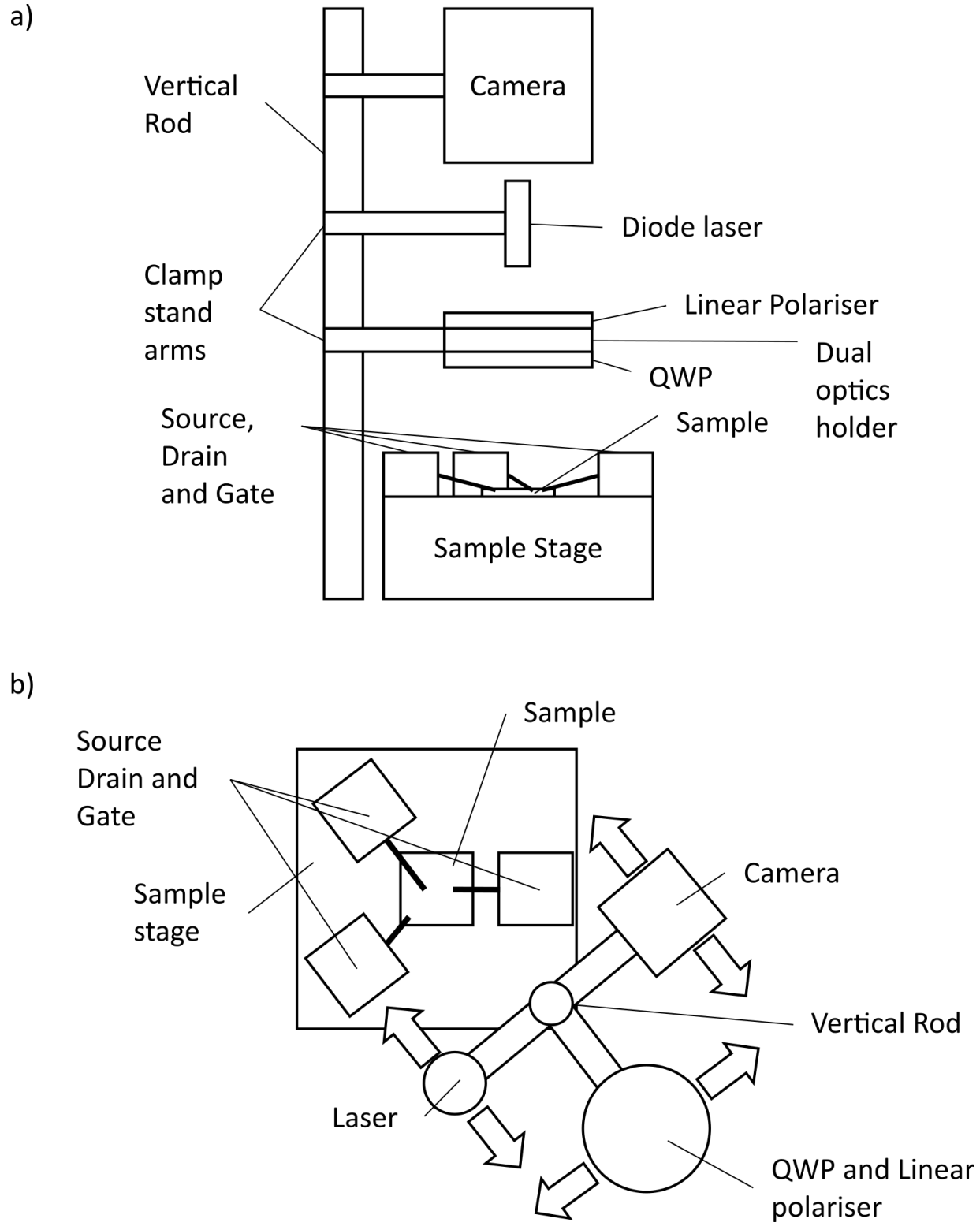


Figure 3.2: Diagram of the experimental setup for CP photoFET measurements. As shown, the laser and polarising optics can be rotated out of position above the sample to allow the source, gate, and drain probes to be attached to each transistor with the aid of a camera. Once the source, drain, and gate electrodes have been connected, the laser and optics are rotated into position over the sample for measurements. Reproduced from [11] with permission from Wiley.

alcohol (15 min) and finally in a 2% concentration solution of Hellmanex III (15 min). The substrates were then subjected to 3 min of UV-Ozone treatment at a power of 80 W using an Emitech K1050X plasma asher.

Solution Proccessing and Spin-Coating

PEDOT:PSS was spin coated onto cleaned substrates at 3000 rpm for 30 s and then annealed at 140°C for 15 min. Solutions of *rac*-, [*M*]-, and [*P*]-aza[6]H:F8T2 were prepared by dissolving aza[6]H and F8T2 separately in toluene at a concentration of 20 mg ml^{-1} before combining the two with a 10 wt% loading ratio of aza[6]H. These solutions were gently heated at 70°C for 15 min to ensure complete dissolution. The aza[6]H:F8T2 solutions were then spin-coated onto the PEDOT:PSS layer at 2000–12000 rpm for 60 s to obtain the desired film thicknesses, followed by annealing at 140°C for 10 min to induce the strong chiroptical response in F8T2.

Vacuum Processing and Thermal Evaporation

The C60 donor layer and the aluminium back contact were thermally evaporated onto the aza[6]H:F8T2 layer using an MBRAUN thermal evaporator and the thickness and evaporation rate of these layers was monitored *in-situ* using an Inficon SQM-160 rate/thickness monitor. The thicknesses of all the device layers were verified using a Bruker DektakXT surface profilometer.

EQE, Responsivity and Photocurrent Dissymmetry

The EQE of the CP OPDs was measured using a Bentham PVE300 photovoltaic device characterisation system. Circularly polarised EQE and g_{ph} spectra of devices were also acquired using the Bentham PVE300 with a wire grid polariser (Thorlabs, WP25M-VIS) and a quarter wave Fresnel rhomb retarder (Thorlabs, FR600QM) to circularly polarise the beam incident on the device under test. A schematic of the equipment used for these measurements is shown in Figure 3.3

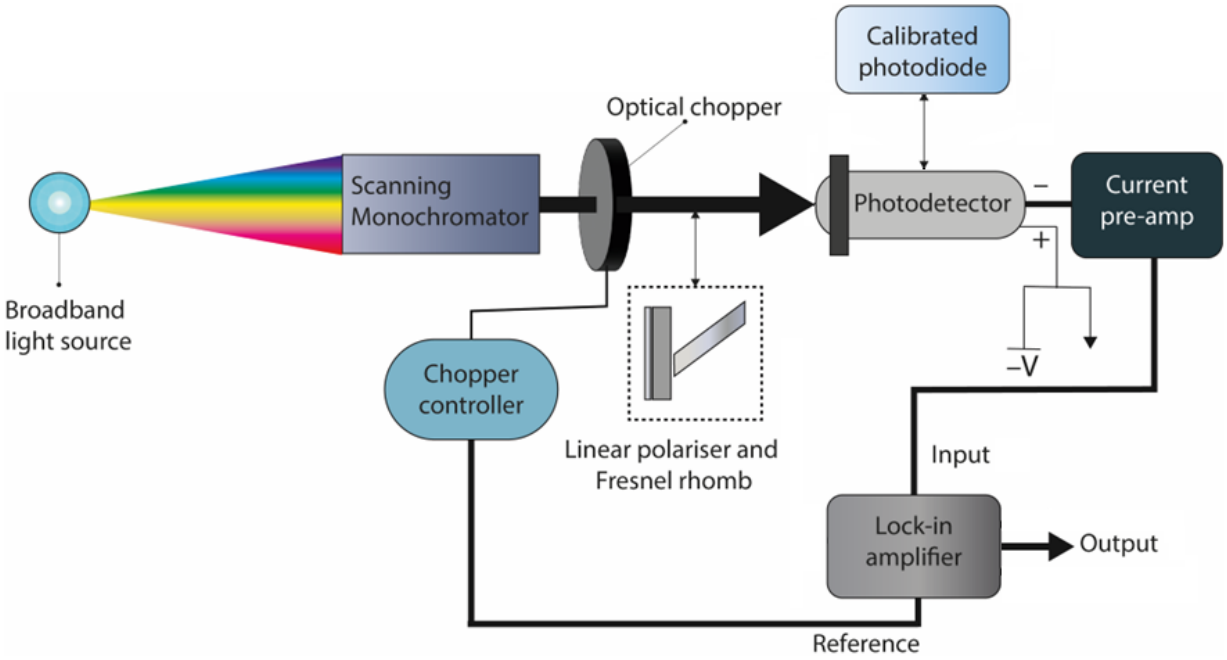


Figure 3.3: Experimental setup for the measurement of EQE, responsivity and spectral photocurrent dissymmetry. The device under test is illuminated with monochromatic light from a white light source that has passed through a scanning monochromator. Monochromatic light is chopped by an optical chopper and the chopped light is directed to a calibrated photodiode or the device under test. A linear polariser and Fresnel rhomb can be added in front of the beam to produce a circularly polarised beam. The photocurrent from the device under test and the calibrated photodiode are converted to voltages, which are measured via sensitive lock-in detection using a lock-in amplifier using the chopper controller signal as a reference frequency. Adapted from [7]

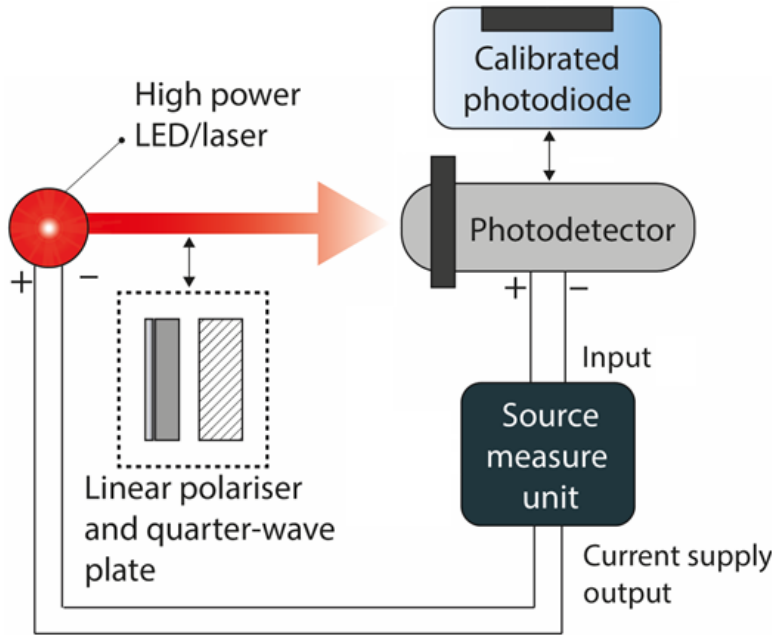


Figure 3.4: Experimental setup for measuring the linear dynamic range and current-voltage characteristics. Light from a high-power LED or laser is directed to a calibrated photodiode (for measuring light intensity) or the device under test. A linear polariser and quarter-wave plate may be added in the path of the light source for a circularly polarised beam. The intensity of the light source is controlled using a digital current source and the photocurrent of the calibrated photodiode and the device under test is measured using a source-measure unit. Adapted from [7]

Current-Voltage Characteristics and Linear Dynamic Range

The current–voltage characteristics and linear dynamic range of the CP OPDs were measured using an Agilent B2902A Precision SMU (100 fA resolution). For illuminated measurements, mounted LEDs (Thorlabs, 470 nm, M470L3; and Thorlabs, 530 nm, M530L4) were used, collimated with an aspheric lens (Thorlabs, ACL2520U-A) and filtered with a bandpass filter (Thorlabs, 470 nm, FB470-10; or Thorlabs, 514.5 nm, FL514.5-1). For measurements of g_{ph} under reverse bias, the collimated and filtered LED output of the mounted LED was circularly polarised using a wire-grid polariser (Thorlabs, WP25M-VIS) and a zero-order quarter-wave plate (Thorlabs, 473 nm, WPQ05M-473; or Thorlabs, 514 nm, WPQ05M-514). The intensity of light incident on the OPDs was measured using a full-spectrum Si p-i-n photodiode (Hamamatsu, S1223-01). A schematic of the equipment used for these measurements is shown in Figure 3.4

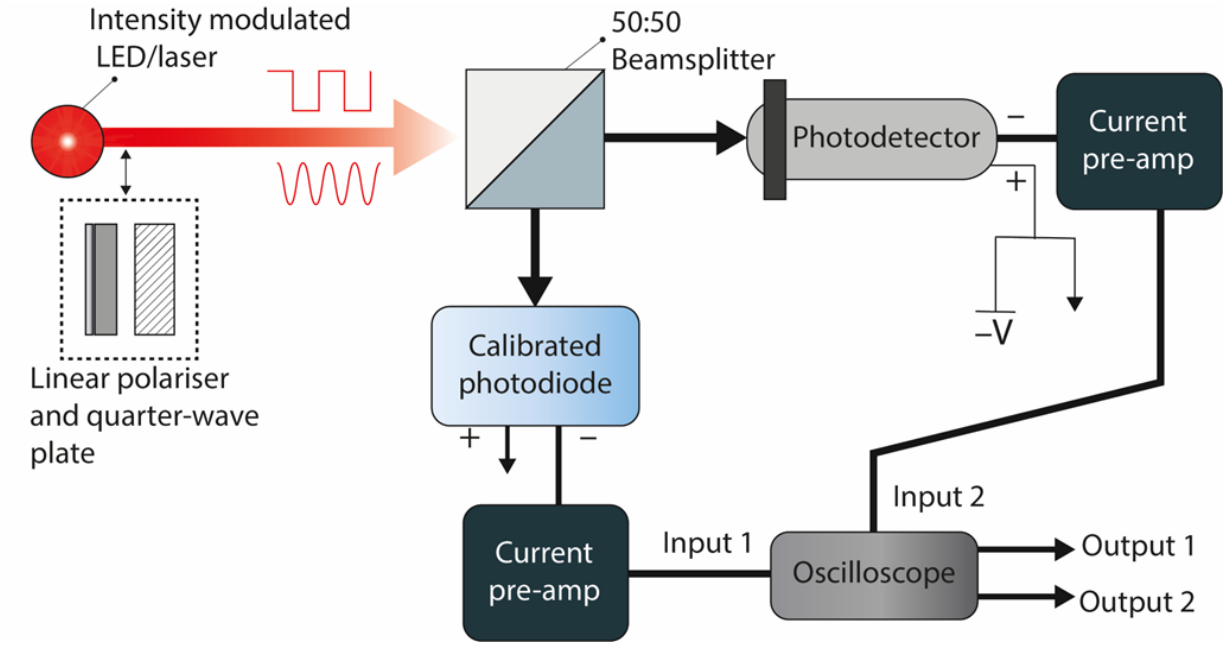


Figure 3.5: Experimental setup for measuring the bandwidth, rise time and fall time. Light from a high-power LED or laser is split equally between a calibrated photodiode (for measurement of light intensity) and the device under test using a beamsplitter. A linear polariser and quarter-wave plate may be added in the path of the light source for a circularly polarised beam. For rise-time and fall-time measurements, a square-wave modulated light source should be used, and for bandwidth measurements, a frequency tuneable sinusoidally modulated light source should be used. The photocurrent of the device under test and the calibrated photodiode are converted to voltages using current preamplifiers and monitored using an oscilloscope. Reproduced with permission from [7]

Response time and Bandwidth

The response time and bandwidth of the OPDs were measured using an Omicron–Laserage LightHUB-6 (488 nm) and a Stanford Instruments SR570 Low-Noise Current Preamplifier (200 kHz bandwidth, 1 μA V^{-1} sensitivity, high bandwidth setting). The output of the current preamplifier was recorded using a Tektronix digital phosphor oscilloscope (DPO 5104B). For response time measurements, a 2 kHz square wave with a 50% duty cycle was used to measure rise and fall times. For both bandwidth and response time measurements, a 2 μW beam with a diameter of 1 mm was modulated using sine waves and square waves, respectively, supplied by an Agilent 33210A 10 MHz function/arbitrary waveform generator. A schematic of the equipment used for these measurements is shown in Figure 3.5

Spectroscopy

Thin-film ellipticity spectra were acquired using a Chirascan CD spectrometer from Applied Photophysics. For solid-state samples, CD spectra should be collected with the sample in various orientations (face-on, back-on, at 0° and rotated at 90° around the optical axis) as proposed by Albano *et al.*[123] This is to identify the so-called "pseudo-CD" or "apparent-CD" in the CD spetra of samples that can arise due to interaction between linear dichroism and linear birefringence in anisotropic solid state samples.[123] UV-Vis spectra were measured using a Shimadzu UV-Vis spectrophotometer (UV-2550). The calculated values of g_{abs} have been corrected for reflection losses using the method devised by Schulz et al.[14]

3.3.3 Methods Used in the Development of Circularly Polarised Imaging Systems

Solution preparation and thin film deposition

F8BT ($M_w = 31$ kDa) and aza[6]H were dissolved in toluene at a concentration of 20 mg/ml and blended to form a 10 wt% aza[6]H solution. The achiral polymers were provided by Cambridge Display Technology (CDT). Fused-silica substrates were rinsed in an ultrasonic bath in a three-step process using acetone, isopropyl alcohol and Hellmanex™ III for 15 min each. They were then transferred to an oxygen plasma asher for 3 min at 80 W before spin-coating. The thin films were spin-coated at 2,000 rpm for 60 s. Non-patterned thin films were then annealed in a nitrogen glovebox, with <0.1 ppm H_2O and O_2.

Spatially Patterned Thin Films

First, homogeneous as-cast F8BT:[*P*]-aza[6]H thin films were deposited as detailed in *Solution preparation and thin film deposition* above, except using a solution concentration of 35 mg/ml. Two different routes were applied to achieve spatial pattern domains with strong chiroptical activity. Route 1): as-cast thin films were turned over and carefully placed face down onto a

ring-shaped metal piece (with a diameter of $\sim$ 4 mm) that was heated at 160 °C, for 10 min. Route 2): 1.5 mm thick viscoelastic PDMS layers were site-selectively masked onto the as-cast thin films, creating well-adhered solvent barriers for later processing. The thin films with PDMS masks were loaded back onto a spin-coater, followed by dispensing $\sim$100 μL toluene. Toluene was thus allowed to cover the samples for $\sim$15 s prior to its removal as the spin-coating process initiated. This method preserves the thin film content underneath the masked area and removes the material elsewhere, exposing the bare fused-silica substrate. For chiral induction in the polymer phase, the PDMS masks were carefully removed prior to thermal annealing treatment performed at 140°C for 10 min. The samples were then immediately quenched onto a cold ($\sim$20 °C) metal surface.

Dual and Single Camera Circular Dichroism Imaging Systems

The single and dual camera systems made use of a 470 nm, 809 mW mounted LED (Thorlabs, M470L5) to illuminate the sample under test. This LED was filtered with a 470 $\pm$ 10 nm bandpass filter (Thorlabs, FBH470-10) and collimated using an aspheric condenser lens with diffuser (Thorlabs, ACL2520U-DG6-A) mounted on a lens tube system (Thorlabs, SM1V05, SM1L03). Left- and right-handed circularly polarised light transmitted through the sample under test is converted to two orthogonal linear polarisations (vertical and horizontal) using a mounted quarter-wave Fresnel rhomb retarder (Thorlabs, FR600QM). In the dual camera system, the vertical and horizontal linear polarisations are directed to two separate cameras by a polarising beamsplitter cube (Thorlabs, CCM1-PBS251/M). In the single-camera setup, transmission of the vertical and horizontal polarisations to a single camera are rapidly switched between using a wire grid polariser (Thorlabs, WP25M-VIS) mounted in a piezoelectric rotation mount (Thorlabs, ELL14K). For dual and single camera imaging systems, USB controlled monochrome Zelux® 1.6 MP CMOS cameras (Thorlabs, CS165MU/M) are used, with images focused onto camera CMOS arrays using a 6 mm focal length f = 1.4 Navitar lens (Thorlabs, MVL6WA).

Thermal Annealing

In-situ thermal annealing of solid-state samples during CD imaging was controlled by a temperature controlled stage (Linkam, LTS40 and T96). The temperature range, ramp rate, and dwell time were pre-programmed using a Linkam Linkpad touchscreen controller. In all cases, the chamber heating rate was 10°C/min and the samples were held at a given temperature for 1 min before CD images were captured.

Control Software

The control software was written in the Python programming language, using the Thorlabs software interface for compact scientific cameras. The result was a multi-threaded programme that allows for real-time image acquisition from the connected camera or cameras. For the 1-CCDI design, the software also controls the piezoelectric motor, ensuring that successive images are of alternating handedness. A Graphical User Interface (GUI) then enables the visualisation and measurement of A_L and A_R side by side or combined as ΔA or ellipticity, either in photos or by using the cursor to read values at a point. A switchable overlay shows the sizes of objects in the photos and calibration options allow for selecting regions-of-interest of the image, first-order setup corrections, and defining the pixel-per-millimetre ratio. The programme is open source and a link to a GitHub repository containing the source code is provided here: `https://github.com/rmdocherty/CPL-Imager`.

Parts List

A full parts list for the 2- and 1-camera CD imaging systems is provided in Table 3.1.

Table 3.1: List of parts used to assemble the two- and one-camera CD imaging systems. Prices are accurate at the time of writing, September 2022.

2 Camera System

Part No.	Description	Price
CS165MU/M	Zelux® 1.6 MP Monochrome CMOS Camera, M6 Taps	£336.04
CS165MU/M	Zelux® 1.6 MP Monochrome CMOS Camera, M6 Taps	£336.04
CCM1-PBS251/M	30 mm Cage Cube-Mounted Polarising Beamsplitter Cube, 420-680 nm, M4 Tap	£253.72
MVL6WA	6 mm EFL, f/1.4, for 1/2" C-Mount Format Cameras, with Lock	£124.79
MVL6WA	6 mm EFL, f/1.4, for 1/2" C-Mount Format Cameras, with Lock	£124.79
FR600QM	Mounted Quarter-Wave Fresnel Rhomb Retarder	£313.62
Total		**£1,489.00**

1 Camera System

Part No.	Description	Price
CS165MU/M	Zelux® 1.6 MP Monochrome CMOS Camera, M6 Taps	£336.04
MVL6WA	6 mm EFL, f/1.4, for 1/2" C-Mount Format Cameras, with Lock	£124.79
ELL14K	Rotation Mount Bundle: ELL14 Mount, Interface Board, Power Supply, Cables	£420.45
WP25M-VIS	Ø25.0 mm Mounted Wire Grid Polarizer, 420-700 nm	£223.78
FR600QM	Mounted Quarter-Wave Fresnel Rhomb Retarder	£313.62
Total		**£1,418.68**

Light Source (with Filter and Collimation Kit)

Part No.	Description	Price
M470L5	470 nm, 809 mW (Min) Mounted LED, 1000 mA	£170.94
FBH470-10	Premium Bandpass Filter, Ø25 mm, CWL = 470 nm, FWHM = 10 nm	£115.31
ACL2520U-DG6-A	Aspheric Condenser Lens w/ Diffuser, Ø25 mm, f=20.1 mm, NA=0.60, 600 Grit, ARC: 350 nm - 700 nm	£23.71
SM1V05	Ø1" Adjustable Lens Tube, 0.31" Travel Range	£23.37
SM1L03	SM1 Lens Tube, 0.30" Thread Depth, One Retaining Ring Included	£9.39
Total		**£342.72**

2 Camera System and Light Source	**£1,831.72**
1 Camera System and Light Source	**£1,761.40**

3.3.4 Methods Used in Device Modelling and Time of Flight Mobility Studies

Substrate Cleaning and Treatment

Substrate cleaning and treatment is identical to that used for photodiode fabrication.

Solution Proccessing and Spin-Coating

Solutions of *rac*-, [*M*]-, and [*P*]-aza[6]H:F8T2 were prepared by dissolving aza[6]H and F8T2 separately in toluene at a concentration of 60 mg/ml before combining the two with a 10 wt% loading ratio of aza[6]H. These solutions were gently heated and stirred at 50°C overnight to ensure complete dissolution. The aza[6]H:F8T2 solutions were then spin-coated onto the substrate in a two step process (700 rpm for 1 min, 2000 rpm for 30 sec), followed by annealing at 140°C for 10 min to induce the strong chiroptical response in F8T2.

Vacuum Processing and Thermal Evaporation

The aluminium back contact was thermally evaporated on the aza[6]H:F8T2 layer using an MBRAUN thermal evaporator and the thickness and evaporation rate of this layer was monitored *in-situ* using an Inficon SQM-160 rate/thickness monitor. The thicknesses of all the device layers were verified using a Bruker DektakXT surface profilometer.

Time of Flight Mobility Measurements

ToF samples were excited using a wavelength-tuneable Q-TUNE-C10 E-O Q-switched diode-pumped tuneable wavelength laser with a temporal pulse width of < 5 ns. The bias applied to ToF samples was provided by a Keithley 237 high voltage source measure unit. ToF traces were recorded using a Siglent SDS6204A 2 GHz digital storage oscilloscope, with acquisition being triggered using a Thorlabs DET025A 2 GHz Si free-space photodetector (400 - 1100 nm)

which monitors the output pulse shape of the excitation source using a UV fused silica beam sampler.

Chapter 4

Bis-PCBM Phototransistor[1]

4.1 Statement of Contribution

The contribution of the experimental results in this chapter is stated below.

Bis[60]PCBM synthesis was performed by Xueyan Hou.

Enantiomeric separation of Bis[60]PCBM was performed by Wenda Shi.

CD, g_{abs} and absorption spectra were collected by Wenda Shi, Jess Wade, and Francesco Salerno.

Theoretical CD spectra and DFT simulations were calculated by Francesco Salerno and Alejandro Santana-Bonilla.

The phototransistor fabrication procedure was developed by Matthew D Ward and Wenda Shi.

Phototransistor characterisation was performed by Matthew D Ward and Wenda Shi.

The model of enhancement of g_{ph} relative to g_{abs} was conceived and tested by Matthew D Ward.

[1]Reuse permissions for this chapter have been included in the appendices.

4.2 Motivation and Novelty

As shown in Table 2.2, there are several examples in the literature of chiral organic phototransistors with a selective response to circularly polarised light, and this architecture represents the first device studied by the Campbell and Fuchter groups.[45] This architecture is of considerable interest as they typically have a significantly larger g_{ph} value than the g_{abs} value of the chiral material used as the active layer in their fabrication, relative to photoconductors and photodiodes. In particular, in the helicene phototransistor previously reported by the Campbell and Fuchter groups, a g_{ph} value of 1.8 can be deduced from the data, which is surprising, given that the values of g_{abs} for small molecules of this type are of the order of 10^{-3}.[45] At the time of publication, few published papers on chiral phototransistors provided mechanistic insight into how this enhancement of g_{ph} relative to g_{abs} arises. In this chapter, we present our study of phototransistors prepared using various enantiomers of Bis[60]PCBM.

This study not only represents the first chiral fullerene phototransistor of its kind, but also allows further study of the underlying mechanisms behind the enhancement of g_{ph} relative to g_{abs} in previously reported chiral phototransistors. On the basis of these studies, we propose a novel model of the g_{ph}-g_{abs} enhancement mechanism, which has been observed in other chiral phototransistors published after this work, further lending weight to this model.

4.3 Introduction

Fullerenes and their derivatives have played an important role in the development of organic semiconductor devices. In particular, they remain widely used in OPVs as electron acceptors[124, 125, 126, 127] while also demonstrating excellent photoresponsivity as broadband photodetectors.[128, 129, 130, 131, 132, 133] Given the poor solubility of C_{60} in common organic solvents, fullerenes must be functionalised to produce more soluble derivatives. Bis[60]PCBM is one such derivative and is among the most utilised solubilised fullerenes, which is easy to synthesize, highly processable, and solar cells based on this material have high power conversion efficiencies. [134, 135, 136, 137, 138, 139, 140, 141] The addition of two stabilising addends

to C_{60} results in a large number of structural isomers, each with varying energetic properties (influencing device voltage) and morphological properties (influencing device current). Despite this, bis[60]PCBM is synthesised and used as an isomeric mixture, and the role of individual isomers on morphological, spectroscopic, and device performance is very poorly understood. In a previous study, Dennis and co-workers separated the 19 structural isomers of bis[60]PCBM and characterised them using a combination of NMR, UV-vis and retention times by HPLC. [142, 143] Although the performance of a single structural isomer of bis[60]PCBM in organic devices was not investigated, isomerically pure fullerene derivatives have generally been reported to exhibit higher power conversion efficiency than the corresponding isomeric mixture.[144, 145] This implies that further study of single bis[60]PCBM isomers may hold significant promise.

The complex isomeric composition of bis[60]PCBM is not limited to structural isomers. Of the 19 synthetically accessible bis[60]PCBM isomers, 13 are chiral, which gives rise to 13 pairs of enantiomers (see Figure 4.1). It is interesting to consider what opportunities could emerge from access to enantiomerically pure fullerenes. To date, chiral fullerene derivatives have been explored primarily as an academic curiosity and in limited applications, with a notable exception perhaps being enantioselective catalysis.[146] Given the importance of this class of materials to organic electronic devices, it is curious that single-enantiomer fullerene devices have yet to be explored in this context. However, it is likely that chiral composition-dependent effects on device performance would be observed,[147, 148] as would the potential to render fullerene devices sensitive to CPL, through CD.

In this work, we separate and systematically study ten pairs of enantiomers from the 19 structural isomers of bis[60]PCBM. We analyse the chiroptical responses of these isomers and elucidate the origin of larger g_{abs} in some isomers over others. Specifically, we show that larger chiroptical responses occur in cases with greater asymmetry of the electron distribution within the fullerene cage. We showcase the application of our single-enantiomer bis[60]PCBM materials in the production of single-enantiomer CP-photoFET devices, with very high photocurrent dissymmetry factors (up to $g_{ph} = 1.27 \pm 0.06$). Thus, our study determines a clear set of design principles for generating chiral fullerene derivatives with maximised chiroptical activity and with significant potential in the burgeoning field of chiral (nano)technology and devices.

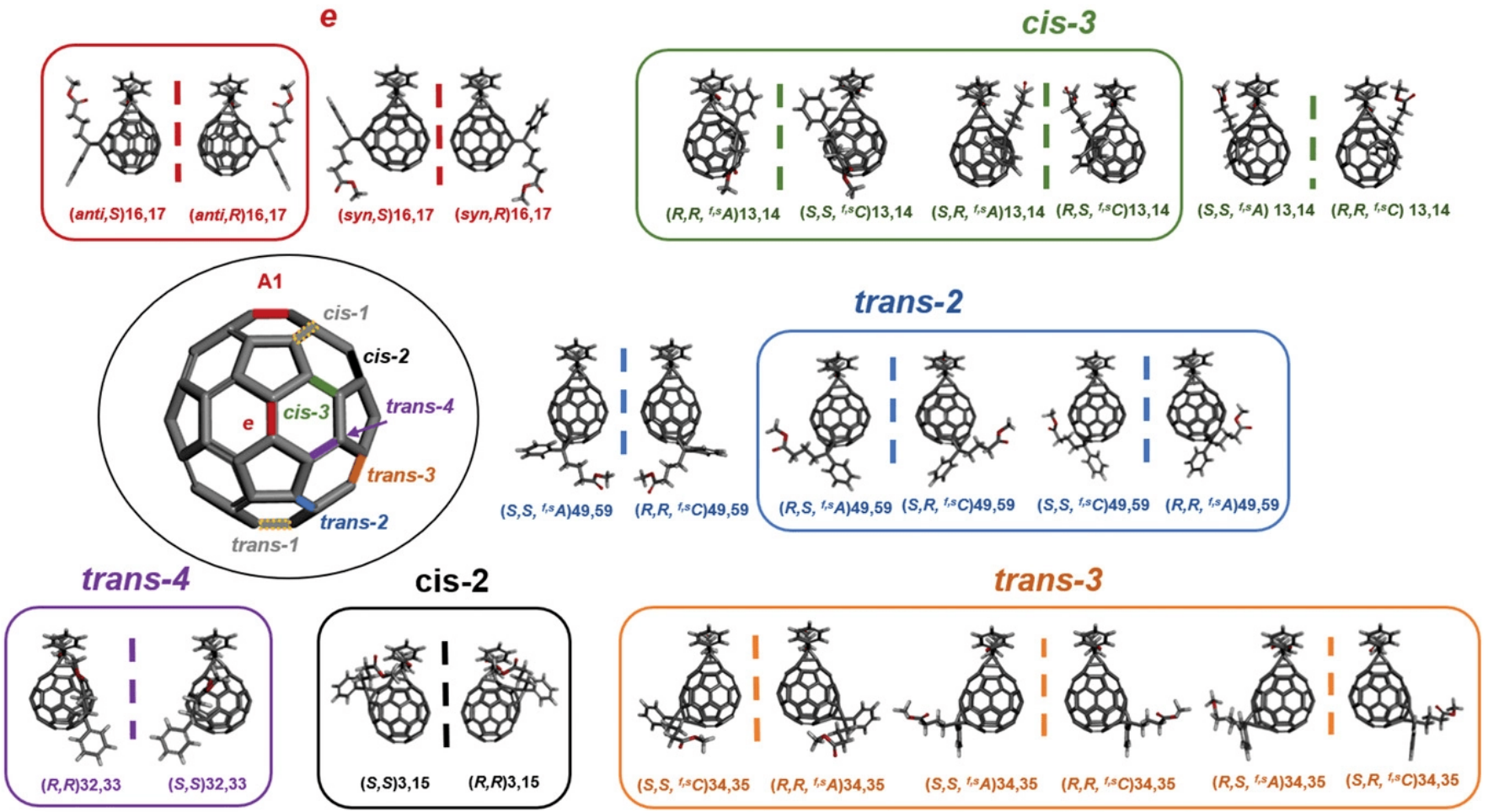


Figure 4.1: The 13 pairs of bis[60]PCBM enantiomers, categorised into six bond types according to the positioning of the second adduct relative to 1,9 position of the first addend (A1): *cis*-2 (black), *cis*-3 (green), *e* (red), *trans*-2 (blue), *trans*-3 (orange) and *trans*-4 (purple) with dotted mirror planes depicted. For each isomer, R/S descriptors refer to addend stereochemistry and ^{f,s}C/^{f,s}A to the fullerene stereochemistry using the method defined by Diederich and Thilgen.[12] All isomer labels should be proceeded by "bis[60]PCBM", i.e., (S,S,^{f,s}C)13,14 becomes (S,S,^{f,s}C)13,14-bis[60]PCBM. The enantiomeric pairs contained within boxes represent those isolated in this study.

4.4 Results and Discussion

For bridged C_{60} monoadducts, such as PCBM, without considering the configuration of the first addend, there are eight remaining non-equivalent double bonds susceptible to the addition of a second addend. Therefore, the formation of the bisadduct gives rise to eight regioisomers: *cis*-1, *cis*-2, *cis*-3, *e*, *trans*-1, *trans*-2, *trans*-3, and *trans*-4 (Figure 4.1).[149, 150, 151] The naming of bond type is defined by the relative position of the second addend with respect to the first. When both addends are found in the same hemisphere, the isomer is named *cis*; if the addends are in opposite hemispheres, the isomer is named *trans*; and if the second addend is in the equatorial plane, the isomer is named e. This naming system also reflects the electronic properties of the isomers, where structural isomers of the same type of bond have similar UV–vis absorption spectra.[142, 149] Here, we only consider six bond types since the *cis*-1 isomer does not form during bis[60]PCBM synthesis in any appreciable amount due to steric effects and the *trans*-1 isomer is not chiral due to the presence of a mirror plane (Figure 4.1). Of the structural isomers contained within these six remaining bond type groups, 13 pairs of enantiomers can be theoretically predicted according to their symmetry properties.[143]

In the case of the bis[60]PCBM derivative employed in this study - the one used principally in organic electronic devices, as for other C_{60} bisadducts previously reported in the literature,[12, 152] some structural isomers are inherently chiral, while others are non-inherently chiral. In a previous study, Dennis and co-workers named the structural isomers of bis[60]PCBM based on the location of the second addend and the symmetry, for example, (C_1)21,40-bis[60]PCBM.[143] Here, we adapt that nomenclature to explicitly include fullerene chirality descriptors and stereochemistry of the addends, according to the systematic system devised by Diederich and Thilgen.[12] The assigned nomenclature used is given in Figure 4.1.

The 19 structural isomers were isolated using the previously reported method and identified by UV–vis, 13C NMR, and retention time (i.e., polarity).[142, 143] The 13 chiral isomers of bis[60]PCBM, obtained as racemates, were subjected to further purification via peak-recycling HPLC using chiral columns (Chiralpak IE and IF). Ten out of 13 pairs of enantiomers were successfully resolved and purified to $> 99\%$, which represents at least one pair of enantiomers

for each bond-type isomer. This isomeric series provides the means to systematically study the chiroptical response of the chiral fullerene isomers as a function of substitution pattern and symmetry for the first time.

To assign the absolute configuration of the isolated bis[60]PCBM stereoisomers, we compared the experimentally obtained CD spectra with the simulated spectra. This approach is increasingly common for the assignment of the absolute configuration and has been previously applied to chiral fullerenes.[153, 154] As expected, all isolated pairs of enantiomers show an equal and opposite CD/g_{abs} response (Figure 4.2). Importantly, diastereomers belonging to the same bond type (*cis*-2, *cis*-3, *trans*-2, etc.) display almost identical CD spectra, with only minor differences in amplitude and excitation energy, which can therefore be considered an inherent stereochemical fingerprint of each addition pattern of these bis[60]PCBM isomers. Therefore, addend substituent stereochemistry appears to have a negligible impact on the shape of the spectra, as has been previously observed in specific examples of similar systems.[155] However, we also observe that the band peak maxima for isomers of the same bond type group can differ in magnitude up to $\approx 30\%$. This is likely due to a match/mismatch effect given by the different reciprocal orientations of the two addends on the C_{60} cage. From an application point of view, the variety of CD responses contained within this series allows access to CPL responsivity across a large region of the UV–vis spectrum of potential usage in CPL detecting devices.

To further investigate how the observed chiroptical properties relate to the isomeric structures of this series, g_{abs} was analysed. The g_{abs} factors of all stereoisomers, ordered by bond type, are shown in Figure 4.3a for representative enantiomers. The magnitude of g_{abs} varies by approximately two orders of magnitude as a function of stereoisomeric series, from 10^{-4} to 10^{-3} (typical of chiral organic small molecules) up to the value of 3×10^{-2}. Values of this order of magnitude are highly uncommon for an isolated molecule in solution.[156] Moreover, a particularly large chiroptical response occurs at ≈ 600 nm, a wavelength longer than that typically achievable with other conjugated chiral small molecules, such as helicenes, biraryls, and cyclophanes.[156]

The six types of bonds can be further divided into two groups according to their g_{abs} val-

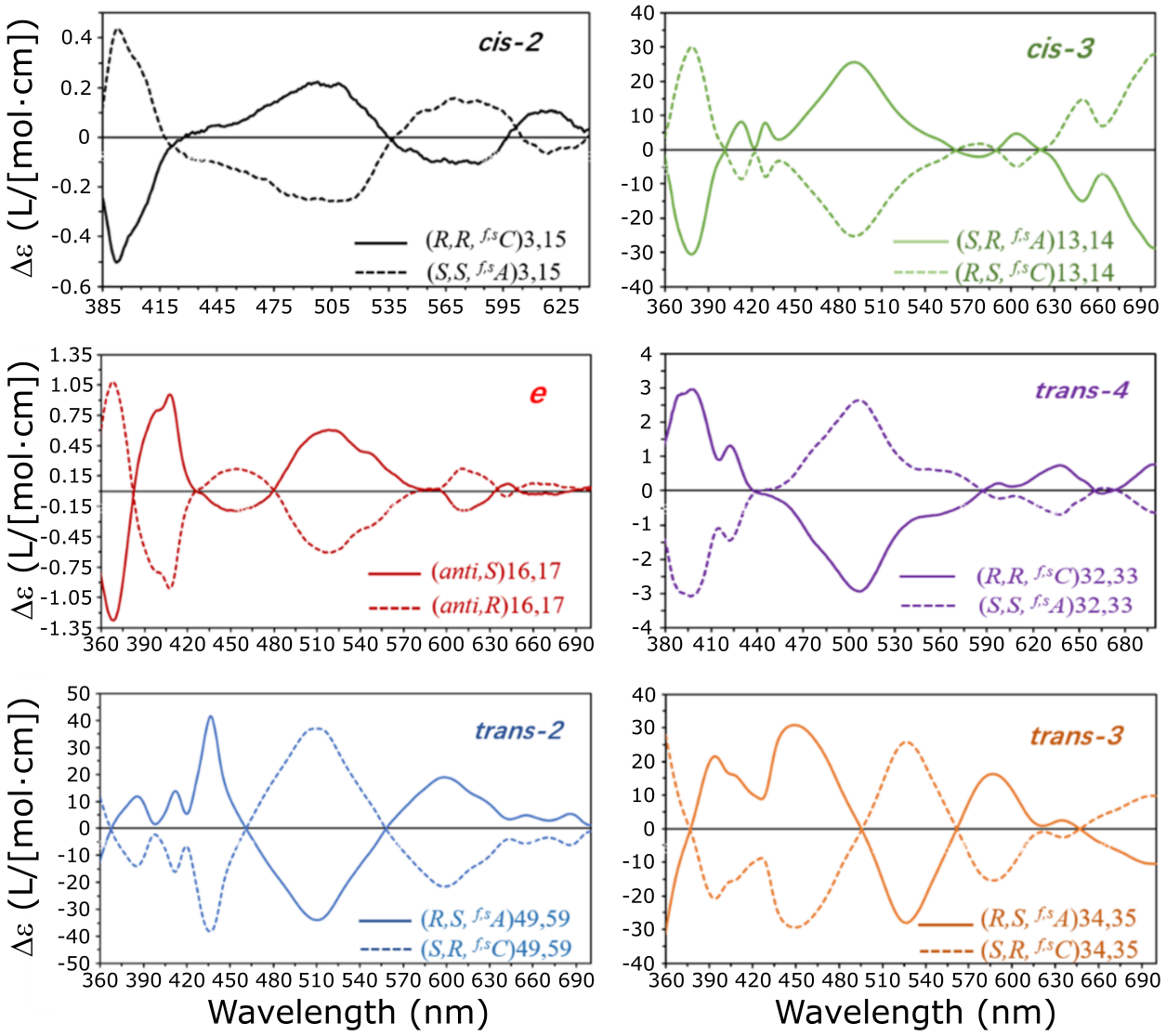


Figure 4.2: Experimental normalised CD spectra of one representative enantiomeric pair per substitution pattern in solution. Note that spectra here are expressed as molar extinction, $\Delta\varepsilon$, where the CD has been normalised for both the path length through the solution and the solution concentration.

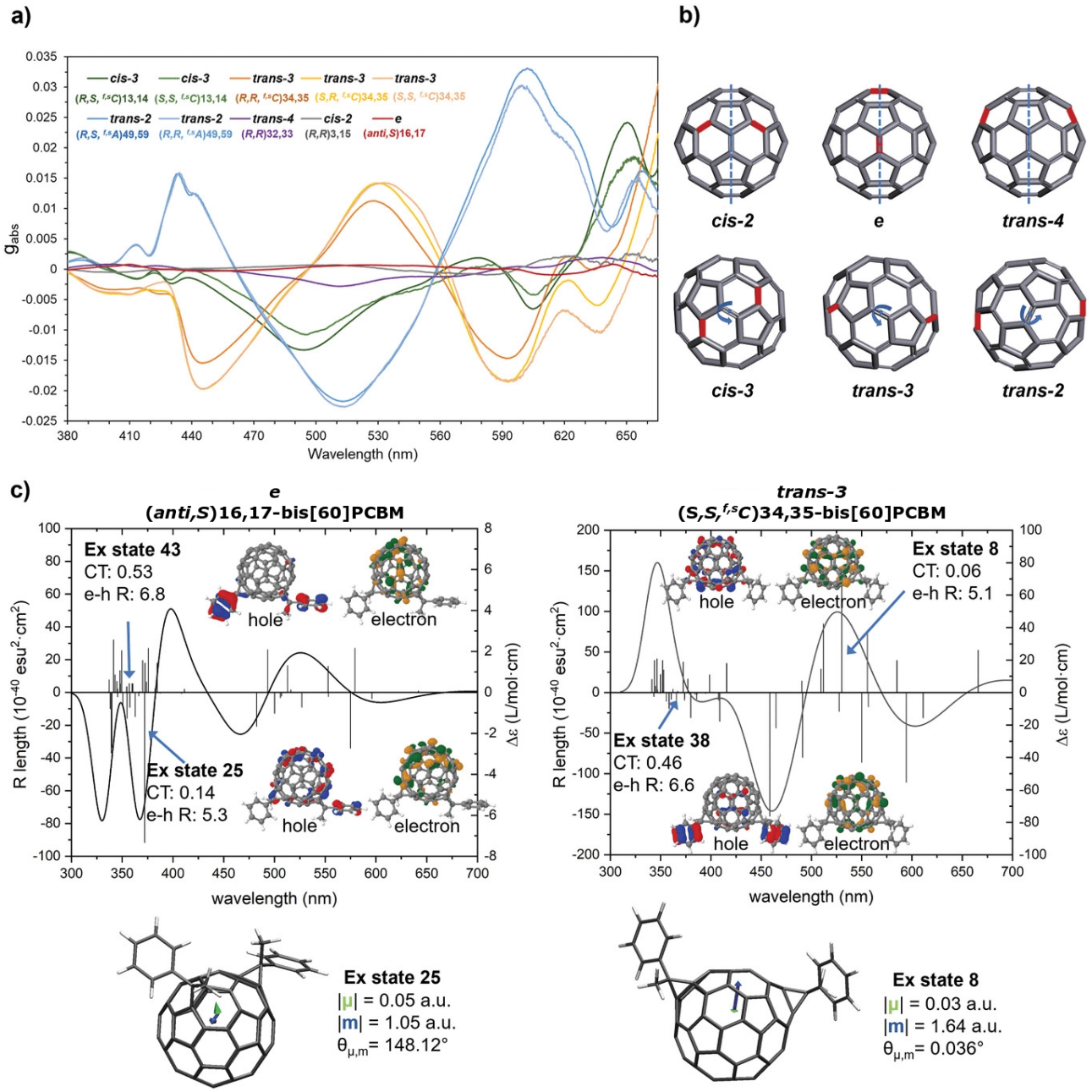


Figure 4.3: a) Absorption dissymmetry factor g_{abs} of one enantiomer per pair of all the isolated bis[60]PCBM enantiomers. b) Six addition patterns on the cage (two types): non-inherently chiral with mirror symmetry (upper row) and inherently chiral with C2 symmetry (bottom row). c) Calculated CD spectra of the *e* isomer (*anti,S*)16,17 (left) and the *trans*-3 isomer (*S,S,* $^{f,s}C$)34,35 (right). The insets highlight the states with highest rotatory strength (state 25 and state 8) and the states with highest charge transfer character (state 43 and state 38). CT refers to the degree of charge transfer character, and e-h R indicates the root-mean-square distance of the electron–hole pair in Angstroms. The molecular pictures represent the distribution of the pair of "hole" (where the electron leaves upon excitation) and "electron" (where the excited electron goes to) for that excited state. On the bottom, electric and magnetic transition dipoles for the excited states 25 and 8 are displayed.

ues. Stereoisomers from *cis*-2, *e*, and *trans*-4 show a relatively low g_{abs} value ($\approx 10^{-3}$), while stereoisomers from *cis*-3, *trans*-2, and *trans*-3 show a g_{abs} value up to one order of magnitude higher ($\approx 10^{-2}$). This significant difference in the chiroptical response can be qualitatively rationalised using symmetry-based arguments. In the group of isomers with lower g_{abs}, the addition pattern on the C_{60} cage (without considering the nature of the addends) contains a mirror plane as shown in Figure 4.3b, upper row. As described above, bis[60]PCBM isomers of these bond type groups (*cis*-2, *e*, and *trans*-4) are non-inherently chiral; that is the chirality arises only by virtue of the stereogenic centres on the addends. This is equivalent to stating that the chromophore is fundamentally achiral and that the chiroptical response derives only from perturbation of the substituents. The group of isomers with higher g_{abs}, instead, has addition patterns with C_2 symmetry (*cis*-3, *trans*-2 and *trans*-3); these bis[60]PCBM isomers are said to be inherently chiral. This means that the fullerene chromophore is inherently chiral, and therefore, the chiroptical response would be expected to increase. Ultimately, this difference in symmetry determines the distortion of the π-electron distribution in the cage, with achiral addition patterns leading to more uniform electron distributions than those that are chiral.

TD-DFT results were further analysed using TheoDORE software, which allows the study of the nature of excited states in greater detail by employing the natural transition orbital (NTO) formalism.[157] In Figure 4.3c, we show part of the analysis for the *e* and *trans*-3 isomers. In both cases, for the states with the highest charge-transfer character, the transition occurs as a movement of π-electrons from the C60 to the addends. In contrast, the states with the highest rotatory strength are described by a strong rotational movement of π-electrons solely on the surface of the cage with a low CT character (weak charge translation).

We observe that the magnetic transition dipole moment is significantly higher in magnitude than the electric transition dipole for those excited states with high rotatory strength. Moreover, these states are characterised by a very small angle θ when the chromophore is chiral, implying a strong coupling between m and μ. This likely accounts for the higher order of magnitude of g_{abs} (via Equation 2.35) observed in those isomers with an inherently chiral substitution pattern. The distance between the addends seems not to play a crucial role since states with high rotatory strength are mainly local and do not involve charge delocalisation onto the addends. Other

chiral aromatic molecules with high dissymmetry factors due to the strong magnetic transition dipole are known in the literature.[158] The reason is likely related to two factors: the curved surface of the backbone, which encourages the circular movement of valence electrons, and the aromatic characteristics (locally and globally) arising from the desymmetrization of the chromophore. Modulation of these two factors allows the interaction of the molecule with the magnetic part of the CP excitation light to be enhanced and should be taken into consideration for the chemical design of new aromatic materials with good chiroptical properties.

With access to single-stereoisomer bis[60]PCBM molecules, we sought to showcase their application in the context of an organic electronic device. Enantiomers of (anti,R)16,17-bis[60]PCBM (e) and (R,R, ^{f,s}A)49,59-bis[60]PCBM (*trans*-2) were separately used to build bottom–gate, bottom–contact organic field-effect transistors (OFETs) on prepatterned substrates. The transfer characteristics of these devices in the dark (Figure 4.4a,b) showed turn-on voltages of $\approx 15-20$ V, low off-currents (1×10^{-11} A) and on/off ratios of 10^3. To the best of our knowledge, these devices represent the first OFETs prepared from a single-isomer bis[60]PCBM material. The performance of these devices could be further optimised through alternative device architecture, fabrication procedure, etc. The device characteristics of the racemic (anti,R/S)16,17-bis[60]PCBM isomer displays comparable device performance under dark conditions (with the exception of a greater turn-on voltage).

The use of an enantiomerically pure semiconductor enables the photoresponse of OFETs to be sensitive to the circular polarisation of light. To study the CPL responsivity of the enantiopure fullerene-based transistors, we illuminated single-enantiomer OFETs using a laser diode at 405 nm, which corresponds to the most easily accessible CD peaks at the onset of absorption for these enantiomers. The transfer characteristics of these devices under left-handed CPL and right-handed CPL are shown in Figure 4.4a,b. The off currents of the devices increase from 10^{-11} to 10^{-10} A, and the turn-on voltages shift from 15 to 20 V to $\approx$ 10 V when exposed to CPL. From these data, it is possible to extract g_{ph}, which is up to -0.26 ± 0.18 for the *trans*-2 isomer (R,R, ^{f,s}A)49,59-bis[60]PCBM device and an impressive 1.27 ± 0.06 using the *e* isomer (anti,R)16,17-bis[60]PCBM photoFET (Figure 4.4a,b). This large and selective CP photoresponse is of potential importance for CPL detectors and suggests significant promise

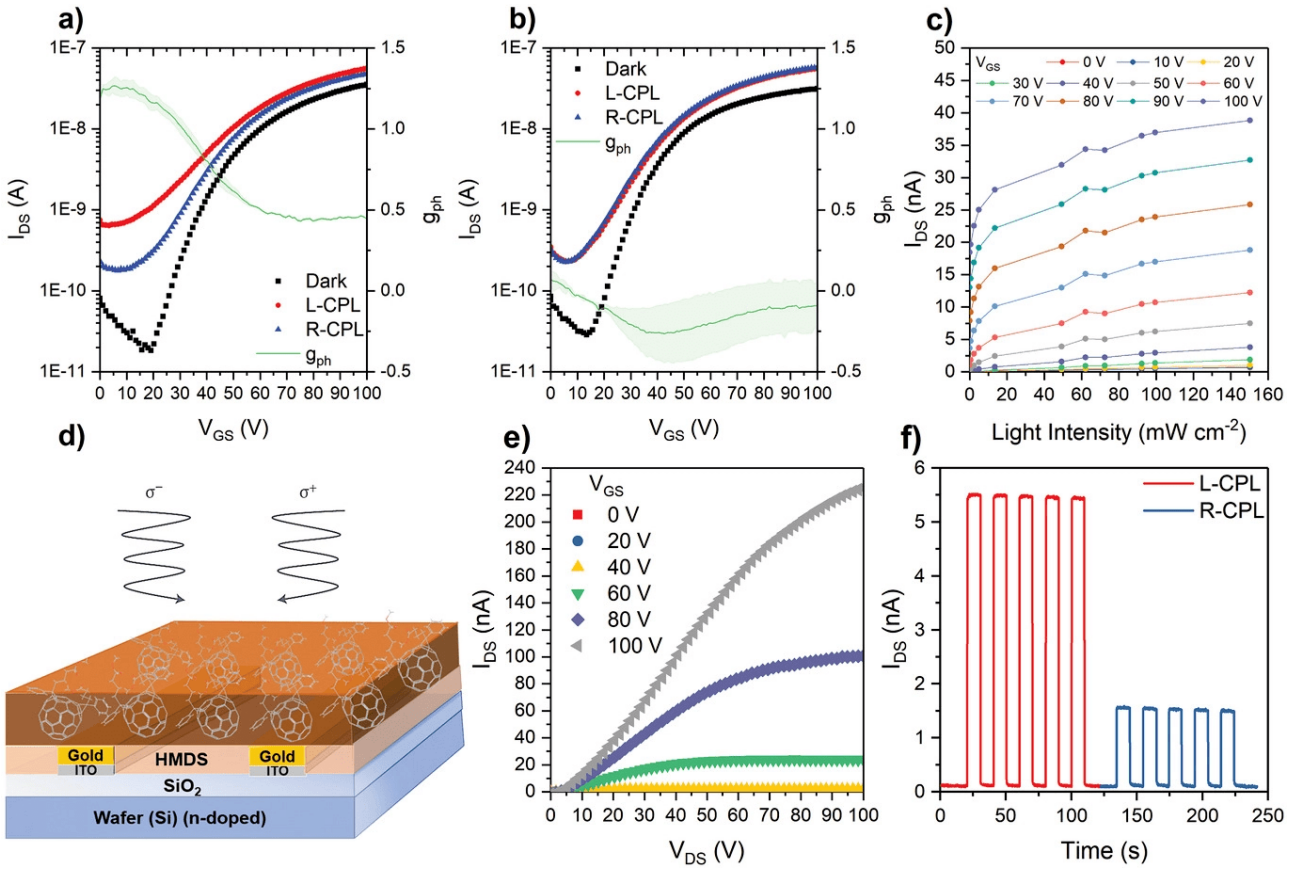


Figure 4.4: Device characteristics of bis[60]PCBM enantiomer pure photo-FETs. a,b) Variation of transfer curves of *e* isomer (anti,R)16,17-bis[60]PCBM (a) and *trans*-2 isomer (R,R, ^{f,s}A)49,59-bis[60]PCBM (b) upon exposure to left-handed and right-handed CPL with 95 and 0.34 $mW\ cm^{-2}$, respectively, compared to curves in the dark. $V_{DS} = 20\ V$. Dissymmetry factors for the photocurrent generation (g_{ph}) and its associated error are given by the green curve and shaded area, respectively. c) The light-intensity response of the *e* isomer (anti,R)16,17-bis[60]PCBM photoFET from 0.48 to 150 $mW\ cm^{-2}$ at different gate voltage from 0 to 100 V, $V_{DS} = 20\ V$. d) The device structure of photoFETs. e) Output characteristics of *e* isomer (anti,R)16,17-bis[60]PCBM photoFET at gate voltage between 0 and 100 V. f) Time-resolved L-CPL and R-CPL photoresponse was measured at 405 nm with an intensity of 92.3 $mW\ cm^{-2}$, a frequency of 0.05 Hz and $V_{DS} = V_{GS} = 40\ V$, showing a high stability and reversibility.

for enantiomerically pure fullerene isomers in such an application. We note that for both photoFETs, g_{ph} is significantly larger than g_{abs} (at 405 nm). This outcome is consistent with our previously reported helicene CP-photoFET.[45]

We propose that the enhancement of g_{ph} relative to g_{abs} arises from two cooperative device mechanisms: CP selective photogeneration of electrons in the channel, which increases the majority carrier density, and CP selective photogeneration of holes, which accumulate at the source electrode, reducing the barrier to electron injection.

As discussed in Section 2.5.2, under illumination, phototransistors may operate under photoconductive or photovoltaic mode, depending on whether V_{GS} is greater than or less than V_{th}.[159, 23] In the photoFET off-state ($V_{GS} < V_{th}$, where V_{th} is the threshold voltage), the photoconductive mode dominates and the majority of charges present in the photoactive layer are photogenerated by incident light.[159, 23] Here, for clarity, we reduce the equation for device photocurrent in this mode of operation (Equation 2.39) to:

$$I_{DS,ph} = AP_{opt} \tag{4.1}$$

where A is a proportionality constant.[159, 23] This linear behaviour is demonstrated in our own photoFETs in Figure 4.5 for $V_{GS} < V_{th}$, where fit parameters of $A = (32.80 \pm 0.82) \times 10^{-12}\ A/W$ and $A = (32.35 \pm 0.40) \times 10^{-12}\ A/W$ are obtained for $V_{GS} = 0\ V$ and $V_{GS} = 5.62\ V$, respectively. When $V_{GS} > V_{th}$ (the "on state"), the photoFET operates in photovoltaic mode.[159, 23] In this we use the following modified form of Equation 2.51 for device photocurrent to account for the mismatch between device area, a_d, and beam area, a_b:

$$I_{DS,ph} = g_m \Delta V_{th} = \frac{BkT}{q} \ln\left(1 + \frac{\eta q P_{opt}}{I_{pd} E} \frac{a_d}{a_b}\right) \tag{4.2}$$

where B is a proportionality constant, E is the photon energy and all other symbols have their usual meanings.[159, 23]

To demonstrate the consistency of our device behaviour with the photovoltaic mode of operation, Equation 4.2 was fitted to plots of $I_{DS,ph}$ as a function of the intensity of unpolarised light

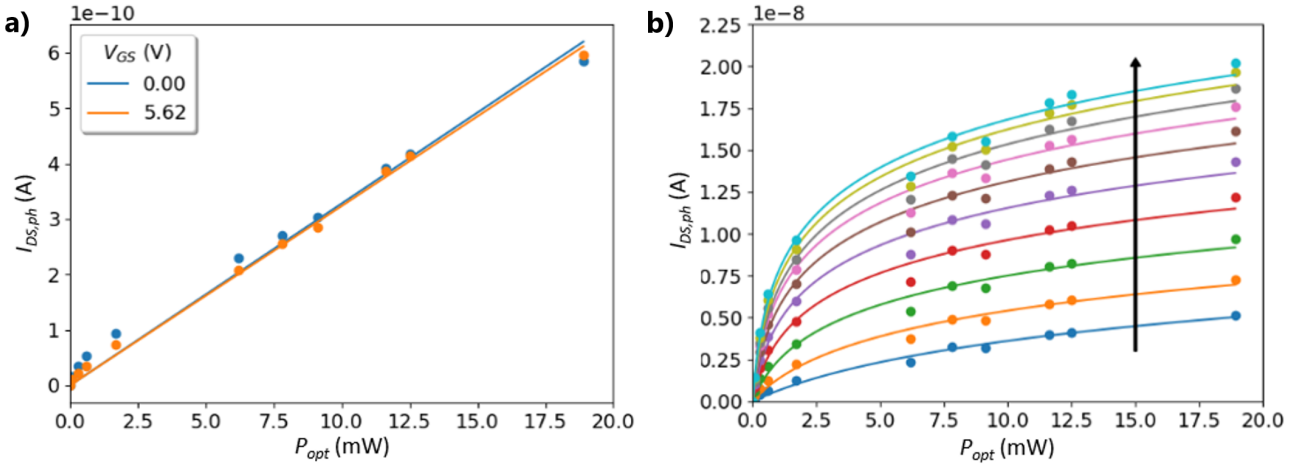


Figure 4.5: Intensity dependence (unpolarised light) of photoFET $I_{DS,ph}$ in the two device modes: photoconductive (a) and photovoltaic (b). Filled circles indicate experimental data and solid lines represent fits to Equation 4.1 (a) and Equation 4.2 (b). The black arrow indicates the direction of increasing V_{GS} from 44.94 V to 95.51 V.

(Figure 4.5b), using B and η/I_{pd} as fitting parameters. As shown, the data was found to be in good agreement theory for $V_{GS} > V_{th}$, with $R^2 > 0.98$ for all fits. B is approximately constant for these fits with increasing V_{GS} (ca. 1×10^{-7} S), however, η/I_{pd} was found to increase. The latter observation suggests an enhancement of η by the transverse electric field of the gate and/or a decrease in I_{pd} due to the depletion of photogenerated holes.

To explain the amplification of g_{ph} relative to g_{abs} for our devices, we propose that two co-operative mechanisms are at work, based on the two regimes of device behaviour. For the same incident intensity of L-CPL and R-CPL, we expect a greater number of photogenerated electrons when illuminated by the strongly absorbed handedness (SAH) relative to the weakly absorbed handedness (WAH)[2]. This is observed as a greater photocurrent for the SAH in the photoconductive regime of Figures 4.4a,b. We also expect a greater number of photogenerated holes for the SAH, which can accumulate at the source electrode. This leads to a lower V_{th} for the SAH relative to the WAH, which means that for a narrow voltage range, the device is in the on state ($V_{GS} > V_{th}$) for the SAH and is in the off state ($V_{GS} < V_{th}$) for the WAH. This leads to a peak in g_{ph} at around $V_{GS} = V_{th}$ for the devices under illumination, which is observed in Figure 4.4a. This is less clear in Figure 4.4b, perhaps due to the increased photodegradation in these devices.

[2]For $g_{ph} > 0$, SAH and WAH are L-CPL and R-CPL respectively. For $g_{ph} < 0$, SAH and WAH are R-CPL and L-CPL.

It is also possible that the enhancement of g_{ph} relative to g_{abs} is influenced by the photoconductive gain of the device rather than solely from the influence of a CPL-selective shift of V_{th}. This is supported by the significant enhancement of g_{ph} (≈ 0.5) relative to g_{abs} for $V_{GS} >> V_{th}$, particularly for the e isomer device (Figure 4.4a). This may be a result of CPL-selective photoconductive gain, that is, gain dependent on the handedness of incident CPL. Recalling Equation 2.60 for g_{ph} and Equation 2.39 for the photocurrent of a photoconductor, we obtain:

$$g_{ph} = 2\left(\frac{\eta_L G_{a,L} - \eta_R G_{a,R}}{\eta_L G_{a,L} + \eta_R G_{a,R}}\right) \tag{4.3}$$

where we have assumed that the incident optical power on the phototransistor is equal for L-CPL and R-CPL. Here, subscripts "L" and "R" are used to distinguish between η and G_a under L- and R-CPL, respectively. In the event that $G_{a,L} = G_{a,R}$, the expression is consistent with g_{ph} for photodetectors without gain (i.e. $G_a = 1$), such as CP-OPDs:

$$g_{ph} = 2\left(\frac{\eta_L - \eta_R}{\eta_L + \eta_R}\right) \tag{4.4}$$

In this case, we might expect $g_{ph} \sim g_{abs}$ as for other CP-OPDs reported in the literature (Table 2.2). For the case where $G_{a,L} \neq G_{a,R}$, we can use Equation 2.41 to show

$$G_{a,L} \neq G_{a,R} \tag{4.5}$$

$$\mu_L \tau_{Rec,L} \neq \mu_R \tau_{Rec,R} \tag{4.6}$$

where subscripts "L" and "R" indicate the values of μ and τ_{Rec} under L- and R-CPL, respectively. This suggests that if the photoconductive gain of the phototransistor is dependent on the handedness of CPL (i.e. $G_{a,L} \neq G_{a,R}$), then the mobility μ and/or recombination time τ_{Rec} of photogenerated carriers in the device are also dependent on the handedness of the exciting CPL. CPL-dependent μ and τ_{Rec} in Bis[60]PCBM should be investigated further by an independent means (e.g. Circularly polarised mobility measurements) as a subject of future study.

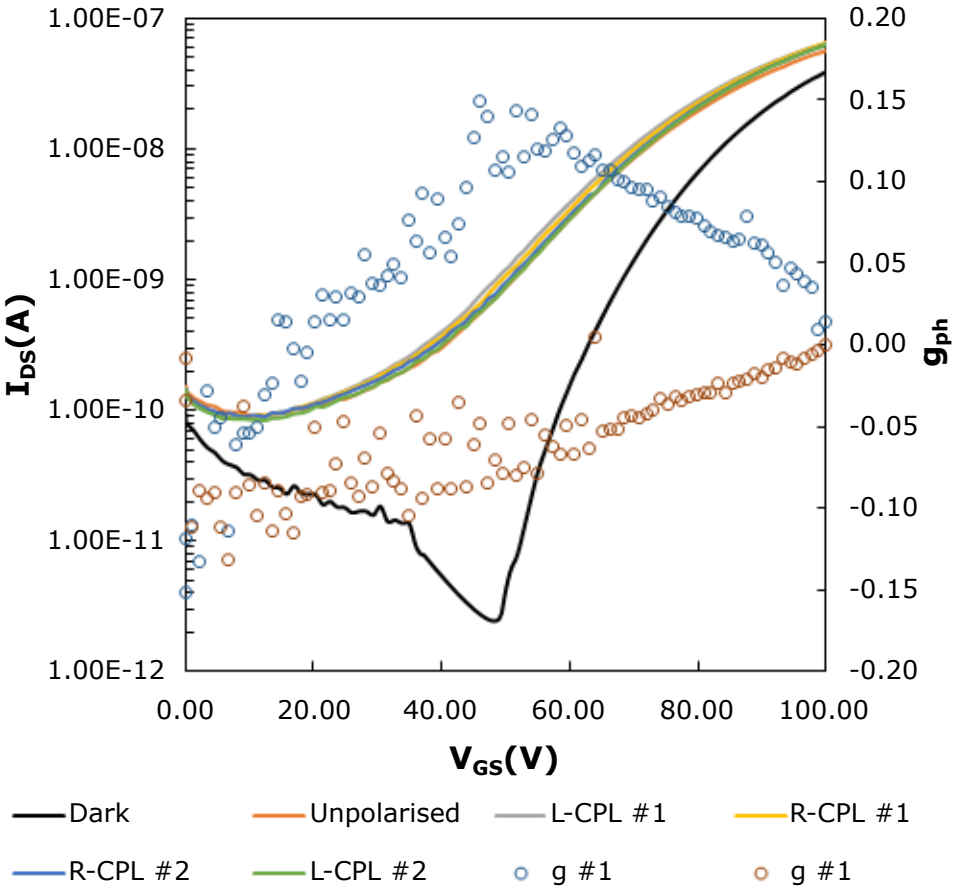


Figure 4.6: Transfer curves of a racemic (anti,R/S)16,17-bis[60]PCBM photoFET in the absence of light and under L-CPL, R-CPL and unpolarised illumination at an intensity of 3.4 $mW\ cm^{-2}$. This device has been measured under each handedness of CPL twice in the following order: L-CPL #1, R-CPL #1, R-CPL #2 and L-CPL #2. g #1 and g #2 correspond to the photocurrent dissymmetry of racemic devices using the photocurrents of L-CPL #1 and R-CPL #1, and L-CPL #2 and R-CPL #2, respectively.

To identify any artefacts in the procedure used to measure the CP response of enantiopure devices and to compare the performance of enantiopure devices relative to their racemic starting materials, the device characteristics of a racemic (anti,R/S)16,17-bis[60]PCBM photoFET were investigated. The transfer characteristics of this device in the absence of light and under L-CPL, R-CPL, and unpolarised illumination are shown in Figure 4.6. Under dark conditions, this device exhibits transfer characteristics analogous to those of the enantiopure *e* isomer (anti,R)16,17-bis[60]PCBM device, albeit with a greater turn-on voltage of 50 V. Also, as might be expected, the transfer curves of these devices under unpolarised light and CPL of equal intensity appear to be similar, suggesting limited CP selectivity. However, calculating g_{ph} for the transfer curves measured with L-CPL (Figure 4.6, L-CPL #1) followed by R-CPL

(R-CPL #1) indicates a significant g_{ph} value of up to 0.15 (g #1) for this racemic device. To further investigate the origin of this anomalous g_{ph}, the order in which the photoFETs were exposed to CPL was reversed – first testing with R-CPL (Figure 4.6, R-CPL #2) followed by illumination with L-CPL (L-CPL #2). This led to a calculated g_{ph} value of a similar magnitude but opposite sign (-0.10) to the g_{ph} calculated previously. This finding, in addition to observations of device performance degradation under intense light exposure near the UV, suggested that these devices are subject to photodegradation, which leads to a non-negligible uncertainty in the calculated value of g_{ph}.

In enantiopure devices, the observed photocurrent dissymmetry is thus a combination of "true" g_{ph} and an artefact g_{ph}, which is only the result of the photodegradation of the device over time, the sign of which is determined by the order of exposure of a given device to L-CPL and R-CPL. Where present, the artefactual g_{ph}, is minimised by reducing the intensity of the illuminating CPL (thereby reducing photodegradation) while also ensuring that the photoresponse of the device remains measurable. Evidence of this procedure is shown in Figure 4.4a,b, where the calculated values of g_{ph} represent the average of g #1 and g #2 for each device and the values of g #1 and g #2 are used as the upper and lower bounds of uncertainty (green shaded area), respectively.

We also note that in our enantiomerically pure devices that photoFET g_{ph} values take the opposite sign to the g_{abs} values of their corresponding films when illuminated at 405 nm. Similar behaviour has already been documented in the literature in prior CP photodetector studies, where devices containing thick active layers were found to exhibit a preferential photoresponse to the opposite handedness of CPL to which they preferentially absorb.[85] This is likely a result of the "filtering out" of the preferentially absorbed handedness of CPL by the CP-selective layer before reaching the photoactive region (the donor-acceptor interface in the case of a photodiode or the channel in the case of a transistor). The consequence of this is that the weakly absorbed handedness has a higher intensity at the photoactive layer and dominates the CP selective response of the device. This leads to the observed inversion of g_{abs} relative to g_{ph}.

Due to the superior CP-selective properties of the *e* isomer (anti,R)16,17-bis[60]PCBM photoFET,

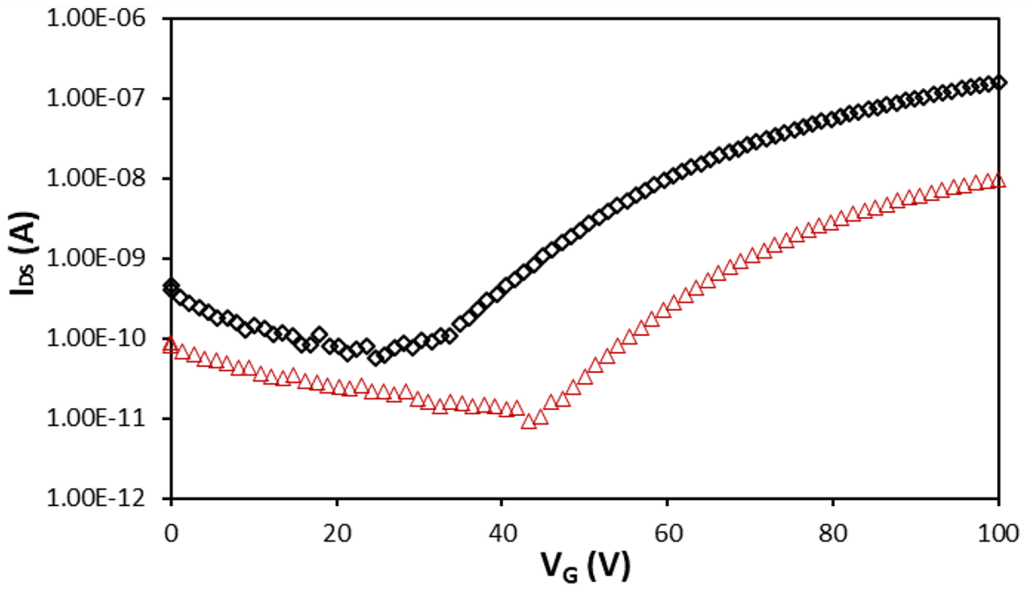


Figure 4.7: Saturation regime (black) $V_{DS} = 100\ V$ and linear regime (red) $V_{DS} = 20\ V$ transfer characteristics under dark conditions for the e isomer (anti,R)16,17-bis[60]PCBM photoFET device.

the characteristics of this device were further studied. The output curve of e isomer (anti,R)16,17-bis[60]PCBM as an n-type material produced well-behaved linear and saturated regions as shown in Figure 4.4e. The transfer curves of this enantiomer were also measured under the saturation regime (Figure 4.7), yielding a saturation electron mobility of $1.44 \times 10^{-5}\ V^{-1}s^{-1}$. The light intensity and time-dependent CP photoresponses of the chiral fullerene-based devices were also explored. These CP photoFETs were very sensitive to light even at low optical power of 0.48 $mW\ cm^{-2}$, where an increase of 1.4 times was observed in the off current compared to that in the dark (Figure 4.4c). The steady-state photocurrent gradually increased and did not reach saturation from $0.48 - 150\ mW\ cm^{-2}$. The time-dependent photoresponse shows a fast symmetric rise time and a fast fall time with a sharp square shape, as well as an obvious dissymmetric CP response shown in Figure 4.4f, a substantial improvement and better reversibility over the long decay seen in helicene CP-photoFETs.[45] The rise and fall times of these devices are less than 43 ms, which is much shorter than reported for PCBM single crystal photodetectors (350-650 ms).[131] Therefore, a device with such a fast light response could, in principle, be applied to detect higher frequency CPL signals for lower latency information transmission.

4.5 Conclusion

We successfully separated and assigned the absolute configurations to ten pairs (six bond types) of bis[60]PCBM enantiomers, one of the most widely used fullerene bisadducts for optoelectronic devices. The broadband UV-vis-NIR chiroptical response indicates great potential in diverse applications and the possibility of tuning the device detection wavelength by employing different isomers. We fabricated the first photoFETs based on enantiomerically pure fullerenes and showed that they were able to discriminate CPL in a highly effective manner. The devices gave excellent g_{ph} (up to 1.27 ± 0.06) and fast response times of less than 43 ms. Such promising properties can be further applied in CP organic photodiodes and other CP photodetecting technologies. For example, the use of patterning techniques—available for solution-processable organic semiconductors—should allow the creation of arrays of CPL-sensitive devices, as well as integration with complementary metal oxide semiconductor (CMOS) electronics. Overall, this study further develops chiral organic materials for CPL detection, positioning enantiopure fullerenes as an exciting material class in such chiral technologies.

Chapter 5

F8T2:aza[6]H Photodiodes[1]

5.1 Statement of Contribution

The contribution of the experimental results in this chapter is stated below.

Matthew D. Ward fabricated and characterised the OPDs.

Matthew D. Ward and Dr. Jessica Wade performed thin film analysis of constituent device layers.

Matthew D. Ward and Xingyuan Shi tested the switching speed and frequency response of OPDs.

Dr. Jochen Brandt purified F8T2 for the preliminary studies of this device architecture.

Tianyi Zhang and Dr. Nicola Gasparini provided equipment and additional support for device switching response and bandwidth measurements.

[1]Reuse permissions for this chapter have been included in the appendices.

5.2 Motivation and Novelty

CP phototransistors, such as those discussed in the previous chapter, can exhibit large g_{ph} values, even when low g_{abs} materials are used as active layers in these devices (see Table 2.2). In spite of this, the phototransistor architecture has several shortcomings that make them unsuitable for a number of CP selective photodetection applications. One example is the long response times typical of these devices, which is an artefact of the long channel lengths ($\sim 1 - 10\ \mu m$ compared to $\sim 10 - 100\ nm$ in photodiodes) of phototransistors, as this leads to longer transit times of photogenerated carriers (Equation 2.42). Scaling up the surface area of phototransistors is also challenging, as this requires the use of arrays of many phototransistors prepared by lithography, which can be time-consuming, costly, and requires specialist lithography equipment with the expertise to operate it.[160]

Prior to the publication of this work, our evaluation of CPL selective photodetectors (Table 2.2) showed that although CP photodiodes did not demonstrate the same high g_{ph} values as phototransistors (approaching 2 in some cases), their full figure of merit profile represented that of an "all-rounder" photodetector with greater response speeds, simpler fabrication protocols, and the possibility of fabricating large-area devices. This work also represented an opportunity to explore the application of the achiral polymer–chiral small molecule blend systems developed by the Campbell and Fuchter Groups in a photodetector architecture.[161, 46, 162, 13, 42, 163]

The result of this work was, at the time of publication, a CP selective photodiode architecture with considerable photocurrent dissymmetry g_{ph}, with absolute values as high as 0.85 and dark currents as low as 10 pA. Impressively, they showcase a linear dynamic range of 80 dB and rise and fall times of $\approx 7\ \mu s$, which significantly outperformed all previously reported CP selective photodetectors. Mechanistically, it is shown that g_{ph} is sensitive to the thickness of both the chiral donor and the achiral acceptor layers and that there is a trade-off between external quantum efficiency and g_{ph}.

5.3 Introduction

The recent research interest in chiral optoelectronic devices has led to the realisation of several CP photodetectors based on organic and organic-inorganic hybrid chiral systems (summarised in Table 2.2). However, all of these systems have their own shortcomings. While devices that incorporate chiral plasmonic nanostructures can exhibit outstanding CP selectivity ($—g_{ph}| \leq 1.6$), they typically suffer from low EQE ($\leq 1\%$) and cannot operate in the visible spectral region.[93, 94] Their widespread application is further hindered by complex fabrication protocols, which often involve slow instrumentation (e.g., electron-beam lithography) that render the mass production of components a challenge.[160] The device architectures that demonstrate the greatest CP selectivity (i.e., approaching $|g_{ph}| \approx 2$, perfect CP selectivity) are based on the field-effect transistor (FET) structure, but these devices suffer from low EQE ($\approx 10^{-2}\%$) and cannot be trivially scaled up.[45, 74, 11] Chiral hybrid organic–inorganic perovskite (HOIP) photodetectors have achieved impressive EQEs ($\approx 57\%$), but unfortunately, the majority of published devices demonstrate poor CP selectivity ($|g_{ph}| \approx 0.1$).[68, 70, 69] More recently, a low-dimensional chiral HOIP has been reported that allows for high CP selectivity in the UV ($|g_{ph}| = 1.9$).[72] Such perovskite devices face challenges relative to competitive technologies however, such as toxicity and instability. Although a handful of chiral OPDs have been reported, they demonstrate modest values of $|g_{ph}|$ (≤ 0.1), and other crucial figures of merit (e.g., EQE, linear dynamic range and response times) are rarely disclosed.[85, 77, 86]

Photoactive achiral polymer–chiral additive blends constitute a particularly attractive and versatile class, demonstrating large g_{abs} and allowing polymers that have been optimised for photodetection to be repurposed for CP discrimination without the need for novel synthesis efforts. Recently, Kim et al. combined achiral polymer poly[3-(6-carboxyhexyl)thiophene-2,5-diyl] (P3CT) with the chiral additive 1,1'-binaphthyl to realise a CP photodiode ($|g_{ph}| = 0.1$, $EQE = 18\%$). Unfortunately, the very slow fall times of these devices ($> 250\ s$) make them practically unsuitable for high frequency domain applications.[77] Our group and others have demonstrated high-efficiency, high-dissymmetry ($|g_{EL}| \approx 1.1$) CP organic light-emitting diodes (OLEDs) based on achiral polyfluorene-based (co-)polymers blended with a chiral small-

molecule (1-aza[6]helicene, hereafter aza[6]H) additive.[161, 46, 162] We have since postulated that the origins of these chiroptical phenomena lie in the formation of a weakly ordered double twist cylinder blue phase, where the aza[6]H serves to template the polymers into twisted fibrils with strong coupling between electric and magnetic transition dipole moments.[13, 42, 163]

Here we report the realisation of highly selective CP OPDs based on a simple, planar heterojunction architecture comprising a poly(9,9-dioctylfluorene-alt-bithiophene) (F8T2):aza[6]H blend electron donor layer and a C_{60} electron acceptor layer. To the best of our knowledge, these devices represent the highest photocurrent dissymmetry ever reported for a CP OPD ($|g_{ph}| = 0.72$ with zero bias), along with fast response times ($t_{rise/fall} \approx 7\mu s$) that are three orders of magnitude faster than those reported for all other CP photodetecting devices. Such fast responses open up the possibility of using these devices for short-range communication using visible light.[164] These devices represent the first CP OPDs with device performance compatible with the demands of real-world technologies and, through mechanistic device analysis, emphasise the importance of both the π-conjugated polymer structure and the device architecture in the ability to differentiate L- and R-CPL.

5.4 Results and Discussion

The use of thermal annealing to induce a giant chiroptical response in F8T2:aza[6]H blends has already been evaluated by our group, and, unless stated otherwise, we followed the optimised protocol (140°C for 10 min in a glovebox filled with N_2, 10 wt% loading ratio of aza[6]H) for all experiments.[15] To ensure that the chiral phase is not affected by the subsequent deposition of the C_{60} layer, we compared the ellipticity spectra of donor-only thin films (F8T2:aza[6]H) with those obtained for the donor–acceptor (D–A) bilayer heterojunction (F8T2:aza[6]H–C_{60}), and find no evidence that the thermally evaporated C_{60} layer disrupts the formation of the chiral phase (Figure 5.1).

We first fabricated a series of CP OPDs of device structure indium tin oxide (ITO)/poly(3,4-ethylenedioxythiophene):polystyrene sulfonate (PEDOT:PSS)/F8T2:aza[6]H/C_{60}/Al (Figure 5.2)

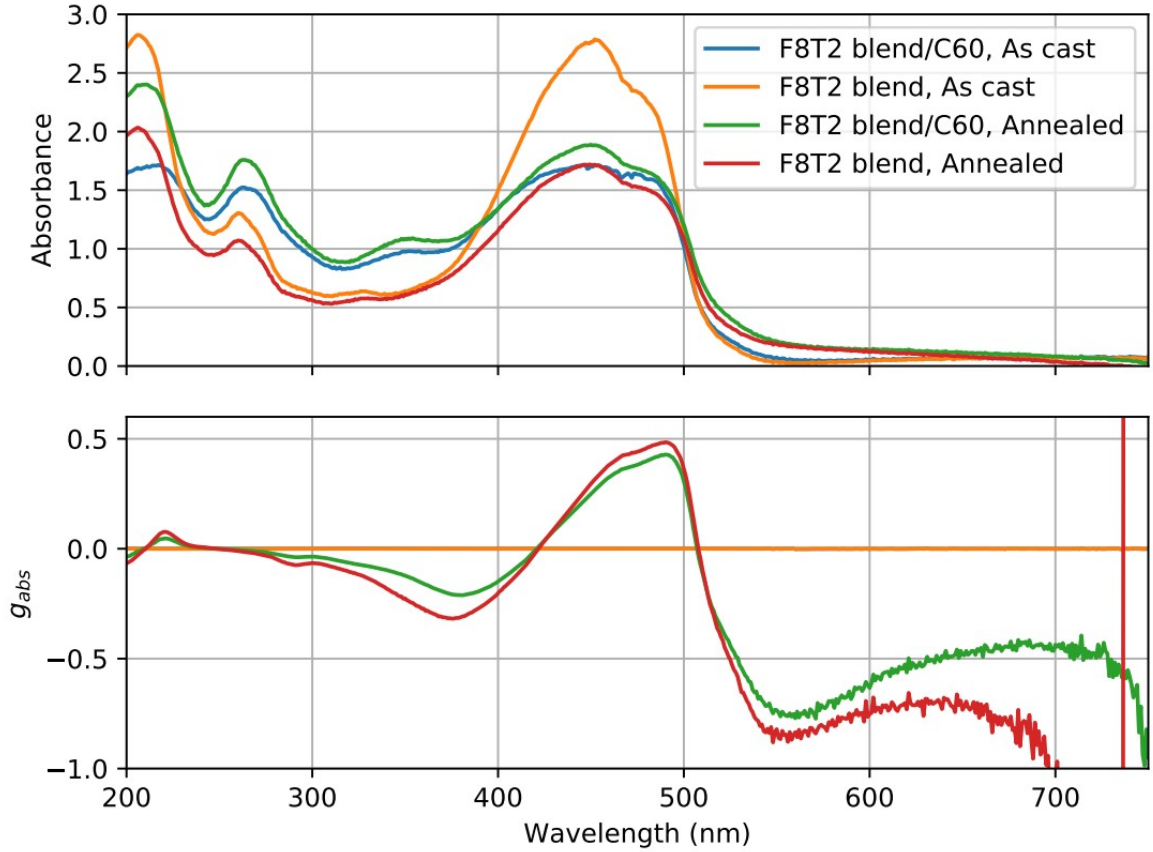


Figure 5.1: Absorption and g_{abs} spectra of F8T2 films and F8T2/C_{60} bilayers before (as cast) and after thermal annealing. As shown, the high g_{abs} chiral phase is only induced after thermal annealing and is not significantly reduced by adding a thermally evaporated C_{60} layer. Further spectroscopic and morphological characterisation of F8T2:aza[6]H blends has been carried out in our previous work and found to be consistent with this study.[13]

with variable thickness of F8T2: aza[6]H (t_D of 77 to 140 nm) and a fixed C_{60} layer thickness ($t_A = 30\ nm$). We previously showed that when considering thick films ($t_D > 150\ nm$) the true g_{abs} of our annealed blend materials does not vary with thickness.[15] The same does not hold true for the thin films ($t_D < 150\ nm$) evaluated here, which we attribute to the strong optical interference of forward and backward traversing waves caused by multiple reflections at the substrate–film and other neighbouring interfaces, typical of optically thin films.[165] The ellipticity (Figure 5.2b), as well as the apparent $|g_{abs}|$ (Figure 5.3), increases with increasing t_D and is equal and opposite for $[M]$- and $[P]$-aza[6]H blends.[15] Irrespective of the polarisation of the excitation, the EQE decreases as t_D increases (Figure 5.2c). As can be expected from the increasing g_{abs}, $|g_{ph}|$ values corresponding to the spectral region of the first CD Cotton band ($\approx 480\ nm$) increase with increasing t_D, from ≈ 0.15 at $t_D = 81\ nm$ to ≈ 0.41 for $t_D = 110\ nm$ (shown in Figure 5.2d case of an $[M]$-aza[6]H-doped CP OPD). We note that g_{ph} is of opposite handedness compared to the corresponding g_{abs}; that is, donor layers that preferentially absorb R-CPL result in higher EQE under L-CPL near the D-A interface and vice versa. Under reverse bias (Figure 5.2e,f) the CP OPDs demonstrate an enhanced g_{ph}; for example, when $t_D = 140\ nm$, $|g_{ph}|$ increases from 0.3 (short circuit) to 0.85 ($-3\ V$).

Next, we evaluated the impact of the C_{60} layer ($t_A = 0 - 50\ nm$) on the performance of the device, using a fixed t_D ($77\ nm$). At all excitation wavelengths probed, EQE initially increases with increasing t_A (Figure 5.4a), until $t_A \geq 40\ nm$, when EQE drops sharply (from $\approx 8\%$ to $\approx 3\%$ for $\lambda > 400\ nm$). Interestingly, the short circuit $|g_{ph}|$ for the longer-wavelength peak (corresponding to the ellipticity peak at around $540\ nm$) increases as t_A decreases (Figure 5.4b), reaching $|g_{ph}| \approx 0.72$ when $t_A = 10\ nm$. This increase is coupled with a blueshift of the wavelength (λ_{ph}) at which the maximum $|g_{ph}|$ occurs ($\lambda_{ph} \approx 540\ nm$ at t_A of $50\ nm$, $\lambda_{ph} \approx 510\ nm$ at t_A of $10\ nm$). The relationship between g_{ph} and t_A is particularly surprising, since the presence of the achiral acceptor layer does not significantly affect the ellipticity (Figure 5.1). We note that there is no significant enhancement of the photocurrent or g_{ph} with increasing reverse bias (Figure 5.4c,d).

Given the trends we observed as a function of t_D and t_A, we selected two device architectures for further study: one targeting the most intense, first Cotton CD band ("**1**", $\lambda = 480\ nm$; with

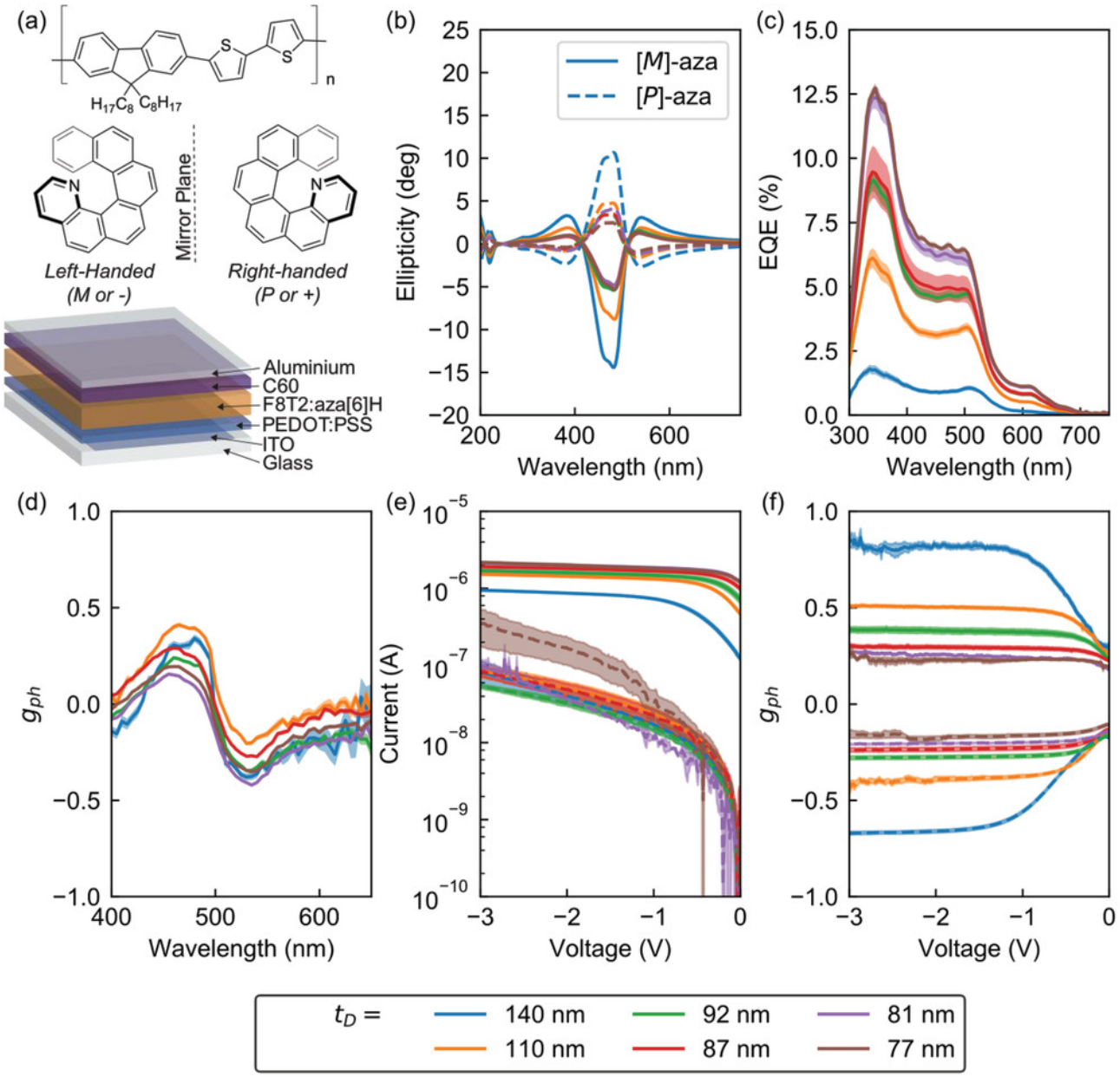


Figure 5.2: Influence of the blend donor layer thickness, t_D, on CP OPD performance while keeping the acceptor layer thickness at 30 nm. a) Molecular structures of F8T2 (top), [M]-aza[6]H and [P]-aza[6]H (middle), and the OPD architecture (bottom). b) Ellipticity of F8T2:[M]- (solid) and [P]-aza[6]H (dashed) blend layers. c) Unpolarised EQE and d) g_{ph} for F8T2:[M]-aza[6]H OPDs at 0 V bias. e) Current–voltage curves of F8T2:[M]-aza[6]H based OPDs under dark conditions (dashed) and unpolarised light (solid; with incident radiation 0.55 $mW\ cm^{-2}$, $\lambda_{ex} = 473\ nm$). f) g_{ph} of F8T2:[M]-aza[6]H (solid) and F8T2:[P]-aza[6]H (dashed) OPDs under reverse bias (0.21 $mW\ cm^{-2}$, $\lambda_{ex} = 473\ nm$). Shaded regions surrounding curves represent the estimated experimental uncertainty in the data.

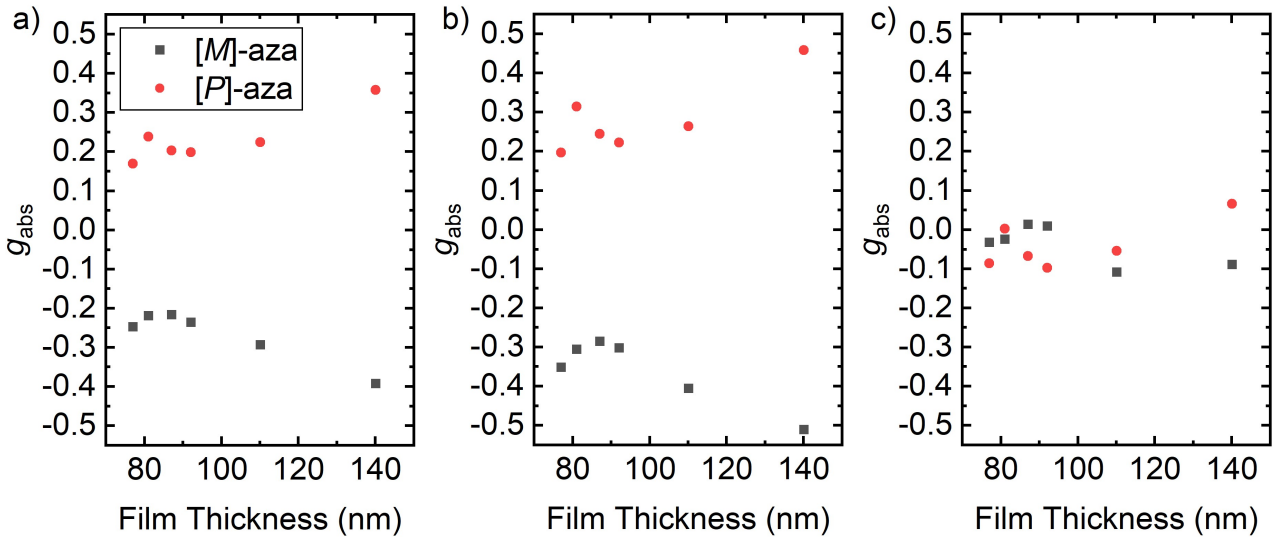


Figure 5.3: g_{abs} as a function of F8T2:aza[6]H film thickness (with corrections for reflection), at wavelengths of (a) 482 nm, (b) 455 nm and (c) 510 nm. Distinct from our prior studies with F8T2:aza[6]helicene films, $|g_{abs}|$ increases with increasing film thickness, even after reflection losses are accounted for.[14, 15] We attribute this to the use of thinner films in this study ($t_A < 150\ nm$) relative to our prior work, which results in coherent thin-film interference in our F8T2:aza[6]H, which is not accounted for in the reflection loss correction devised by Schulz *et al.* and implemented here.[14]

$t_D = 87\ nm$ and $t_A = 30\ nm$) and the other targeting the longer-wavelength CD band ("**2**", $\lambda = 540\ nm$; $t_D = 77\ nm$, and $t_A = 20\ nm$). These architectures maximise the difference in EQE under L-CPL and R-CPL at their target wavelengths to optimise both EQE and g_{ph}. In both cases, EQE (Figure 5.5a) and g_{ph} (Figure 5.5b) are enhanced under reverse bias, reaching $|g_{ph}| > 0.1$ at an EQE of 5.2% for band **1** (solid, $-1\ V$ bias) and $|g_{ph}| > 0.4$ at an EQE of 8.4% for band **2** (dashed, $-0.5\ V$ bias). Both devices exhibit a linear response to increasing light intensity ($\lambda_{ex} = 473\ nm$) of more than four orders of magnitude (Figure 5.5c,d), yielding linear dynamic range (LDR) values of ≈ 80 dB. Under a 488 nm square wave modulated (i.e., on/off) excitation, these devices demonstrate average rise and fall times of $\approx 7\ \mu s$ (Figure 5.5e) and under sinusoidally varying light intensities, the bandwidths of these devices are comparable, reaching up to 56 kHz (Figure 5.5f).

These results not only showcase the first example of the versatile achiral polymer–chiral small-molecule additive blend systems in CP OPDs but also provide a simple platform for understanding the fundamental mechanisms that underpin their device performance. The decrease in EQE with increasing t_D (Figure 5.2b) can be understood by considering photogeneration and

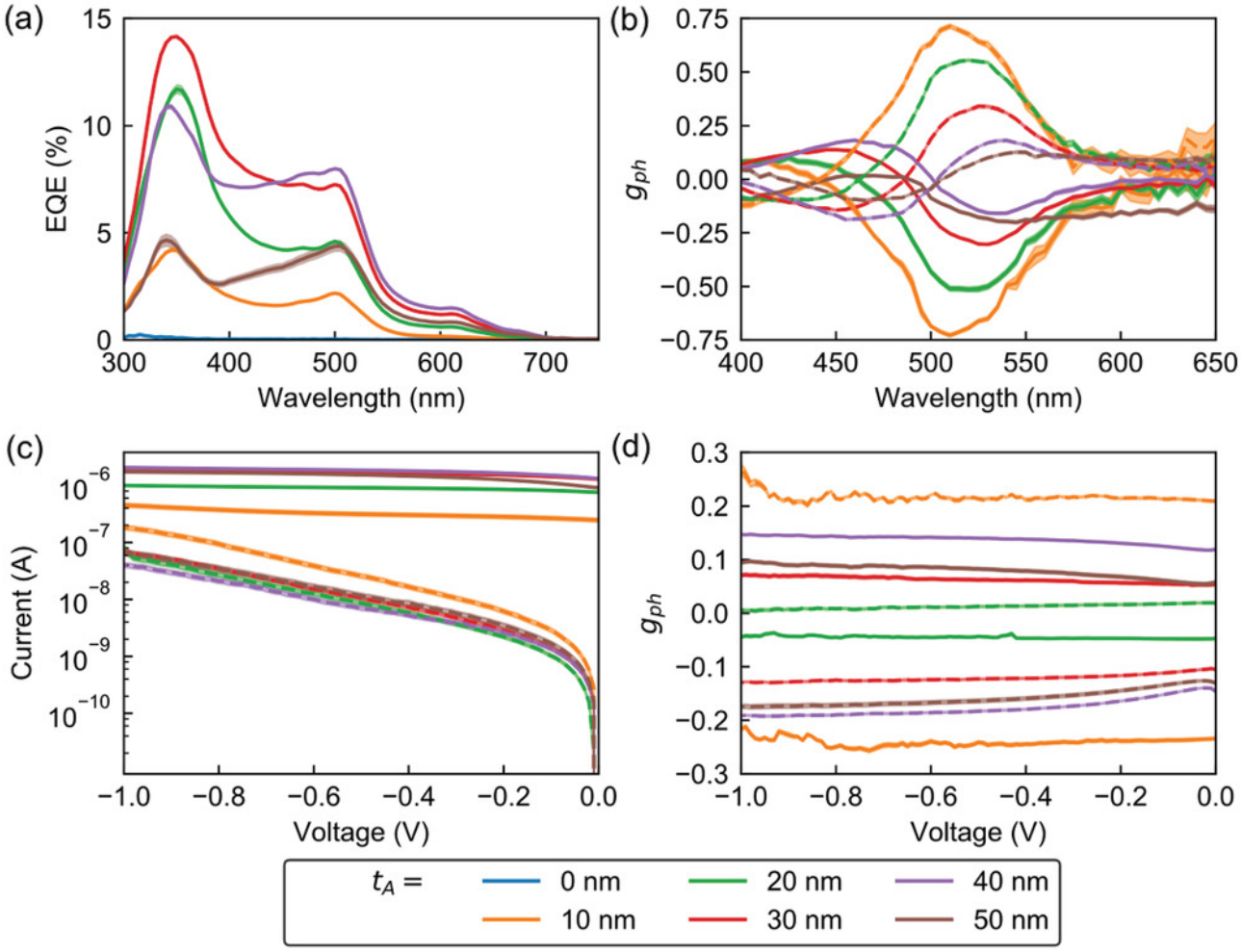


Figure 5.4: Influence of C_{60} acceptor layer thickness, t_A, on CP OPD performance with a fixed donor layer thickness of 77 nm. a) Unpolarised EQE and b) g_{ph} for F8T2:[M]- (solid) and [P]-aza[6]H (dashed) OPDs at zero bias. c) Current–voltage curves of F8T2:[M]-aza[6]H devices under dark conditions (dashed) and unpolarised light (solid; with incident radiation 0.57 $mW\ cm^{-2}$, $\lambda_{ex} = 473\ nm$). d) g_{ph} of F8T2:[M]-aza[6]H (solid) and F8T2:[P]-aza[6]H (dashed) OPDs under reverse bias (0.22 $mW\ cm^{-2}$, $\lambda_{ex} = 473\ nm$). Shaded regions surrounding curves represent the estimated experimental uncertainty in the data.

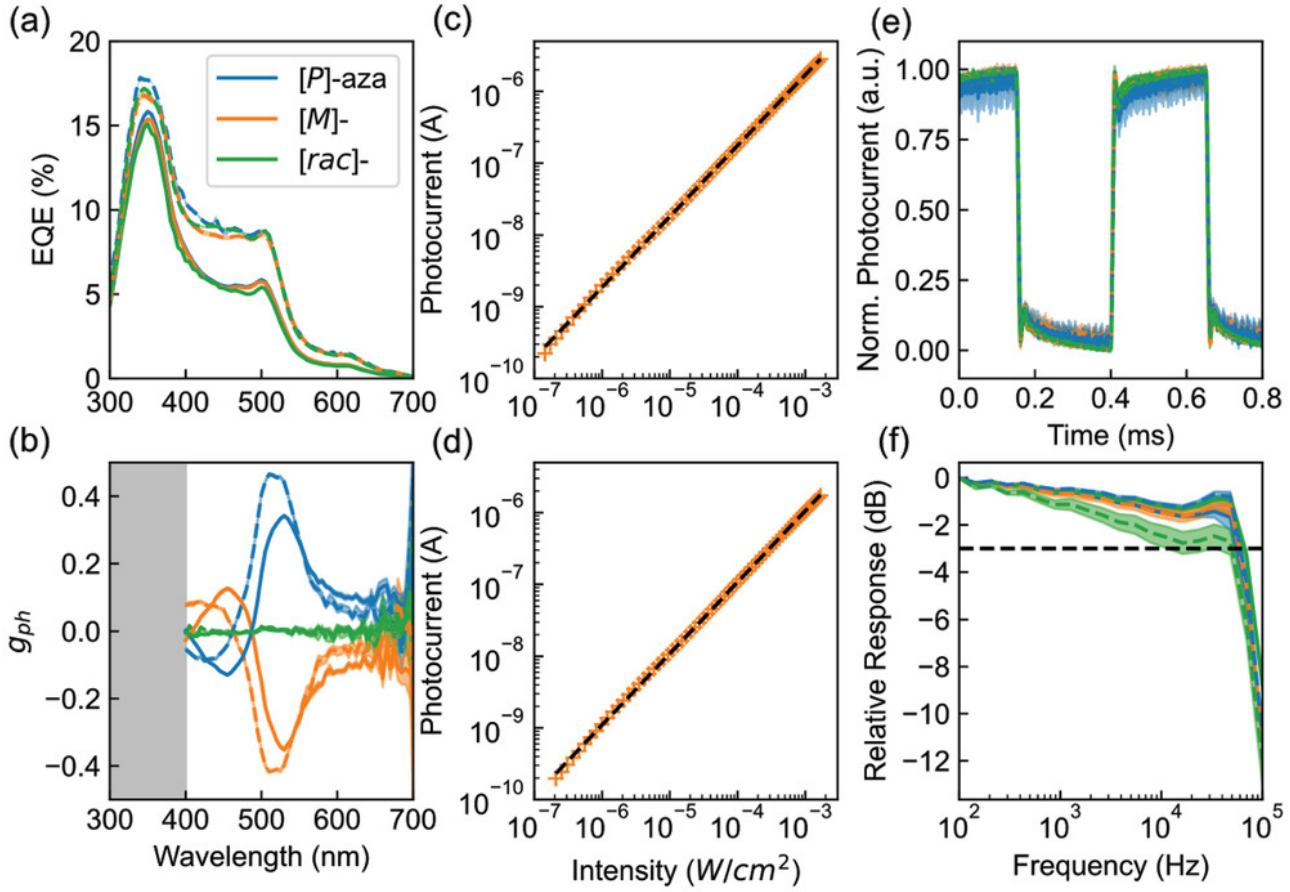


Figure 5.5: Device characteristics of optimised OPDs incorporating $[M]$-, $[P]$-, or $[rac]$-aza[6]H chiral additives. a) Reverse-biased unpolarised EQE and b) reverse biased g_{ph} for OPDs fine-tuned for operation in CD band **1** (solid, $-1\ V$ bias) or CD band **2** (dashed, $-0.5\ V$ bias). Note that the quarter-wave plate used in b) does not operate at a quarter-wave retardance below 400 nm (Grey). Unpolarised LDR of c) band **1**-oriented OPDs and d) band **2**-oriented OPDs, where dashed lines indicate the line of best fit. e) Non-CP switching response of band **1** (solid) and band **2** (dashed) OPDs under pulsing by a 2 kHz square-wave modulated laser. f) Frequency response of OPDs of band **1** (solid) and band **2** (dashed) OPDs, where the horizontal black line indicates the -3 dB point where the device bandwidth is determined. Incident radiation $\lambda_{ex} = 473\ nm$ for obtaining c) and d); and $\lambda_{ex} = 488\ nm$ used for e) and f). The shaded regions surrounding the curves represent the estimated experimental uncertainty in the data.

subsequent dissociation of excitons. As t_D is considerably greater than the exciton diffusion length of F8T2 ($\approx 8\ nm$), it can be assumed from a first approximation that statistically, most excitons generated in the donor layer more than $\approx 8\ nm$ from the D–A interface would not dissociate before annihilation and therefore do not contribute to the measured photocurrent.[75] As t_D increases, the proportion of incident photons that are absorbed before reaching the D–A interface increases, reducing the light intensity at the D-A interface, decreasing EQE. On the other hand, g_{ph} increases with increasing t_D, and is always opposite in sign to g_{abs} (Figure 5.2b,d,f). This behaviour has previously been observed using a planar heterojunction architecture by Meskers and co-workers, and can be explained by considering the mechanism illustrated in Figure 5.6a.[85] For F8T2:[M]-aza[6]H devices, R-CPL is more strongly absorbed than L-CPL in the donor layer. As a result, the intensity of light that reaches the D–A interface is greater for L-CPL than it is for R-CPL, which leads to an inversion of g_{ph} relative to g_{abs}. As t_D increases, this "filter effect" is further enhanced, which serves to increase $|g_{ph}|$. The enhancement of $|g_{ph}|$ under reverse bias, which is particularly apparent when t_D is high (Figure 5.2f), suggests that the efficiency of either exciton generation, exciton dissociation, or charge extraction does not increase equally with reverse bias under L- and R-CPL. Further studies are required to elucidate the precise origins of this interesting phenomenon.

While increasing t_D has a detrimental impact on device performance, the same is not true for the achiral acceptor layer (t_A) (Figure 5.4a,c). Consistent with an exciton diffusion length of $\approx 40\ nm$ for C_{60}, EQE and photocurrent increase until $t_A = 40\ nm$, i.e., a length until which most excitons can diffuse to the D–A interface thus contribute to the photocurrent.[75] When the C_{60} acceptor layer thickness exceeds the exciton diffusion length ($t_A > 40\ nm$), EQE and photocurrent decrease sharply. We attribute this to the absorption of light in the excessively thick C_{60} layer, which nonselectively reduces the light intensity that is reflected to and beyond the D–A interface from the aluminium electrode. At the same time, when the CP OPDs are excited in the low energy band ($\approx 540\ nm$), $|g_{ph}|$ is dramatically enhanced by decreasing t_A (Figure 5.4b,d). We suggest that this behaviour is the result of two cooperative mechanisms (Figure 5.6b). As described above, for F8T2:[M]-aza[6]H devices, selective absorption of R-CPL results in a greater $|g_{ph}|$ under L-CPL. The L-CPL transmitted through the achiral C_{60} layer

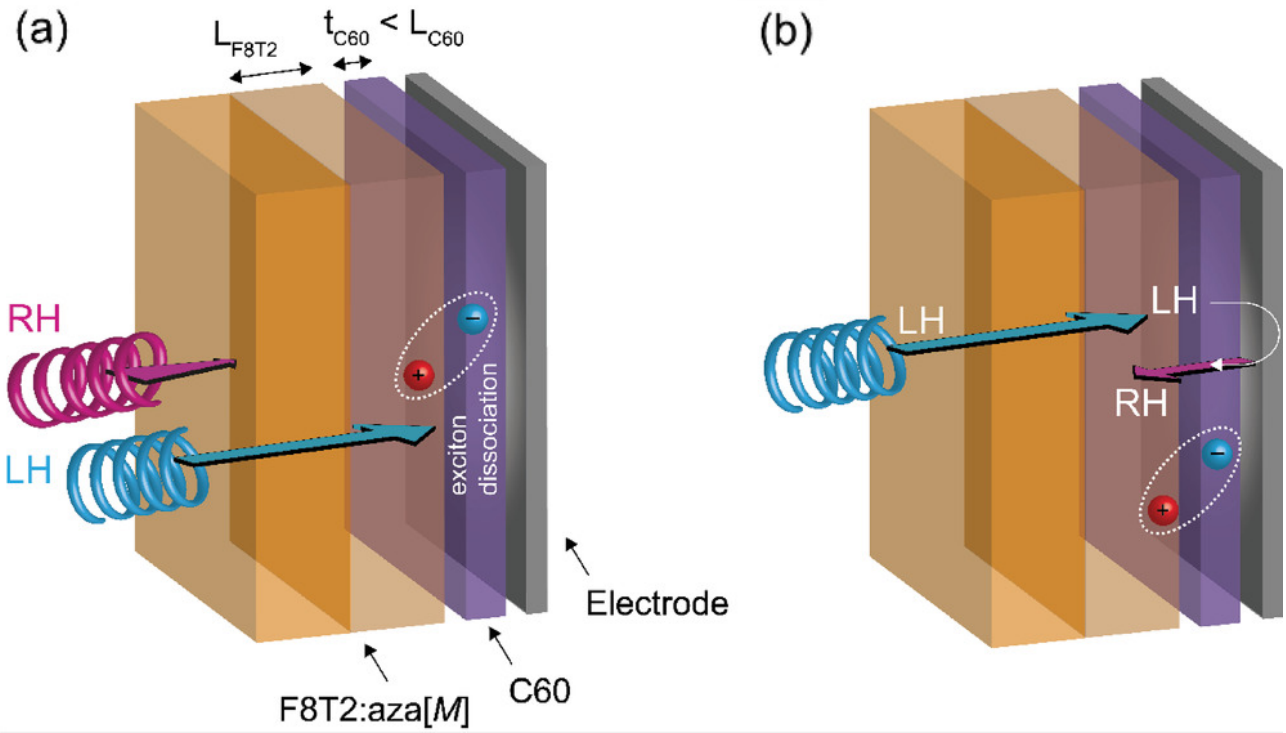


Figure 5.6: Proposed mechanism for the influence of a) t_D and b) t_A on CP OPD performance. For F8T2:[M]-aza[6]H devices, R-CPL is more strongly absorbed than L-CPL in the donor layer, therefore, the intensity of light that reaches the D–A interface is greater under L-CPL than under R-CPL, leading to an inversion of g_{ph} relative to g_{abs}. For thin t_A layers, the L-CPL transmitted through the achiral C_{60} layer is reflected off the back aluminium electrode, after which the handedness inverts (L-CPL becomes R-CPL, and vice versa). Following reflection, the CPL is of the appropriate handedness to be more preferentially absorbed by the chiral donor layer near the interface.

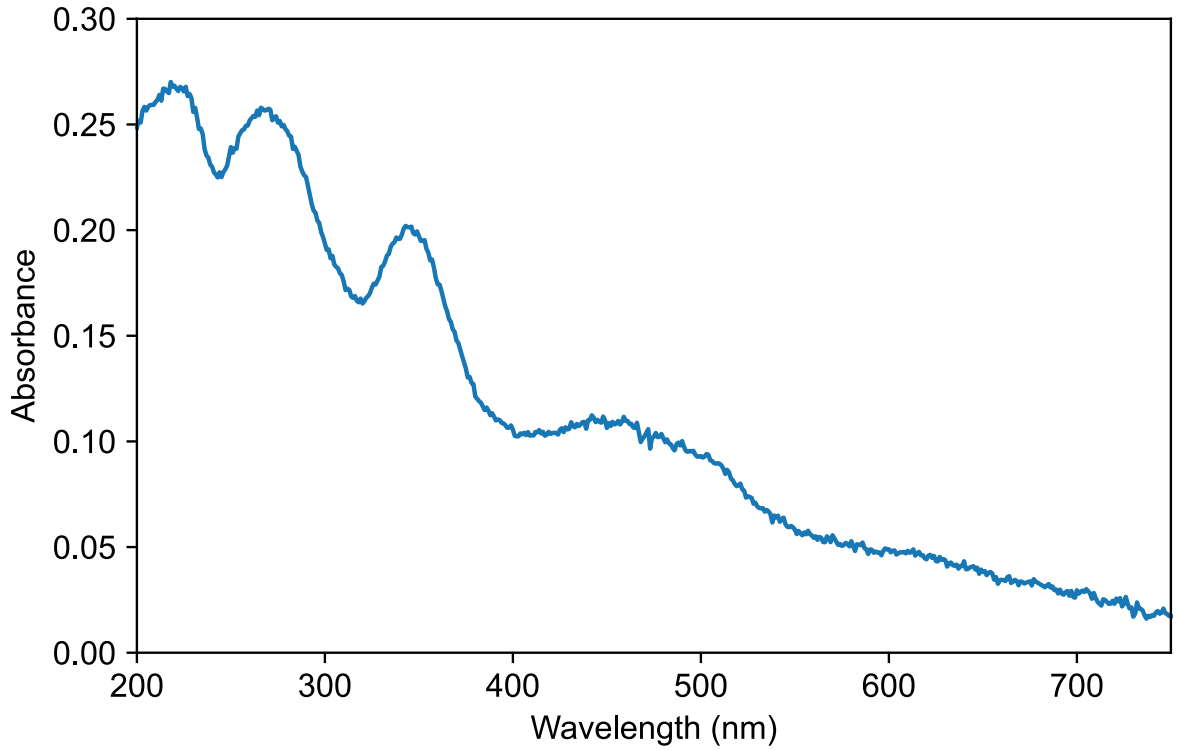


Figure 5.7: Absorption spectrum of a 50 nm C_{60} film. We attribute the lack of significant enhancement of $|g_{ph}|$ corresponding to the high energy band (**1**) to the greater absorbance at this wavelength relative to the absorbance at the wavelength of the longer wavelength band (**2**).

is reflected off the back aluminium electrode, after which the handiness is reversed (L-CPL becomes R-CPL, and vice versa). Following reflection, the CPL is the appropriate handedness to be preferentially absorbed by the chiral donor layer near the heterojunction interface. As t_A decreases, the amount of light transmitted through the acceptor layer increases, which ultimately increases g_{ph}. We attribute the lack of significant enhancement of $|g_{ph}|$ in the high-energy band (**1**) to the stronger absorbance of C_{60} at this wavelength (Figure 5.7). We also observe a shift in the peak caused by band **1** from 500 nm toward 600 nm. We assign this behaviour to the stronger absorbance of C_{60} at 500 nm relative to 600 nm, allowing more photons to return to the donor–acceptor interface at longer wavelengths for thicker C_{60} layers. The effect of internal reflection of CPL from the back metallic electrode has also been noted in some CP OLED works.[166] There is an important difference between the two scenarios however: in CP OLEDs, reflection from the back electrode decreases the dissymmetry factor of CP emission, whereas in CP OPDs it increases the dissymmetry factor of CP detection.

The optimised devices represent an ideal balance between device performance and CP selectivity (Figure 5.5; and Table 2.2). To the best of our knowledge, these devices exhibit the highest LDRs ($\approx$ 80 dB) and the fastest switching times ($t_{rise/fall} \approx 7\ \mu s$) of any CP OPDs ever reported. In particular, our switching times are three orders of magnitude faster than those reported in the literature (Table 2.2). We note that the response times of our CP OPDs correspond to a bandwidth of up to 56 kHz. Therefore, these CP OPDs could be used in principle in conjunction with two CPL emitters for high-speed visible light wireless communications; with two 56 kHz CPL transmission channels (L-CPL and R-CPL) offering a total transmission bandwidth of up to 112 kHz.[167] Alongside increasing the speed of data transmission, the use of CPL adds an additional degree of freedom for information encryption, as any eavesdroppers using unpolarised photodetectors will only detect a meaningless superposition of L-CPL and R-CPL signals.

5.5 Conclusion

We present highly selective circularly polarised organic photodiodes with state-of-the-art device performance based on a chiral π-conjugated polymer donor and an achiral C_{60} acceptor in a bilayer planar heterojunction. The simplicity of this architecture allows us to investigate several interesting photophysical and chiroptical phenomena, the findings of which can inform the design of future CP-relevant materials and devices. For example, CP absorption in the donor phase and subsequent inversion upon reflection at the metallic counter electrode results in oppositely handed g_{ph} and g_{abs}. Meanwhile, g_{ph} is largest for the thinnest acceptor layers ($g_{ph} = 0.72$ when $t_A = 10\ nm$), which we attribute to the beneficial impact of CPL inversion on the photocurrent that is greatest for the thinnest acceptor layers.

This study emphasises that in the pursuit of high-performance, high-selectivity planar heterojunction CP OPDs, a compromise must be reached between intense g_{ph} and strong EQE. Despite this, our optimised devices demonstrate impressive figures of merit, with EQE of $5-10\%$, rise and fall times of $\approx 7\ \mu s$, dark currents down to 10 pA, and state-of-the-art linear dynamic

ranges of $\approx$ 80 dB. The strong CP selectivity, coupled with very fast response times, has the potential to transform many real-world applications, including CP-light encrypted, high-speed next-generation data transmission technologies, such as visible light communications.

In order to compete with existing methods of CPL discrimination, such as a conventional Silicon photodiode filtered by a quarter waveplate and linear polariser, further improvements in EQE ($60 - 80\%$ at $\lambda = 400 - 600nm$ for a Si photodiode) and selectivity of CPL photoresponse ($g_{ph} \sim 2$ using linear polariser and QWP filter systems) are required.[98]

5.6 Estimation of Experimental Uncertainties

The uncertainty associated with each unpolarised EQE trace has been calculated using the standard error of the mean of the measurements of 6 functionally identical OPDs. Therefore, this uncertainty provides an indication of device-to-device variability in a 6-device batch. Once device-to-device variability has been quantified, 20 EQE traces are taken of one device in a 6-device batch under each circular polarisation to calculate g_{ph}. This large number of repetitions is required to minimise the noise in this signal (due to the small difference in EQE under L-CPL and R-CPL). The uncertainty associated with each g_{ph} spectrum is estimated as the standard error of the mean for these 20 measurements of g_{ph} for a single device.

The uncertainty associated with each unpolarised current–voltage curve and reverse bias g_{ph} plot has been calculated using the standard error of the mean of measurements of 6 functionally identical OPDs.

The LDR plots for the band **1** and band **2** devices are traces from two representative OPDs from each batch of 6 devices of the band **1** and band **2** devices tested. As such, we estimate an uncertainty of 100 fA for these individual measurements, attributed to the resolution of our source measure unit.

The uncertainty associated with both $t_{rise/fall}$ and bandwidth measurements represents the standard error of the mean for 6 functionally identical OPDs.

Chapter 6

Circularly Polarised Imaging System[1]

6.1 Statement of Contribution

The contribution of the experimental results in this chapter is stated below.

Matthew D. Ward conceived the designs of the 1- and 2-camera circularly polarised imaging systems.

Matthew D. Ward and Ronan Docherty constructed the 1- and 2-camera circularly polarised imaging systems.

Ronan Docherty created the open source Python programme to control the 1- and 2-camera circularly polarised imaging systems.

Dr. Xingyuan Shi prepared spatially patterned F8BT:[*P*]-aza[6]H films.

Matthew D. Ward measured F8BT:[*P*]-aza[6]H and F8BT:[*M*]-aza[6]H films using the 1- and 2-camera circularly polarised imaging systems.

Matthew D. Ward and Dr. Xingyuan Shi cross-compared imaging data from the 1-camera circularly polarised imaging system with Beamline 23 of the diamond light source, with assistance from Prof. Giuliano Siligardi.

[1]Reuse permissions for this chapter have been included in the appendices.

Louis Minion provided a cross-comparison of existing CP selective imaging systems published in the literature and provided advice on avoiding artefacts in imaging systems identified in these prior studies.

6.2 Motivation and Novelty

In the previous two chapters, we have successfully implemented chiral organic semiconductor materials to produce two high-performance CP selective photodetectors. One aspect of the development of the CP selective photodetectors that is commonly overlooked is the difficult and time-consuming process of identifying suitable candidate chiral semiconductor materials and optimising their processing conditions, such as the choice solvent, spin-coating speeds, thermal annealing temperature, and solvent annealing conditions to maximise their chiroptical response (e.g. g_{abs}). One such means of accelerating this process by the group was the use of Beamline 23 at the diamond light source, which allows the measurement of the CD spectrum of solid-state samples of chiral semiconductors *in situ* during thermal annealing of solution processed samples.[168] This approach enables the thermal annealing of these samples to be rapidly optimised for application in CP OLED and CP photodetector architectures; however, access to this facility is subject to a successful application for rapid access to the facility. Access during a rapid access period is also limited to ∼1 week, which means that candidate materials must be prioritised and tested efficiently.

To allow candidate chiral semiconductors to be rapidly screened for further study at Beamline 23 and to rapidly optimise materials for CP selective devices, we developed two compact, low-cost (<£2,000) circularly polarised imaging systems. The performance of these imaging systems was cross-compared with that of Beamline 23, showing good agreement for our previously optimised F8BT:[*P*/*M*]-aza[6]H blends, with a sensitivity of 250 mdeg and a spatial resolution of 100 μm.

To the best knowledge of the author, these circularly polarised imaging systems represent the lowest cost devices reported in the literature capable of spatially mapping solid state samples in real time with a time resolution of <1 s.

6.3 Introduction

Measurements of the CD, and circularly polarised luminescence present an essential tool for investigating the chiroptical response of novel organic chiral semiconductors. The results of these experiments are critical for the design of innovative materials and devices. The majority of approaches to characterising the chiroptical response are expensive, which precludes them from widespread use. These pieces of equipment are rarely compact or modular, making *in situ* measurements challenging and restricting their location to dedicated characterisation laboratories. For example, commercially available CD spectropolarimeters require considerable bench space, cannot provide spatially resolved information, are difficult to adapt for *in situ/operando* characterisation and typically require expensive accessories for custom measurements.[123] Further, the software required to acquire and analyse spectra is rarely open source, with costly licences and upkeep fees.

Spatially resolved CD measurements are essential for understanding and optimising the structural organisation of functional materials. They can be used in the development of fabrication protocols to find the conditions that lead to a homogeneous chiroptical response across a thin film, which is key for the realisation of defect-free devices that make use of CPL. A summary of CD imaging systems that allow for such spatially resolved measurements reported in the literature is provided in Table 6.1.

The first CD microscopes were constructed by Maestre and co-workers in the 1980s; however, the use of imperfect electronic polarisation modulation techniques led to parasitic artefacts affecting their measurements (Table 6.1, row a).[171, 172] In an attempt to mitigate these issues, Kahr and co-workers proposed a visible-light microscope based on mechanical modulation, but the measurement process still resulted in artefacts appearing in the CD signals (Table 6.1, row b).[173, 178] Recently, CD imaging using the collimated beamlight of synchrotron facilities has enabled high resolution spatially resolved chiroptical measurements, but accessing synchrotron facilities is non-trivial, measurements are time consuming, and synchrotron operating costs are considerable (Table 6.1, row c).[168, 179, 180, 181] Additionally, CD spectra can only be acquired across a limited spectral range (200–650 nm), which renders the characterisation of

Table 6.1: Comparison of previously published CD-imaging systems.

Description	Spatial Resolution	Comments	Ref
a) Photo-elastically modulated input light adapted to a scanning confocal microscope.	200 nm	High spatial resolution and sensitivity. Affected by signals originating from sinusoidal polarisation modulation and sample linear birefringence/dichroism.[169, 170]	[171, 172]
b) Commercial microscope, wave plate and linear polariser. Spectrograph and cooled CCD detector enable spectrally resolved CD measurements.	500 nm	Avoids problems associated with electronic modulation but complicated calibration procedure and requires a commercial microscope.	[173, 174]
c) Collimated synchotron radiation micro-beam, piezoelectric stage and photoelastic modulator.	50 μm	High sensitivity enabled by synchrotron radiation, but access is restricted to synchrotron users and the raster scanning technique is slow.	[168]
d) Laser scanning confocal microscope adapted with a photo-elastic modulator.	< 1 μm	High sensitivity afforded by collimated laser, but requires an expensive commercial scanning microscope.	[175]
e) Scanning near-field optical collection mode microscope combined with photoelastic modulator.	$\sim$100 nm	Beyond diffraction limit resolution, but requires complex and expensive instrumentation.	[176]
f) Nano-structured chiral meta-lens designed to separate L- and R-CPL.	5 μm	Extraordinary sensitivity, but requires a bespoke meta-material lens and restricted to highly specialist users.	[177]
g) This work.	100 μm	Compact, low-cost CD imaging with a high temporal resolution of 0.2 s.	

emerging materials (e.g. low-bandgap non-fullerene acceptors) impossible. Characterisation in the infrared is critical for the realisation of highly selective CPL photodetectors for efficient, next-generation optical communications that make use of CPL to double the communication bandwidth.[31, 182] It should be noted that of the custom systems reported to date (Table 6.1), none provide access to the open source software required to operate the instrument.

CD measurements as a function of temperature allow users to monitor different phases within their materials and identify the optimum processing conditions to maximise the chiroptical response.[15] Additionally, chiroptical imaging systems capable of making non-destructive measurements *in situ*/*operando*, that is, under conditions relevant for device operation, can help to uncover the fundamental mechanisms responsible for CPL emission and spin-selective charge transport. Measurements at high and low temperatures can more accurately replicate the optical responses of functional materials as the active layers of real-world devices. For example, light-emitting diodes (LEDs) have operating temperatures of ∼85°C, while spin valves typically require cryogenic cooling. It is therefore inappropriate to characterise only the room temperature CD response when attempting to determine structure-performance relationships. Finally, rapid acquisition of CD spectra during chemical synthesis can permit the design of materials with the desired spectral features. As such, the design of a low-cost, compact, and modular CD spectropolarimeter is of considerable research interest.

Here we present an alternative approach to the chiroptical characterisation of functional materials. The entire apparatus can be assembled at low cost (<£2,000), and operates using open source software based on free Python libraries. We demonstrate that the instrument is capable of measuring CD signals as weak as 250 mdeg and visualising features as small as 100 μm. The system is entirely modular, allowing for the integration of stages for temperature or environmental control, and accommodating upgrades to light sources or detectors as they become more readily available. All custom components (e.g. the housing and sample holders) can be 3D printed and assembled on any surface, removing the need for an optical table and allowing this tool to be used in any lab setting. The low cost and portability of this system also make it suitable for Physics and Chemistry education and outreach activities to visualise chirality on the macro- and micro-scale. In spite of the low cost and small size of this system, the measured

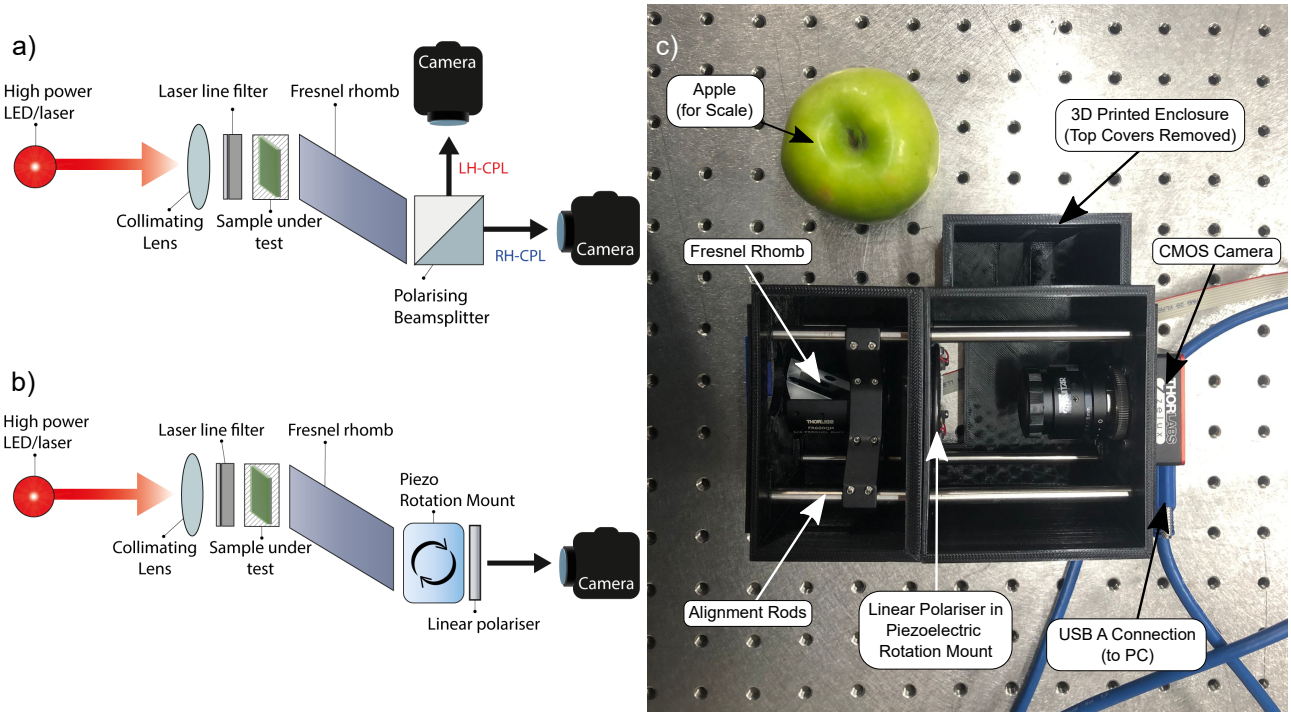


Figure 6.1: Schematics of the two- (a) and one-camera (b) circular dichroism imaging systems developed in this work alongside a photograph of the optimised system (c) with a black 3D printed enclosure to block stray light and enable system portability.

ellipticity is almost identical to that achieved using a benchtop spectropolarimeter.

6.4 Imaging system design

We developed two simple CD imaging systems (Figure 6.1, see Section 3.3.3 for a priced parts list). As shown, collimated monochromatic light from a high-power LED or laser is passed through the sample under test. A Fresnel rhomb is used to separate the transmitted L- and R-CPL into two linear polarisations. Fresnel rhomb retarders feature broadband performance (400-1550 nm) at a remarkably low cost (<£400). Alternatives such as broadband quartz QWPs and photoelastic modulators were considered; however, both are prohibitively expensive (>£2,000 and >£10,000, respectively). Additionally, the 34.8 Hz frame rate of the low-cost camera used in this setup is slower than the 50 kHz switching speed of a photoelastic modulator, rendering them unsuitable for this application.

The two-camera circular dichroism imager (2-CCDI), uses a polarising beamsplitter to direct

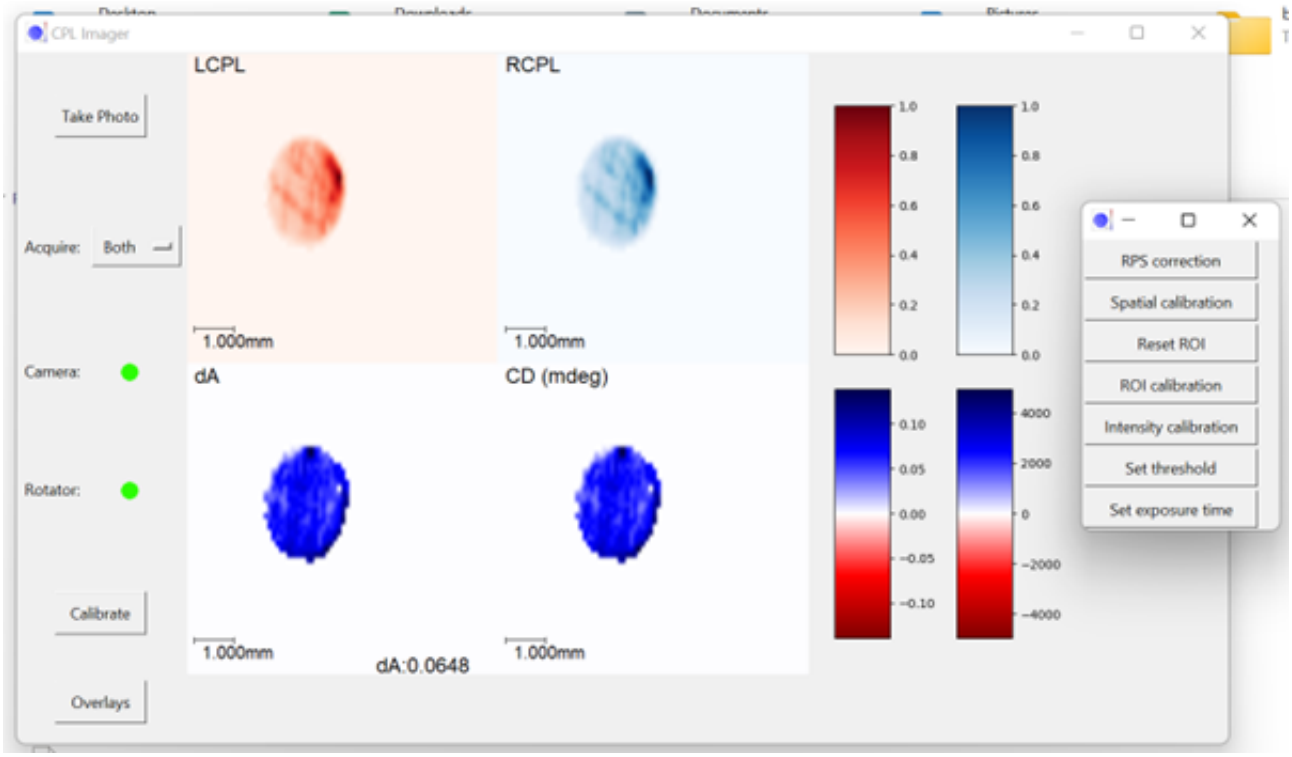


Figure 6.2: A screenshot of the custom open source python graphical user interface used to control the one- and two-camera circular dichroism imagers.

the two linear polarisations from the Fresnel rhomb (corresponding to L-CPL and R-CPL) to two separate monochrome CMOS cameras. Our open source software allows for L- and R-CPL images of the sample to be viewed independently, digitally aligned to account for small discrepancies in camera alignment and, using Equation 2.7, generate images of spatially mapped ΔA and ellipticity. A screenshot of the GUI which forms the control system of the 1- and 2-camera systems is shown in Figure 6.2.

The one-camera circular dichroism imager (1-CCDI), uses an LP mounted on a piezoelectric rotation mount at the output of the Fresnel rhomb. The piezoelectric rotation mount is capable of rotating the LP at a rate of 430° s^{-1}, allowing the LP to rapidly switch between L- and R-CPL trasmission in approximately 0.2 s. To map ΔA and ellipticity, L-CPL and R-CPL images are acquired sequentially. The software displays images of the sample under L- and R-CPL transmission, the mapped ΔA and the ellipticity (Equation 2.7) in real time.

The 1-CCDI has considerable advantages over the 2-CCDI counterpart. The 2-CCDI is less compact, requiring two cameras on perpendicular arms of the beamsplitter, and is more com-

plicated to assemble, as care must be taken to ensure identical path lengths/sample imaging areas for the two cameras. Even with careful assembly, post-processing is required to align the L- and R-CPL images for reliable calculations of ΔA. Additionally, the 2-CCDI cannot resolve small asymmetries in the photoresponses of individual pixels within the two cameras, which can lead to artefacts in the measurement of ΔA. The 1-CCDI, on the other hand, requires no co-alignment, and identical pixel responsivity under L- and R-CPL illumination is guaranteed. One shortcoming of the 1-CCDI approach is the delay of 0.2 s between the L- and R-CPL images – the 2-CCDI systems can capture L- and R-CPL images simultaneously – but this acquisition time is comparable to most commercial instruments.

These imaging systems permit the measurement of the sample under ambient conditions as well as in chambers with environmental control. These can allow for measurements as a function of temperature and under conditions relevant for device operation at a fixed wavelength. Further, replacing the LED or laser in these systems with a tuneable light source could allow for the acquisition of spectrally resolved information.

6.5 Results and Discussion

To evaluate the performance of our compact CCDI systems, we fabricated thin films of poly(9,9-dioctylfluorene-alt-benzothiadiazole) (F8BT hereafter) blended with enantiopure [P]- and [M]-1-aza[6]helicene ([P]- and [M]-aza[6]H hereafter) which have been extensively studied by our group. [15, 183, 162, 184, 163] When spin-coated into solid state films, F8BT:[P]- and F8BT:[M]-aza[6]H demonstrate negligible ellipticity (<100 mdeg) in the absorption band of F8BT in their "as-cast" (i.e. non-annealed) state. Thermally annealing these films above 80°C can increase ellipticity in the F8BT absorption band considerably, reaching over 4000 mdeg at an optimal annealing temperature of approximately 130°C.[15]

Figure 6.3 visualises the outputs of the 2-CCDI system for F8BT:[P]- and [M]-aza[6]H films (λ_{ex} = 470 nm) as a function of temperature (50°C to 200°C at a rate of 10°C/minute). The Linkam chamber used for the temperature and environmental control of heated samples has a

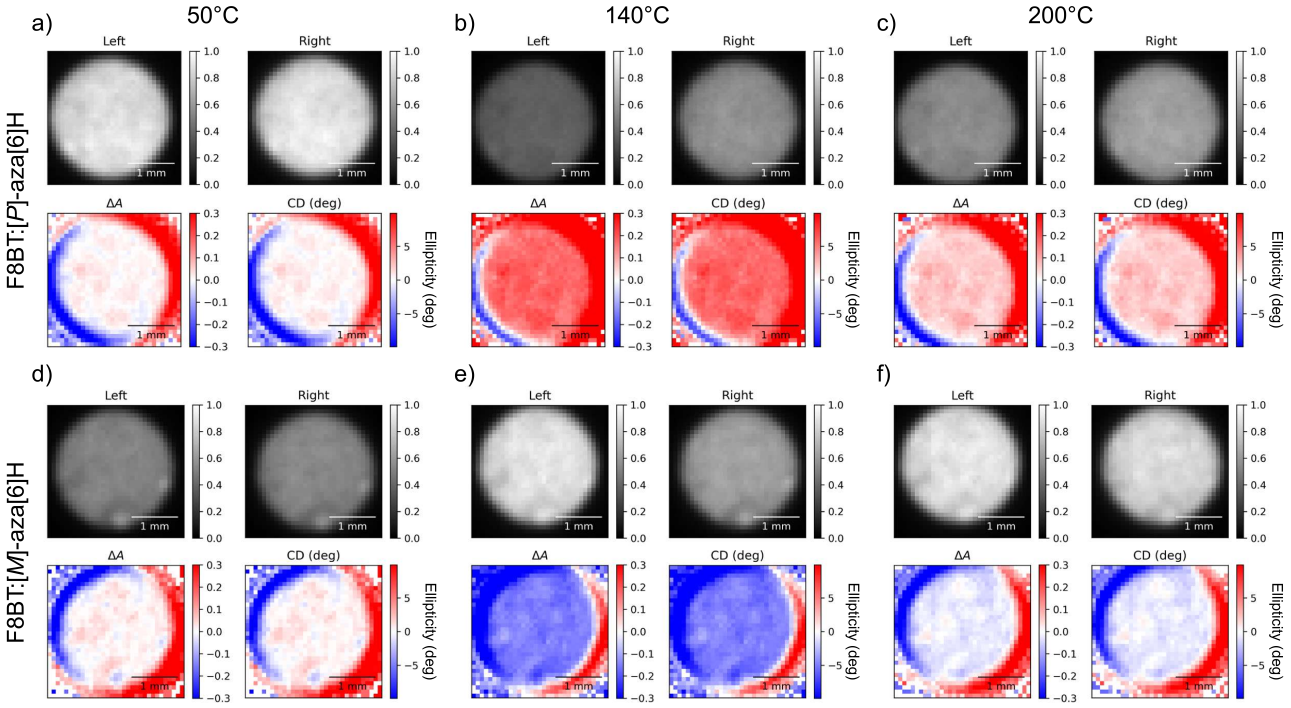


Figure 6.3: Circular dichroism images of solid state F8BT:[P]-aza[6]H (a, b, c) and F8BT:[M]-aza[6]H (d, e, f) films at annealing temperatures of 50°C (a, d), 140°C (b, e), and 200°C (c, f) taken using the two camera circular dichroism imaging system at a wavelength of 470 nm. In each subfigure, "Left" and "Right" indicate the transmitted intensities of L-CPL and R-CPL (respectively), $\Delta A = A_L - A_R$ and "CD" is the measured ellipticity calculated using equation 2.7. The z-axis of "Left" and "Right" correspond to the intensity values of each camera pixel on a unitless linear intensity scale from 0-1. The z-axis of "ΔA" images are, like absorbance, unitless. The z-axis of "CD" images responds to the ellipticity of each pixel expressed in degrees.

circular aperture of 2.5 mm, which limits the size of the mapped area to this diameter.

Remarkably, the CD response as a function of temperature is consistent with data acquired in our previous study of F8BT:aza[6]H blends using the CDi capabilities of the Diamond Light Source.[15] Specifically, F8BT:[M]- and [P]-aza[6]H show negative and positive ellipticity, respectively, of equal magnitude at each annealing temperature. Further, the relationship between annealing temperature and the magnitude of ellipticity is consistent with our previous studies, increasing monotonically from 50°C to a maximum ellipticity at 140°C (indicating the formation of a chiral phase with a strong chiroptical response), above which the chiral phase is destroyed and the ellipticity decreases. In an attempt to align the images of the two cameras we used both an optical cage system and post-processing, but minimal misalignment and reflection from the internal surface of the Linkam chamber aperture results in circular artefacts which appear as a red and blue "halo" around the circular edge of each sample image. To mitigate

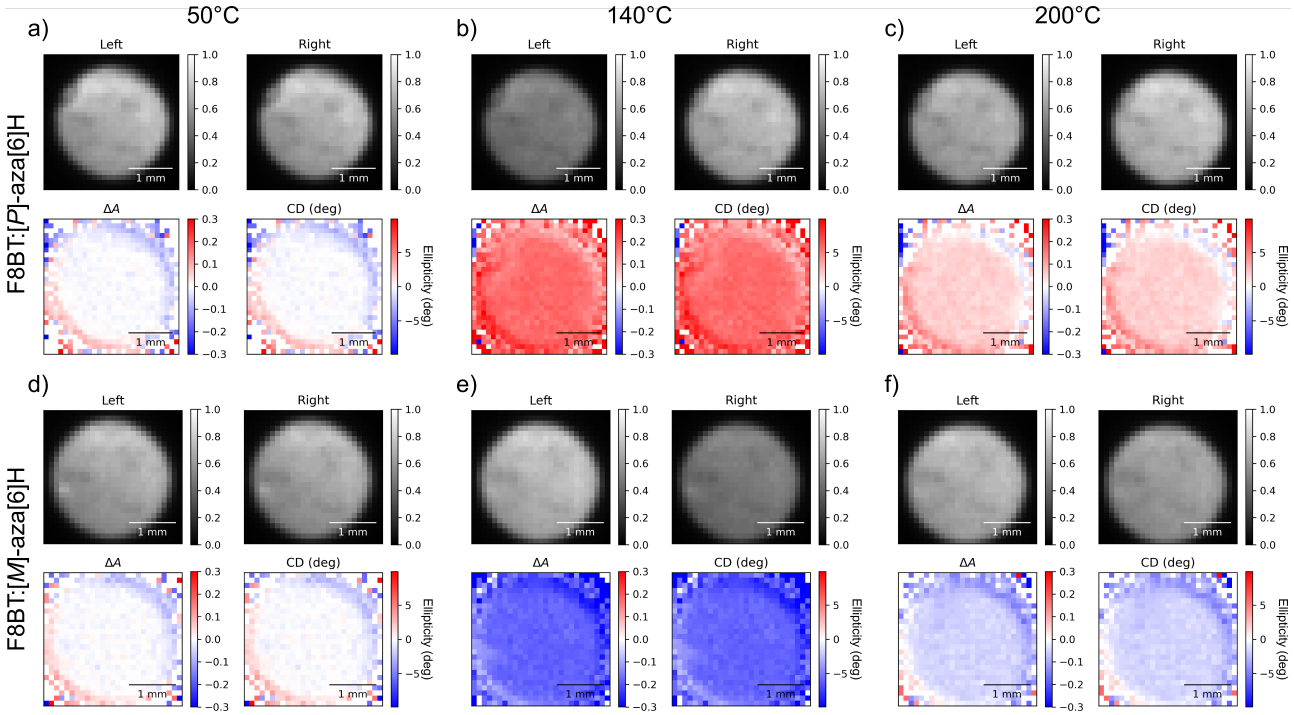


Figure 6.4: Circular dichroism images of solid state F8BT:[P]-aza[6]H (a, b, c) and F8BT:[M]-aza[6]H (d, e, f) films at annealing temperatures of 50°C (a, d), 140°C (b, e), and 200°C (c, f) taken using the one camera circular dichroism imaging system at a wavelength of 470 nm. In each subfigure, "Left" and "Right" indicate the transmitted intensities of L-CPL and R-CPL (respectively), $\Delta A = A_L - A_R$ and "CD" is the measured ellipticity calculated using equation 2.7. The z-axis of "Left" and "Right" correspond to the intensity values of each camera pixel on a unitless linear intensity scale from 0-1. The z-axis of "ΔA" images are, like absorbance, unitless. The z-axis of "CD" images responds to the ellipticity of each pixel expressed in degrees.

for these artefacts, we performed the same experiment using the 1-CCDI system (Figure 6.4). As shown, the use of a single camera in the 1-CCDI reduces the size of this halo artefact considerably due to the absence of misalignment between two CMOS sensors.

Figure 6.5 illustrates the average ellipticity of the F8BT:[M]- and [P]-aza[6]H films as a function of temperature for the 1-CCDI system, which can be calculated by averaging the individual pixels within the CMOS array. Promisingly, these results are highly consistent with those reported in our previous work,[15] with ellipticity increasing significantly above 90°C to a maximum at $130 - 140$°C before gradually decreasing at higher annealing temperatures. As these measurements are quick to perform and the instrumentation is low-cost and compact, it would be trivial to perform measurements during sample preparation. This would allow fabrication protocols (e.g., solvent choice, spin-coating speed, etc.) to be rapidly refined and optimised.

To estimate the weakest detectable chiroptical response, we calculated the standard deviation of the pixel values used to generate Figure 6.5 for T $< 90°C$ (i.e., no detectable chiroptical response). These results indicate that the lowest CD value we can reliably measure is ∼250 mdeg. To improve sensitivity to weak chiroptical responses, the cameras could be replaced with a thermoelectrically cooled CMOS array and a compact, camera-mounted enclosure with an integrated sample holder to eliminate noise contributions from external light sources.

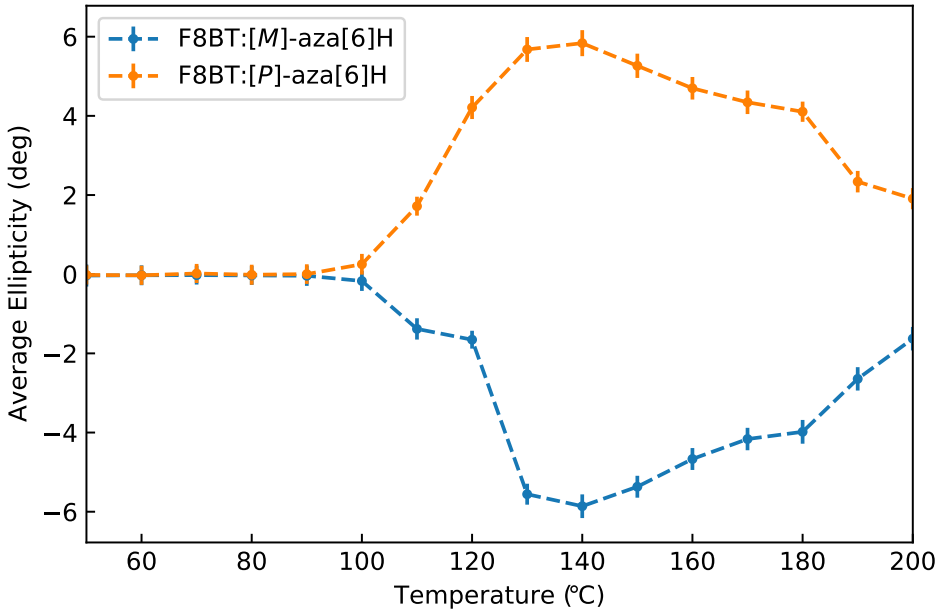


Figure 6.5: Spatially averaged ellipticity of solid state F8BT:[M]-aza[6]H and F8BT:[P]-aza[6]H samples measured using the one camera system at a wavelength of 470 nm.

To test the spatial resolution of the 1-CCDI system, we consider two F8BT:[P]-aza[6]H thin films which were intentionally patterned using thermal and solvent annealing (see Section 3.3.3) to produce domains of strong/weak chiroptical response (Figure 6.6). As shown, features could be easily resolved using the low-cost cameras and, due to being measured outside the Linkam chamber in air, show no halo artefacts. We performed measurements on the same samples using the highly collimated light of the Diamond Light Source and found good agreement (Figure 6.7), with a spatial resolution of 100 μm. This resolution may be further improved through the use of microscope optics. [185]

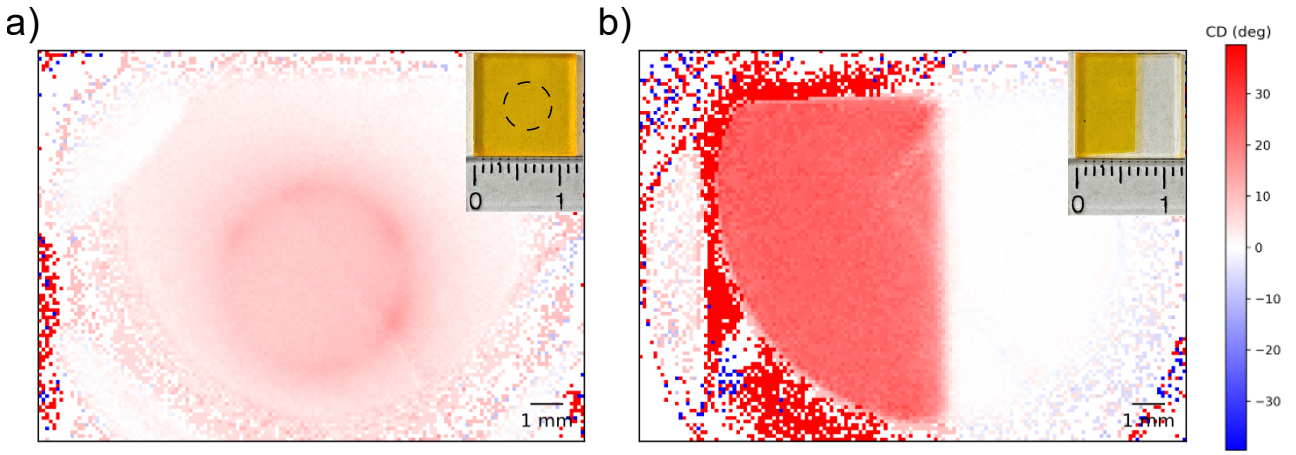


Figure 6.6: Spatially patterned solid state films of thermally annealed F8BT:[*P*]-aza[6]H with ring (a) and step (b) profiles (see Section 3.3.3). Images were captured using the 1-CCDI system under ambient conditions at a wavelength of 470 nm and using a conventional visible light camera (inset, scale in cm). Note that the circular pattern (a) is not noticeable when using the visible light camera, and as such, the intended patterning shape is indicated by a dotted line overlay.

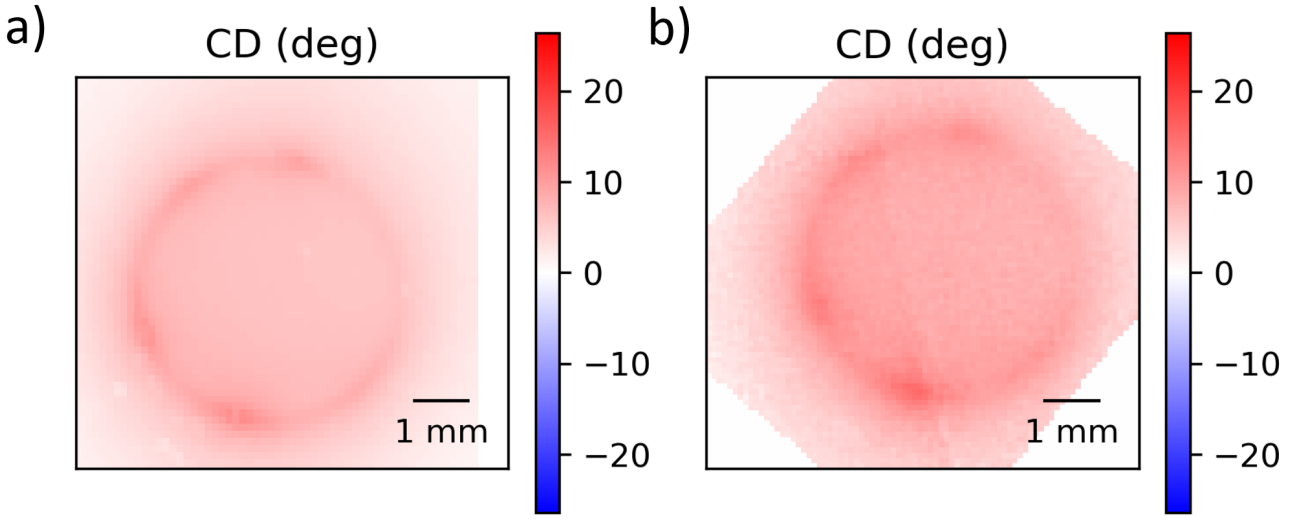


Figure 6.7: A direct cross-comaprison between CD images of spatially patterned solid state F8BT:[P]-aza[6]H captured using Beamline 23 at the diamond light source (a) and the one camera CD imaging system (b).

6.6 Conclusion

We have designed and built a highly versatile, low-cost, compact, and modular chiral imaging system for the analysis of chiral functional materials which is capable of detecting CD as weak as 250 mdeg and has a spatial resolution of 100 μm. We have also developed an open source Python control software for this system which is available at our GitHub repository https://github.com/rmdocherty/CPL-Imager.

Presently, the chiroptical response is characterised at a single excitation wavelength, but a tunable monochromatic light source would allow for measurements over a full spectral range. While we have presented this apparatus as a means to characterise the CP absorbance (i.e., CD measurements), with appropriate filters, spatially resolved CP luminescence could also be acquired (as demonstrated by Baguenard *et al.* [186]), making this instrument an "all-in-one" portable chiroptical probe.

This instrument continues to be under active development, with new features being added regularly. We anticipate being able to improve the sensitivity of this system through the use of a compact, camera-mounted chamber for sample mounting to block stray light sources. We are also in the process of in-depth analysis of potential sources of noise in these measurements, such as light source stability and dark shot noise in our camera. In both cases, noise may be suppressed by using active temperature control, such as a water- or fan-cooled light source and a thermoelectrically cooled CMOS array camera. With these modifications and the use of microscope optics, we aim to improve the spatial resolution and sensitivity of this system to below 100 μm and 100 mdeg, respectively. The basic camera systems developed in this work lower the barriers to entry to studying chiroptical semiconductors, such as equipment cost, facility access, and instrumentation expertise. We hope that lowering these barriers will encourage other research groups to contribute to the exciting and rapidly growing field of chiral organic materials.

Chapter 7

Device Modelling and Time of Flight Mobility

7.1 Statement of Contribution

The TMO model was developed by Matthew D Ward based on prior work by Gilot *et al.*[85]

Spectroscopic ellipsometry data was provided by Bernhard Dörling of the Campoy-Quiles group and Dr. Jess Wade.

The Time of Flight (ToF) mobility setup was constructed and calibrated by Matthew D Ward and Dr. Xingyuan Shi.

Python-based control software for the ToF setup was developed by Matthew D Ward.

7.2 Motivation and Novelty

Since the beginning of this project, several organic photodetectors with selectivity in their response to CPL have been reported in the literature, but very few explore the structure-function relationship between device architecture and the reported value of g_{ph} beyond simple

heuristic models (including my own studies). A deeper understanding of this structure-function relationship is required for devices that show larger values g_{ph} relative to their g_{abs} values as this mechanism remains, for the most part, unclear. Furthermore, it remains unknown why, in several cases, the reported value of g_{ph} appears to increase significantly under bias.

Taking our own studies in aggregate with those reported in the literature, it appears that there may be selectivity in the transport of polarons excited by L- or R-CPL in CP-selective photodetectors. This is evidenced by enhancement in g_{ph} under reverse bias for photodiode architectures and the fact that lateral device structures, such as phototransistors and photoconductors, show a far greater enhancement of g_{ph} relative to the g_{abs} of the chiroptical layer, relative to vertical device structures (i.e., photodiodes, see Table 2.2). The latter point is particularly important as lateral device structures have far greater polaron transit lengths ($L \gtrsim 1\ \mu m$) relative to vertical photodiode structures ($L \gtrsim 100\ nm$) and therefore any CP-selective transport properties could be expected to be greater for lateral device structures relative to vertical device structures.

Several studies have attempted to map the structure of the device of a given photodetector to the reported value of g_{ph} using the TMO method; however, this approach does not address the possibility of CP selective charge transport. This chapter represents a brief summary of an ongoing study, in which we use the F8T2 photodiode as a test bed to establish whether TMO alone is an adequate model to determine the g_{ph} value of a photodiode under zero bias and reverse bias conditions. We also explore whether there are measurable differences in the mobility of holes photogenerated by L-CPL and R-CPL using ToF mobility measurements. To the best of our knowledge, this represents the first study of CP-dependent mobility using the ToF mobility method.

7.3 Introduction

In our previous studies of the planar F8T2:[P/M]-aza[6]H photodiode, we proposed a heuristic two-part model to explain the enhancement of g_{ph} when the thickness of the achiral C_{60} layer is decreased and when the chiral F8T2:[P/M]-aza[6]H thickness is increased. In this chapter,

we attempt to understand the behaviour of this device architecture more rigorously by using a TMO approach similar to that employed by Gilot *et al.* in their study of CP selective planar photodiodes.[85]

Here we show that TMO modelling is a sufficient model to explain the relationship between device performance and the thickness of the chiral F8T2:[*P/M*]-aza[6]H donor layer. On the other hand, studies of variable C_{60} thickness by the same method leads to a conflict with the experimental data, with models using greater thicknesses of C_{60} appearing to show higher g_{ph} values. These findings suggest that TMO alone is not a sufficient model to relate the architecture of the device to its CP selectivity.

To address the shortcomings of the TMO model, we investigate the possibility of selective transport of charges excited by L-CPL and R-CPL in the chiral F8T2:[*P/M*]-aza[6]H donor layer. This is studied using the ToF mobility method. To the best knowledge of the author, this represents the first study of CPL selective charge transport using the ToF method. By this method, we show that the transport of charges in this layer is highly dispersive, with a minimum estimated mobility of $\approx 0.3\ cm^2V^{-1}s^{-1}$. No evidence of CP selective hole transport is found by this method.

7.4 Results and Discussion

In order to generate a TMO simulation of the F8T2:[*P/M*]-aza[6]H photodiode, the complex refractive index of the device layers was measured by ellipsometry. The values of n and k for the constituent device layers are shown in Figure 7.1. The values of k for the F8T2:[*P*]-aza[6]H are converted to k_L and k_R using Equations 2.104 and 2.105, respectively. To test the circularly polarised TMO approach against our experimental observations, we prepared a CP-TMO model of our ITO/PEDOT:PSS/F8T2:[*P*]-aza[6]H/C_{60}/Al photodiode architecture, with layer thicknesses to match our devices prepared in Chapter 5.

In the interpretation of these TMO models, we assume that only those excitons generated (and thus the optical power, Q, absorbed) within a diffusion length of the donor-acceptor interface

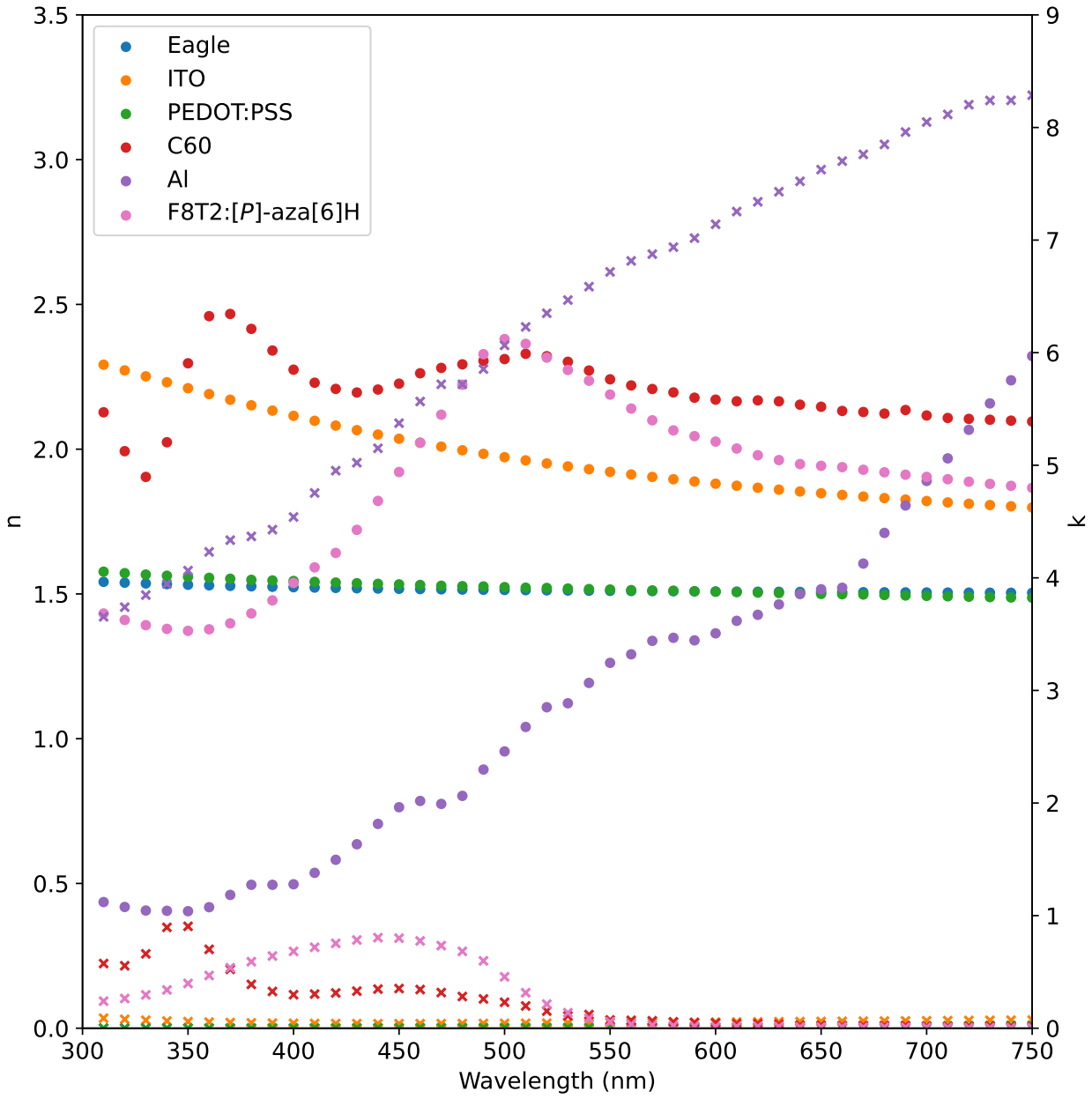


Figure 7.1: Real (n, filled circles) and imaginary (k, crosses) components of the complex refractive indices of the device layers in a ITO/PEDOT:PSS/F8T2:[P]-aza[6]H/C_{60}/Al photodiode.

can contribute to the measured device photocurrent. For C_{60}, diffusion lengths of 30-40 nm are widely reported.[75] As such, we assume that all excitons generated in the C_{60} layer contribute to the measured device photocurrent. For the F8T2 blend layer, we assume a diffusion length of $\leq$8 nm based on 8 nm diffusion lengths reported in the literature for F8T2.[75] Finally, we assume that the g_{ph} of a given device architecture correlates to the optical power absorbed under L- and R-CPL normalised for average power absorption (i.e. $g_Q = 2(Q_L - Q_R)/(Q_L + Q_R)$).

To investigate the influence of the thickness of the F8T2 blend layer on device performance, we studied theoretical power absorption in our photodiode architecture using a fixed C_{60} thicknesses of 30 nm and F8T2 thicknesses that correspond to those used in Figure 5.2 (77, 81, 87, 92, 110, and 140 nm). The results of excitation under L-CPL and R-CPL at 470 nm (corresponding to one of the g_{ph} peaks) are shown for the F8T2 blends in Figure 7.2. For clarity, only C_{60} thicknesses of 77 nm and 140 nm are shown as they are representative of the trend observed for the complete device series.

As shown, interference between forward and rearward travelling electric fields has a significant impact on the location and intensity of power absorption in the F8T2 blend and C_{60} layers as shown by the oscillatory behaviour of $|E|^2$ and the change in the location of maxima and minima of the electric field when the thickness of the F8T2 blend is varied. As the thickness of the F8T2 blend layer increases, the optical power absorbed ($Q(x)$) at the donor-acceptor interface decreases. This is consistent with experimental observations of decreased EQE with increasing thickness of the F8T2 blend layer. The difference in absorbed power under L- and R-CPL normalised for average power absorption (i.e., $g_Q = 2(Q_L - Q_R)/(Q_L + Q_R)$) has the opposite sign relative to the CD of the F8T2:[P]-aza[6]H layer. This suggests that, consistent with our previous study, the F8T2 blend acts as a CP-selective filter layer, filtering out the preferentially absorbed handedness of CPL far from the donor-acceptor interface, with the weakly absorbed handedness dominating the device response. In addition, the magnitude of g_Q increases near the donor-acceptor interface with increasing thickness of the F8T2 blend layer. This corresponds to the larger value of g_{ph} observed experimentally as the thickness of the chiral donor layer increases.

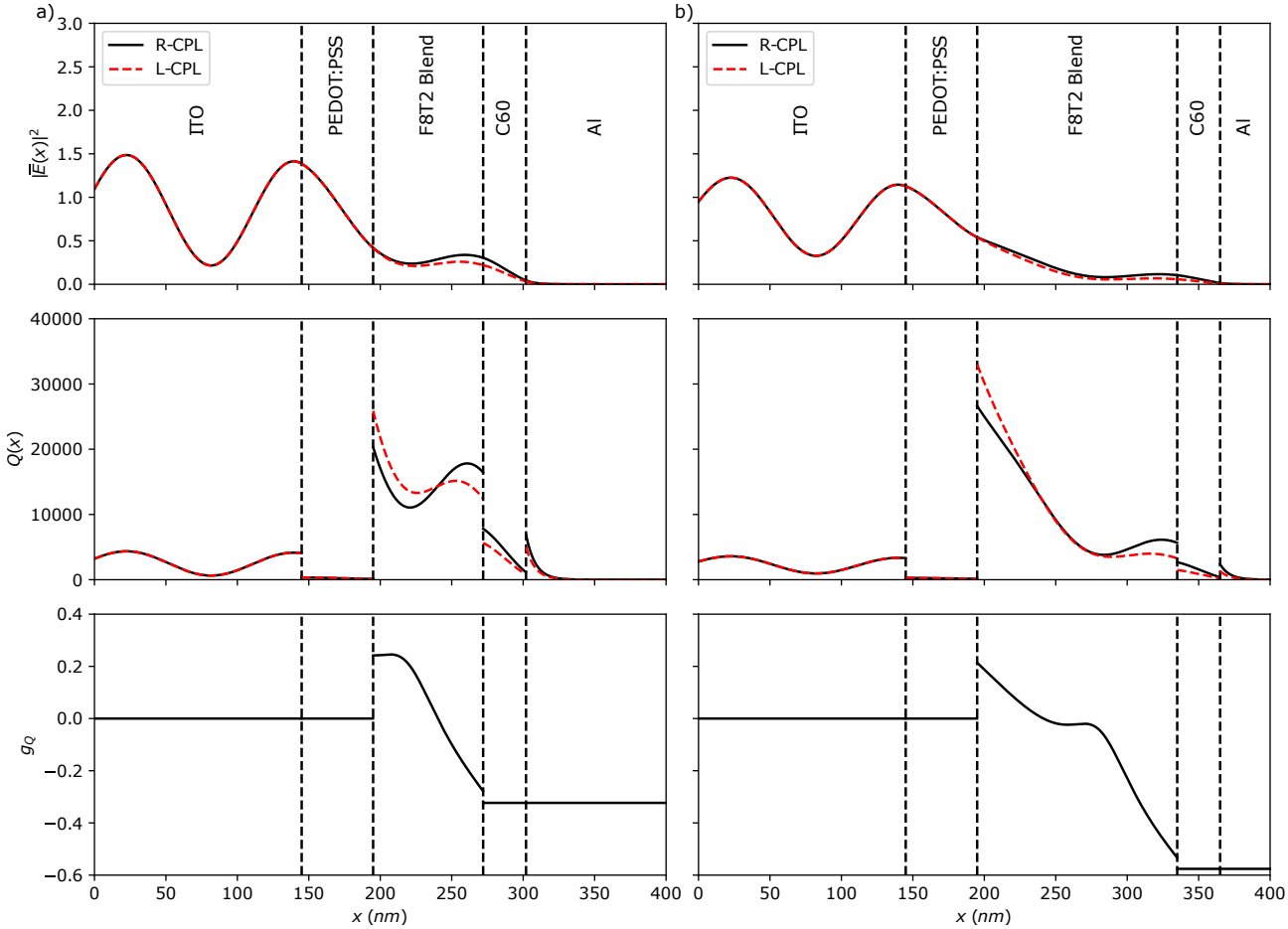


Figure 7.2: Transfer matrix optics model of an ITO/PEDOT:PSS/F8T2:[P]-aza[6]H/C_{60}/Al photodiode excited at a wavelength of 470 nm. Here a C_{60} thickness of 30 nm and F8T2:[P]-aza[6]H thicknesses of 77 nm (a) and 140 nm (b) are studied. $|E|^2$ is the intensity of the optical electric field, Q is the time-averaged absorption of optical power, and g_Q indicates the difference in time-averaged absorption of optical power under L- and R-CPL normalised by their average (i.e. $g_Q = 2(Q_L - Q_R)/(Q_L + Q_R)$).

To investigate the influence of the thickness of the C_{60} layer on device performance, we replicated the devices studied in Figure 5.4 using our TMO model (Figure 5.4). Here, we use a fixed thickness of 77 nm for the F8T2 blend layer and explore the same range of thicknesses of the C_{60} layer explored experimentally (10, 20, 30, 40, and 50 nm). For clarity, we include only the results for C_{60} thicknesses of 10 and 40 nm, since these results are representative of the larger data set. In this case, we also used an excitation wavelength of 510 nm, corresponding to the longer wavelength g_{ph} peak, which is most strongly affected by changes in the thickness of the C_{60} layer.

As shown in the TMO model, the integrated optical power absorbed in the C_{60} layer increases considerably when the thickness of the C_{60} layer increases from 10 to 40 nm. This is consistent with experimental observations of an increase in EQE as the thickness of C_{60} increases from 10 to 40 nm. g_Q is largely unchanged in the F8T2 blend at the donor-acceptor interface; however, the integrated g_Q in the C_{60} layer increases slightly as the thickness of C_{60} increases. This would imply that the g_{ph} value for these photodiodes should increase with increasing C_{60} thickness, but this is the opposite of what is observed experimentally. This suggests that TMO is an insufficient model to explain the behaviour of our CP OPDs and that other mechanisms excluded from the TMO must be taken into account.

One such mechanism studied further was the possibility of selective transport of charges generated by L- or R-CPL. To explore this possibility, a ToF mobility setup was constructed (see Section 3.3.4 for details). To benchmark the performance of this system, the ToF mobility of a glassy phase PFO sample was measured (Figure 7.4). As shown, the PFO sample shows the characteristic low dispersion ToF current profile, with a sharp rise associated with the arrival of the $\sim 5\ ns$ excitation pulse and initial photogeneration of excitons, followed by a plateau due to the transit of holes across the thickness of the device and finally, the so-called "knee point" which marks the extraction of holes at the opposing electrode. For this 1.8 μm device at a 10 V bias, we can extract a hole transit time of approximately 88 ns at room temperature. By Equation 2.106, this yields a ToF mobility of $3.7 \times 10^{-2}\ cm^2V^{-1}s^{-1}$, which is consistent with the mobility reported by Shi *et al.* for glassy PFO. [187]

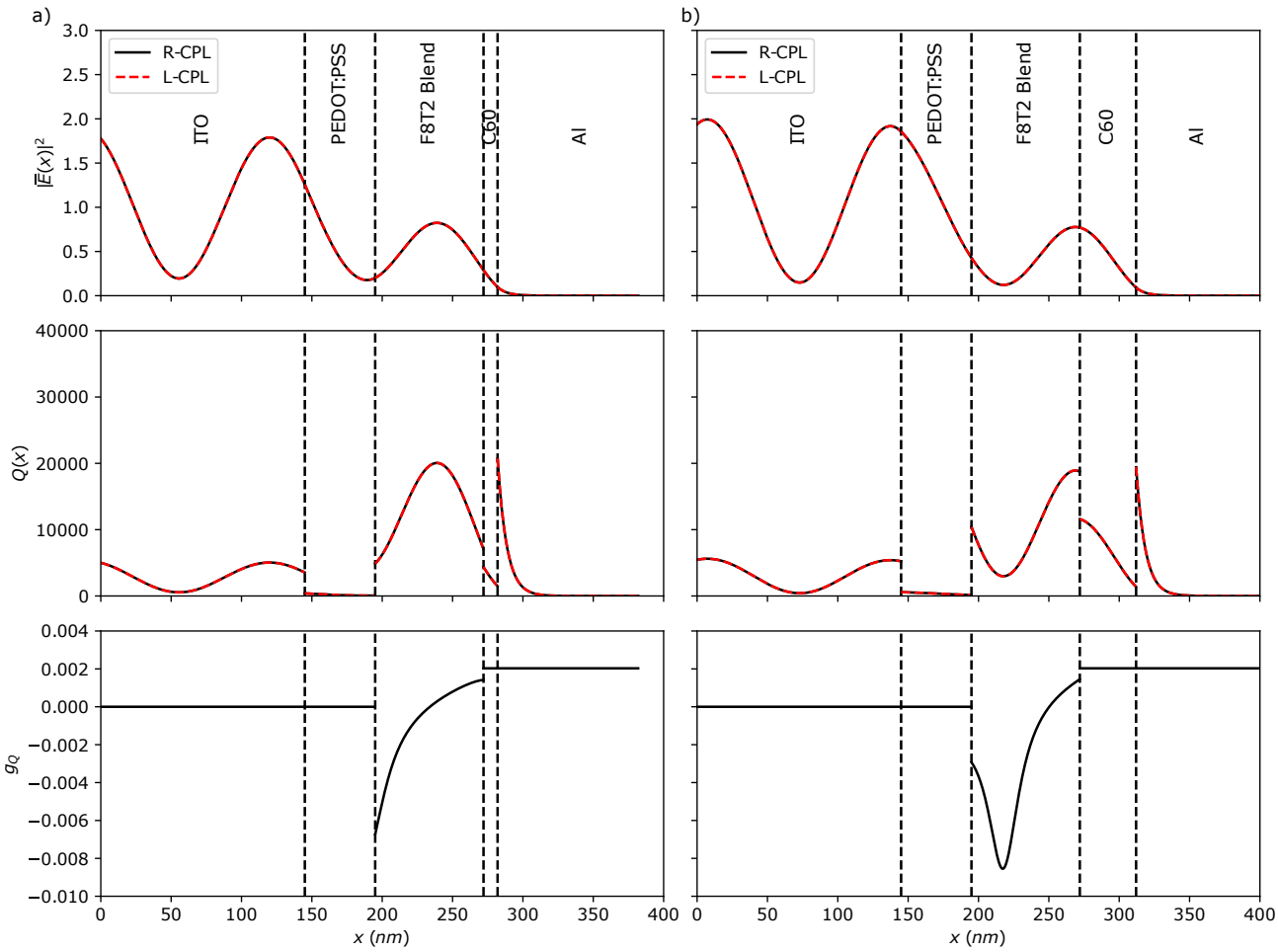


Figure 7.3: Transfer matrix optics model of an ITO/PEDOT:PSS/F8T2:[P]-aza[6]H/C_{60}/Al photodiode excited at a wavelength of 510 nm. Here a F8T2:[P]-aza[6]H thickness of 77 nm and a C_{60} acceptor layer thickness of 10 nm and (a) and 40 nm (b) are studied. $|E|^2$ is the intensity of the optical electric field, Q is the time-averaged absorption of optical power, and g_Q indicates the difference in time-averaged absorption of optical power under L- and R-CPL normalised by their average (i.e. $g_Q = 2(Q_L - Q_R)/(Q_L + Q_R)$)

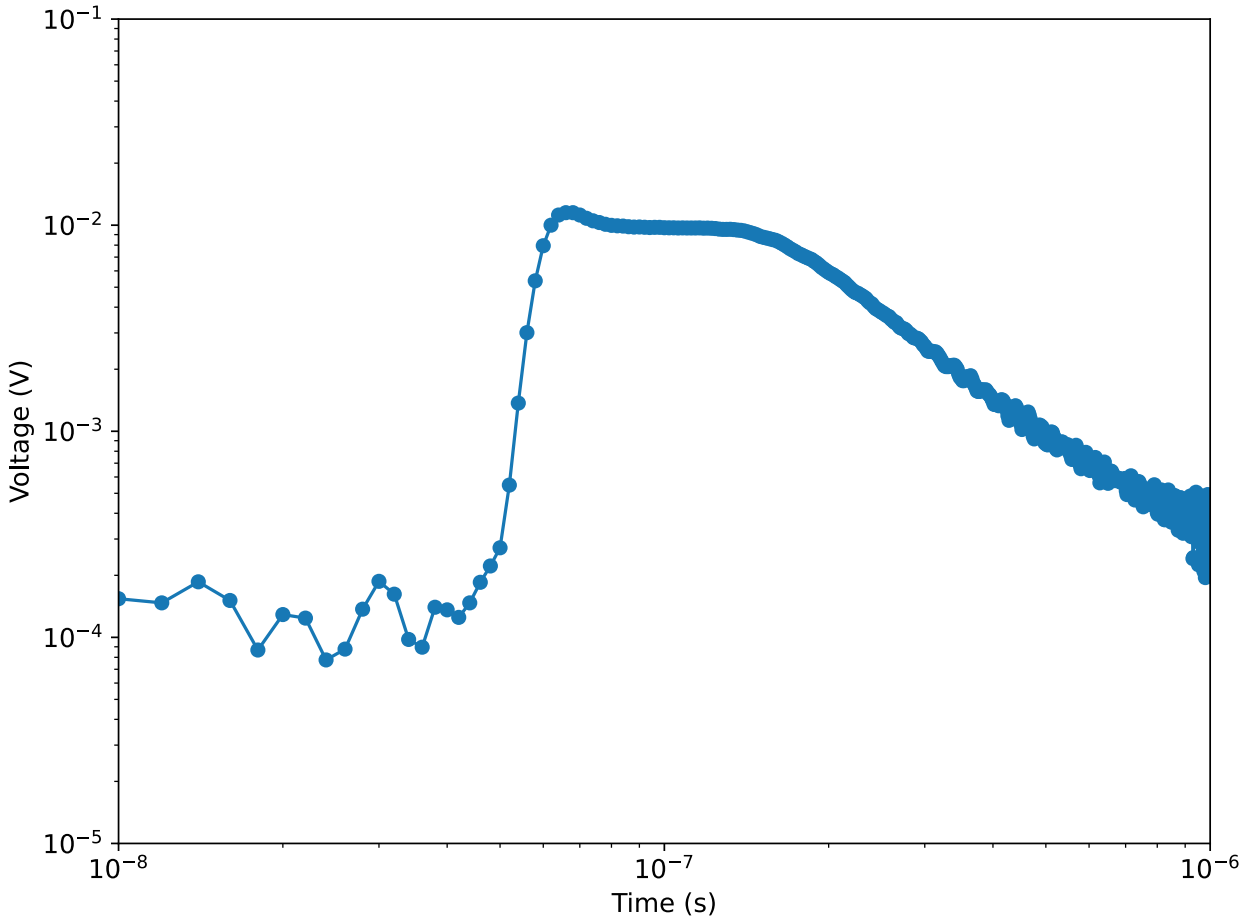


Figure 7.4: Time of flight mobility current transient for a glassy phase PFO sample with a thickness of 1.8 μm at a bias of 10 V.

Following the benchmarking of the ToF setup using Glassy PFO, $2.131 \pm 0.045\ \mu m$ thick samples of F8T2:[M]-aza[6]H were prepared for study. The ToF transients of these devices under unpolarised and CP excitation are shown in Figure 7.5. As shown by the unpolarised ToF transients (Figure 7.5a), charge transport in F8T2:[M]-aza[6]H appears to be highly dispersive, without a clear knee point indicating the time of charge extraction. This prevents a straightforward calculation of the mobility of holes within this layer; however, an upper bound of mobility may be estimated using the falling edge of the Time of Flight (ToF) transient curve. Using an upper bound to the transit time of 13.8 ns, this results in a minimum ToF mobility of $\approx 0.3\ cm^2V^{-1}s^{-1}$ at a bias of 10 V. This lower bound mobility is an order of magnitude higher than previously reported values for neat F8T2 films ($0.001 - 0.01\ cm^2V^{-1}s^{-1}$).[108] Due to the difficulties in identifying the knee points in these transients, we propose that this mobility should be verified using a second method, which also makes use of optically excited carriers, such as photoCELIV.[188]

Circularly polarised ToF transients (Figure 7.5b) also suffer from highly dispersive transport, making the determination of the hole transit time a challenge. It is also clear from the L- and R-CPL transients at the same bias voltage that, aside from differences in the amplitude of ToF transients arising from g_{abs}, there appears to be no significant difference in the rate of charge extraction under L-CPL and R-CPL. Using the same lower bound estimation method, we obtain a minimum mobility of $\approx 0.3\ cm^2V^{-1}s^{-1}$ at a bias of 10 V for both L- and R-CPL excitation, displaying no significant difference from the unpolarised case.

7.5 Conclusion

In this work, we attempt to develop a transfer matrix optics model of our previously published CP OPDs which make use of F8T2:[P/M]-aza[6]H blends as our chiral donor layer and thermally evaporated C_{60} as our acceptor layer. Predictions from this model suggest that F8T2:[P/M]-aza[6]H acts as a CPL filter, with the strongly absorbed handedness of CPL being "filtered out" far from the donor-acceptor interface. This leads to an inversion of g_{ph} relative to g_{abs}, with the

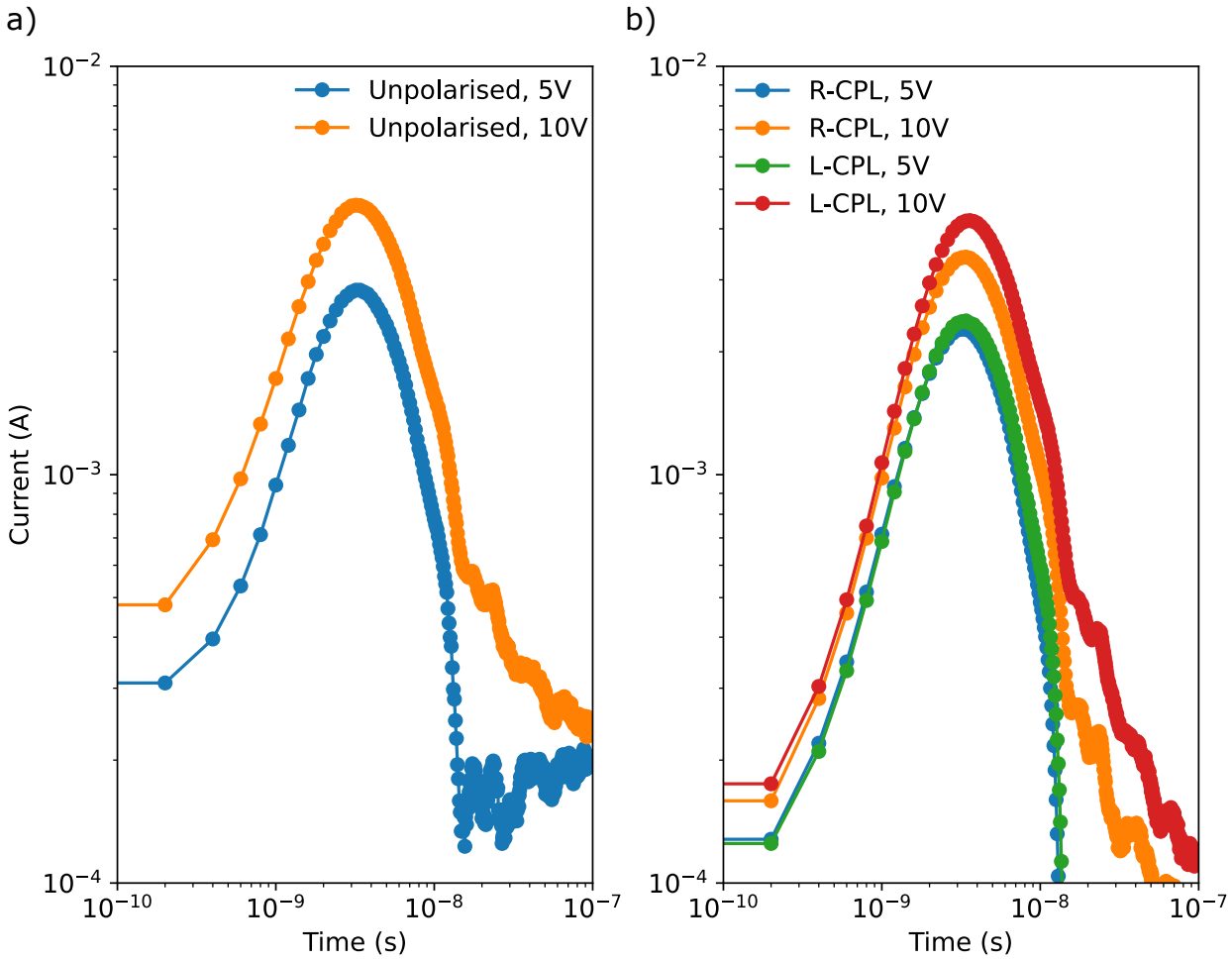


Figure 7.5: Time of flight mobility transients of 2.131 ± 0.045 μm thick samples of F8T2:[M]-aza[6]H measured using unpolarised (a) and circularly polarised (b) excitation at 470 nm under 5 and 10V biases

value of g_{ph} increasing with the thickness of the F8T2:[P/M]-aza[6]H filter/donor layer. This is consistent with our experimental data on the effect of varying the thickness of the chiral donor layer on device performance in Chapter 5.

Our transfer matrix model also suggests that *both* EQE and g_{ph} for a device with a 77 nm chiral F8T2:[P/M]-aza[6]H filter/donor layer should increase with the thickness of the C_{60} layer up to 40 nm. This is in conflict with our experimental observations, which show an increase in EQE and a decrease in g_{ph} as the thickness of C_{60} increases from 10 to 40 nm. This suggests that our TMO model alone is insufficient to explain the behaviour of our F8T2:[P/M]-aza[6]H based photodiode.

To explore other mechanisms that influence CP selective device behaviour, we investigated the possibility of the selective transport of charges generated by L- and R-CPL using the ToF mobility method. Measurements of unpolarised ToF transients of 2.131 ± 0.045 μm thick F8T2:[M]-aza[6]H samples show highly dispersive transport, with a lower bound room temperature mobility of ≈ 0.3 $cm^2V^{-1}s^{-1}$. ToF transients measured under L- and R-CPL do not show a significant difference in their charge transport profile, suggesting that there is no selective transport of charges excited by L-CPL or R-CPL.

Chapter 8

Conclusion

8.1 Summary of PhD Work

The goal of this thesis was to develop novel organic photodetector architectures to better understand the structure-function relationship between the device architecture and the CP selectivity of chiral organic photodetectors. The achievements of this PhD, broken down into its constituent chapters, are provided below.

In Chapter 4, we demonstrated the first chiral fullerene phototransistor capable of a selective photoresponse to CPL. These devices show considerable photocurrent dissymmetry, with g_{ph} values as high as 1.27 ± 0.06. The objective of this chapter was to explore the mechanism responsible for the significant enhancement of g_{ph} relative to g_{abs} in these devices that has been previously reported in the literature for the CP photoFET architecture. To this end, we developed a model based on the photoinduced threshold shift experienced by phototransistors on exposure to light. Under this model's prediction, at gate voltages close to the threshold voltage for unpolarised illumination, the transistor transitions to the "on" state for one handedness of CPL and transitions to the "off" state for the opposing handedness, leading to significantly enhanced g_{ph} at gate voltages close to the threshold voltage. This model is consistent with experimental data for the reported fullerene photoFET devices.

In Chapter 5, our attention is turned to the structure-function relationship of a planar photodiode architecture making use of a chiral blend donor (F8T2:[P/M]-aza[6]H) and an achiral C_{60} acceptor. In this work, we demonstrate that large g_{ph} values can be achieved by using thick layers of the chiral donor to filter out one handedness of CPL far from the donor-acceptor interface, while sacrificing conventional device properties such as EQE in the process. We also encountered the surprising result that decreasing the thickness of the achiral C_{60} acceptor below its diffusion length resulted in an expected loss of EQE, but an unexpected increase in g_{ph}. This study indicated that both chiral and achiral layers must be optimised in a device to balance conventional photodetector figures of merit with those specific to CPL discrimination. This led to the fabrication of optimised CP selective organic photodiodes with the fastest response times reported to date ($\approx 7\ \mu s$) while also retaining a highly selective response to CPL ($g_{ph} > 0.1$).

In Chapter 6 we address the difficulty in identifying suitable candidate materials for CP selective photodetectors by developing two CD imaging systems. These imaging systems enable spatial mapping of chiral materials with a spatial resolution of 100 μm and a CD resolution of up to 250 mdeg. By enabling real-time imaging of chiral samples, these systems allow processing conditions such as thermal annealing to be optimised for candidate chiral semiconductors *in situ*, significantly accelerating the turnaround for the testing of novel chiral semiconductors in photodetector architectures.

In Chapter 7, we attempt to more rigorously model the behaviour of [P/M]-aza[6]H blends/C_{60} based planar heterojunction photodiodes using transfer matrix optics. While the empirical dependence of g_{ph} on the thickness of the chiral F8T2:[P/M]-aza[6]H donor layer is replicated by this model, the influence of C_{60} thickness on the CP selectivity of the device conflicts with the experimental data. This suggested that TMO alone is an incomplete model of device behaviour. To explore other possible CP selective device mechanisms leading to disparity between experimental data and our TMO model, we made use of the ToF mobility method to probe for selective transport of holes excited by L- and R-CPL in F8T2:[M]-aza[6]H blends. Due to the dispersive nature of hole transport in F8T2:[M]-aza[6]H, only a lower bound of $\approx 0.3\ cm^2V^{-1}s^{-1}$ can be placed on the mobility of holes in this layer. No evidence of selective

transport of holes excited by L-CPL or R-CPL is found from ToF studies, suggesting that CP selective charge transport is not a contributing factor to CP selectivity in our in F8T2:[*P/M*]-aza[6]H based photodiodes.

8.2 Future Work

Based on the outcomes of the exprimental chapters of this thesis, we propose the following studies to further develop a more rigorous understanding of the mechanisms of CP selective photodetection in chiral organic photodetectors.

1. In Chapter 5, we propose that a significant factor that leads to the enhancement of g_{ph} as the thickness of C_{60} decreases is the increased reflection of CPL back to the chiral F8T2:[*P/M*]-aza[6]H donor layer. To further verify this, we propose a follow-up study using the same photodiode architecture in which the thickness of the reflective aluminium back contact is decreased until this layer becomes semi-transparent. In doing so, the back reflection of CPL to the chiral donor layer may be suppressed, allowing this model to be further verified.

2. In Chapter 5, we study a conventional organic photodiode architecture that demonstrates inversion of g_{ph} relative to the g_{abs} value of the chiral donor used in this device. Prior studies of CP *emmissive* OLEDs by Wan *et al.* demonstrate an inversion of CPL emission handedness when the device architecture is changed from a conventional to an inverted architecture. It would be of great interest to explore inverted photodiode structures based on F8T2:[*P/M*]-aza[6]H/C_{60} architecture to probe for similar inversion in the selective *detection* of CPL.

3. In Chapter 5 we propose that one factor leading to the enhancement of g_{ph} relative to g_{abs} may be a selective dissociation efficiency for excitons excited using L-CPL and R-CPL. If present, the selectivity of this dissociation may also be enhanced under reverse bias, which may explain the increase in g_{ph} with increasing reverse bias. We propose the approach of

circularly polarised photoluminesence quenching using a C_{60} acceptor layer under voltage bias to probe for CP selective exciton dissociation in this system.

4. Our studies of ToF mobility in Chapter 7 demonstrate that charge transport in F8T2:[M]-aza[6]H blend films is highly dispersive, preventing reliable transit times from being determined from ToF transients. Despite this, we estimate a lower bound mobility of $\approx 0.3\ cm^2V^{-1}s^{-1}$, which is considerably higher than that reported in the literature for neat F8T2 films. We propose that this lower bound hole mobility should be verified using a second method that makes use of photogenerated charges, such as photo-CELIV.

Bibliography

[1] Jochen R. Brandt, Francesco Salerno, and Matthew J. Fuchter. The added value of small-molecule chirality in technological applications. *Nature Reviews Chemistry 2017 1:6*, 1(6):1–12, 6 2017.

[2] Wikimedia Commons. File:circular.polarization.circularly.polarized.light circular.polarizer creating.left.handed.helix.view.svg — wikimedia commons, the free media repository, 2022. [Online; accessed 24-April-2023].

[3] Wikimedia Commons. File:fresnel rhomb linear to elliptical.svg — wikimedia commons, the free media repository, 2022. [Online; accessed 11-May-2024].

[4] Wikimedia Commons. File:electric vectors 1.png — wikimedia commons, the free media repository, 2020. [Online; accessed 24-April-2023].

[5] Hiroki Tanaka, Mina Ikenosako, Yuka Kato, Michiya Fujiki, Yoshihisa Inoue, and Tadashi Mori. Symmetry-based rational design for boosting chiroptical responses. *Communications Chemistry*, 1(1):38, Jul 2018.

[6] Jake L. Greenfield, Jessica Wade, Jochen R. Brandt, Xingyuan Shi, Thomas J. Penfold, and Matthew J. Fuchter. Pathways to increase the dissymmetry in the interaction of chiral light and chiral molecules. *Chemical Science*, 12(25):8589–8602, 7 2021.

[7] Matthew D. Ward, Wenda Shi, Nicola Gasparini, Jenny Nelson, Jessica Wade, and Matthew J. Fuchter. Best practices in the measurement of circularly polarised photodetectors. *J. Mater. Chem. C*, 10:10452–10463, 2022.

[8] Heinz Bässler Anna Köhler. *Fundamentals of Organic Semiconductor Devices*, chapter 4, pages 307–388. John Wiley & Sons, Ltd, 2015.

[9] Peter Peumans, Aharon Yakimov, and Stephen R. Forrest. Small molecular weight organic thin-film photodetectors and solar cells. *Journal of Applied Physics*, 93(7):3693–3723, 4 2003.

[10] W. E. Spear. Drift mobility techniques for the study of electrical transport properties in insulating solids. *Journal of Non-Crystalline Solids*, 1(3):197–214, 4 1969.

[11] Wenda Shi, Francesco Salerno, Matthew D. Ward, Alejandro Santana-Bonilla, Jessica Wade, Xueyan Hou, Tong Liu, T. John S. Dennis, Alasdair J. Campbell, Kim E. Jelfs, and Matthew J. Fuchter. Fullerene Desymmetrization as a Means to Achieve Single-Enantiomer Electron Acceptors with Maximized Chiroptical Responsiveness. *Advanced Materials*, 33(1):2004115, 1 2021.

[12] Carlo Thilgen and François Diederich. Structural aspects of fullerene chemistrya journey through fullerene chirality. *Chemical Reviews*, 106(12):5049–5135, 2006. PMID: 17165683.

[13] Jessica Wade, James N. Hilfiker, Jochen R. Brandt, Letizia Liirò-Peluso, Li Wan, Xingyuan Shi, Francesco Salerno, Seán T.J. Ryan, Stefan Schöche, Oriol Arteaga, Tamás Jávorfi, Giuliano Siligardi, Cheng Wang, David B. Amabilino, Peter H. Beton, Alasdair J. Campbell, and Matthew J. Fuchter. Natural optical activity as the origin of the large chiroptical properties in π-conjugated polymer thin films. *Nature Communications 2020 11:1*, 11(1):1–11, 12 2020.

[14] Matthias Schulz, Jennifer Zablocki, Oliya S. Abdullaeva, Stefanie Brück, Frank Balzer, Arne Lützen, Oriol Arteaga, and Manuela Schiek. Giant intrinsic circular dichroism of prolinol-derived squaraine thin films. *Nature Communications*, 9(1):2413, 12 2018.

[15] Jessica Wade, James N. Hilfiker, Jochen R. Brandt, Letizia Liirò-Peluso, Li Wan, Xingyuan Shi, Francesco Salerno, Seán T. J. Ryan, Stefan Schöche, Oriol Arteaga, Tamás Jávorfi, Giuliano Siligardi, Cheng Wang, David B. Amabilino, Peter H. Beton, Alasdair J. Campbell, and Matthew J. Fuchter. Natural optical activity as the origin of the

large chiroptical properties in π-conjugated polymer thin films. *Nature Communications*, 11(1):6137, 2020.

[16] G A Chamberlain. Organic solar cells: A review. *Solar Cells*, 8(1):47–83, 1983.

[17] Amal K Ghosh and Tom Feng. Rectification, space-charge-limited current, photovoltaic and photoconductive properties of Al/tetracene/Au sandwich cell. *Journal of Applied Physics*, 44(6):2781–2788, 1973.

[18] N S Sariciftci, D Braun, C Zhang, V I Srdanov, A J Heeger, G Stucky, and F Wudl. Semiconducting polymer-buckminsterfullerene heterojunctions: Diodes, photodiodes, and photovoltaic cells. *Applied Physics Letters*, 62(6):585–587, 1993.

[19] G Yu, J Gao, J C Hummelen, F Wudl, and A J Heeger. Polymer Photovoltaic Cells: Enhanced Efficiencies via a Network of Internal Donor-Acceptor Heterojunctions. *Science*, 270(5243):1789–1791, 1995.

[20] Lei Zhu, Ming Zhang, Jinqiu Xu, Chao Li, Jun Yan, Guanqing Zhou, Wenkai Zhong, Tianyu Hao, Jiali Song, Xiaonan Xue, Zichun Zhou, Rui Zeng, Haiming Zhu, Chun Chao Chen, Roderick C.I. MacKenzie, Yecheng Zou, Jenny Nelson, Yongming Zhang, Yanming Sun, and Feng Liu. Single-junction organic solar cells with over 19% efficiency enabled by a refined double-fibril network morphology. *Nature Materials 2022 21:6*, 21(6):656–663, 5 2022.

[21] Meyer Burger. Solar modules from Meyer Burger Technology. `https://www.meyerburger.com/en/solar-module`, 2023.

[22] Heliatek. Heliatek Pilot Projects. `https://www.heliatek.com/en/references/`, 2023.

[23] Kang-Jun Baeg, Maddalena Binda, Dario Natali, Mario Caironi, and Yong-Young Noh. Organic Light Detectors: Photodiodes and Phototransistors. *Advanced Materials*, 25(31):4267–4295, 8 2013.

[24] Ross D. Jansen-van Vuuren, Ardalan Armin, Ajay K. Pandey, Paul L. Burn, and Paul Meredith. Organic Photodiodes: The Future of Full Color Detection and Image Sensing. *Advanced Materials*, 28(24):4766–4802, 6 2016.

[25] Hossein Anabestani, Seyedfakhreddin Nabavi, and Sharmistha Bhadra. Advances in flexible organic photodetectors: Materials and applications. *Nanomaterials*, 12(21), 2022.

[26] Yan-Cheng Lin, Wei-Chen Yang, Yun-Chi Chiang, and Wen-Chang Chen. Recent advances in organic phototransistors: Nonvolatile memory, artificial synapses, and photodetectors. *Small Science*, 2(4):2100109, 2022.

[27] Hao Ren, Jing-De Chen, Yan-Qing Li, and Jian-Xin Tang. Recent progress in organic photodetectors and their applications. *Advanced Science*, 8(1):2002418, 2021.

[28] Kyu Bo Cho, Chang Mok Shin, Dong Hoan Seo, Sang Gug Park, Yang Hoi Doh, and Soo Joong Kim. Optical encryption system based on circular polarization and interferometer. *Pacific Rim Conference on Lasers and Electro-Optics, CLEO - Technical Digest*, 2:425, 2003.

[29] R. Farshchi, M. Ramsteiner, J. Herfort, A. Tahraoui, and H. T. Grahn. Optical communication of spin information between light emitting diodes. *Applied Physics Letters*, 98(16):162508, 4 2011.

[30] Noah A. Rubin, Gabriele D'Aversa, Paul Chevalier, Zhujun Shi, Wei Ting Chen, and Federico Capasso. Matrix fourier optics enables a compact full-stokes polarization camera. *Science*, 365(6448):eaax1839, 2019.

[31] Etienne Rochat, Michael C. Parker, and Stuart D. Walker. Polarisation and wavelength division multiplexing at 1.55μm for bandwidth enhancement of multimode fibre based access networks. *Optics Express*, 12(10):2280–2292, 5 2004.

[32] Hakob Margaryan, Nelson Tabirian, Tigran Sargsyan, Petros Gasparyan, Nune Hakobyan, Valeri Abrahamyan, Hakob Chilingaryan, and David Pokhsraryan. Device for real-time measuring of circular dichroism at a specific wavelength. *Journal of the Optical Society of America B*, 36(5):D66–D69, 5 2019.

[33] Sara Peña-Gutiérrez, María Ballesta, and Santiago Royo. A full Stokes imaging polarimeter based on a consumer CMOS camera. In Ettore Stella, editor, *Multimodal Sensing: Technologies and Applications*, volume 11059, pages 288–295. International Society for Optics and Photonics, SPIE, 6 2019.

[34] Shih Schön Lin, Konstantin M. Yemelyanov, Edward N. Pugh, and Nader Engheta. Polarization enhanced visual surveillance techniques. In *Conference Proceeding - IEEE International Conference on Networking, Sensing and Control*, volume 1, pages 216–221, 2004.

[35] J. S. Tyo, M. P. Rowe, E. N. Pugh, and N. Engheta. Target detection in optically scattering media by polarization-difference imaging. *Applied Optics*, 35(11):1855–1870, 4 1996.

[36] Viktor V. Dremin, Dmytro Anin, Oleksii Sieryi, Mariia A. Borovkova, Juha Näpänkangas, Igor V. Meglinski, and Alexander V. Bykov. Imaging of early stage breast cancer with circularly polarized light. In *Proc. SPIE 11363, Tissue Optics and Photonics*. SPIE-Intl Soc Optical Eng, 4 2020.

[37] A. D. McNaught and A. Wilkinson. Chirality Definition. In *IUPAC Compendium of Chemical Terminology (the "Gold Book")*. Blackwell Scientific Publications, Oxford, 2nd edition, 1997.

[38] Li Wan, Jessica Wade, Xuhua Wang, Alasdair J. Campbell, and Matthew J. Fuchter. Engineering the sign of circularly polarized emission in achiral polymer – chiral small molecule blends as a function of blend ratio. *Journal of Materials Chemistry C*, 10(13):5168–5172, 3 2022.

[39] Agnieszka Szumna. Inherently chiral concave molecules—from synthesis to applications. *Chem. Soc. Rev.*, 39:4274–4285, 2010.

[40] Volker Böhmer, Dagmar Kraft, and Moniralsadat Tabatabai. Inherently chiral calixarenes. In J. Vicens, Z. Asfari, and J. M. Harrowfield, editors, *Calixarenes 50th Anniversary: Commemorative Issue*, pages 17–39. Springer Netherlands, Dordrecht, 1994.

[41] Yong-Bin Wang, Shao-Hua Xiang, and Bin Tan. *Introduction and Characteristics*, chapter 1, pages 1–12. John Wiley & Sons Ltd, 2021.

[42] Li Wan, Xingyuan Shi, Jessica Wade, Alasdair J Campbell, and Matthew J Fuchter. Strongly Circularly Polarized Crystalline and β-Phase Emission from Poly(9,9-dioctylfluorene)-Based Deep-Blue Light-Emitting Diodes. *Advanced Optical Materials*, n/a(n/a):2100066, 2021.

[43] Beth Rice, Luc M. LeBlanc, Alberto Otero-de-la Roza, Matthew J. Fuchter, Erin R. Johnson, Jenny Nelson, and Kim E. Jelfs. A computational exploration of the crystal energy and charge-carrier mobility landscapes of the chiral [6]helicene molecule. *Nanoscale*, 10:1865–1876, 2018.

[44] Ying Yang, Beth Rice, Xingyuan Shi, Jochen R. Brandt, Rosenildo Correa da Costa, Gordon J. Hedley, Detlef-M. Smilgies, Jarvist M. Frost, Ifor. D. W. Samuel, Alberto Otero-de-la Roza, Erin R. Johnson, Kim E. Jelfs, Jenny Nelson, Alasdair J. Campbell, and Matthew J. Fuchter. Emergent Properties of an Organic Semiconductor Driven by its Molecular Chirality. *ACS Nano*, 11(8):8329–8338, 8 2017.

[45] Ying Yang, Rosenildo Correa da Costa, Matthew J. Fuchter, and Alasdair J. Campbell. Circularly polarized light detection by a chiral organic semiconductor transistor. *Nature Photonics*, 7(8):634–638, 8 2013.

[46] Ying Yang, Rosenildo Correa da Costa, Detlef-M. Smilgies, Alasdair J. Campbell, and Matthew J. Fuchter. Induction of Circularly Polarized Electroluminescence from an Achiral Light-Emitting Polymer via a Chiral Small-Molecule Dopant. *Advanced Materials*, 25(18):2624–2628, 5 2013.

[47] Matthew D. Ward, Jessica Wade, Xingyuan Shi, Jenny Nelson, Alasdair J. Campbell, and Matthew J. Fuchter. Highly Selective High-Speed Circularly Polarized Photodiodes Based on π-Conjugated Polymers. *Advanced Optical Materials*, 10:2101044, 2022.

[48] Eugene Hecht. *Optics, Global Edition*, chapter 8. Polarization. Pearson Education, Limited, 5 edition, 2016.

[49] S. E. Braslavsky. Glossary of terms used in photochemistry, 3rd edition (iupac recommendations 2006). *Pure and Applied Chemistry*, 79(3):293–465, 2007.

[50] Edward Collett. *Field Guide to Polarization*, chapter The Polarization Ellipse. SPIE Press, 2005.

[51] Commission 40. Radio astronomy (radio astronomie). *Transactions of the International Astronomical Union*, 15(2):165–167, 1973.

[52] IEEE Antenna Standards Committee. Ieee standard test procedures for antennas. *ANSI/IEEE Std 149-1979*, pages 1–144, 1979.

[53] Applied Photophysics. Circular dichroism faqs. `https://www.photophysics.com/faqs/methods-techniques/circular-dichroism-faqs/`, 2023.

[54] S. Pancharatnam. Achromatic combinations of birefringent plates. *Proceedings of the Indian Academy of Sciences - Section A*, 41(4):130–136, Apr 1955.

[55] Jr W. Curtis Johnson. Circular dichroism instrumentation. In G.D. Fasman, editor, *Circular Dichroism and the Conformational Analysis of Biomolecules*, Siberian School of Algebra and Logic, pages 635–652. Springer US, 1996.

[56] N. Berova, K. Nakanishi, and R.W. Woody. Circular dichroism: An introduction. In *Circular Dichroism: Principles and Applications*. Wiley, 2000.

[57] Nina Berova, Lorenzo Di Bari, and Gennaro Pescitelli. Application of electronic circular dichroism in configurational and conformational analysis of organic compounds. *Chemical Society Reviews*, 36(6):914, 2007.

[58] B. Nordén, A. Rodger, and T. Dafforn. *Linear Dichroism and Circular Dichroism: A Textbook on Polarized-Light Spectroscopy*, chapter 10 Circular Dichroism Formalism. Royal Society of Chemistry, 2019.

[59] P. W. (Peter William) Atkins and R. S. Friedman. *Molecular quantum mechanics. / Peter Atkins and Ronald Friedman.* Oxford University Press, Oxford, 5th ed. edition, 2011.

[60] D.P. Craig and T. Thirunamachandran. *Molecular Quantum Electrodynamics: An Introduction to Radiation-molecule Interactions*. Dover Books on Chemistry Series. Dover Publications, 1998.

[61] Jessica Wade, Francesco Salerno, Rachel C. Kilbride, Dong Kuk Kim, Julia A. Schmidt, Joel A. Smith, Luc M. LeBlanc, Emma H. Wolpert, Adebayo A. Adeleke, Erin R. Johnson, Jenny Nelson, Tadashi Mori, Kim E. Jelfs, Sandrine Heutz, and Matthew J. Fuchter. Controlling anisotropic properties by manipulating the orientation of chiral small molecules. *Nature Chemistry*, 14(12):1383–1389, Dec 2022.

[62] B. Nordén, A. Rodger, and T. Dafforn. *Linear Dichroism and Circular Dichroism: A Textbook on Polarized-Light Spectroscopy*, chapter 4 Circular Dichroism of Biological Macromolecules. Royal Society of Chemistry, 2019.

[63] Nina Berova, Lorenzo Di Bari, and Gennaro Pescitelli. Application of electronic circular dichroism in configurational and conformational analysis of organic compounds. *Chemical Society Reviews*, 36(6):914–931, 2007.

[64] B. Nordén, A. Rodger, and T. Dafforn. *Linear Dichroism and Circular Dichroism: A Textbook on Polarized-Light Spectroscopy*, chapter 8 Analysis of Circular Dichroism: Electric Dipole Allowed Transitions. Royal Society of Chemistry, 2019.

[65] Kang-Jun Baeg, Maddalena Binda, Dario Natali, Mario Caironi, and Yong-Young Noh. Organic light detectors: Photodiodes and phototransistors. *Advanced Materials*, 25(31):4267–4295, 2013.

[66] Kwok K. Ng S.M. Sze. *Photodetectors and Solar Cells*, pages 663–742. John Wiley & Sons, Ltd, 2006.

[67] Jiaying Wu, Hyojung Cha, Tian Du, Yifan Dong, Weidong Xu, Chieh-Ting Lin, and James R. Durrant. A Comparison of Charge Carrier Dynamics in Organic and Perovskite Solar Cells. *Advanced Materials*, 34:2101833, 11 2022.

[68] Chao Chen, Liang Gao, Wanru Gao, Cong Ge, Xinyuan Du, Zha Li, Ying Yang, Guangda Niu, and Jiang Tang. Circularly polarized light detection using chiral hybrid perovskite. *Nature Communications*, 10(1):1927, 12 2019.

[69] Dong Li, Xitao Liu, Wentao Wu, Yu Peng, Sangen Zhao, Lina Li, Maochun Hong, and Junhua Luo. Chiral Lead-Free Hybrid Perovskites for Self-Powered Circularly Polarized Light Detection. *Angewandte Chemie International Edition*, 60(15):8415–8418, 4 2021.

[70] Lin Wang, Yongxiang Xue, Minghuan Cui, Yanmin Huang, Hongyu Xu, Chaochao Qin, Jien Yang, Haitao Dai, and Mingjian Yuan. A Chiral Reduced-Dimension Perovskite for an Efficient Flexible Circularly Polarized Light Photodetector. *Angewandte Chemie International Edition*, 59(16):6442–6450, 4 2020.

[71] Jiaqi Ma, Haizhen Wang, Dehui Li, J Ma, H Wang, and D Li. Recent Progress of Chiral Perovskites: Materials, Synthesis, and Properties. *Advanced Materials*, 33(26):2008785, 7 2021.

[72] A. Ishii and T. Miyasaka. Direct detection of circular polarized light in helical 1D perovskite-based photodiode. *Science Advances*, 6(46):3274–3285, 11 2020.

[73] Tianjun Liu, Wenda Shi, Weidong Tang, Zilu Liu, Bob C. Schroeder, Oliver Fenwick, and Matthew J. Fuchter. High Responsivity Circular Polarized Light Detectors based on Quasi Two-Dimensional Chiral Perovskite Films. *ACS Nano*, 16(2):2682–2689, 2 2022.

[74] Junjie Cheng, Feng Ge, Can Zhang, Yan Kuai, Penghui Hou, Yifeng Xiang, Douguo Zhang, Longzhen Qiu, Qijin Zhang, and Gang Zou. Enabling discrimination capability in an achiral F6BT-based organic semiconductor transistor ¡i¿via¡/i¿ circularly polarized light induction. *Journal of Materials Chemistry C*, 8(27):9271–9275, 7 2020.

[75] Oleksandr V. Mikhnenko, Paul W.M. Blom, and Thuc Quyen Nguyen. Exciton diffusion in organic semiconductors, 7 2015.

[76] Fawen Guo, Bin Yang, Yongbo Yuan, Zhengguo Xiao, Qingfeng Dong, Yu Bi, and Jinsong Huang. A nanocomposite ultraviolet photodetector based on interfacial trap-controlled charge injection. *Nature Nanotechnology*, 7(12):798–802, Dec 2012.

[77] Na Yeon Kim, Jihoon Kyhm, Hyemi Han, Soo Jin Kim, Jongtae Ahn, Do Kyung Hwang, Ho Won Jang, Byeong Kwon Ju, and Jung Ah Lim. Chiroptical-Conjugated Polymer/Chiral Small Molecule Hybrid Thin Films for Circularly Polarized Light-Detecting Heterojunction Devices. *Advanced Functional Materials*, 29(11):1808668, 3 2019.

[78] Yuliar Firdaus, Vincent M. Le Corre, Safakath Karuthedath, Wenlan Liu, Anastasia Markina, Wentao Huang, Shirsopratim Chattopadhyay, Masrur Morshed Nahid, Mohamad I. Nugraha, Yuanbao Lin, Akmaral Seitkhan, Aniruddha Basu, Weimin Zhang, Iain McCulloch, Harald Ade, John Labram, Frédéric Laquai, Denis Andrienko, L. Jan Anton Koster, and Thomas D. Anthopoulos. Long-range exciton diffusion in molecular non-fullerene acceptors. *Nature Communications*, 11(1):5220, 10 2020.

[79] Pei Cheng, Gang Li, Xiaowei Zhan, and Yang Yang. Next-generation organic photovoltaics based on non-fullerene acceptors. *Nature Photonics*, 12(3):131–142, 2 2018.

[80] Li Zhang, Inho Song, Jaeyong Ahn, Myeonggeun Han, Mathieu Linares, Mathieu Surin, Hui Jun Zhang, Joon Hak Oh, and Jianbin Lin. π-Extended perylene diimide double-heterohelicenes as ambipolar organic semiconductors for broadband circularly polarized light detection. *Nature Communications*, 12(1):142, 1 2021.

[81] Xiaobo Shang, Inho Song, Hiroyoshi Ohtsu, Yoon Ho Lee, Tianming Zhao, Tatsuhiro Kojima, Ji Hyung Jung, Masaki Kawano, and Joon Hak Oh. Supramolecular Nanostructures of Chiral Perylene Diimides with Amplified Chirality for High-Performance Chiroptical Sensing. *Advanced Materials*, 29(21):1605828, 6 2017.

[82] Joon Hak Oh, Sang Kyu Kwak, Xiaobo Shang, Inho Song, Jeong Hyeon Lee, Jaeyong Ahn, Jin Chul Kim, Wanuk Choi, Hiroyoshi Ohtsu, and Jin Young Koo. Surface-doped quasi-2d chiral organic single crystals for chiroptical sensing. *ACS Nano*, 14(10):14146–14156, 10 2020.

[83] Ji Hao, Haipeng Lu, Lingling Mao, Xihan Chen, Matthew C. Beard, and Jeffrey L. Blackburn. Direct Detection of Circularly Polarized Light Using Chiral Copper Chloride-Carbon Nanotube Heterostructures. *ACS Nano*, 15(4):7608–7617, 4 2021.

[84] Paul Grey, Susete N Fernandes, Diana Gaspar, Elvira Fortunato, Rodrigo Martins, Maria H Godinho, Luis Pereira, P Grey, S N Fernandes, D Gaspar, E Fortunato, R Martins, M H Godinho, and L Pereira. Field-Effect Transistors on Photonic Cellulose Nanocrystal Solid Electrolyte for Circular Polarized Light Sensing. *Advanced Functional Materials*, 29(21):1805279, 5 2019.

[85] Jan Gilot, Robert Abbel, Cirish Lakhwani, E. W. Meijer, Albertus P.H.J. Schenning, and Stefan C.J. Meskers. Polymer photovoltaic cells sensitive to the circular polarization of light. *Advanced Materials*, 22(20):E131–E134, 5 2010.

[86] Matthias Schulz, Frank Balzer, Dorothea Scheunemann, Oriol Arteaga, Arne Lützen, Stefan C. J. Meskers, and Manuela Schiek. Chiral Excitonic Organic Photodiodes for Direct Detection of Circular Polarized Light. *Advanced Functional Materials*, 29(16):1900684, 4 2019.

[87] Zhongxuan Wang, Mingsheng Gao, Xiaotao Hao, and Wei Qin. Helical-chiroptical nanowires generated orbital angular momentum for the detection of circularly polarized light. *Applied Physics Letters*, 116(5):053301, 2 2020.

[88] Jingying Wang, Haipeng Lu, Xin Pan, Junwei Xu, Haoliang Liu, Xiaojie Liu, Dipak R. Khanal, Michael F. Toney, Matthew C. Beard, and Z. Valy Vardeny. Spin-Dependent Photovoltaic and Photogalvanic Responses of Optoelectronic Devices Based on Chiral Two-Dimensional Hybrid Organic-Inorganic Perovskites. *ACS Nano*, 15(1):588–595, 1 2021.

[89] Xinyuan Zhang, Xitao Liu, Lina Li, Chengmin Ji, Yunpeng Yao, and Junhua Luo. Great Amplification of Circular Polarization Sensitivity via Heterostructure Engineering of a Chiral Two-Dimensional Hybrid Perovskite Crystal with a Three-Dimensional MAPbI3Crystal. *ACS Central Science*, 7(7):1261–1268, 7 2021.

[90] Jiaqi Ma, Chen Fang, Chao Chen, Long Jin, Jiaqi Wang, Shuai Wang, Jiang Tang, and Dehui Li. Chiral 2D Perovskites with a High Degree of Circularly Polarized Photoluminescence. *ACS Nano*, 13(3):3659–3665, 3 2019.

[91] Jun Wang, Chen Fang, Jiaqi Ma, Shuai Wang, Long Jin, Wancai Li, and Dehui Li. Aqueous Synthesis of Low-Dimensional Lead Halide Perovskites for Room-Temperature Circularly Polarized Light Emission and Detection. *ACS Nano*, 13(8):9473–9481, 8 2019.

[92] Yingjie Zhao, Yuchen Qiu, Jiangang Feng, Jiahui Zhao, Gaosong Chen, Hanfei Gao, Yuyan Zhao, Lei Jiang, and Yuchen Wu. Chiral 2D-Perovskite Nanowires for Stokes Photodetectors. *Journal of the American Chemical Society*, 143(22):8437–8445, 6 2021.

[93] Wei Li, Zachary J. Coppens, Lucas V. Besteiro, Wenyi Wang, Alexander O. Govorov, and Jason Valentine. Circularly polarized light detection with hot electrons in chiral plasmonic metamaterials. *Nature Communications*, 6(1):8379, 9 2015.

[94] Jingyang Peng, Benjamin P. Cumming, and Min Gu. Direct detection of photon spin angular momentum by a chiral graphene mid-infrared photodetector. *Optics Letters*, 44(12):2998–3001, 6 2019.

[95] Wang Xiao, Xiaoyi Shi, Yun Zhang, Wei Peng, and Yun Zeng. Circularly polarized light detector based on 2D embedded chiral nanostructures. *Physica Scripta*, 94(8):085501, 4 2019.

[96] Hyemi Han, Yoo Jin Lee, Jihoon Kyhm, Jae Seung Jeong, Jae Hoon Han, Min Kyu Yang, Kyung Min Lee, Yeongyu Choi, Tae Hoon Yoon, Hyunsu Ju, Suk kyun Ahn, and Jung Ah Lim. High-Performance Circularly Polarized Light-Sensing Near-Infrared Organic Phototransistors for Optoelectronic Cryptographic Primitives. *Advanced Functional Materials*, 30(52):2006236, 12 2020.

[97] Hongzhi Zheng, Bo Ju, Xiaojun Wang, Wenhui Wang, Minjie Li, Zhiyong Tang, Sean Xiao An Zhang, and Yan Xu. Circularly Polarized Luminescent Carbon Dot Nanomaterials of Helical Superstructures for Circularly Polarized Light Detection. *Advanced Optical Materials*, 6(23):1801246, 12 2018.

[98] Si photodiode S2386-18K — Hamamatsu Photonics.

[99] Xiong Gong, Minghong Tong, Yangjun Xia, Wanzhu Cai, Ji Sun Moon, Yong Cao, Gang Yu, Chan Long Shieh, Boo Nilsson, and Alan J. Heeger. High-detectivity polymer pho-

todetectors with spectral response from 300 nm to 1450 nm. *Science*, 325(5948):1665–1667, 9 2009.

[100] 45 GHz Fiber-Optic Detector.

[101] Chenglong Li, Hailu Wang, Fang Wang, Tengfei Li, Mengjian Xu, Hao Wang, Zhen Wang, Xiaowei Zhan, Weida Hu, and Liang Shen. Ultrafast and broadband photodetectors based on a perovskite/organic bulk heterojunction for large-dynamic-range imaging. *Light: Science & Applications*, 9(1):1–8, 3 2020.

[102] F N Hooge. 1/f noise sources. *IEEE Transactions on Electron Devices*, 41(11):1926–1935, 1994.

[103] Si PIN photodiode S8729 — Hamamatsu Photonics.

[104] Marcin Kielar, Olivier Dhez, Gilles Pecastaings, Arnaud Curutchet, and Lionel Hirsch. Long-Term Stable Organic Photodetectors with Ultra Low Dark Currents for High Detectivity Applications. *Scientific Reports*, 6(1):39201, 12 2016.

[105] Zhiping Wang, Qianqian Lin, Francis P. Chmiel, Nobuya Sakai, Laura M. Herz, and Henry J. Snaith. Efficient ambient-air-stable solar cells with 2D–3D heterostructured butylammonium-caesium-formamidinium lead halide perovskites. *Nature Energy*, 2(9):17135, 8 2017.

[106] Yun Huang, Hui Xiong Deng, Feng Wang, Kai Xu, Zhen Xing Wang, Qi Sheng Wang, Feng Mei Wang, Xue Ying Zhan, Shu Shen Li, Jun Wei Luo, and Jun He. Highly sensitive and fast phototransistor based on large size CVD-grown SnS2 nanosheets. *Nanoscale*, 7(33):14093–14099, 9 2015.

[107] Md Shofiqul Islam. Analytical modeling of organic solar cells including monomolecular recombination and carrier generation calculated by optical transfer matrix method. *Organic Electronics*, 41:143–156, 2 2017.

[108] Ruth Rawcliffe, Donal D.C. Bradley, and Alasdair J. Campbell. Comparative measurements of charge transport in semiconducting polymers and their devices. In Zakya H.

Kafafi and Paul A. Lane, editors, *Organic Light-Emitting Materials and Devices VIII*, volume 5519, pages 89 – 99. International Society for Optics and Photonics, SPIE, 2004.

[109] Ruth Rawcliffe, Donal D. C. Bradley, and Alasdair J. Campbell. Comparison between bulk and field effect mobility in polyfluorene copolymer field effect transistors. In Christos D. Dimitrakopoulos, editor, *Organic Field Effect Transistors II*, volume 5217, pages 25 – 34. International Society for Optics and Photonics, SPIE, 2003.

[110] R. Naaman and David H. Waldeck. Chiral-induced spin selectivity effect. *The Journal of Physical Chemistry Letters*, 3(16):2178–2187, 2012. PMID: 26295768.

[111] Ron Naaman and David H. Waldeck. Spintronics and chirality: Spin selectivity in electron transport through chiral molecules. In MA Johnson and TJ Martinez, editors, *ANNUAL REVIEW OF PHYSICAL CHEMISTRY, VOL 66*, volume 66 of *Annual Review of Physical Chemistry*, pages 263–281. Annual Reviews, 2015.

[112] Patrick Odenthal, William Talmadge, Nathan Gundlach, Ruizhi Wang, Chuang Zhang, Dali Sun, Zhi Gang Yu, Z. Valy Vardeny, and Yan S. Li. Spin-polarized exciton quantum beating in hybrid organic-inorganic perovskites. *Nature Physics*, 13(9):894–899, 9 2017.

[113] Daniel Niesner, Max Wilhelm, Ievgen Levchuk, Andres Osvet, Shreetu Shrestha, Miroslaw Batentschuk, Christoph Brabec, and Thomas Fauster. Giant Rashba Splitting in CH3NH3PbBr3 Organic-Inorganic Perovskite. *Physical Review Letters*, 117(12), 9 2016.

[114] Ron Naaman and David H. Waldeck. Spintronics and Chirality: Spin Selectivity in Electron Transport Through Chiral Molecules. *Annual Review of Physical Chemistry*, 66(1):263–281, 4 2015.

[115] Anna A. Szumska, Henning Sirringhaus, and Jenny Nelson. Symmetry based molecular design for triplet excitation and optical spin injection. *Physical Chemistry Chemical Physics*, 21(35):19521–19528, 2019.

[116] Shiheng Liang, Rugang Geng, Baishun Yang, Wenbo Zhao, Ram Chandra Subedi, Xiaoguang Li, Xiufeng Han, and Tho Duc Nguyen. Curvature-enhanced spin-orbit coupling

and spinterface effect in fullerene-based spin valves. *Scientific Reports*, 6(1):19461, Jan 2016.

[117] Daniel Huertas-Hernando, Francisco Guinea, and Arne Brataas. Spin-orbit coupling in curved graphene, fullerenes, nanotubes, and nanotube caps. *Physical Review B*, 74(15):155426, 2006.

[118] GA Steele, F Pei, EA Laird, JM Jol, HB Meerwaldt, and LP Kouwenhoven. Large spin-orbit coupling in carbon nanotubes. *Nature communications*, 4(1):1573, 2013.

[119] M. J. Frisch, G. W. Trucks, H. B. Schlegel, G. E. Scuseria, M. A. Robb, J. R. Cheeseman, G. Scalmani, V. Barone, G. A. Petersson, H. Nakatsuji, X. Li, M. Caricato, A. V. Marenich, J. Bloino, B. G. Janesko, R. Gomperts, B. Mennucci, H. P. Hratchian, J. V. Ortiz, A. F. Izmaylov, J. L. Sonnenberg, D. Williams-Young, F. Ding, F. Lipparini, F. Egidi, J. Goings, B. Peng, A. Petrone, T. Henderson, D. Ranasinghe, V. G. Zakrzewski, J. Gao, N. Rega, G. Zheng, W. Liang, M. Hada, M. Ehara, K. Toyota, R. Fukuda, J. Hasegawa, M. Ishida, T. Nakajima, Y. Honda, O. Kitao, H. Nakai, T. Vreven, K. Throssell, J. A. Montgomery, Jr., J. E. Peralta, F. Ogliaro, M. J. Bearpark, J. J. Heyd, E. N. Brothers, K. N. Kudin, V. N. Staroverov, T. A. Keith, R. Kobayashi, J. Normand, K. Raghavachari, A. P. Rendell, J. C. Burant, S. S. Iyengar, J. Tomasi, M. Cossi, J. M. Millam, M. Klene, C. Adamo, R. Cammi, J. W. Ochterski, R. L. Martin, K. Morokuma, O. Farkas, J. B. Foresman, and D. J. Fox. Gaussian˜16 Revision C.01, 2016. Gaussian Inc. Wallingford CT.

[120] Sebastian Mai, Felix Plasser, Johann Dorn, Maria Fumanal, Chantal Daniel, and Leticia González. Quantitative wave function analysis for excited states of transition metal complexes. *Coordination Chemistry Reviews*, 361:74–97, 2018.

[121] Stefanie A. Mewes, Jan-Michael Mewes, Andreas Dreuw, and Felix Plasser. Excitons in poly(para phenylene vinylene): a quantum-chemical perspective based on high-level ab initio calculations. *Phys. Chem. Chem. Phys.*, 18:2548–2563, 2016.

[122] F. Plasser. Theodore: A toolbox for a detailed and automated analysis of electronic excited state computations. *The Journal of Chemical Physics*, 152(8):084108, 2020.

[123] Gianluigi Albano, Gennaro Pescitelli, and Lorenzo Di Bari. Chiroptical Properties in Thin Films of π-Conjugated Systems. *Chemical Reviews*, 120(18):10145–10243, 9 2020.

[124] Guihua Yu, Jing Gao, Jan C Hummelen, Fred Wudl, and Alan J Heeger. Polymer photovoltaic cells: enhanced efficiencies via a network of internal donor-acceptor heterojunctions. *Science*, 270(5243):1789–1791, 1995.

[125] Alexander B. Sieval and Jan C. Hummelen. *Fullerene-Based Acceptor Materials*, chapter 7, pages 209–238. John Wiley & Sons, Ltd, 2014.

[126] Chien-Hung Chiang and Chun-Guey Wu. Bulk heterojunction perovskite–pcbm solar cells with high fill factor. *Nature Photonics*, 10(3):196–200, Mar 2016.

[127] Ramasamy Ganesamoorthy, Govindasamy Sathiyan, and Pachagounder Sakthivel. Review: Fullerene based acceptors for efficient bulk heterojunction organic solar cell applications. *Solar Energy Materials and Solar Cells*, 161:102–148, 2017.

[128] Zheng Tang, Zaifei Ma, Antonio Sánchez-Díaz, Sascha Ullbrich, Yuan Liu, Bernhard Siegmund, Andreas Mischok, Karl Leo, Mariano Campoy-Quiles, Weiwei Li, and Koen Vandewal. Polymer:fullerene bimolecular crystals for near-infrared spectroscopic photodetectors. *Advanced Materials*, 29(33):1702184, 2017.

[129] Krisztina Szendrei, Fabrizio Cordella, Maksym V. Kovalenko, Michaela Böberl, Günther Hesser, Maksym Yarema, Dorota Jarzab, Oleksandr V. Mikhnenko, Agnieszka Gocalinska, Michele Saba, Francesco Quochi, Andrea Mura, Giovanni Bongiovanni, Paul W. M. Blom, Wolfgang Heiss, and Maria Antonietta Loi. Solution-processable near-ir photodetectors based on electron transfer from pbs nanocrystals to fullerene derivatives. *Advanced Materials*, 21(6):683–687, 2009.

[130] Xiaoming Zhao, Tianjun Liu, Hongli Liu, Shirong Wang, Xianggao Li, Yuteng Zhang, Xueyan Hou, Zilu Liu, Wenda Shi, and T. John S. Dennis. Organic single-crystalline p–n

heterojunctions for high-performance ambipolar field-effect transistors and broadband photodetectors. *ACS Applied Materials & Interfaces*, 10(49):42715–42722, 2018.

[131] Xiaoming Zhao, Tianjun Liu, Xueyan Hou, Zilu Liu, Wenda Shi, and T. John S. Dennis. [60]pcbm single crystals: remarkably enhanced band-like charge transport, broadband uv-visible-nir photo-responsivity and improved long-term air-stability. *J. Mater. Chem. C*, 6:5489–5496, 2018.

[132] Xiaoming Zhao, Tianjun Liu, Wenda Shi, Xueyan Hou, Zilu Liu, and T. John S. Dennis. Understanding charge transport in endohedral fullerene single-crystal field-effect transistors. *The Journal of Physical Chemistry C*, 122(16):8822–8828, 2018.

[133] Xiaoming Zhao, Tianjun Liu, Yuzhou Cui, Xueyan Hou, Zilu Liu, Xingyi Dai, Jie Kong, Wenda Shi, and T. John S. Dennis. Antisolvent-assisted controllable growth of fullerene single crystal microwires for organic field effect transistors and photodetectors. *Nanoscale*, 10:8170–8179, 2018.

[134] Junfeng Yan and Brian R. Saunders. Third-generation solar cells: a review and comparison of polymer:fullerene, hybrid polymer and perovskite solar cells. *RSC Adv.*, 4:43286–43314, 2014.

[135] Martijn Lenes, Gert-Jan A. H. Wetzelaer, Floris B. Kooistra, Sjoerd C. Veenstra, Jan C. Hummelen, and Paul W. M. Blom. Fullerene bisadducts for enhanced open-circuit voltages and efficiencies in polymer solar cells. *Advanced Materials*, 20(11):2116–2119, 2008.

[136] Jenny Nelson. Polymer:fullerene bulk heterojunction solar cells. *Materials Today*, 14(10):462–470, 2011.

[137] Martijn Lenes, Steve W. Shelton, Alex B. Sieval, David F. Kronholm, Jan C. (Kees) Hummelen, and Paul W. M. Blom. Electron trapping in higher adduct fullerene-based solar cells. *Advanced Functional Materials*, 19(18):3002–3007, 2009.

[138] Myoung Hee Yun, Gi-Hwan Kim, Changduk Yang, and Jin Young Kim. Towards optimization of p3ht:bispcbm composites for highly efficient polymer solar cells. *J. Mater. Chem.*, 20:7710–7714, 2010.

[139] Long Ye, Shaoqing Zhang, Deping Qian, Qi Wang, and Jianhui Hou. Application of bis-pcbm in polymer solar cells with improved voltage. *The Journal of Physical Chemistry C*, 117(48):25360–25366, 2013.

[140] Hung-Wei Liu, Deng-Yang Chang, Wen-Yen Chiu, Syang-Peng Rwei, and Leeyih Wang. Fullerene bisadduct as an effective phase-separation inhibitor in preparing poly(3-hexylthiophene)–[6,6]-phenyl-c61-butyric acid methyl ester blends with highly stable morphology. *J. Mater. Chem.*, 22:15586–15591, 2012.

[141] Florian Steiner, Samuel Foster, Arthur Losquin, John Labram, Thomas D. Anthopoulos, Jarvist M. Frost, and Jenny Nelson. Distinguishing the influence of structural and energetic disorder on electron transport in fullerene multi-adducts. *Mater. Horiz.*, 2:113–119, 2015.

[142] W. Shi, X. Hou, T. Liu, X. Zhao, A. B. Sieval, J. C. Hummelen, and T. J. S. Dennis. Purification and electronic characterisation of 18 isomers of the opv acceptor material bis-[60]pcbm. *Chem. Commun.*, 53:975–978, 2017.

[143] Tong Liu, Isaac Abrahams, and T. John S. Dennis. Structural identification of 19 purified isomers of the opv acceptor material bispcbm by 13c nmr and uv–vis absorption spectroscopy and high-performance liquid chromatography. *The Journal of Physical Chemistry A*, 122(16):4138–4152, 2018. PMID: 29498855.

[144] Fei Zhang, Wenda Shi, Jingshan Luo, Norman Pellet, Chenyi Yi, Xiong Li, Xiaoming Zhao, T. John S. Dennis, Xianggao Li, Shirong Wang, Yin Xiao, Shaik Mohammed Zakeeruddin, Dongqin Bi, and Michael Grätzel. Isomer-pure bis-pcbm-assisted crystal engineering of perovskite solar cells showing excellent efficiency and stability. *Advanced Materials*, 29(17):1606806, 2017.

[145] Tomokazu Umeyama and Hiroshi Imahori. Isomer effects of fullerene derivatives on organic photovoltaics and perovskite solar cells. *Accounts of Chemical Research*, 52(8):2046–2055, 2019. PMID: 31318521.

[146] Jesús M. Fernández-García, Paul J. Evans, Salvatore Filippone, María Ángeles Herranz, and Nazario Martín. Chiral molecular carbon nanostructures. *Accounts of Chemical Research*, 52(6):1565–1574, 2019. PMID: 31181912.

[147] Xiaobo Shang, Inho Song, Hiroyoshi Ohtsu, Yoon Ho Lee, Tianming Zhao, Tatsuhiro Kojima, Ji Hyung Jung, Masaki Kawano, and Joon Hak Oh. Supramolecular nanostructures of chiral perylene diimides with amplified chirality for high-performance chiroptical sensing. *Advanced Materials*, 29(21):1605828, 2017.

[148] Pierre Josse, Ludovic Favereau, Chengshuo Shen, Sylvie Dabos-Seignon, Philippe Blanchard, Clément Cabanetos, and Jeanne Crassous. Enantiopure versus racemic naphthalimide end-capped helicenic non-fullerene electron acceptors: Impact on organic photovoltaics performance. *Chemistry – A European Journal*, 23(26):6277–6281, 2017.

[149] Francis Djojo, Andrea Herzog, Iris Lamparth, Frank Hampel, and Andreas Hirsch. Regiochemistry of twofold additions to [6,6] bonds in c60: Influence of the addend-independent cage distortion in 1,2-monoadducts. *Chemistry – A European Journal*, 2(12):1537–1547, 1996.

[150] Andreas Hirsch, Iris Lamparth, and Heinrich R. Karfunkel. Fullerene chemistry in three dimensions: Isolation of seven regioisomeric bisadducts and chiral trisadducts of c60 and di(ethoxycarbonyl)methylene. *Angewandte Chemie International Edition in English*, 33(4):437–438, 1994.

[151] Tiantian Cao, Ning Chen, Guangxin Liu, Yingbo Wan, José Darío Perea, Yijun Xia, Zhaowei Wang, Bo Song, Ning Li, Xiaohong Li, Yi Zhou, Christoph J. Brabec, and Yongfang Li. Towards a full understanding of regioisomer effects of indene-c60 bisadduct acceptors in bulk heterojunction polymer solar cells. *J. Mater. Chem. A*, 5:10206–10219, 2017.

[152] Hiroshi Ito, Yasuhiro Ishida, and Kazuhiko Saigo. Preparation and identification of bis(formylmethano)[60]fullerene isomers: the first systematic study on bifunctionalized [60]fullerenes with dissymmetric addends. *Tetrahedron Letters*, 46(50):8757–8760, 2005.

[153] Guochun Yang, Yanling Si, and Zhongmin Su. Theoretical study on the chiroptical optical properties of chiral fullerene c60 derivative. *The Journal of Physical Chemistry A*, 115(46):13356–13363, 2011. PMID: 21999769.

[154] Hitoshi Goto, Nobuyuki Harada, Jeanne Crassous, and François Diederich. Absolute configuration of chiral fullerenes and covalent derivatives from their calculated circular dichroism spectra. *J. Chem. Soc., Perkin Trans. 2*, pages 1719–1724, 1998.

[155] Francis Djojo and Andreas Hirsch. Synthesis and chiroptical properties of enantiomerically pure bis- and trisadducts of c60 with an inherent chiral addition pattern. *Chemistry – A European Journal*, 4(2):344–356, 1998.

[156] Hiroki Tanaka, Yoshihisa Inoue, and Tadashi Mori. Circularly polarized luminescence and circular dichroisms in small organic molecules: Correlation between excitation and emission dissymmetry factors. *ChemPhotoChem*, 2(5):386–402, 2018.

[157] F. Plasser. TheoDORE: A toolbox for a detailed and automated analysis of electronic excited state computations. *The Journal of Chemical Physics*, 152(8), 02 2020. 084108.

[158] Sota Sato, Asami Yoshii, Satsuki Takahashi, Seiichi Furumi, Masayuki Takeuchi, and Hiroyuki Isobe. Chiral intertwined spirals and magnetic transition dipole moments dictated by cylinder helicity. *Proceedings of the National Academy of Sciences*, 114(50):13097–13101, 2017.

[159] Tobat P. I. Saragi, Joscha Londenberg, and Josef Salbeck. Photovoltaic and photoconductivity effect in thin-film phototransistors based on a heterocyclic spiro-type molecule. *Journal of Applied Physics*, 102(4), 08 2007. 046104.

[160] T. R. Groves. 3 - Electron beam lithography. In Martin Feldman, editor, *Nanolithography*, pages 80–115. Woodhead Publishing, 11 2014.

[161] Dong-Myung Lee, Jin-Wook Song, Yu-Jin Lee, Chang-Jae Yu, and Jae-Hoon Kim. Control of Circularly Polarized Electroluminescence in Induced Twist Structure of Conjugate Polymer. *Advanced Materials*, 29(29):1700907, 8 2017.

[162] Li Wan, Jessica Wade, Francesco Salerno, Oriol Arteaga, Beth Laidlaw, Xuhua Wang, Thomas Penfold, Matthew J. Fuchter, and Alasdair J. Campbell. Inverting the Handedness of Circularly Polarized Luminescence from Light-Emitting Polymers Using Film Thickness. *ACS Nano*, 13(7):8099–8105, 2019.

[163] Beth Laidlaw, Julien Eng, Jessica Wade, Xingyuan Shi, Francesco Salerno, Matthew Fuchter, and Thomas James Penfold. On the factors influencing the chiroptical response of conjugated polymer thin films. *Chem. Commun.*, pages 1–4, 2021.

[164] Harald Haas, Liang Yin, Yunlu Wang, and Cheng Chen. What is LiFi? *Journal of Lightwave Technology*, 34(6):1533–1544, 3 2016.

[165] Ardalan Armin, Mike Hambsch, Il Ku Kim, Paul L Burn, Paul Meredith, and Ebinazar B Namdas. Thick junction broadband organic photodiodes. *Laser & Photonics Reviews*, 8(6):924–932, 11 2014.

[166] Francesco Zinna, Umberto Giovanella, and Lorenzo Di Bari. Highly Circularly Polarized Electroluminescence from a Chiral Europium Complex. *Advanced Materials*, 27(10):1791–1795, 3 2015.

[167] Alexander L. Kanibolotsky, Nicolas Laurand, Martin D. Dawson, Graham A. Turnbull, Ifor D.W. Samuel, and Peter J. Skabara. Design of Linear and Star-Shaped Macromolecular Organic Semiconductors for Photonic Applications. *Accounts of Chemical Research*, 52(6):1665–1674, 6 2019.

[168] Rohanah Hussain, Tamás Jávorfi, and Giuliano Siligardi. CD Imaging at High Spatial Resolution at Diamond B23 Beamline: Evolution and Applications. *Frontiers in Chemistry*, 9:128, 4 2021.

[169] Yohji Shindo, Masayuki Nakagawa, and Yasuhiro Ohmi. On the Problems of CD Spectropolarimeters. II: Artifacts in CD Spectrometers. *Appl. Spectrosc.*, 39(5):860–868, 9 1985.

[170] Yohji Shindo, Motohide Nishio, and Shiro Maeda. Problems of CD spectrometers (V): Can we measure CD and LD simultaneously? Comments on differential polarization microscopy (CD and linear dichroism). *Biopolymers*, 30(3-4):405–413, 1990.

[171] William Mickols and Marcos F. Maestre. Scanning differential polarization microscope: Its use to image linear and circular differential scattering. *Review of Scientific Instruments*, 59(6):867, 6 1988.

[172] M F Maestre and J E Katz. A circular dichroism microspectrophotometer. *Biopolymers*, 21(9):1899–1908, 1982.

[173] Kacey Claborn, Eileen Puklin-Faucher, Miki Kurimoto, Werner Kaminsky, and Bart Kahr. Circular Dichroism Imaging Microscopy: Application to Enantiomorphous Twinning in Biaxial Crystals of 1,8-Dihydroxyanthraquinone. *Journal of the American Chemical Society*, 125(48):14825–14831, 12 2003.

[174] Marius Morgenroth, Mirko Scholz, Min Ju Cho, Dong Hoon Choi, Kawon Oum, and Thomas Lenzer. Mapping the broadband circular dichroism of copolymer films with supramolecular chirality in time and space. *Nature Communications*, 13(1):210, 2022.

[175] Matteo Savoini, Paolo Biagioni, Stefan C.J. Meskers, Lamberto Duò, Bert Hecht, and Marco Finazzi. Spontaneous formation of left- and right-handed cholesterically ordered domains in an enantiopure chiral polyfluorene film. *Journal of Physical Chemistry Letters*, 2(12):1359–1362, 6 2011.

[176] Tetsuya Narushima and Hiromi Okamoto. Circular dichroism nano-imaging of two-dimensional chiral metal nanostructures. *Phys. Chem. Chem. Phys.*, 15(33):13805–13809, 2013.

[177] M Khorasaninejad, W T Chen, A Y Zhu, J Oh, R C Devlin, D Rousso, and F Capasso. Multispectral Chiral Imaging with a Metalens. *Nano Letters*, 16(7):4595–4600, 2016.

[178] John H. Freudenthal, Eva Hollis, and Bart Kahr. Imaging chiroptical artifacts. *Chirality*, 21(1E):E20–E27, 1 2009.

[179] Gianluigi Albano, Marcin Górecki, Gennaro Pescitelli, Lorenzo Di Bari, Tamás Jávorfi, Rohanah Hussain, and Giuliano Siligardi. Electronic circular dichroism imaging (CD i) maps local aggregation modes in thin films of chiral oligothiophenes. *New Journal of Chemistry*, 43(36):14584–14593, 9 2019.

[180] Francesco Zinna, Claudio Resta, Marcin Górecki, Gennaro Pescitelli, Lorenzo Di Bari, Tamás Jávorfi, Rohanah Hussain, and Giuliano Siligardi. Circular Dichroism Imaging: Mapping the Local Supramolecular Order in Thin Films of Chiral Functional Polymers. *Macromolecules*, 50(5):2054–2060, 3 2017.

[181] Dora M. Răsădean, Tiberiu M. Gianga, Tamás Jávorfi, Rohanah Hussain, Giuliano Siligardi, and G. Dan Pantoș. Mapping the Chiroptical Properties of Local Domains in Thin Films of Chiral Silicon Phthalocyanines by CD Imaging. *Molecules 2020, Vol. 25, Page 6048*, 25(24):6048, 12 2020.

[182] S Thomas Lee and M K Hari. Circular polarization division multiplexing for faster coherent fiber optic communication systems. In *2012 International Conference on Optical Engineering (ICOE)*, pages 1–2, 2012.

[183] Li Wan, Jessica Wade, Xingyuan Shi, Shengda Xu, Matthew J. Fuchter, and Alasdair J. Campbell. Highly Efficient Inverted Circularly Polarized Organic Light-Emitting Diodes. *ACS Applied Materials & Interfaces*, 12(35):39471–39478, 9 2020.

[184] Hao Yan, Jessica Wade, Li Wan, Sooncheol Kwon, Matthew J. Fuchter, Alasdair J. Campbell, and Ji-Seon Kim. Enhancing hole carrier injection via low electrochemical doping on circularly polarized polymer light-emitting diodes. *Journal of Materials Chemistry C*, 10(25):9512–9520, 6 2022.

[185] Tamas Javorfi, Tiberiu-Marius Gianga, Rohanah Hussain, and Giuliano Siligardi. Oral Communication. In *18th International Conference of Chiroptical Spectroscopy (CD2022), Oral Communication*, 2022.

[186] Bruno Baguenard, Amina Bensalah-Ledoux, Laure Guy, François Riobé, Olivier Maury, and Stephan Guy. Theoretical and experimental analysis of circularly polarized lumi-

nescence spectrophotometers for artifact-free measurements using a single CCD camera. *Research Square*, 7 2022.

[187] Xingyuan Shi, Vojtech Nádaždy, Aleksandr Perevedentsev, Jarvist M. Frost, Xuhua Wang, Elizabeth von Hauff, Roderick C. I. MacKenzie, and Jenny Nelson. Relating chain conformation to the density of states and charge transport in conjugated polymers: The role of the β-phase in poly(9,9-dioctylfluorene). *Phys. Rev. X*, 9:021038, May 2019.

[188] Andrius Aukštuolis, Nerijus Nekrašas, Kristijonas Genevičius, and Giedrius Juška. Investigation of charge carrier mobility and recombination in pbdttpd thin layer structures. *Organic Electronics*, 90:106066, 2021.

Appendix A

Reuse Permissions for Chapter 2

Pathways to increase the dissymmetry in the interaction of chiral light and chiral molecules

J. L. Greenfield, J. Wade, J. R. Brandt, X. Shi, T. J. Penfold and M. J. Fuchter, Chem. Sci., 2021, 12, 8589 DOI: 10.1039/D1SC02335G

This article is licensed under a Creative Commons Attribution 3.0 Unported Licence. You can use material from this article in other publications without requesting further permissions from the RSC, provided that the correct acknowledgement is given.

Best practices in the measurement of circularly polarised photodetectors

M. D. Ward, W. Shi, N. Gasparini, J. Nelson, J. Wade and M. J. Fuchter, J. Mater. Chem. C, 2022, 10, 10452 DOI: 10.1039/D2TC01224C

This article is licensed under a Creative Commons Attribution 3.0 Unported Licence. You can use material from this article in other publications without requesting further permissions from the RSC, provided that the correct acknowledgement is given.

Appendix B

Reuse Permission for Chapter 3

Best practices in the measurement of circularly polarised photodetectors

M. D. Ward, W. Shi, N. Gasparini, J. Nelson, J. Wade and M. J. Fuchter, J. Mater. Chem. C, 2022, 10, 10452 DOI: 10.1039/D2TC01224C

This article is licensed under a Creative Commons Attribution 3.0 Unported Licence. You can use material from this article in other publications without requesting further permissions from the RSC, provided that the correct acknowledgement is given.

RightsLink

Help | Live Chat



Fullerene Desymmetrization as a Means to Achieve Single-Enantiomer Electron Acceptors with Maximized Chiroptical Responsiveness

Author: Wenda Shi, Francesco Salerno, Matthew D. Ward, et al

Publication: Advanced Materials

Publisher: John Wiley and Sons

Date: Nov 23, 2020

© 2020 The Authors. Advanced Materials published by Wiley-VCH GmbH

Open Access Article

This is an open access article distributed under the terms of the Creative Commons CC BY license, which permits unrestricted use, distribution, and reproduction in any medium, provided the original work is properly cited.

You are not required to obtain permission to reuse this article.

For an understanding of what is meant by the terms of the Creative Commons License, please refer to Wiley's Open Access Terms and Conditions.

Permission is not required for this type of reuse.

Wiley offers a professional reprint service for high quality reproduction of articles from over 1400 scientific and medical journals. Wiley's reprint service offers:

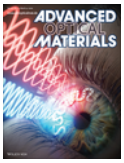
• Peer reviewed research or reviews
• Tailored collections of articles
• A professional high quality finish
• Glossy journal style color covers
• Company or brand customisation
• Language translations
• Prompt turnaround times and delivery directly to your office, warehouse or congress.

Please contact our Reprints department for a quotation. Email corporatesaleseurope@wiley.com or corporatesalesusa@wiley.com or corporatesalesDE@wiley.com.

© 2022 Copyright - All Rights Reserved | Copyright Clearance Center, Inc. | Privacy statement | Data Security and Privacy | For California Residents | Terms and ConditionsComments? We would like to hear from you. E-mail us at customercare@copyright.com

RightsLink

Help | Live Chat



Highly Selective High-Speed Circularly Polarized Photodiodes Based on π-Conjugated Polymers

Author: Matthew D. Ward, Jessica Wade, Xingyuan Shi, et al

Publication: Advanced Optical Materials

Publisher: John Wiley and Sons

Date: Nov 2, 2021

© 2021 The Authors. Advanced Optical Materials published by Wiley-VCH GmbH

Open Access Article

This is an open access article distributed under the terms of the Creative Commons CC BY license, which permits unrestricted use, distribution, and reproduction in any medium, provided the original work is properly cited.

You are not required to obtain permission to reuse this article.

For an understanding of what is meant by the terms of the Creative Commons License, please refer to Wiley's Open Access Terms and Conditions.

Permission is not required for this type of reuse.

Wiley offers a professional reprint service for high quality reproduction of articles from over 1400 scientific and medical journals. Wiley's reprint service offers:

• Peer reviewed research or reviews
• Tailored collections of articles
• A professional high quality finish
• Glossy journal style color covers
• Company or brand customisation
• Language translations
• Prompt turnaround times and delivery directly to your office, warehouse or congress.

Please contact our Reprints department for a quotation. Email corporatesaleseurope@wiley.com or corporatesalesusa@wiley.com or corporatesalesDE@wiley.com.

© 2022 Copyright - All Rights Reserved | Copyright Clearance Center, Inc. | Privacy statement | Data Security and Privacy | For California Residents | Terms and ConditionsComments? We would like to hear from you. E-mail us at customercare@copyright.com

Appendix C

Reuse Permission for Chapter 4

RightsLink

Help Live Chat



Fullerene Desymmetrization as a Means to Achieve Single-Enantiomer Electron Acceptors with Maximized Chiroptical Responsiveness

Author: Wenda Shi, Francesco Salerno, Matthew D. Ward, et al

Publication: Advanced Materials

Publisher: John Wiley and Sons

Date: Nov 23, 2020

© 2020 The Authors. Advanced Materials published by Wiley-VCH GmbH

Open Access Article

This is an open access article distributed under the terms of the Creative Commons CC BY license, which permits unrestricted use, distribution, and reproduction in any medium, provided the original work is properly cited.

You are not required to obtain permission to reuse this article.

For an understanding of what is meant by the terms of the Creative Commons License, please refer to Wiley's Open Access Terms and Conditions.

Permission is not required for this type of reuse.

Wiley offers a professional reprint service for high quality reproduction of articles from over 1400 scientific and medical journals. Wiley's reprint service offers:

• Peer reviewed research or reviews
• Tailored collections of articles
• A professional high quality finish
• Glossy journal style color covers
• Company or brand customisation
• Language translations
• Prompt turnaround times and delivery directly to your office, warehouse or congress.

Please contact our Reprints department for a quotation. Email corporatesaleseurope@wiley.com or corporatesalesusa@wiley.com or corporatesalesDE@wiley.com.

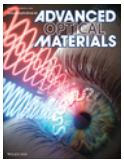
© 2022 Copyright - All Rights Reserved | Copyright Clearance Center, Inc. | Privacy statement | Data Security and Privacy | For California Residents | Terms and ConditionsComments? We would like to hear from you. E-mail us at customercare@copyright.com

Appendix D

Reuse Permission for Chapter 5

RightsLink

Help | Live Chat



Highly Selective High-Speed Circularly Polarized Photodiodes Based on π-Conjugated Polymers

Author: Matthew D. Ward, Jessica Wade, Xingyuan Shi, et al

Publication: Advanced Optical Materials

Publisher: John Wiley and Sons

Date: Nov 2, 2021

© 2021 The Authors. Advanced Optical Materials published by Wiley-VCH GmbH

Open Access Article

This is an open access article distributed under the terms of the Creative Commons CC BY license, which permits unrestricted use, distribution, and reproduction in any medium, provided the original work is properly cited.

You are not required to obtain permission to reuse this article.

For an understanding of what is meant by the terms of the Creative Commons License, please refer to Wiley's Open Access Terms and Conditions.

Permission is not required for this type of reuse.

Wiley offers a professional reprint service for high quality reproduction of articles from over 1400 scientific and medical journals. Wiley's reprint service offers:

• Peer reviewed research or reviews
• Tailored collections of articles
• A professional high quality finish
• Glossy journal style color covers
• Company or brand customisation
• Language translations
• Prompt turnaround times and delivery directly to your office, warehouse or congress.

Please contact our Reprints department for a quotation. Email corporatesaleseurope@wiley.com or corporatesalesusa@wiley.com or corporatesalesDE@wiley.com.

© 2022 Copyright - All Rights Reserved | Copyright Clearance Center, Inc. | Privacy statement | Data Security and Privacy | For California Residents | Terms and ConditionsComments? We would like to hear from you. E-mail us at customercare@copyright.com

Appendix E

Reuse Permission for Chapter 6

Development of low-cost, compact chiroptical imaging systems

M. D. Ward, R. Docherty, L. Minion, X. Shi, K. Anson, G. Siligardi, J. Nelson, J. Wade and M. J. Fuchter, Nanoscale, 2024, 16, 11623 DOI: 10.1039/D4NR01651C

This article is licensed under a Creative Commons Attribution 3.0 Unported Licence. You can use material from this article in other publications without requesting further permissions from the RSC, provided that the correct acknowledgement is given.